Collisions of low-energy antiprotons and protons with atoms and molecules

A theoretical study

DISSERTATION

zur Erlangung des akademischen Grades

doctor rerum naturalium
(Dr. rer. nat.)
im Fach Physik

eingereicht an der
Mathematisch-Wissenschaftlichen Fakultät I
Humboldt-Universität zu Berlin

von
Dipl.-Phys. Armin Lühr
geboren am 23.02.1980 in Braunschweig

Präsident der Humboldt-Universität zu Berlin:
Prof. Dr. Dr. h.c. Christoph Markschies

Dekan der Mathematisch-Wissenschaftlichen Fakultät I:
Prof. Dr. Lutz-Helmut Schön

Gutachter:
1. Priv.-Doz. Dr. A. Saenz
2. Prof. Dr. Hans Jürgen Lüdde
3. Prof. Dr. Tom Kirchner

eingereicht am: 04.01.2010
Tag der mündlichen Prüfung: 18.02.2010

Abstract

Antiproton ($\bar{p}$) collisions have evolved to a powerful tool for the testing of dynamic electron correlations in atoms and molecules. While advances in the understanding of $\bar{p}$ collisions with the simplest one- and two-electron atoms, H and He, have been achieved experiment and theory did not agree for low-energy $\bar{p}$ + He collisions ($< 40\,\mathrm{keV}$), stimulating a vivid theoretical activity. On the other hand, only very few theoretical $\bar{p}$ studies can be found considering molecular as well as other atomic targets, in contrast to proton (p) collisions. This is in particular true for $\bar{p}$ impacts on H_2 despite its fundamental role in representing the simplest two-electron molecule. The obtained results may be useful for the $\bar{p}$ experiments at CERN (e.g., antihydrogen production) and in particular for the facility design of low-energy $\bar{p}$ storage rings (e.g., at FLAIR) where a precise knowledge of the $\bar{p}$ interaction with the dominant residual-gas molecule H_2 is needed.

In this work a nonperturbative, time-dependent numerical approach is developed which describes ionization and excitation of atoms or molecules by either $\bar{p}$ or p impact based on the impact-parameter method. A spectral close-coupling method is employed for solving the time-dependent Schrödinger equation in which the scattering wave function is expanded in (effective) one- or two-electron eigenstates of the target. This includes for the first time a full two-electron, two-center description of the H_2 molecule in $\bar{p}$ collisions. The radial part of the one-electron eigenstates is expanded in B splines while the two-electron basis is obtained with a configuration-interaction approach.

Calculations are performed for $\bar{p}$ collisions with H, ${H_2}^+$, and H_2 as well as with He and alkali-metal atoms Li, Na, K, and Rb. Additionally, data are obtained for p collisions with H_2, Li, Na, and K. The developed method is tested and validated by detailed comparison of the present findings for p impacts and for $\bar{p}$ + He collisions with literature data. On the other hand, total and differential cross sections for ionization and excitation of the targets by $\bar{p}$ impact complement the sparse literature data of this kind. Results gained from different targets as well as from $\bar{p}$ and p impact are compared with each other and assessed. Furthermore, results obtained with one-electron model potentials are compared to the full two-electron description of H_2. Finally, stopping powers for $\bar{p}$ impacts are determined. A case study for H, H_2, and He is performed which distinguishes for the first time systematically between the stopping powers of atomic and molecular hydrogen. In this work special emphasis is put on the detailed investigation of $\bar{p}$ + H_2 collisions. This includes the dependence of the cross sections on the internuclear distance and on the molecular orientation relative to the projectile trajectory.

Zusammenfassung

Stöße mit Antiprotonen ($\bar{p}$) haben sich zu einer mächtigen Methode zur Untersuchung von dynamischen Elektronenkorrelationen in Atomen und Molekülen entwickelt. Während Fortschritte beim Verständnis von $\bar{p}$-Stößen mit den einfachsten Ein- und Zwei-Elektronen-Atomen H und He erreicht wurden, stimmten Experiment und Theorie für $\bar{p}$ + He Stöße bei niedrigen Energien ($< 40\,\mathrm{keV}$) jedoch nicht überein, was eine lebhafte theoretische Aktivität zur Folge hatte. Andererseits existieren nur sehr wenige Studien für Moleküle aber auch andere Atome, im Gegensatz zu Stößen mit Protonen (p). Dies gilt im Besonderen für H_2, trotz seiner fundamentalen Rolle als einfachstes Zwei-Elektronen-Molekül. Die erhaltenen Ergebnisse dürften von Nutzen für die $\bar{p}$-Experimente am CERN und im Speziellen für die technische Auslegung von Speicherringen für $\bar{p}$ mit niedrigen Energien wie z.B. bei FLAIR sein.

In dieser Arbeit wird eine, zeitabhängige, nicht störungstheoretische numerische Methode entwickelt, welche Ionisation und Anregung von Atomen oder Molekülen in Stößen mit entweder $\bar{p}$ oder p beschreibt und auf der *impact-parameter* Methode basiert. Es wird eine spektrale *close-coupling* Methode verwendet, um die zeitabhängige Schrödinger-Gleichung zu lösen, in welcher die Wellenfunktion in (effektive) Ein- oder Zwei-Elektronen-Eigenzustände des Targets entwickelt wird. Dies beinhaltet auch eine erstmalige volle Zwei-Elektronen-Beschreibung von H_2 in $\bar{p}$-Stößen.

Rechnungen werden für $\bar{p}$-Stöße mit H, ${H_2}^+$, und H_2 sowie He und den Alkaliatomen Li, Na, K und Rb durchgeführt. Daten für p-Stöße werden für H_2 und die Alkaliatomen Li, Na und K erzielt. Die Methode wird durch einen detaillierten Vergleich der erhaltenen Ergebnisse für p-Stöße und für $\bar{p}$ + He mit Literaturdaten verifiziert. Andererseits ergänzen die totalen und differentiellen Wirkungsquerschnitte für Ionisation und Anregung der Targets in $\bar{p}$-Stößen die spärliche Literatur. Sowohl die Resultate für verschiedene Targets als auch für $\bar{p}$- und p-Stöße werden miteinander verglichen. Ein Schwerpunkt dieser Arbeit liegt auf der Untersuchung von $\bar{p}$ + H_2, welche die Abhängigkeit der Wirkungsquerschnitte vom Kernabstand und von der relativen Ausrichtung der molekularen Achse beinhaltet. Weiterhin werden Ergebnisse mit Ein-Elektronen-Modellpotentialen erzielt und mit der vollen Zwei-Elektronen-Beschreibung von H_2 verglichen. Außerdem werden Energieverluste in $\bar{p}$-Stöße bestimmt. Eine detaillierte Fallstudie für H, H_2 und He wird durchgeführt, welche erstmals systematisch zwischen atomaren und molekularen Wasserstoff unterscheidet. Sie beinhaltet auch eine kritische Diskussion der theoretischen und experimentellen Literatur.

List of publications

Eight peer-reviewed publications originate from the results discussed in this work [1–8]. They are listed below in chronological order and are cited in the following by the corresponding capital letters [A] to [H].

[A] A. Lühr and A. Saenz, **Antiproton and proton collisions with the alkali-metal atoms Li, Na, and K.** Phys. Rev. A **7**7, 052713 (2008).

[B] A. Lühr and A. Saenz, **Antiproton collisions with molecular hydrogen.** Phys. Rev. A **7**8, 032708 (2008).

[C] A. Lühr, Y. V. Vanne, and A. Saenz, **Parameter-free one-center model potential for an effective one-electron description of molecular hydrogen.** Phys. Rev. A **7**8, 042510 (2008).

[D] A. Lühr, N. Fischer, and A. Saenz, **Interaction of antiprotons with Rb atoms and a comparison of antiproton stopping powers of the atoms H, Li, Na, K, and Rb.** Hyperfine Interact. **1**94, 51 (2009).

[E] A. Lühr and A. Saenz, **Collisions of low-energy antiprotons with molecular hydrogen: ionization, excitation and stopping power.** Hyperfine Interact. **1**94, 59 (2009).

[F] A. Lühr and A. Saenz, **Stopping power of antiprotons in H, $\mathbf{H_2}$, and He targets.** Phys. Rev. A **7**9, 042901 (2009).

[G] A. Lühr and A. Saenz, **Collisions of antiprotons with hydrogen molecular ions.** Phys. Rev. A **8**0, 022705 (2009).

[H] A. Lühr and A. Saenz, **Full two-electron calculations of antiproton collisions with molecular hydrogen.** Phys. Rev. A **8**1, 010701 (R) (2010).

Contents

Part I.

Introduction

Introduction

Ordinary matter which surrounds us is made up of atoms and molecules. The idea that matter is build up of small elementary quantities which cannot be divided in smaller portions was already discussed 2500 years ago by the Greek philosophers Leukipp and Demokrit who are considered as the founders of atomism.[a] But only in the beginning of the last century the concept that atoms are composed of electrons which orbit a positively charged nucleus was established. Thereby, it was found in experiments with ions colliding on matter that the atomic nucleus comprises nearly the whole mass of the atom while its extension is five orders of magnitude smaller compared to that of the total atom. It was the growing interest in the understanding of atoms, their constituents, and their interactions which finally lead to the formulation of the quantum theory.

Ion collisions — what are they good for?

The interest in ion collisions and their importance initially originated from the desire for a fundamental understanding of the constitution of matter. Later on they became a versatile tool to also probe the inherent dynamics of the studied systems. While at the beginning atomic and molecular systems were in the focus, the increase of the impact energy allowed for subatomic studies. The increase of energy corresponds to a decrease of the associated deBroglie wavelength of the ions and permits therefore resolutions which are necessary in nuclear and even elementary particle physics. Currently, unprecedented energies in ion collisions are achieved at the LHC (Large Hadron Collider) at CERN which was built to help scientists to answer key unresolved questions in particle physics.

On the other hand, ion collisions with atoms and molecules have evolved from a technique for fundamental research to a subject with significant importance for various applications. This is due to the precise characterization of the involved interaction processes, like the ionization and excitation of the target atoms, transfer of electrons between target and projectile, and the energy loss of the projectile while traversing the target medium. These processes are elementary to many other branches of research as the physics of the atmosphere, astrophysics, radiation physics but are also of interest for other subjects like quantum chemistry, biophysics, or even medicine. The last subject may be used here as an example for the transition from fundamental to applied research by briefly introducing the conceptual idea behind cancer therapy employing ion collisions.

---

[a] The name *atom* comes from the ancient Greek $\alpha\tau o\mu o\zeta$ / *atomos*, which means uncuttable, or indivisible, something that cannot be divided further. However, the physical entities called *atoms* are composed of electrons and a nucleus which consists of protons and neutrons. The latter two nuclear constituents can be further divided into quarks. Thus, the elementary particles, i.e. electrons and quarks, rather than the atoms may be considered in a philosophical sense as the elementary indivisible quantities.

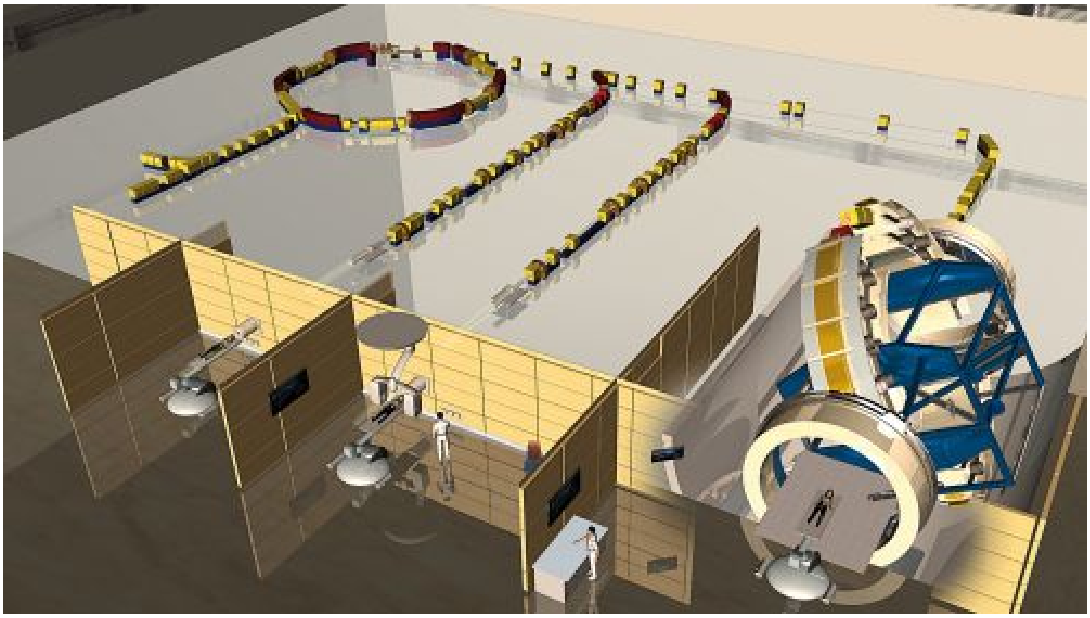

Figure 0.1.: *Heidelberger Ionenstrahl-Therapiezentrum HIT for Heavy Ion Therapy. The accelerator ring and the beam lines to the three treatment places are schematically shown. Reproduced from [9].*

The aim of this so called particle therapy is to destroy the tumor cells with minimal harm of the surrounding tissue. Therefore, the physical dose and the biological effect have to be maximal within the tumor. In the healthy tissue, however, they should be as small as possible. Ions penetrate into the human body and finally get stuck at a certain depth which is determined by the initial ion velocity due to the energy loss. Thereby, the dose along the ion trajectory is small and only at its end in a small volume where the ions are stopped the dose has a sharp localized maximum also referred to as Bragg peak. This dose maximum can be shifted all over the tumor by varying the initial ion velocity. It is the understanding and controlling of the resulting dose distribution which requires a thorough knowledge of the involved collision processes.

The biological effect of a successful radiation therapy is given by the irreparable damaging of the genetic constitution of the cancer cells by what these cells are finally killed. In comparison to X-rays, which traverse the whole body with a maximal dose close to the skin, particle therapy with the same physical dose results in an improved biological effect, since a considerably greater damage of the tumor can be achieved without additional stressing of the healthy tissue. Fundamental research, especially for particle therapy using carbon ions, has been performed at the Gesellschaft für Schwerionenforschung (GSI) at Darmstadt during the last decade. The achieved understanding has been transferred into the Heidelberger Ionenstrahl-Therapiezentrum (HIT) [9] for cancer therapy which was just inaugurated in November 2009 and is shown schematically in Fig. 0.1.

Antiproton physics — questioning the perfection of the mirror

There is considerable speculation why the observable universe is apparently almost entirely matter. It is unclear, whether there exist other places that are almost entirely antimatter instead. However, under the assumption of the *Big Bang*[b] scenario, at this time the apparent asymmetry of matter and antimatter in the visible universe is one of the greatest unsolved problems in physics.

The Dirac theory, a fundamental relativistic quantum-mechanical description, provides solutions which describe matter as well as antimatter. According to this theory an interesting property of free antiparticles is that they can be treated mathematically as if they were particles of the same mass and of oppositely signed charge of the same absolute value going backward in space and time. This is the consequence of one of the most important symmetries of Nature: CPT invariance. It states that the following operations: charge conjugation C (i.e. changing particles into antiparticles), parity change P (i.e. the mirror reflection of space coordinates), and time reversal T, when performed simultaneously, do not change the measurable physical properties of the system. The properties of the antiproton are therefore predicted by CPT symmetry to be exactly related to those of the proton. In particular, the mass and lifetime of the antiproton is predicted to be the same as those of the proton, and the electric charge and magnetic moment of the antiproton to be opposite in sign and equal in magnitude to those of the proton. CPT symmetry is a basic consequence of quantum field theory and no violations of it have ever been detected. Although its validity may be considered to be likely, it is not verified despite the fundamental role CPT symmetry plays in the theoretical description of physics.

With the advent of the low-energy antiproton ring (LEAR) and later on also the antiproton decelerator (AD) both being a part of CERN a new branch of physics was established. It covers a scientific area where atomic and molecular physics overlap with nuclear as well as particle physics. Thereby, antiprotons are slowed down to velocities which are of similar magnitude as the Bohr velocity, i.e., the velocity of an electron in a hydrogen atom. Phenomena occurring in the corresponding energy regime are often well described by atomic and molecular physics. One process which may happen in interactions of low-energy antiprotons with atoms and molecules is the antiproton capture. Thereby, a relatively heavy antiproton, which is approximately 1836 times heavier than an electron, is capture by a positive nucleus similarly to an electron in ordinary atoms and molecules. In the resulting antiprotonic atoms[c] the antiproton is due to its heavy mass compared to the electron on average much closer to the nucleus and can be used as sensitive probe for effects of the nucleus such as the hyperfine interaction.

---

[b] The *Big Bang* is a cosmological model of the initial conditions and subsequent development of the universe. The term *Big Bang* generally refers to the idea that the universe has expanded from a primordial hot and dense initial condition at some finite time in the past and continues to expand to this day.

[c] Also other exotic atoms are known. Among these are muonic and mesonic atoms in which one or more of the orbital electrons has been replaced by a muon or meson, respectively. The muon is a lepton and it may be well described as a heavy electron, while a meson is build up of quarks and can also interact via the strong force with the nucleus.

Furthermore, when the wave functions of the captured antiproton and the protons of the nucleus start to considerably overlap, also the short-ranged strong interaction which is exchanged between quarks starts to play a role. This is of course in contrast to the leptonic electrons which do not interact via the strong force. The strong interaction may eventually lead to annihilation of the antiproton and one of the protons of the nucleus. The energy released in the annihilation is determined by the fundamental equivalence $E = m\,c^2$ between energy E and mass m, where the proportionality factor is given by the square of speed of light in a vacuum c^2. Afterward, the energy E [d] usually redistributed among a number of reaction products as, e.g., lighter particles like mesons and photons which are created. The physical properties of the sum of all final products is constraint by the conservation laws. In order to detect antiprotonic systems in experiments these annihilation products and their properties are usually measured. Afterward, the characteristics of the initial antiprotonic systems are reconstructed using the measured data of the annihilation products and the conservation laws.

At CERN there are currently four international collaborations working at the AD. These are ASACUSA [10], ATHENA / ALPHA [11, 12], ATRAP [13], and AEGIS [14], all concentrating on the physics involving slow antiprotons. Their major research subjects may be briefly summarized by the following four topics, while this list is not meant to be exclusive.

First, the formation of stable atoms formed by antimatter starting with the most basic system antihydrogen which consists of an antiproton and a positron. The production of antihydrogen has already been successfully demonstrated by more than one of the collaborations and for the first time at the AD in 2002 [15, 16]. However, in order to perform high-precision measurements with the antiatoms it is inevitable to have full control over these objects. This includes the ability to trap and deexcite a considerable number of antihydrogen into the electronic ground state which is the focus of the current experimental activities [11–14].

Second, there is the testing of CPT invariance by comparing matter with antimatter. There are two main attempts to achieve highly accurate experimental confirmation. The transition from the 1s to the 2s state, which is known very precisely for hydrogen atoms [e] [17, 18], should be compared to the same transition in antihydrogen [13]. Another approach is the detailed study of antiprotonic atoms, e.g., helium atoms with an electron replaced by an antiproton [10, 19–21].

Third, the nature of gravity of antimatter is still not known yet. Thereby, the gravitational influence of antimatter on antimatter as well as on ordinary matter has to be considered. It can only be measured accurately using neutral antimatter like antihydrogen. The force on charged antiparticles due to the Coulomb interaction would otherwise dominate by far the gravitational interaction. The Earth's local gravitational acceleration g on antihydrogen is intended to be determined experimentally in a first direct

---

[d] The released energy E in the annihilation is at least 1.876 GeV which corresponds to the sum of the rest masses m_0 of antiproton and proton. E is larger, if the sum of the kinetic energies of proton and antiproton was nonzero and therefore $m > m_0$.

[e] The 1s to 2s two-photon transition in hydrogen atoms is with an accuracy of about 1 part in 10^{14} one of the experimentally best accessible quantities in physics.

measurement [14, 22]. A relative precision of 1% should be achieved by observing the vertical displacement of the shadow image produced by an antihydrogen beam, as it horizontally traverses a Moiré deflectometer.

Finally, fundamental collisions involving low-energy antiprotons as projectiles with impact energies $E < 10$ MeV are of interest for detailed studies of various targets such as atoms, molecules, surfaces and condensed matter [10]. There are a number of features which make these collisions a unique system [23]. Since this work deals with the theoretical description of low-energy antiproton impacts on atoms and molecules the following paragraphs discuss the corresponding physics and the state of the art in some detail.

Antiproton collisions — magnifying glass for dynamic correlation

A central point of atomic and molecular physics is the description of charged particles moving in a Coulomb field. One of the simplest and most basic systems which provides an insight into dynamic processes of charged particles is the collision of antiprotons with atoms. Although the experimental production of low-energy antiprotons is demanding,[f] this effort is compensated by a number of advantages, especially regarding the description of the collision processes. The heavy mass of the antiproton allows for a semiclassical theoretical description in which the projectile moves on a classical trajectory while the electrons are treated quantum-mechanically. In contrast to electrons, a semiclassical approach is applicable in the case of antiprotons even for impact velocities around and below the Bohr velocity v_0. Furthermore, the investigation of "slow" ionizing collisions is possible. In contrast to positively charged projectiles, for antiprotons there is no complication regarding the ionization of the target due to charge transfer, i.e. the capture of target electrons by the projectile.

Further attention is drawn to this topic due to the upcoming Facility for Antiproton and Ion Research (FAIR) [24] with the international collaborations FLAIR (Facility for Low-energy Antiproton and Ion Research) [25] and SPARC (Stored Particle Atomic Research Collaboration) [26], both intending to investigate antiproton-driven processes and even kinematically complete collision experiments [27]. A considerable amount of new experimental data can be expected in the near future. These experimental efforts complement the recent intense activity dealing with the mostly theoretical study of antihydrogen–hydrogen scattering at very low energies [28–33].

However, already the design of FLAIR requires a reliable knowledge of low-energy antiproton cross sections. In order to estimate the requirements of the vacuum system, especially in low-energy (antiproton) storage rings, a precise knowledge of the interactions with the residual gases is necessary. In particular the maximally acceptable residual-gas pressure is of central interest, since the collisions of antiprotons with residual-gas atoms and molecules may influence the properties of the antiproton beam, which may lead to a reduction of the life time of the beam. Due to the considerable expenses for producing low-energy antiprotons it is important to minimize the antiproton loss. On the other

---

[f] An illustrative and also informative description of the "antimatter factory" AD at CERN can be found under the link http://livefromcern.web.cern.ch/livefromcern/ antimatter/factory/AM-factory00.html.

Figure 0.2.: *Schematic drawings of the currently built Facility for Antiproton and Ion Research (FAIR) at the GSI at Darmstadt (left) and of the setup of the incorporated Facility for Low-energy and Ion Research (FLAIR) on an enlarged scale (right). Reproduced from [24, 25]. Note the scales of these facilities.*

hand high demands on the vacuum system are technically very challenging considering the large scale of the facility. Note, the residual gas in the storage rings is supposed to consist mainly of molecular hydrogen.

Furthermore, a thorough understanding of the fundamental interactions occurring in collisions with antiprotons is obviously an important prerequisite for the high-precision low-energy antiproton activities performed at CERN (introduced before) as well as the planned experiments at FAIR. Thereby, quantities like the ionization and excitation cross sections of the involved atoms and molecules as well as the resulting stopping powers are of interest in order to estimate experimental accuracies and possible corrections.

State of the art — achievements and open issues

In what follows the discussion concentrates on the status of two major topics related to antiproton collisions at the time before this work was initiated. First, the description of the collision process itself in the case of atomic and molecular targets with an emphasis on ionization. Second, the attempt to understand the stopping powers in light gases. These two issues were considered to be relevant, since in both cases obvious disagreement between experiment and theory existed or the theoretical description was not at all satisfactory.

Ionization

Although the number of antiproton collision experiments with atoms and molecules [34–39] was limited due to the required effort for the production of low-energy antiprotons, a considerable amount of theoretical studies employing a variety of different methods were performed focusing on hydrogen atoms, e.g., [40–49] and helium, e.g., [50–59]. Theoretical data, though much less in quantity, were also provided for other atomic targets, e.g., for alkali-metal [60, 61] and argon [62] atoms. While the theoretical description of the one-electron hydrogen-atom target turned out to be achievable — even including full quantum-mechanical treatments — it became clear that the proper description of the two-electron helium atom in antiproton collisions is much more demanding. It is the increasing importance of the dynamic electron-electron correlation effects with decreasing impact energy in the case of helium which circumvents a simple description including only static correlation.

A comparison of a selection of single-ionization cross sections for antiproton impact on helium atoms obtained in different calculations is shown in Fig. 0.3 together with data from the two measurements which were performed at CERN. As can be seen in Fig. 0.3, in the case of helium targets most theoretical approaches were able to reproduce the experimental data for single ionization at high impact energies beyond the maximum of the cross section ($E > 200$ keV), where a perturbative first-Born description is sufficient. However, experiment and theory did not agree at all for impact velocities below the mean ground-state electron velocity (≈ 40 keV), stimulating a vivid theoretical discussion. But even the different theoretical methods were not able to uniquely describe the single ionization below the maximum. An interesting difference between the proton and antiproton impacts also at high energies was experimentally recognized for the double-ionization cross sections of the He atom [35–37], and its origin was qualitatively explained by means of an interference picture [23, 63]. The quantitative description of double-ionization of He atoms was, however, not satisfactory, amounting to more than a factor of 10 difference among the theoretical calculations especially for low energies, below the maximum.

Antiproton collisions with helium atoms evolved due to their discussed favorable properties to a benchmark system for the study of dynamic electron-electron correlation effects and became therefore a good candidate for stringent tests of different theoretical approaches for the description of many-particle systems. Thereby, also a competition was started concerning the applicability and reliability of large-scale methods and numerical calculations like, e.g., time-dependent close-coupling calculations using a basis expansion [53, 58] or even computationally much more demanding expansions on a lattice [56]. Note, in the latter calculation each of the two electrons was only treated in two spatial dimensions.

Figure 0.3 clearly reveals that the description of the collision process below 40 keV was not conclusive at all, and partly it was even missing for $E < 1$ keV.[g] On the other hand it is worthwhile to note that currently and in the next years antiproton collision

---

[g] There are calculations for antiproton impacts with much lower energies ($\lesssim 10$ eV) where the capture of the antiproton by the target is the dominant process. This is, however, not the focus of this work.

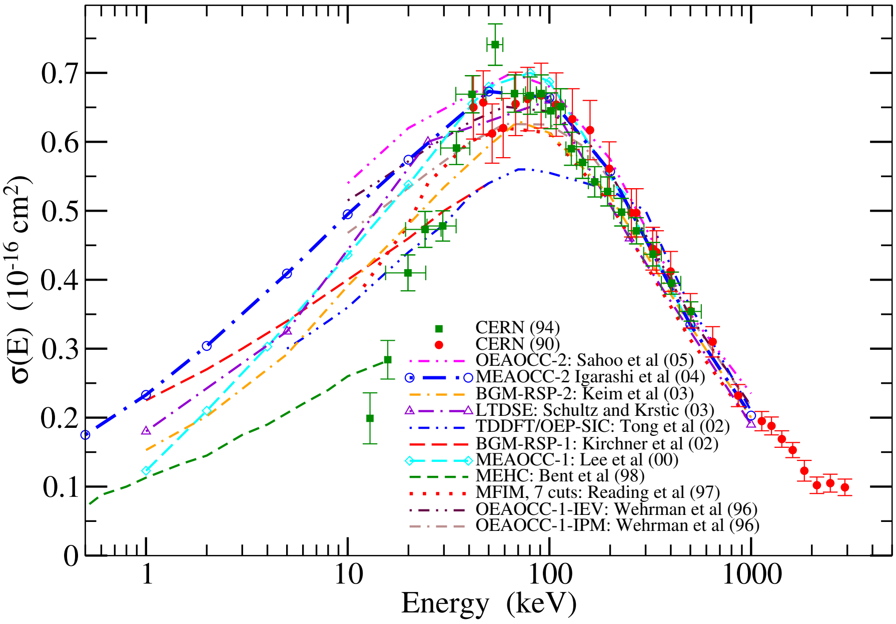

Figure 0.3.: *Single-ionization cross section for antiproton collisions with helium atoms as a function of the impact energy. A selection of theoretical calculations [50–59] is compared to two measurements performed at CERN [34, 35]. See Chapter 5.2 for a detailed discussion.*

experiments at the AD are primarily performed at low energies in the range of 10 eV to 25 keV [64, 65] using antiprotons which are accelerated from an antiproton trap [66] recently developed by the ASACUSA collaboration at CERN.

Also for molecular targets measurements were made for ionization in antiproton collisions on molecular hydrogen [35, 38]. Again, a notable difference between proton and antiproton impacts could be seen regarding the ionization cross sections, where detailed work was done for proton impacts only, e.g., [67–71]. In contrast, the theoretical work on antiproton collisions involving molecules was still comparably sparse. Certainly, the accurate description of a four-particle system like a hydrogen *molecule*, consisting of two electrons and *two* nuclei, is a further step in complexity compared to a helium *atom*. In the case of antiproton impacts on molecular hydrogen only a single calculation was published by Ermolaev [72], who used an atomic hydrogen target with a scaled nuclear charge in order to mimic the correct ionization potential. However, it turned out to be unsatisfactory for $E \leq 200$ keV reproducing atomic rather than molecular hydrogen. Recently, a molecular one-electron description of the target in antiproton collisions was employed for molecular hydrogen cations by Sakimoto [73]. This elaborate work examined the dependence of the ionization cross section on the internuclear distance and the orientation of the molecular hydrogen cation.

Note, at that time an experimental campaign was initiated [65] using the AD at CERN which was heading for new measurements of the ionization cross sections especially for impact energies between 3 and 25 keV.[h] It was planned to start with helium targets considering single and double ionization in order to tackle the disagreement between experiment and theory as well as the obvious spread of theoretical results for low energies. Further experimental efforts were also planned for hydrogen (atomic and molecular) targets.

Stopping power

Probably the most basic quantity in interactions of particles with a surrounding medium is the stopping power dE/dx which is the change of the kinetic energy E of the projectile per unit length x in the stopping medium. It is used in applications such as nuclear physics, radiation detectors, cancer therapy, space exploration, etc. The stopping power, which is directly related to the energy loss of the projectile, is often well accessible in experiments. The foundations for a quantum mechanical theory of the energy loss were already established in 1930 by Bethe [74]. His pioneering work includes, however, only a first-order term which is not sensitive to the sign of the projectile charge. Although many additional higher-order correction terms have been suggested and used, the applicability of Bethe's theory is limited to intermediate and high impact energies. At lower energies different stopping powers for positively and negatively charged projectiles are expected, known as *Barkas effect*, requiring a higher-order description.

Considering the stopping power of antiprotons first measurements were made with the LEAR facility at CERN for solid silicon [75] followed by a number of other solid targets. For energies above the stopping maximum, these stopping powers were found to be in general *smaller* by 35 - 55% compared to proton impact on the same targets. Therefore, it was a surprise when a measurements of the stopping powers of antiprotons in the simplest gases, i.e. molecular hydrogen and helium atoms, indicated fundamental differences [76]. The antiproton stopping powers determined for hydrogen molecules and helium atoms were about 20% *larger* [76–78] than those for protons in contrast to the earlier findings for solids. This unexpected behavior for hydrogen molecules and helium atoms could so far not be explained by theory. Other measurements for antiproton [79] and negative muon[i] [80–83] impact on hydrogen molecules and helium atoms neither reproduced the unexpected behavior of the former experiment for energies beyond the stopping maximum nor did any two of the experimental curves agree with each other for all impact energies. However, uncertainties in the experimental data analysis could not be fully excluded. It was stated by an experimentalist [80] that "the error of the measured dE/dx curve would be reduced drastically if a point at low energies could be fixed safely", making an accurate theoretical prediction of the stopping powers at low energies extremely valuable.

---

[h] The upper limit of the energy results from the maximal voltage which can be applied to the apparatus, while the lower bound is given by the minimal acceleration for which the stray fields do not disturb the antiproton beam substantially [65].

[i] Negative muons are about a factor of 8.88 lighter than antiprotons. However, except for deviations at small projectile velocities v the total stopping powers for antiprotons and negative muons with the same v should be the same.

A peculiarity in the case of antiproton stopping powers in hydrogen targets is the fact that all experiments [76, 77, 79, 81–83] were done with *molecules* while the theoretical description, e.g., [84–87], concentrated on *atomic* targets. The attempt to simply compare the theoretical results for hydrogen atoms with the molecular data from experiment turned out not to be meaningful, especially at low impact energies. Similarly to the case of ionization of helium, the theoretical description of the stopping power of antiprotons in helium gas [84], was reasonable only for high energies while it was rather poor for energies around and below the stopping maximum.

Problem specification and objectives

Regarding the described state of the art of low-energy antiproton collisions a number of open issues existed when this thesis was started. Out of these, five problems were specified — as listed below — and pursued in this work.

Implementation of a nonperturbative close-coupling method.

A fundamental step to perform a new theoretical investigation of low-energy ion collisions is the development and implementation of a numerical method. Here the emphasis is on negative projectiles, i.e. antiprotons. Thereby, a nonperturbative close-coupling approach using a spectral expansion is considered as most appropriate. It should be rather efficient, in order to allow for extensive convergence studies even for complex collision systems, and flexible concerning the choice of different targets. The final goal of the development within this work is the treatment of molecules including a full two-electron description as well as the consideration of different internuclear distances and molecular orientations. Therefore, the variety of possible targets may include simple molecules as, e.g., molecular hydrogen cations and hydrogen molecules, but also atomic targets like atomic hydrogen and He, which may be considered in the limit of vanishing internuclear distance. The use of model potentials for the target description enlarges the number of possible targets even further, including also large many-electron systems.

Performing rigorous testings of the developed method.

A thorough testing of the developed method and its implementation is a fundamental precondition to perform subsequent calculations. The convergence studies play a central role. Although they are known to be laborious and sometimes even computationally demanding, it is the only way to achieve or even improve accurate results. On the other hand, a comprehensive comparison of the obtained results with literature data — for cases where the latter exist — is necessary in order to learn more about the range of applicability of the employed assumptions and approximations when they are used in further calculations.

Providing a substantial amount of theoretical collision data.

In view of the ongoing (experimental) activities dealing with low-energy antiprotons at CERN and the planned experiments at FAIR a large set of theoretical data should be prepared. The variety of atoms and molecules which are (theoretically) discussed should be enlarged since the theoretical literature data are confined to only a few targets.

Theoretical data for collisions with molecular hydrogen.
A main focus of this work is to provide an adequate description of antiproton collisions with hydrogen molecules. Due to the complexity of this target originating from its two-center two-electron character no appropriate theoretical treatment existed. It is one of the aims to provide such an advanced and complex description for a molecule. On the other hand, especially for a complex system, it is advantages to employ a simple description, which is still applicable. Therefore, also model potentials for the description of molecular hydrogen are considered in detail in order to figure out their properties and ranges of applicability, especially in proton and antiproton collisions. The knowledge of these ranges is elementary in any further application.

Improving the understanding of stopping powers at low energies.
Finally, another focus is the study of the energy loss of low-energy antiprotons in helium and molecular hydrogen targets. An improved understanding as well as accurate (theoretical) data are eagerly awaited. They are useful for the design of low-energy antiproton storage rings like those planned for FLAIR, for resolving the obvious discrepancies between different experimental measurements in the case of helium and molecular hydrogen, and also for a number of further applications.

Structure — road map to answer the problem

The scope of this work may be summarized by two central attempts. First, the development and implementation of a numerical method for the description of antiproton collisions with atoms and in particular with molecules. Second, the extensive application of this method in order to provide a large amount of theoretical data concentrating on low-energy antiproton collisions. Part II and III of this work, respectively, are mainly concerned with these two aspects.

After this introduction Part I of this work provides a brief overview of ion collisions and introduces central notions and basic concepts being fundamental for the used description of the collision phenomena. Additionally, required developments and the structure of the numerical method are specified.

Part II (comprising Chapters 2 to 4) elaborates on the *implementation of a nonperturbative close-coupling method.* In the beginning the generation of the time-independent basis is described for one- and two-electron atomic as well as for molecular targets. Also, model descriptions are introduced for alkali-metal and helium atoms as well as for hydrogen molecules using atomic one-electron model potentials. Thereby, a number of properties of a newly proposed model potential for molecular hydrogen are determined and discussed. In Chapter 3 the decisive equations for the close-coupling method are laid down. Afterward, the time-dependent coupling matrix elements are formulated in three steps for one-electron atoms as well as for one- and two-electron molecules. Finally, the first-Born approximation is briefly introduced as a first-order treatment of the collision process. The extraction of cross sections from the results of the calculations is reviewed in Chapter 4. Therein, transition probabilities and their interpretation in the case of one-electron models as well as the calculation of different cross sections is discussed for atomic targets. At the end of Part II, the focus goes over to cross sections for molecular targets.

The results obtained in this work, the following conclusions, and a summary are presented in Part III (comprising Chapters 5 to 8 and a summary). In Chapter 5 *rigorous testings of the developed method are performed* using (effective) one- and full two-electron calculations for proton–alkali-metal atoms and antiproton–helium collisions which are rather well studied in the literature. *A substantial amount of theoretical collision data is provided* for antiproton impacts on alkali-metal atoms. Also a critical discussion of literature data for single-ionization of helium in antiproton collisions is given based on the present findings. *Theoretical data for collisions with molecular hydrogen* are presented in Chapter 6. First, molecular hydrogen cations are considered in order to verify the method applied to molecular targets. This is performed by comparing the results for ionization with literature data while the first cross sections for excitation complement the literature. Also, the role of the molecular orientation is revealed. Afterward, the model-potential and the full two-electron descriptions are employed in order to obtain cross sections for hydrogen molecules. The comparison of the results uncovers the range of applicability of the model potential. Furthermore, the dependence of the cross sections on the internuclear distance as well as on different molecular orientations is studied in detail. Finally, the use of a sequential two-step description of the production of protons in antiproton–hydrogen molecule collisions, i.e. dissociative (double) ionization, is discussed. An *improved understanding of stopping powers at low energies* for antiproton collisions with hydrogen, helium, and alkali-metal targets is the objective of Chapter 7. A case study for atomic and molecular hydrogen as well as for helium is performed including a critical discussion of the experimental and theoretical literature data in order to clarify and improve the state of the art. Chapter 8 comprises the conclusions and an outlook. While additional remarks highlight findings from different chapters in a common context, the outlook presents closely related future projects. Part III closes with a summary of the central aspects of the developed method as well as the achieved insights.

Finally, Part IV provides a selection of obtained numerical data in tabulated form, additional information, and a list of abbreviations. Also, it contains the bibliography. In this work *atomic units* are used unless otherwise stated. A note on atomic units can be found in appendix IV.

This work was realized in the *Modern Optics* group at the Department of Physics of the Humboldt-Universität zu Berlin under the supervision of PD Dr. Alejandro Saenz. It was supported by the BMBF (Bundesminesterium für Bildung und Forschung) as a part of the project *FLAIR Horizon*.

1. Ion collisions

1.1. Basic concepts

An inelastic reaction in atomic physics is one in which an electron, or several electrons, are transferred from one electronic state to another, either bound or unbound. This work deals with the description of inelastic reactions in ion-atom and ion-molecule collisions. However, also other reactions, as discussed below, may take place in such collisions which in general cannot be excluded in the dynamical description of the collision process.

A typical rather simple atomic collision experiment [a] might be considered which is illustrated schematically in Fig. 1.1. A homogeneous, well-collimated beam of monoenergetic particles A is directed towards a target containing the scatterers B. Single scattering conditions are assumed using a sufficiently thin target. After the collision between a beam particle A and a target particle B, some or all the particles emerging from the interaction region are registered by detectors, which are placed outside the path of the incident beam ($\theta > 0$), so that undeflected particles are not recorded. Several process can occur.

Types of collision

Collisions between ions and atoms A and B are classified, according to the final products of the reaction, into three broad categories. First there is the *elastic* scattering in which the internal energies of A and B and accordingly the total kinetic energy do not change, but the incident particles are deflected through a certain angle:

$$\mathrm{A} + \mathrm{B} \rightarrow \mathrm{A} + \mathrm{B}. \tag{1.1}$$

Then there are *inelastic* reactions in which either ion/atom A or B, or both, are excited (or de-excited) to a different energy level with which this work is chiefly concerned:

$$\begin{aligned} \mathrm{A} + \mathrm{B} &\rightarrow \mathrm{A}^* + \mathrm{B} \\ \mathrm{A} + \mathrm{B} &\rightarrow \mathrm{A}\ \ + \mathrm{B}^* \\ \mathrm{A} + \mathrm{B} &\rightarrow \mathrm{A}^* + \mathrm{B}^*\,. \end{aligned} \tag{1.2}$$

---

[a] There are of course much more advanced experimental setups like the COLTRIMS (Cold Target Recoil Ion Momentum Spectroscopy) [88] which allow for kinematically complete collision experiments.

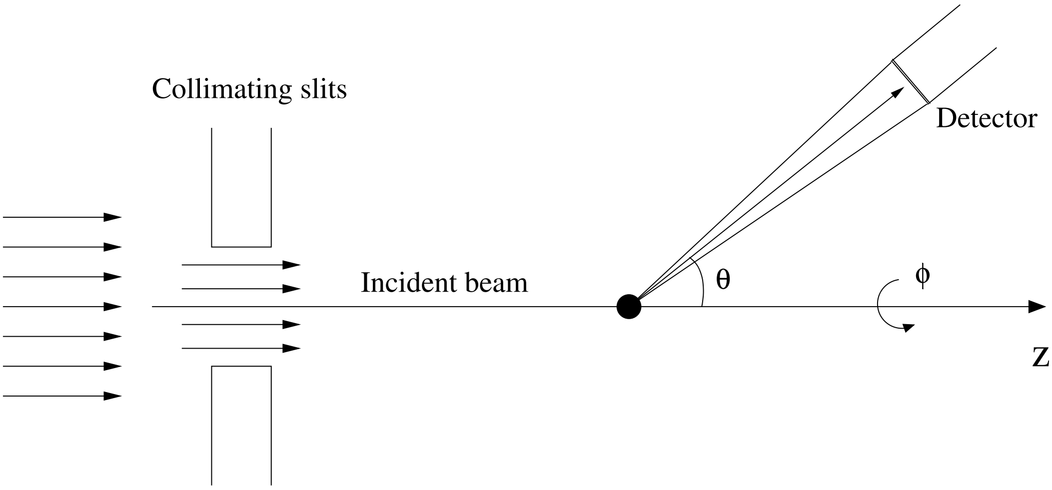

Figure 1.1.: Schematic diagram of a scattering experiment.

Included in this category are those reactions in which one or both atoms are ionized and one or more electrons are ejected, leaving a positive ion, or ions:

$$\begin{aligned} &\mathrm{A} + \mathrm{B} \rightarrow \mathrm{A} + \mathrm{B}^{+} + e^{-} \\ &\mathrm{A} + \mathrm{B} \rightarrow \mathrm{A}^{+} + \mathrm{B} + e^{-} \\ &\mathrm{A} + \mathrm{B} \rightarrow \cdots . \end{aligned} \tag{1.3}$$

Finally, there are reactions in which one or more electrons are transferred between A and B. These are the charge exchange, or electron capture, reactions:

$$\mathrm{A} + \mathrm{B} \rightarrow \mathrm{A}^{+} + \mathrm{B}^{-}. \tag{1.4}$$

Although some theoretical models can be developed in which only one of these processes is considered, in general, since the processes in Eqs. (1.1)–(1.4) are coupled this work is concerned in some degree with all types of collisions. However, in the case of negative projectiles like antiprotons no electron capture can be expected.

Channels

In the description of collisions the term *channel* is frequently used. A channel is a possible mode of fragmentation of the composite system (A+B) during the collision. It is characterized by the number and the nature — this includes also different internal states — of the fragments into which the system (A+B) can be decomposed. In elastic collisions the two colliding particles A and B remain in the initial channel, while inelastic collisions or reactions are processes leading from a given initial channel to a different final channel. Furthermore, there is a distinction between open and closed channels. A channel is said to be *open* if the corresponding collision is allowed by known conservation laws (such as energy conservation); otherwise it is said to be *closed*.

Cross sections

The results of collision experiments are usually expressed in terms of quantities called *cross sections.* Here, Ref. [89] might be quoted which defines

> *the cross section for a certain type of event in a given collision as the ratio of the number of events of this type per unit time and per unit scatterer, to the flux of the incident particles with respect to the target.*

A cross section has accordingly the dimension of an area.

As an example the simple collision experiment shown in Fig. 1.1 should be reconsidered with a uniform beam of N_p particles per unit time and unit area incident upon a target made of n_T scattering centers. The number of incident particles elastically scattered per unit time in a small solid angle $d\Omega$ centered about a direction $\Omega \equiv (\theta, \phi)$ with respect to the z axis is denoted by dN'. Under these conditions the number dN' of incident particles emerging per unit time in the solid angle $d\Omega$

$$dN' = N_p \, n_T \, \sigma(\theta, \phi) \, d\Omega \tag{1.5}$$

is proportional to N_p, n_T, and $d\Omega$. The proportionality factor $\sigma(\theta, \phi)$, which is also often written as

$$\sigma(\theta, \phi) = \frac{d\sigma}{d\Omega}(\theta, \phi) \tag{1.6}$$

is called the *differential scattering cross section.* The total scattering cross section is obtained by integrating the differential cross section over all scattering angles,

$$\sigma = \int \frac{d\sigma}{d\Omega}(\theta, \phi) \, d\Omega = \int_0^{2\pi} d\phi \int_0^{\pi} d\theta \, \sin\theta \, \frac{d\sigma}{d\Omega}(\theta, \phi) \, . \tag{1.7}$$

1.2. Different impact-energy intervals

In this section different intervals of the impact energy E of the projectile are discussed. The classification by energy is motivated by the fact that different phenomena are dominating the collision process within certain energy intervals of the ion. Furthermore, the applicability of most approximations is only given in a finite energy range. The proposed subdivision is also often done in terms of the impact velocity v_p of the projectile instead of its energy. However, these two quantities are usually — for not too low energies — understood as being (classically) related.[b] Thereby v_p is related to the velocity v_e of the target electrons. It has to be emphasized that this work and therefore also the following description deals only with non-relativistic energies (confer the introduction to Chapter 3 for a short discussion on the importance of relativistic effects).

In what follows, a phenomenological overview of the collision process is given ordered by the impact energy or rather impact velocity. Therefore, the impact of a point-like energetic particle of charge Z_p and velocity v_p on a light atomic target consisting of a

---

[b] The corresponding conversion formula is given in Eq. (.1) of Appendix IV.

nucleus of charge Z_T and a (few) electron(s) moving with the speed v_e is regarded. The atom has the single-ionization potential I^+. A certain focus is set on the ionization process with the single-ionization cross section σ^+.

High energies

At very high projectile velocities ($v_p \gg v_e$), the interaction with the atomic electrons is short-lasting, and for projectiles of low charge, it can be described adequately by first-order perturbation theory. In this limit, the first Born [c] results for the single-ionization cross section (cf. Bethe [74] and Inokuti [90]) depend on the projectile parameters as

$$\sigma^+ \propto |Z_p|\, v_p^{-2} \, \ln v_p \, . \tag{1.8}$$

This means that σ^+ is independent of the projectile mass and of the sign of its charge in this region. The same is of course true for excitation.

Intermediate to low energies

Moving to lower impact velocities first the ionization phenomena for projectiles of mass much larger than the electron mass, like antiprotons or (highly charged) positive ions, are considered. Here, the interaction takes longer time and hence the target wave function may be modified during the first part of the collision. The predominant effect at rather large v_p is the *polarization* of the target's electron cloud which pulls the electrons toward a positive particle and pushes them away from a negative one, resulting in a larger cross section for a positive than for a negative projectile. At the same time angular momentum is transferred to the electrons.

Another effect causing a difference between the σ^+ for projectiles of opposite charges stems from the so-called *"saddle-point" ionization*. The reason for the name is that for the impact of positive particles, a region of reduced net force on the atomic electrons is created at the saddle point in the combined potential of the projectile and the target nucleus. This is then supposed to lead to an enhanced cross section for ionization by positive particles as compared to that for negative ones. But there is no compelling evidence for anomalously large cross sections at the saddle point.

In any case, the two above-mentioned effects are clearly connected with distant encounters. The reason why they are important at high projectile velocities is simply that here distant collisions give the largest contribution to the total single-ionization cross section.

For projectile velocities near and below that of the target electrons ($v_p \leq v_e$), a number of other effects come into play. They are especially strong in the close encounters that are most important at low projectile velocities. Here there is ample time for modifications of the target wave function during the first part of the collision. For close encounters, the advent of the projectile inside the orbit of the target electrons creates an *increased*

---

[c] The first Born approximation is shortly introduced in Sec. 3.3.

or *decreased binding* of the electrons which leads to an increase or a decrease of σ^+, depending on whether the projectile is negative or positive.

Furthermore, in slow, close collisions, equivelocity particles of opposite charge do not follow the same trajectory. A positive projectile is deflected away from the central, high-density part of the target electron cloud by the Coulomb force from the target nucleus. Also, a positive projectile will be decelerated during the encounter with the target Coulomb field. Since the ionization cross section decreases with decreasing v_p in the discussed region, this leads to a reduction of σ^+ relative to the value for negative particles, for which the velocity is enhanced during the encounter. These effects of deflection and velocity change are in one term called *Coulomb trajectory effects.* However, these effects become negligible if the projectile can be considered as "energetic" [d]. That means, it has either a large mass compared to that of an electron or a large velocity. Since, the former is true for antiprotons and positive ions the Coulomb trajectory effects are very small down to approximately a tenth of the Bohr velocity v_0.

Finally, at $v_p \lesssim v_e$, for positive particles, the *capture* of a target electron into a bound state of the projectile becomes very likely. This alternative final channel subtracts probability from the pure ionization channel.

All these mechanisms (binding, Coulomb trajectory, electron capture) reduce the ionization cross section for positive-projectile impact relative to that for negative-particle impact. This results in a crossover of σ^+ being smaller for positive than for negative projectiles at $v_p < v_e$.

Very low energies

At very low projectile velocities ($v_p \ll v_e$) the projectile-atom encounter is adiabatic, and may be described through quasimolecular models. According to Kimura et al. [91, 92], during the approach of a proton, the atomic electron wave function evolves into a molecular orbital, the binding energy of which depends on the internuclear distance. Hereby, the target electron becomes either more tightly bound, or it is promoted to an excited state. In the second half of the collision, the quasimolecular orbital may return to the atomic ground state, it may stay in the excited state or the electron may be captured by the projectile. In this picture there is very little probability for ionization. For antiprotons, on the other hand, the binding energy of the quasimolecular states decreases, if the projectile comes close to the target nucleus, and hence the electron leaves the target. Due to these *molecular orbital effects* the ionization cross section for positive projectiles can be expected to be much smaller than for antiprotons.

In order to complete the discussion, the realm of projectile velocities may be briefly regarded which are so small that the projectile kinetic energy approaches that of the target ionization potential. Here, the "lack of energy" reduces the available phase space for final ionization states, thus reducing σ^+ for both negative and positive particles until σ^+ approaches zero (for protons of velocity $v_p \approx 0.03\, v_0$ in the case of a helium target [23]). For antiproton impact, on the other hand, the ionization cross section

---

[d] The importance of the influence on the trajectory is further discussed in Sec. 1.3.

never becomes zero. On the contrary, at these very low velocities, the antiproton can be captured by the target nucleus into a (highly) excited bound state [20, 93]. These systems are often interpreted as atoms with a heavy electron, like in the case of muons, or as a molecular system with one negative nucleus. Eventually, the antiproton cascades down to the antiprotonic-atom ground state by what a lot of potential energy is gained. This leads to a release of target electrons.

1.3. The impact-parameter method

As was already discussed before, it is meaningful to categorize ion-atom collisions according to their impact energy or to be more precise according to the impact velocity of the ions. At very low energies the theory of ion-atom scattering is usually discussed in terms of an angular momentum decomposition of the quantum-mechanical coupled equations. However, the number of partial waves required for convergence drastically increases with the initial relative velocity v_p of the projectile and becomes very large when v_p is greater than a few tenths of v_0, i.e., an atomic unit of velocity [e] (as impressively shown in Table 3.1 of Ref. [94]). Also, as v_p is increased the kinetic energy of the heavy particle motion becomes large compared with changes in electronic energies. In a heavy-particle atomic collision at an energy above ≈ 100 eV [f], the following conditions are usually met [92]:

(i) the de Broglie wavelength of the relative motion of the heavy particles (nuclei) is small compared with atomic dimensions;

(ii) the relative momentum of the nuclei, k, satisfies the relation $k^2/2\mu \gg \Delta E$, where μ is the reduced mass of the colliding system and ΔE is the inelasticity (energy defect of relevant states) in the collision;

(iii) $\cos^{-1}(\mathbf{k}_i \cdot \mathbf{k}_f) = \theta \ll 1$, i.e., most scattering of the projectile occurs at "small" scattering angles.

Under such circumstances, the nuclei can be assumed to move classically along some trajectory. The electrons experience an intrinsically time-dependent force field due to the moving nuclei, and hence the electronic wave function must satisfy a time-dependent Schrödinger equation (TDSE). Although this semiclassical picture is an approximation and misses quantum effects such as tunneling, which can be important at very low energies, the merit of using the semiclassical representation is to provide an intrinsically simpler picture of the collision dynamics and of course to simplify the computations. It should be stressed that the use of a semiclassical approximation (SCA) is known to provide quantitatively accurate results under the conditions of interest in the present work (cf., e.g., [95]).

---

[e] Atomic units, as defined in Appendix IV, are employed throughout this work, except where stated.

[f] As stated in Appendix IV, this is the laboratory energy of the projectile per atomic mass units measured in eV.

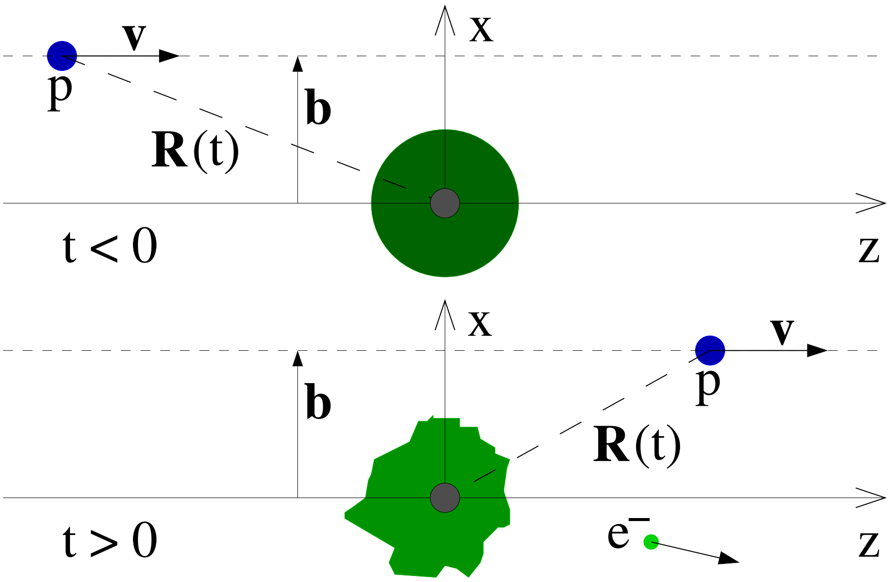

Figure 1.2.: *Sketch of the semiclassical impact-parameter method. The target is placed in the origin of the coordinate system. Upper panel ($t < 0$): the projectile moves on a (rectilinear) trajectory $\mathbf{R}(t)$ defined by the velocity $\mathbf{v}$ and the impact parameter $\mathbf{b}$ towards the target. Lower panel ($t > 0$): after the collision the electron cloud of the target may be left in an excited state or an electron may be ejected while the projectile continues to move on the given trajectory.*

In the SCA different kinds of trajectories may be used which include or exclude a reaction of the target on the projectile. The former leads to bended trajectories and is appropriate for very low impact velocities. A way how to determine the deflection function for classical trajectories is presented in Section 2.3 of Ref. [94]. In the energy regime covered by this work, however, the reaction on the projectile can be disregarded since it only minutely affects the results for $\bar{p}$ and p collisions for $E \gtrsim 1$ keV as has been shown in a number of calculations, e.g., Refs. [58, 96]. Therefore, in the present work the SCA is employed in its simplest form using only straight-line trajectories.

The resulting geometry of the collision process used in what follows is sketched in Fig. 1.2. The trajectory of the projectile p,

$$\mathbf{R}(t) = \mathbf{b} + \mathbf{v}_p\, t\,, \tag{1.9}$$

is determined by the impact parameter $\mathbf{b}$ and $\mathbf{v}_p$. The coordinate system in the laboratory frame is defined with the z and x axis parallel to $\mathbf{v}_p$ and $\mathbf{b}$, respectively.

The strength of the Coulomb interaction between the projectile and the target electrons is proportional to $1/R(t)$ and therefore time- or more precisely position-dependent but independent of v_p. It becomes very small for large distances but reaches zero only in the limit $R \to \infty$. Therefore, the starting and ending point of the trajectory have to be chosen sufficiently large when solving the TDSE in order to circumvent dependencies on their choice.

1.4. Overview of the developed method

The aim of this work is first, to develop a numerical method for calculations of ion collisions with atoms and molecules which finally is capable of describing molecular two-electron target systems. Furthermore, it is intended to apply the method in order to produce a large number of different data sets for a relatively broad variety of targets. These two demands require a rather efficient realization of the numerical description. In the last part of this chapter the status of available numerical methods prior to this work is reviewed and the required new developments are identified. Finally, the structure of the developed program package for the description of the ion collision process is presented.

1.4.1. Initial status and required developments

The present work took advantage of two already existing program packages which were implemented before in order to describe photon interactions with either atoms or molecules in a time-independent way. The first is capable of the calculation of dipole matrix elements of one-electron and two-electron atoms like hydrogen and helium. But also the treatment of alkali-metal and earth-alkaline atoms is possible by employing one- and two-active electron model descriptions, respectively. It was mainly initiated by Chang and Tang [97, 98]. The second program package can be considered as a derivative work or rather an extension of the former. It is capable of the description of homonuclear diatomic molecules with one and two electrons, i.e., in particular also the hydrogen molecular ion ${H_2}^+$ and the hydrogen molecule H_2 and employs a one-center expansion of the wave function. It was mainly developed by Apalategui and Saenz [99–101].

From these two program packages the parts which describe the electronic structure of the atoms and molecules, respectively, were inherited and adopted to the special needs of the present problem. Furthermore, the description of the total collision process required a number of new developments. These are the formulation of the matrix elements of the interaction between the projectile and the target, the implementation of the time-propagation, i.e. the close-coupling method, and the development of ways how to extract the observables from the transition amplitudes which are obtained after the collision.

1.4.2. Structure of the numerical method

In this work the program package Impact (IMpact PArameter Calculation Tool) has been developed. It can be divided into four main parts which are responsible for

a) the structure calculations, i.e., the determination of eigenstates and the corresponding energies of the target,

b) the pre-calculation of the coupling matrix elements for different positions of the projectile along given trajectories,

c) the solving of the TDSE by performing the close-coupling calculations,

d) the extraction of the various cross sections of interest.

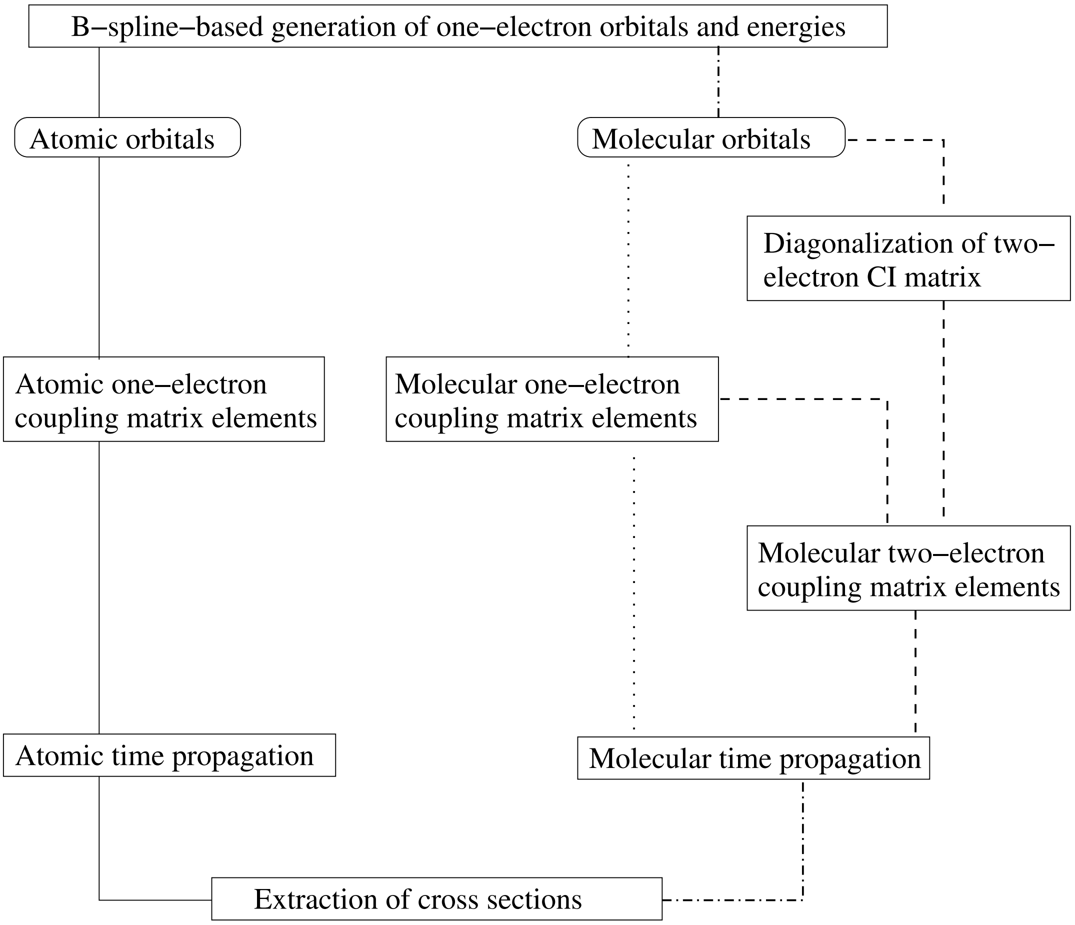

Figure 1.3.: *Schematic flow chart of the computational procedure. There are two main threads treating (i) (spherical-symmetric) atomic targets (—) and (ii) molecular two-center targets ($- \cdot -$). The latter thread is capable of one-electron ($\cdots$) and two-electron (– –) targets. Additionally, it can also treat atoms in the limit of vanishing internuclear distance R_{nuc} .*

These are visualized in the flow chart in Fig. 1.3. In order to account for the different characteristics of the targets — having different symmetries, one or two electrons, and so on — three variants of IMPACT exist. These are

i) IMPACT_ONE, for spherical ONe-Electron targets

ii) IMPACT_MONO, for Molecular ONe-electron Orbitals of homo-nuclear diatomic molecules

iii) IMPACT_MOT, for homo-nuclear diatomic MOlecules with Two electrons

which are the implementations of the three threads sketched in the flow chart in Fig. 1.3. In the following (only) the general structure of the Impact package should be discussed briefly. The underlying physics is introduced in more detail in the following Chapters 2 to 4.

First, one-electron orbitals and energies are generated based on a basis of B splines for either an atom or molecule with one or two nuclei, respectively. Second, the time-dependent interaction potential is expressed in a set of coupling matrices for different time steps, or projectile positions, by calculating the according matrix elements in the orbital basis. Various sets of matrices are needed for different trajectories. Third, in the case of (effective) one-electron targets the pre-calculated matrix elements together with the orbital energies are used as input for the time propagation, i.e., integration of the TDSE. Here either atomic or molecular symmetries have to be considered. Finally, the cross sections can be extracted from the collision wave function which is obtained after the collision, i.e., the projectile is sufficiently far away from the nuclei.

Currently, the two-electron description is only implemented in the molecular framework, which is, however, also capable of an atomic description in the limit of vanishing internuclear distance R_{nuc}. Principally, a purely atomic two-electron description is possible in a very similar way but has not been implemented in this work. For two-electron targets the first step is extended by building up a configuration-interaction (CI) matrix consisting of configurations of the above mentioned orbitals. Its diagonalization yields the eigenvectors and eigenenergies of the target. Second, the sets of coupling matrices for the two-electron target are determined using the coefficients of the two-electron eigenvectors and the one-electron coupling matrix elements between the orbitals. The steps three and four are practically the same as in the molecular one-electron case. However, some differences may occur in the extraction of the cross sections due to the existence of other possible final channels like doubly-excited or -ionized states.

The way how the the four parts a) to d) of the Impact package are realized is discussed in some detail in the next three chapters. The following Chapter 2 deals with the part a), that is the target description. Obviously, this part depends very much on the specific target and is therefore discussed separately for different targets. Afterward, the parts b) and c) are treated in Chapter 3. While the close-coupling method is introduced in a general form, since it is used with only minor changes for all targets of interest in this work. The required coupling elements depend of course on the specific target and are therefore again discussed separately. Finally, the last part d) is discussed in Chapter 4, that is the way how the transition probabilities and cross sections are extracted for one- and two-electron targets as well as in the case that model potentials are employed.

Part II.

Method

2. Description of the target

A time-dependent close-coupling approach is chosen in which the scattering wave function is expanded in (time-independent) eigenstates of the target. It is the outcome of the electron structure calculation, i.e. the eigenstates and eigenenergies, which contains all information of the target under consideration during the whole simulation of the time-dependent collision process. Therefore, a precise description of the electron structure of the target is a prerequisite on the way to achieve accurate theoretical collision data. The electronic orbitals are constructed out of products of a radial and an angular part, where the former is expanded in a B spline basis and the latter in spherical harmonics.

Besides the discussion on the electronic structure calculations this chapter also introduces model potentials for a simplified description of complex many-electron targets. Two model potentials are designated for the hydrogen molecule and helium atom and one for the alkali-metal atoms. The former two model potentials are discussed in detail by comparing their properties like excitation energies, oscillator strengths and so on with theoretical and experimental data for the hydrogen molecule.

2.1. Electronic structure calculations

The program code for the structure calculations which provides the eigenstates and energies of the target system is based on a set of functions and routines originally developed by Chang et al. [97]. It is a B-spline-based configuration-interaction (CI) procedure providing also the possibility of the use of frozen-core Hartree-Fock (FCHF) orbitals for divalent atoms, like the alkaline earth metals. Initially, it was used for the calculation of photoionization of the two-electron atom helium [102] and the single- and multiphoton ionization of the divalent alkaline earth metal atom magnesium [103]. Although the included procedures were already described earlier by Chang (e.g. [97, 98]) some basic characteristics should also be discussed here.

The mentioned structure code was further developed in order to be capable to also describe homo-nuclear diatomic molecules using a one-center expansion. This extension was implemented by Apalategui et al. [99, 100] in order to calculate photon-induced processes involving H_2^+ and H_2 [100, 101, 104].

The general structure of the code for the electron description, i.e. the determination of the eigenstates and eigenenergies, is the following. First, orbitals, which may be used in a one-electron basis, are determined by diagonalizing an (effective) one-electron Hamiltonian in a finite spherical space with a radius R_B also referred to as radial box. This yields the one-electron wave functions ψ and the corresponding energies ϵ. Thereby, the radial part of ψ is expanded in B splines which are briefly introduced in Sec. 2.1.1 and the angular part in spherical harmonics. The finite size of the box leads to discretized positive-energy states. Second, for two-electron systems a CI matrix is build up using products of two orbitals as configurations. The ionic one-electron Hamiltonian, which corresponds to the two-electron system under consideration, is diagonalized in order to obtain the orbitals in accordance to what was done in the first step. Finally, the diagonalization of the CI matrix yields the eigenvectors and eigenenergies of the two-electron target. In Secs. 2.1.2 and 2.1.3 the first step is explained in more detail for atoms and molecules, respectively, while Sec. 2.1.4 is briefly concerned with the second step. B splines, which are used as a basis for the expansion of the radial part of the orbitals, are introduced in the following section.

2.1.1. B spline basis

A detailed description of the basic properties of the basis splines, more commonly referred to as B splines, can be found elsewhere, e.g. in Refs. [105, 106]. The present discussion is limited to those features which are related to the calculation of the one-electron radial functions ρ. These radial functions enter in the orbitals which are used directly for the description of (effective) one-electron targets or are employed in the construction of the CI configurations in the case of two-electron targets.

A B spline is a polynomial of order $K-1$. It is a $\mathbf{L}^2$ integrable function with a finite support of K neighboring segments. Following [105, 106] the interval $[0, R_B]$ defining the radial box may be divided into segments. The endpoints of these segments are given by the knot sequence $\{t_\nu\}, \nu = 1, 2, \ldots, N+K$. B splines are not all orthogonal but they only overlap with maximal $2(K-1)$ other neighboring B splines resulting in a banded overlap matrix. The B splines are defined recursively by

$$B_\nu^{(1)}(x) = \begin{cases} 1 & if \; t_\nu \leq x < t_{\nu+1} \\ 0 & otherwise \end{cases} \tag{2.1}$$

and

$$B_\nu^{(K)}(x) = \frac{x - t_\nu}{t_{\nu+K-1} - t_\nu} B_\nu^{(K-1)} + \frac{t_{\nu+K} - x}{t_{\nu+K} - t_{\nu+1}} B_{\nu+1}^{(K-1)} . \tag{2.2}$$

In the case that one denominator is zero the corresponding quotient is defined as zero.

In a bound-state calculation, the set of B splines of order K and total number N is often defined with an exponentially increasing knot sequence. The choice of such a knot sequence satisfies the need for *densely* populated B splines near the nucleus in order to accommodate the fast raising inner s orbitals at small r. On the other hand, a more *evenly* populated set of B splines at larger r is required, if the oscillating behavior of the positive-energy orbitals at large distance should also be properly represented. As a result, for transitions involving both bound and continuum states, a sine-like knot sequence t_ν defined by [97, 99]

$$t_\nu = 0\,, \quad \nu = 1, \ldots, K \tag{2.3}$$

$$t_\nu = R_B \sin\left[\frac{\pi}{2}\left(\frac{(\nu - K)\,\Delta h}{R_B}\right)^y\right], \quad \nu = K+1, \ldots, N \tag{2.4}$$

$$t_\nu = R_B\,, \quad \nu = N+1, \ldots, N+K \tag{2.5}$$

is chosen, where $\Delta h = R_B/(N-K+1)$. The distribution of knot points can be adjusted by changing the position of the first non-zero knot t_{K+1}, which in turn determines the value of y according to Eq. (2.4). By employing such a knot sequence, the small- and large-r behavior of the orbital functions can be taken into account while the size of the B spline set can be limited to a modest value of N in the calculations.

Unlike Slater-type orbitals, which favor the small r region close to the nucleus, the B splines tend to treat the entire physical region more uniformly all having a similar amplitude between $r = 0$ and $r = R_B$. On the other hand the B splines have only a local support in contrast to Gaussian-type orbitals for which problems may occur due to their infinite spatial extension. The former property leads to an improved description of continuum states which are not localized. Due to the latter property only a small number of B splines basis functions overlap which results in a banded overlap matrix. Another key advantage in the application of B splines is their independence of any *a priori* procedure in selecting nonlinear parameters for exponential functions as, e.g., in the case of Gaussian functions.

2.1.2. Generation of the atomic one-electron basis

Because the potential $V(r)$ of a one-electron atom is central, the according Schrödinger equation may be separated in spherical polar coordinates [89]. Thus a particular solution of this equation

$$\psi_{nlm}(\mathbf{r}) = \rho_{nl}(r)\, Y_l^m(\omega)\,, \tag{2.6}$$

can be expressed as a product of radial one-electron functions ρ and spherical harmonics Y_l^m, where r and ω are the radial and angular components of the electron position vector $\mathbf{r}$, respectively. The eigenstates ψ can be characterized by the atomic quantum numbers n, l, and m where n is the principal quantum number and l and m denote the angular momentum and its projection on the z axis, respectively. The nonrelativistic functions ρ satisfy the radial part of the Schrödinger equation of the form

$$-\frac{1}{2}\frac{d^2\rho_{nl}}{dr^2} + V_{\text{eff}}(r)\,\rho_{nl} = \epsilon\,\rho_{nl}\,, \tag{2.7}$$

where $V_{\text{eff}}(r)$ is the effective potential which is the sum of $V(r)$ and the l dependent 'centrifugal barrier' potential [89].

The radial solution ρ [a] is expanded in terms of a set of B splines $B_\nu^{(K)}$ of order K

---

[a] The index nl is omitted in this paragraph for simplicity.

defined between $r = 0$ and $r = R_B$, i.e.,

$$\rho(r) = \sum_{\nu=1}^{N} c_\nu \, B_\nu^{(K)}(r)\,, \tag{2.8}$$

At the endpoints $r = 0$ and $r = R_B$ of the radial box all B splines are equal to zero except for $B_1^{(K)}$ and $B_N^{(K)}$, i.e.,

$$B_1^{(K)}(r = 0) = 1 \quad and \quad B_N^{(K)}(r = R_B) = 1. \tag{2.9}$$

In the calculation, the radial functions ρ are subject to the boundary conditions, $\rho(0) = \rho(R_B) = 0$, which can be satisfied if the conditions

$$c_1 = c_N = 0 \tag{2.10}$$

are adopted. Substitution of Eq. (2.8) into Eq. (2.7) leads together with the boundary conditions Eq. (2.10) to an $(N-2) \times (N-2)$ generalized eigenvalue problem with the eigenvector $\mathbf{C}$,

$$\mathbf{H}\,\mathbf{C} = \epsilon\,\mathbf{S}\,\mathbf{C}, \tag{2.11}$$

where $\mathbf{H}$ and $\mathbf{S}$ are $(N-2) \times (N-2)$ matrices given by

$$H_{ij} = -\frac{1}{2}\,\langle\, B_i^{(K)} \,|\, \frac{d^2}{dr^2} \,|\, B_j^{(K)} \,\rangle + \langle\, B_i^{(K)} \,|\, V \,|\, B_j^{(K)} \,\rangle\,; \tag{2.12}$$

$$S_{ij} = \langle\, B_i^{(K)} \,|\, B_j^{(K)} \,\rangle\,; \quad i \; and \; j = 2, \ldots, (N-1)\,. \tag{2.13}$$

For technical aspects on how to numerically solve the right hand sides of Eqs. (2.12) and (2.13) taking advantage of the discussed properties of B splines confer Refs. [105, 106].

The radial eigenfunction ρ_{nl} of Eq. (2.7) corresponding to an energy eigenvalue $\epsilon_{nl} = \epsilon_n$ is given by

$$\rho_{nl}(r) = \sum_{\nu=2}^{N-1} c_\nu^{(nl)} \, B_\nu^{(K)}(r)\,, \tag{2.14}$$

where the set of $N-2$ coefficients $c_\nu^{(nl)}$ forms the eigenvector,

$$C_{nl} = (c_2^{(nl)}, c_3^{(nl)}, \ldots, c_{N-1}^{(nl)}), \tag{2.15}$$

which is obtained by solving the eigenequation (2.11) using standard routines.

The diagonalization of the matrix $\mathbf{H}$ yields in total $N-2$ eigenfunctions and corresponding energies for every considered orbital angular momentum l. The calculated eigenfunctions of the first few lowest negative-energy solutions ϵ_{nl} for each l are completely confined in a box of radius R_B. Their energies agree with the numerical results of Eq. (2.7) from direct integration. The two or three highest negative-energy solutions which are close to the threshold can normally not be mapped directly to the bound states of the system. They are rather pseudostates which fulfill the boundary condition

$\rho(R_B) = 0$. However, since they also span the Hilbert space it is useful to keep them as part of the one-electron basis. The positive-energy (discretized continuum) orbitals, with energy ϵ_{nl} up to few atomic units, exhibit an oscillating behavior at large r. In practice, only those positive-energy orbitals with momentum $k_{nl} = (2\epsilon_{nl})^{\frac{1}{2}}$ appear in the nearly complete set of discretized radial functions ρ_{nl} that satisfy the boundary conditions $\rho_{nl}(r = 0) = \rho_{nl}(r = R_B) = 0$ or as formulated in Ref. [97] for large R_B

$$k_{nl}\, R_B + \frac{Z}{k_{nl}}\, \ln(2k_{nl}\, R_B) - \frac{l\pi}{2} + \delta_C + \delta_l = \mu\pi\,. \tag{2.16}$$

Here δ_C and δ_l are the Coulomb and short range phase shift, respectively, Z is the nuclear charge, and μ is an integer. Note, asymptotically as $r \to \infty$, the wave function of an outgoing electron with momentum k_{nl} is proportional to a sine function with an argument which is equal to the left hand side of Eq. (2.16). The asymptotic behavior is discussed, e.g., in Ref. [107]. For a pure hydrogenic potential, i.e., for

$$V_{\text{eff}}(r) = -\frac{Z}{r} + \frac{1}{2}\,\frac{l(l+1)}{r^2} \tag{2.17}$$

δ_l vanishes and δ_C equals the analytical Coulomb phase shift [107].

2.1.3. Generation of the molecular one-electron basis

In the Born-Oppenheimer approximation [b] the total wave function for a one-electron molecular ion $\tilde{\psi}_k^{(\Lambda)}$ separates into the product of the electronic and nuclear wave functions

$$\tilde{\psi}_k^{(\Lambda)}(\mathbf{r}, \mathbf{R_{nuc}}) = \frac{\chi_{\nu j}^{(k)}(R_{\text{nuc}})}{R_{nuc}}\, Y_j^{\tilde{m}}(\Theta, \Phi)\, \psi_k(\mathbf{r}; R_{nuc})\,, \tag{2.18}$$

where $\chi_{\nu j}^{(k)}$ is an eigenfunction of the molecular vibration in the electronic potential of the state ψ_k, $Y_j^{\tilde{m}}$ is a spherical harmonic, and $\Lambda = (\nu, j, \tilde{m})$ is the set of the vibrational and rotational quantum numbers. $\mathbf{R}_a = -\mathbf{R}_{\text{nuc}}/2$, $\mathbf{R}_b = \mathbf{R}_{\text{nuc}}/2$ and $\mathbf{r}$ are the position vectors of the nuclei and the electron, respectively (see Fig. 2.1), where $\mathbf{R_{nuc}} = (R_{\text{nuc}}, \Theta, \Phi)$
.

In contrast to atomic targets, which are spherically symmetric, the Hamiltonian of a diatomic homonuclear one-electron molecular ion is invariant under different symmetry transformations. Instead of the atomic quantum numbers the electronic part of the molecular one-electron eigenstates ψ_k can be characterized by $k = (n, m, \pi)$, where π is the parity with the possible values g for *gerade* and u for *ungerade* symmetry, m is the projection of the angular momentum on the internuclear axis, and n is the principal quantum number. Note, the electronic angular momentum l is not a conserved quantity for diatomic molecules.

---

[b] An introduction to the concepts used in the Born-Oppenheimer approximation is given, e.g., in Chapter 10 of Ref. [89]. The basic assumption is that the relative motion of the nuclei is much slower compared to the motion of the electrons. Therefore, the description of nuclei and electron motion may be decoupled.

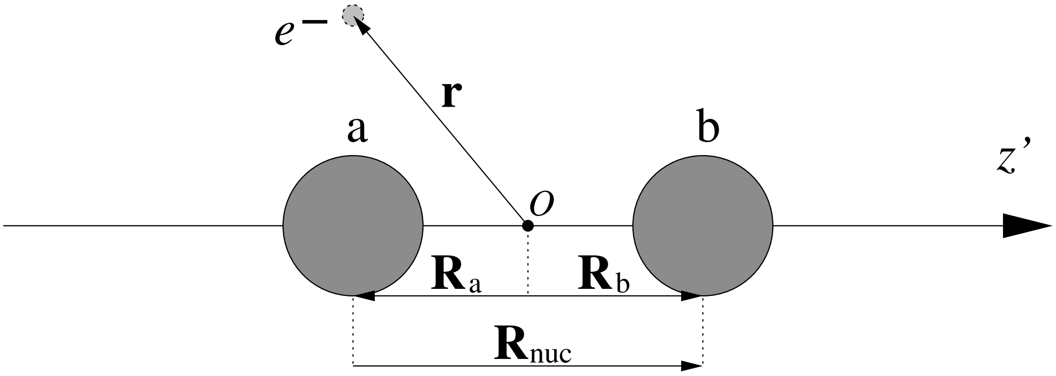

Figure 2.1.: *Sketch of the one-center expansion of* H_2^+. *The vector* $\mathbf{r}$ *gives the electron position measured from the midpoint* O *of the internuclear axis which is chosen as* z' *axis in the molecule-fixed space. The two nuclei are located at* $\boldsymbol{R}_a = -\boldsymbol{R}_{nuc}/2$ *and* $\boldsymbol{R}_b = \boldsymbol{R}_{nuc}/2$.

The wave function $\psi_k(\mathbf{r}; R_{\text{nuc}})$ satisfies the electronic part of the time-independent Schrödinger equation

$$H_{1\text{el}}(R_{\text{nuc}})\, \psi^m_{n\pi}(\mathbf{r}; R_{\text{nuc}}) = \epsilon^m_{n\pi}(R_{\text{nuc}})\, \psi^m_{n\pi}(\mathbf{r}; R_{\text{nuc}}) \tag{2.19}$$

for a one-electron molecule with a fixed internuclear distance R_{nuc}, i.e., the electronic wave function $\psi_k(\mathbf{r}; R_{\text{nuc}})$ depends parametrically on R_{nuc}. The one-electron Hamiltonian,

$$H_{1\text{el}}(R_{\text{nuc}}) = T_{1\text{el}} + V(\mathbf{r}, \mathbf{R_{nuc}}) + \frac{Z_A\, Z_B}{R_{\text{nuc}}}\,, \tag{2.20}$$

is the sum of the electronic part of the kinetic and the potential operator and the potential energy of the two nuclei. The last term leads only to an energy shift of the electronic potential curve, since it does not consist of electronic coordinates. The energy shift is proportional to the product of the charges Z_A and Z_B of the nuclei A and B, respectively. Note, so far only the case $Z_A = Z_B$ is implemented in the method used in this work. In the case of the simplest molecule, i.e. a molecular hydrogen cation, the product $Z_A\, Z_B$ is unity in atomic units.

For the description of the electronic wave functions a one-center expansion around the midpoint of the internuclear axis

$$\psi^m_{n\pi}(\mathbf{r}; R_{\text{nuc}}) = \sum_{l=l_{\text{m}in}(m,\pi)}^{l_{\text{m}ax}(\pi)} \rho^m_{nl}(r; R_{\text{nuc}})\, Y^m_l(\omega) \tag{2.21}$$

is used, which is sketched in Fig. 2.1, and r and ω are the radial and angular variables of the electron, respectively. In the expansion in Eq. (2.21) only even or odd values of l contribute depending on whether π is gerade or ungerade, respectively, and $l_{\text{m}in} \geq m$. Note, $l_{\text{m}in}$ and $l_{\text{m}ax}$ are merely basis-set parameters. The angular part is described with spherical harmonics $Y^m_l(\omega)$. The radial part $\rho^m_{nl}(r)$ is again expanded in a basis of B

splines of the order 8 using a finite box with a radius of 100 a.u.

In view of the one-center expansion of the electronic wave function in Eq. (2.21), the molecular potential of $H_{1\text{el}}$ in Eq. (2.20),

$$V(\mathbf{r}, \mathbf{R}_{\text{nuc}}) = -\frac{1}{|\mathbf{r}-\mathbf{R}_{\text{a}}|} - \frac{1}{|\mathbf{r}-\mathbf{R}_{\text{b}}|} = -\frac{1}{|\mathbf{r}+\frac{\mathbf{R}_{\text{nuc}}}{2}|} - \frac{1}{|\mathbf{r}-\frac{\mathbf{R}_{\text{nuc}}}{2}|}\,, \tag{2.22}$$

is expressed as a one-center potential around the midpoint of the internuclear axis as sketched in Fig. 2.1. The potential may be further expanded using the relation found by Legendre,

$$\frac{1}{|\mathbf{r}_1-\mathbf{r}_2|} = \sum_{s=0}^{\infty} \tilde{V}_s(r_1, r_2)\, P_s(\cos\gamma)\,, \tag{2.23}$$

where γ is the angle between the two vectors $\mathbf{r}_1$ and $\mathbf{r}_2$, the P_s are the Legendre polynomials and $\tilde{V}_s(r_1, r_2)$ is given by

$$\tilde{V}_s(r_1, r_2) = \begin{cases} r_1^s\,/\,r_2^{(s+1)}\,, & for\ r_1 \leq r_2 \\ r_2^s\,/\,r_1^{(s+1)}\,, & for\ r_1 > r_2 \end{cases}\,. \tag{2.24}$$

Due to the parity of the Legendre polynomials the following symmetries

$$\begin{aligned} P_s(-\cos\gamma) &= \ \ P_s(\cos\gamma)\,, \qquad for\ s = 0, 2, 4, \ldots \\ P_s(-\cos\gamma) &= -P_s(\cos\gamma)\,, \qquad for\ s = 1, 3, 5, \ldots \end{aligned} \tag{2.25}$$

can be exploited together with the expressions in Eqs. (2.23) and (2.24) to bring the molecular potential in Eq. (2.22) in the form

$$\begin{aligned} V(\mathbf{r}, R_{nuc}) &= -\sum_{s=0}^{\infty} \tilde{V}_s(r, R_{\text{nuc}}/2)\ [P_s(\cos\gamma) + P_s(-\cos\gamma)] & (2.26) \\ &= -2\sum_{s=0}^{\infty} \tilde{V}_s(r, R_{\text{nuc}}/2)\, P_s(\cos\gamma)\,,\ s\ even & (2.27) \\ &= -2\sum_{s=0}^{\infty} \tilde{V}_s(r, R_{\text{nuc}}/2)\sqrt{\frac{4\pi}{2s+1}}\, Y_s^0(\omega)\,,\ s\ even & (2.28) \end{aligned}$$

where in Eq. (2.28) the addition theorem for spherical harmonics is used and the z'-axis of the *molecule-fixed* space is chosen along the internuclear axis (see Fig. 2.1). The expansion in Eq. (2.23) — and therefore also in Eq. (2.28) — becomes exact only in the limit $s \to \infty$. However, it is known to converge often already using a finite s_{max} as an upper limit of the sum. Therefore, s_{max} is an expansion parameter. Actually, if the ansatz of Eq. (2.21) is used for $\psi_{n\pi}^m$ then $s_{\text{max}} = 2l_{\text{max}}$ holds and thus l_{max} becomes the decisive expansion parameter.

Finally, the radial part $\rho_{nl}^m(r)$ — which is expanded in a basis of B splines — of the one-electron wave function $\psi_{n\pi}^m(\mathbf{r}; R_{\text{nuc}})$ in Eq. (2.21) is solved for a fixed R_{nuc}. This is done in the way explained in the previous Sec. 2.1.2 for one-electron atoms. The molecular potential in the form of Eq. (2.28) is used as the central potential $V(r)$ which enters in Eq. (2.7).

2.1.4. Generation of the molecular two-electron basis

The Schrödinger equation for the electrons of an H_2 molecule in the Born-Oppenheimer approximation has the form

$$H_{2el}(\mathbf{r}_1, \mathbf{r}_2; R_{\mathrm{nuc}})\Phi_n^{\Omega}(\mathbf{r}_1, \mathbf{r}_2; R_{nuc}) = E_n(R_{\mathrm{nuc}})\Phi_n^{\Omega}(\mathbf{r}_1, \mathbf{r}_2; R_{\mathrm{nuc}}) \tag{2.29}$$

where $\Phi_n^{\Omega}(\mathbf{r}_1, \mathbf{r}_2; R_{\mathrm{nuc}})$ is the electronic wave function and E_n the corresponding energy. A set of quantum numbers is denoted by $\Omega = (M, \Pi, S, M_S)$, where M is the total azimuthal quantum number, Π represents the inversion symmetry (g for *gerade* and u for *ungerade*), S is the total electronic spin, and M_S its projection onto the molecular axis. The electronic Hamiltonian H_{2el} of the H_2 molecule is given by

$$\begin{aligned} H_{2el}(\mathbf{r}_1, \mathbf{r}_2; R_{\mathrm{nuc}}) = & -\frac{1}{2}\sum_{i=1}^{2}\nabla_i^2 - \sum_{i=1}^{2}\left(\frac{1}{|\mathbf{r}_i - \mathbf{R}_a|} + \frac{1}{|\mathbf{r}_i - \mathbf{R}_b|}\right) + \frac{1}{R_{\mathrm{nuc}}} \\ & + \frac{1}{|\mathbf{r}_1 - \mathbf{r}_2|} \, . \end{aligned} \tag{2.30}$$

In order to obtain the two-electron wave functions Φ_j^{Ω} and energies E_j a CI approach is used. For this purpose, the two-electron Hamiltonian H_{2el} in Eq. (2.30) is expanded in a basis formed by two-electron configurations $\Upsilon^{\Omega}_{n\eta, n'\eta'}(\mathbf{r}_1, \mathbf{r}_2)$. These configurations are expressed in terms of Slater determinants formed by *ionic* one-electron orbitals ψ (here the ones of $H_2{}^+$ which are obtained according to Sec. 2.1.3),

$$\Upsilon^{\Omega}_{i=(n\eta, n'\eta')}(\mathbf{r}_1, \mathbf{r}_2) = \frac{1}{\sqrt{2}}\left(\psi_n^{\eta}(\mathbf{r}_1)\psi_{n'}^{\eta'}(\mathbf{r}_2) + (-1)^S\, \psi_{n'}^{\eta'}(\mathbf{r}_1)\psi_n^{\eta}(\mathbf{r}_2)\right) , \tag{2.31}$$

where a plus occurs for singlet spin symmetry ($S = 0$ and symmetric spatial wave function), a minus occurs for triplet symmetry ($S = 1$), and $\eta = (m, \pi)$ is the set of quantum numbers of the one-electron states. The ansatz in Eq. (2.31) assures that the basis functions $\Upsilon_i^{\Omega}(\mathbf{r}_1, \mathbf{r}_2)$ are properly symmetrized with respect to electron interchange.

Therefore, the two-electron eigenstate, $\Phi_j^{\Omega}(\mathbf{r}_1, \mathbf{r}_2)$, may be expanded in the $\Upsilon_i^{\Omega}(\mathbf{r}_1, \mathbf{r}_2)$,

$$\Phi_j^{\Omega}(\mathbf{r}_1, \mathbf{r}_2) = \sum_{i=1}^{N_C} C_{ij}\, \Upsilon_i^{\Omega}(\mathbf{r}_1, \mathbf{r}_2) \, , \tag{2.32}$$

where the C_{ij} are the CI coefficients. Inserting this equation in the stationary Schrödinger equation in Eq. (2.29), a matrix eigenvalue problem is obtained from which the unknown CI coefficients C_{ij} are determined. Note, the products of two molecular one-electron basis states ψ and accordingly the $\Upsilon_i^{\Omega}(\mathbf{r}_1, \mathbf{r}_2)$ are already eigenstates of all terms in the upper row of H_{2el} in Eq. (2.30), excluding the electron-electron interaction term in the second row of Eq. (2.30). Therefore, the major task which still remains is the calculation of the electron-electron interaction between different configurations $\Upsilon_i^\Omega(\mathbf{r}_1, \mathbf{r}_2)$. The size of the CI basis, i.e. the number N_C of used configurations $\Upsilon_i^\Omega(\mathbf{r}_1, \mathbf{r}_2)$, determines the number of eigenvalues and eigenvectors that are obtained.

As can be seen from Eq. (2.31) the accuracy of the one-electron wave functions, i.e. orbitals ψ, is crucial for a good representation of the two-electron wave functions. The one-electron wave functions $\psi(\mathbf{r})$ used to construct the configurations $\Upsilon_i^\Omega(\mathbf{r}_1, \mathbf{r}_2)$ are obtained as explained in the previous Secs. 2.1.2 and 2.1.3.

Note, in the limit $R_{nuc} \to 0$ the Hamiltonian H_{2el} in Eq. (2.30) formally switches over to the one of a helium atom, if the term for the nuclear repulsion $1/R_{\text{nuc}}$ is removed. Therefore, the presented approach is also capable of the description of helium atoms. In that case also the orbitals ψ have to be calculated of course in the limit $R_{nuc} \to 0$ corresponding to a helium ion. Accordingly, the term $1/R_{nuc}$ has to be removed in Eq. (2.20). Though, it should be mentioned that the method is optimized for the symmetries of a diatomic molecule rather than exploiting the spherical symmetry of an atom.

2.2. Model potentials for H_2 and He

From the very beginning of quantum mechanics the hydrogen atom has been considered as one of the standard model systems. The reason lies in the simplicity of the theoretical description of this most basic atomic system. On the other hand, the description of the hydrogen molecule is obviously a lot more involved due to the much larger number of degrees of freedom. Compared to the atomic case the complexity of the molecule arises, e.g., from the electron-electron interaction due to the second electron and the anisotropy of the charge distribution which may lead to an orientational dependence of a physical quantity. Additionally, there is vibrational and rotational motion of the nuclei and even in a Born-Oppenheimer approximation one has to deal with potential curves for all electronic states and their rovibrational excitations.

Consequently, it is desirable to have a description, although simplified, of the hydrogen molecule at hand which is of similar complexity as the one of the hydrogen atom. This allows for an easy adoption of already existing numerical methods, which have been implemented for spherical one-electron problems, to the description of molecular hydrogen.

A second motivation becomes even more important in the era of fast improving computational resources which may make the full or at least improved description of H_2 molecules and many-electron atoms feasible even in time-dependent processes: A comparison of results achieved with a calculation involving a full hydrogen molecule with the outcome of a simplified model description of H_2 which has atomic rather than molecular properties and accounts for the second electron only by screening. An analysis of the differences can yield the importance of the influence of two-electron as well as of molecular effects, like the deviation from a spherically symmetric charge distribution.

One aim of this work is to perform such a comparison. Therefore, two simple one-electron, single-centered model potentials are considered. The first is the rather traditional approach of employing the potential of a hydrogen-like atom with an appropriate scaled nuclear charge. Accordingly, this model of a scaled hydrogen is denoted as H_{scal} in this work. The second model was recently proposed by the coworkers Vanne and Saenz [108]. This model potential V_{mod} tries to improve the description of the H_2 molecule without increasing the complexity. In what follows the two model potentials and their properties are presented. Furthermore, additional effort is spent in this work to examine the two model potentials in more detail by applying them in calculations of excitation energies, transition moments and oscillator strengths as well as photoionization cross sections. The outcome of these studies is contrasted with experimental data and theoretical results obtained with a full description of the H_2 molecule. A similar discussion was performed in [C].

2.2.1. Scaled hydrogen atom H_{scal}

In order to compare the properties of the proposed model potential V_{mod} in Eq. (2.36) with another quite popular (see, e.g., [72]) simple artificial atomic model a scaled hydrogen atom H_{scal} may be introduced. Its potential

$$V_{scal}(r) = -\frac{Z_{\mathrm{scal}}}{r} \tag{2.33}$$

differs from the one of a normal H atom only by the scaled nuclear charge Z_{scal}. The correct ionization potential of H_2 at a given R_{nuc} can be obtained for H_{scal}, if the nuclear charge is scaled as

$$Z_{\mathrm{scal}}(R_{\mathrm{nuc}}) = \left(I_{\mathrm{H}_2}(R_{\mathrm{nuc}}) \;/\; I_{\mathrm{H}} \right)^{1/2} . \tag{2.34}$$

It may be alluded that due to the scaling of the nuclear charge in Eq. (2.33) *all* energies ϵ_j of the bound states of H_{scal} are affected in the same way, i.e., they are shifted in comparison to the H atom as

$$\epsilon_j\,[\mathrm{H}_{scal}] = (Z_{scal})^2\,\epsilon_j\,[\mathrm{H}] . \tag{2.35}$$

Although the ionization potential of the H_2 molecule is by construction exactly reproduced by the scaled hydrogen atom it can be expected that this is not the case for the energies of the bound states, since the potential in Eq. (2.33) does not have the correct r dependence. Furthermore, one may expect problems in the description of molecular properties that are very sensitive to the asymptotic long range behavior like tunneling ionization in intense electric or electromagnetic fields.

2.2.2. Parameter-free one-center one-electron H_2 model

In order to obtain a simple model for a complex system the right balance has to be found, i.e., a model has to be devised which reflects the characteristics of the full description. It is known that, e.g., ionization processes of H_2 can be very sensitive to the ionization potential I_{H_2} and the properties of the bound states depend on the exact form of the Coulomb potential. Hence, it is important that the model potential agrees in these properties with those of the molecule. An appropriate trade-off for the description of

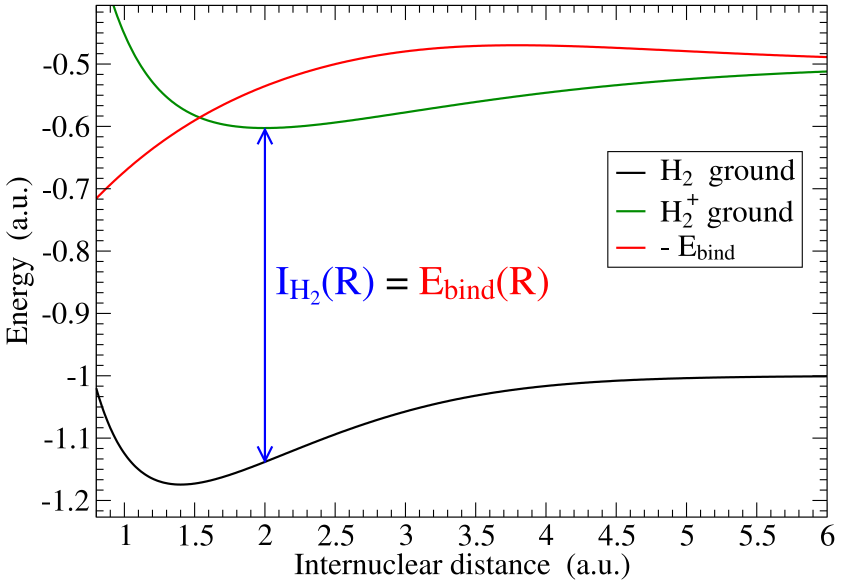

Figure 2.2.: *Potential curves for the ground states of* $H_2{}^+$ *and* H_2 *as well as the* H_2 *binding energy or ionization potential as a function of the internuclear distance* R_{nuc}.

H_2 molecules may be achieved by using the following simple parameter-free one-center model potential [108],

$$V_{\rm mod}(r) = -\frac{1}{r} - \frac{\alpha}{|\alpha|\, r} \exp\left[-\frac{2\, r}{|\alpha|^{1/2}}\right] , \tag{2.36}$$

for an effective one-electron description of molecular hydrogen with the radial coordinate r and a dimensionless parameter α. The model potential satisfies the conditions $V_{\rm mod}(r) \to -1/r$ for $r \to \infty$ and describes therefore the long-range behavior of an effective H_2 potential correctly as being hydrogen-atom-like. Furthermore, it reduces to the potential of a hydrogen atom H for $\alpha \to 0$ with an ionization potential $I_{\rm H} = 0.5$ a.u.

In order to describe an H_2 molecule with a fixed internuclear distance $R_{\rm nuc}$ a certain α has to be determined which fulfills the requirement that the ionization potential of the model $I_{\rm mod}(\alpha)$ is equal to the ionization potential $I_{\rm H_2}(R_{\rm nuc})$ of the H_2 molecule at the considered fixed distance $R_{\rm nuc}$. In Table .2 in the appendix values of α are given which yield the ionization potentials of H_2 for internuclear distances $R_{\rm nuc}$ in a range from 0.8 a.u. to 2.5 a.u. This is basically the interval in which the expectation value of the vibrational ground state of the H_2 nuclei is nonzero. The dependence of α on $R_{\rm nuc}$ in the same interval is also shown in Fig. 2.3. For a fixed $R_{\rm nuc}$ the ionization potential $I_{\rm H_2}(R_{\rm nuc})$ is obtained by subtracting the ground-state potential-energy curve of H_2 which was very accurately calculated by Wolniewicz [109] from the ground-state energies of H_2^+. These three energy curves are shown in Fig. 2.2 as a function of $R_{\rm nuc}$.

For the limit $R_{\rm nuc} \to 0$ the value $\alpha = 0.903570$ is obtained which yields the correct ionization potential of the helium atom [110]. That is, the model potential in Eq. (2.36)

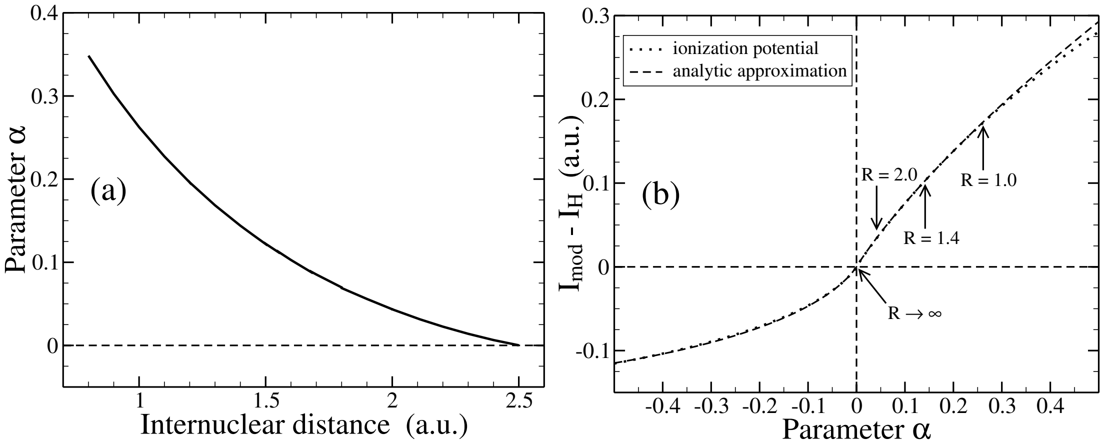

Figure 2.3.: *(a) The value of α as a function of the internuclear distance R_{nuc}. (b) Dependence of the ionization potential of the H_2 model on α. The exact curve for the ionization potential [108] is compared to the analytic approximation I_{mod} which is given in Eq. (2.37).*

can also be used in order to approximately describe a He atom as an effective one-electron system.

Since the model potential can be adopted to different internuclear distances R_{nuc} with the help of α it is possible to study vibrational effects as has been proposed in [111–113]. Cross sections which account for the vibrational motion of the H_2 nuclei in collisions of H_2 targets modeled by V_{mod} with antiprotons are presented in Chapter 6. They are achieved by employing closure, exploiting the linear behavior of the ionization cross section with R_{nuc}, and performing the calculations at $R_{\mathrm{nuc}} = \langle\, R_{\mathrm{nuc}} \,\rangle = 1.448$ a.u. ($\alpha = 0.13308$). A further discussion on how to obtain cross sections being independent on R_{nuc} and including the vibrational effects of the nuclei can be found in Sec. 6.2.3.

The exact dependence of the ionization potential $I_{\mathrm{mod}}(\alpha)$ on α for a system described by V_{mod} can be determined numerically (cf. [108]) and is presented in Fig. 2.3. However, an advantage of the model proposed in Eq. (2.36) is the possibility to approximate $I_{\mathrm{mod}}(\alpha)$ quite accurately with an analytic expression,

$$I_{\mathrm{mod}}(\alpha) \approx I_{\mathrm{H}} + \alpha \times \begin{cases} (\,1 + \sqrt{|\alpha|}\,)^{-11/4}\,, & \alpha < 0 \\ (\,1 + \sqrt{|\alpha|}\,)^{-1}\,, & \alpha \geq 0 \end{cases}\,, \tag{2.37}$$

which is *not* a fit of the numerical data and is also shown in Fig. 2.3. For instance, at $R_{\mathrm{nuc}} = 1.4$ a.u. the numerically determined ionization potential and $I_{\mathrm{mod}}(\alpha)$ given by Eq. (2.37) differ only by 0.01%. The dependence on α simplifies even further in the limit $|\,\alpha\,| \to 0$ where the ionization potential becomes $I_{\mathrm{mod}}(\alpha) \to I_{\mathrm{H}} + \alpha$ and depends only linearly on α as can be seen in Table .2 in the appendix.

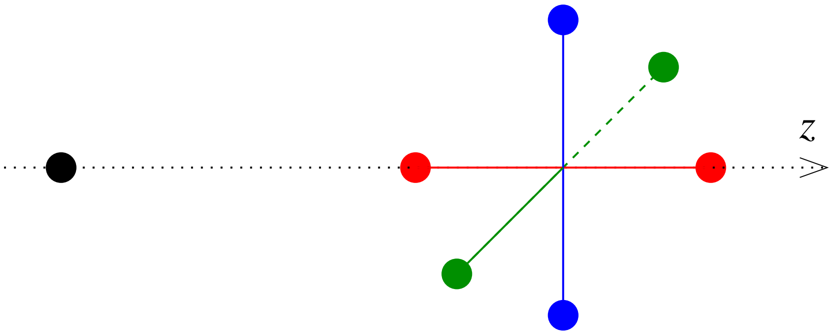

Figure 2.4.: *Sketch of three orthogonal orientations of the* H_2 *molecule. One orientation is parallel (red) and the other two are perpendicular (blue and green) with respect to a given axis. The axis might be determined by a physical quantity like an electro-magnetic field or as indicated here by a trajectory of a projectile.*

2.2.3. Applications of the model potentials for H_2

It is one aim of the present work to further examine the simple single-centered, effective one-electron model potential proposed in Eq. (2.36) and to find out why it describes the properties of the hydrogen molecule in the applications to different physical systems (cf. Refs. [108] and [B]) so well. But also the limitations of the model in the description of H_2 molecules should be analyzed. Therefore, in this work quantities like excitation energies, electronic transition moments, and oscillator strengths are calculated as a function of the internuclear distance and are compared to literature data for a full H_2 molecule. Also, the model is used to determine photoionization cross sections in order to test its applicability to different physical processes. Its application to the calculation of ionization and excitation cross sections in collisions with projectiles, namely $\bar{p}$ and p, is presented in more detail in Chapter 6.

Since the model potential of Eq. (2.36) is isotropic it is naturally qualified for describing orientationally-averaged H_2 molecules. This is often the case in experimental studies in which non-aligned isotropically-distributed molecules are investigated. Optical excitations from the $1s$ into p states of the model H_2 are consequently compared with both possible dipole-allowed transitions into $^1\Sigma_u$ and $^1\Pi_u^{+/-}$ states of the H_2 molecule. A simple orientational averaging yields in this case the factors 1/3 and 2/3 for a weighting of the results for the symmetries $^1\Sigma_u$ (parallel) and $^1\Pi_u$ (perpendicular), respectively. These factors can also be motivated from a geometrical point of view considering one parallel and two perpendicular orientations with respect to a given (symmetry) axis as sketched in Fig. 2.4 in the case of a collision process. On the other hand, the isotropy is of course a limitation of the model. For example, in the case of multiphoton excitations interference terms prevent a determination of simple weighting factors the way just proposed [101, 108].

In what follows, it should be investigated how satisfyingly the proposed model potential works in practice with respect to various applications. First, excitation energies, transition moments, and oscillator strengths are considered. Afterward, V_{mod} is used

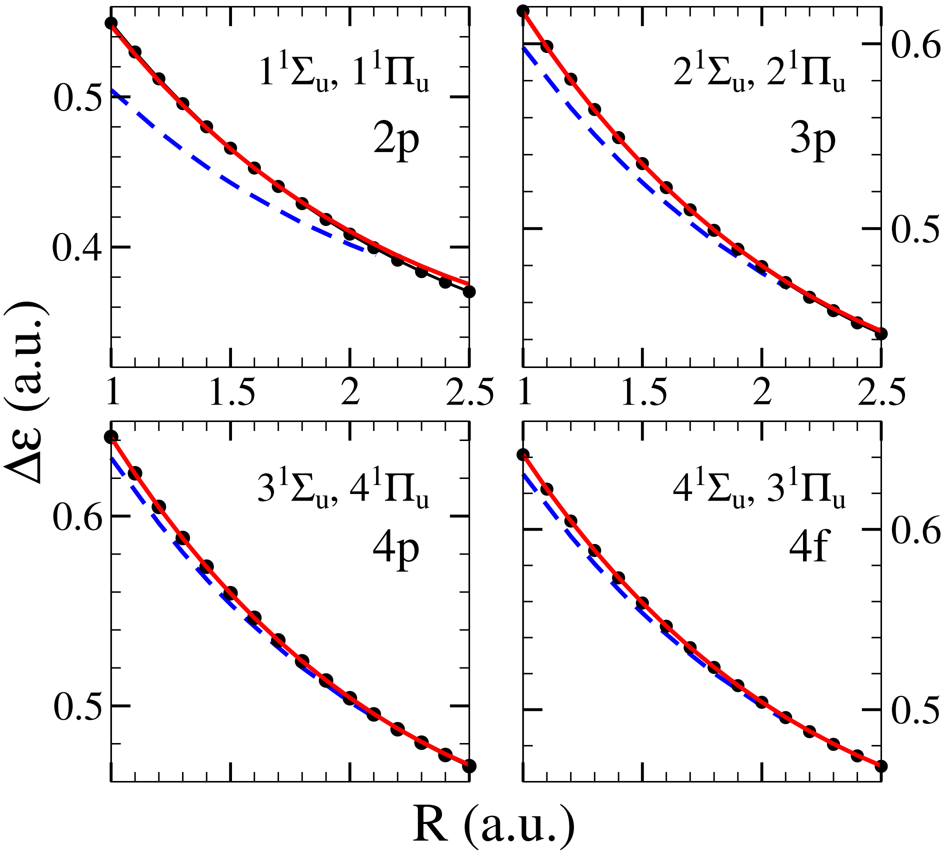

Figure 2.5.: *Excitation energies $\Delta\epsilon$ of the H_2 molecule as a function of R_{nuc} for transitions from the ground state $1^1\Sigma_g$ to the four orientationally-averaged, energetically-lowest, dipole-allowed final states consisting of the symmetries $^1\Sigma_u$ and $^1\Pi_u$. Molecular calculation by Staszewska and Wolniewicz [114, 115]: black circles. Present excitation energies for corresponding transitions from 1s to 2p, 3p, 4p, and 4f: red solid curve, model potential V_{mod}; blue dashed curve, hydrogen atom with scaled nuclear charge H_{scal}.*

for the description of ionization and excitation of an H_2 molecule in interactions with photons and in collisions with $\bar{p}$ and p while the results for the collisions are discussed in Chapter 6. The findings are compared to corresponding experimental and theoretical results for an H_2 molecule as well as to results obtained with H_{scal}.

Excitation energies

In Fig. 2.5 excitation energies (EE) for the energetically-lowest dipole-allowed final states of the H_2 molecule with the symmetries $n\,^1\Sigma_u$ and $n\,^1\Pi_u$ with $n = 1, \ldots, 4$ are given in the range of internuclear distances 1 a.$u. \leq R_{\rm nuc} \leq 2.5$ a.u. They are taken from the very accurate calculations by Staszewska and Wolniewicz [109, 114, 115]. The orientationally-averaged molecular EE are given as circles. The corresponding four EE for an atomic system are the energy differences $\Delta\epsilon$ between the ground state and the $2p$, $3p$, $4p$, and $4f$ state, respectively.

It can be seen that in all of the four cases the EE of the model potential approximates the orientationally-averaged EE of the H_2 molecule very well in the whole R_{nuc} range considered here. Only for the transition into the $2p$ state the EE obtained with the model potential are slightly higher than those for H_2 for large $R_{\rm nuc}$. It is known that in the R_{nuc} range which is considered here the $4\,^1\Sigma_u$ and $3\,^1\Pi_u$ states possess a dominant $(1s4f)$ contribution [116, 117]. Consequently, these states cannot be compared to a p state of the model potential but should instead be compared to the $4f$ state.

In contrast to the findings for $V_{\rm mod}$ the results for the scaled hydrogen atom H_{scal} differ from the correct $\Delta\epsilon$ curves especially for small R_{nuc} while they come close to the correct values for $R_{\rm nuc} > 2$ a.u. For large $R_{\rm nuc}$ this trend could have been expected since the H_2 molecule becomes more and more like two distant H atoms and therefore can be modeled by the hydrogen-atom-like H_{scal}. However, it is known that transition probabilities, e.g. in the case of excitation of alkali-metal atoms shown in this work explicitly in Sec. 5.1, can depend considerably on the EE. Therefore, they should be described accurately, especially around the equilibrium distance $R_{\rm nuc} \approx 1.4$ a.u.

Transition moments and oscillator strengths

Another test of the capability of the model potential $V_{\rm mod}$ given in Eq. (2.36) can be performed by considering transition moments (TM) which are known to be much more sensitive to the accuracy of the wave functions than the energies. The dipole TM into the state $|\,nl\,\rangle$ for fixed $R_{\rm nuc}$,

$$M(nl) = \sqrt{2}\,\langle\,1s\,|\,x\,|\,nl\,\rangle\,, \tag{2.38}$$

are computed for the same transitions which have already been discussed in the context of the EE, where n and l are the principal and angular momentum quantum numbers, respectively. The factor $\sqrt{2}$ in Eq. (2.38) accounts for the two electrons in the H_2 molecule. TM from the H_2 ground state $1\,^1\Sigma_g$ to the dipole-allowed final states $^1\Sigma_u$ and $^1\Pi_u$ were calculated by Wolniewicz and Staszewska [115, 116], Spielfiedel [117], and Drira [118]. The orientationally-averaged molecular TM are compared to the results obtained with the present model potential, whereas the wrong assignment done in [118] for molecular states with dominant $(1s4p)$ or $(1s4f)$ configuration is corrected as proposed in [115–117]. Also the TM for the scaled hydrogen atom H_{scal} are calculated. In Fig. 2.6 only the results by Wolniewicz and Staszewska which might be considered as the most accurate are presented together with the outcome for $V_{\rm mod}$ and H_{scal}.

In general, the present TM achieved with $V_{\rm mod}$ agree with the data for the full H_2 molecule. For $R_{\rm nuc} > 1.5$ a.u. there is some deviation for the transition into the $2p$ state which could have been expected, since the electron-electron interaction and the effects due to the two nuclei are most prominent for the lowest excited states. Otherwise, all TM to higher states match the literature data very well. It may be noted that even the molecular states $4\,^1\Sigma_u$ and $3\,^1\Pi_u$ — both with dominant $(1s4f)$ character at small $R_{\rm nuc}$

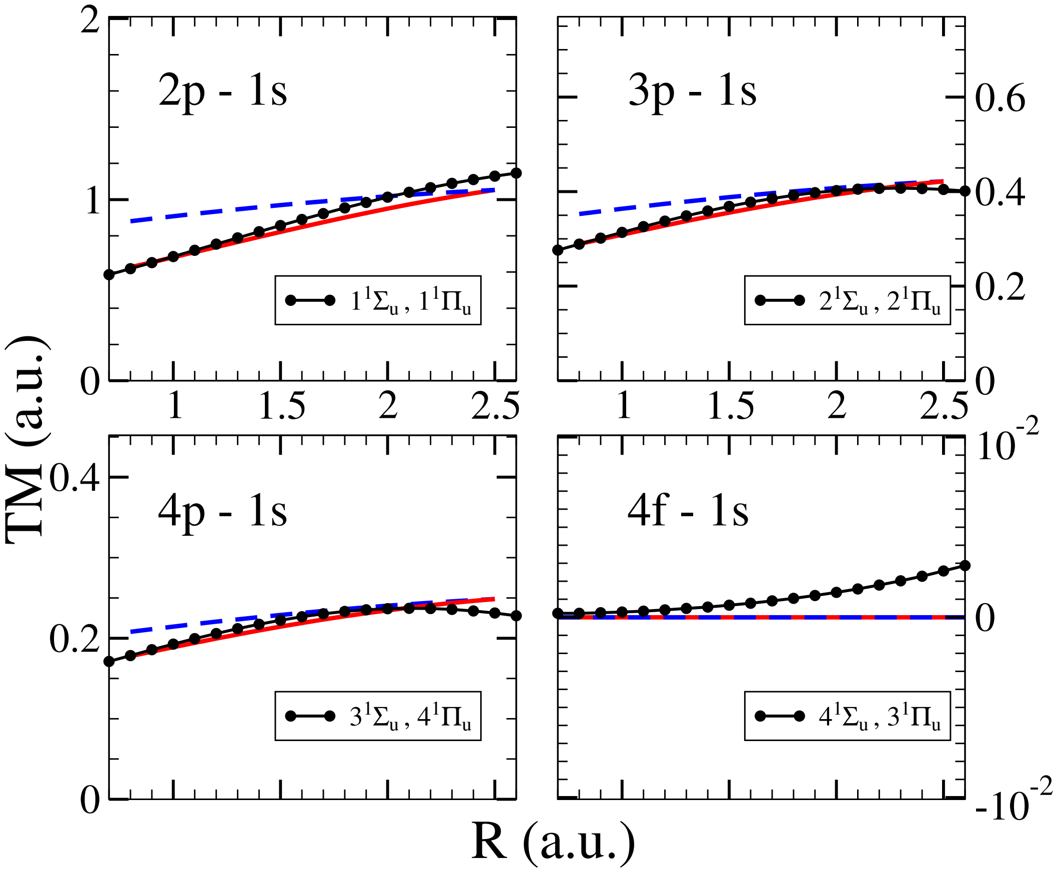

Figure 2.6.: *The same as in Fig. 2.5 but for electronic transition moments (TM) of the H_2 molecule. Molecular calculation by Wolniewicz and Staszewska [115, 116], black circles (Note the different scales, especially for the $4f-1s$ transition.)*

— are again nicely represented by the non-dipole-allowed $4f$ state of the model. The EE as well as the vanishing TM of the $4f$ state match the corresponding orientationally-averaged results of the H_2 molecule.

The TM calculated for H_{scal} show for all s to p transitions a different dependence on R_{nuc} than the TM for H_2. For small R_{nuc} they are too large and for $R_{\text{nuc}} \to 2.5$ a.u. they approach the TM calculated for V_{mod}. The deviations indicate that, especially at small R_{nuc}, the properties of the wave functions obtained with V_{scal} differ considerably from those of a real H_2 molecule.

A similar comparison of the four discussed transitions has been performed for the oscillator strengths in Ref. [C]. Therein, it has been concluded that the matching of the model with the H_2 molecules is of comparable quality as for the TM. However, the analytic expression for the oscillator strengths for H_{scal} is independent of R_{nuc}, since the EE and TM which enter in the expression scale with R_{nuc} in a reciprocal way, leading finally to the cancellation of the R_{nuc} dependence. The oscillator strengths for H_{scal} are therefore only for large R_{nuc} similar to those of V_{mod}.

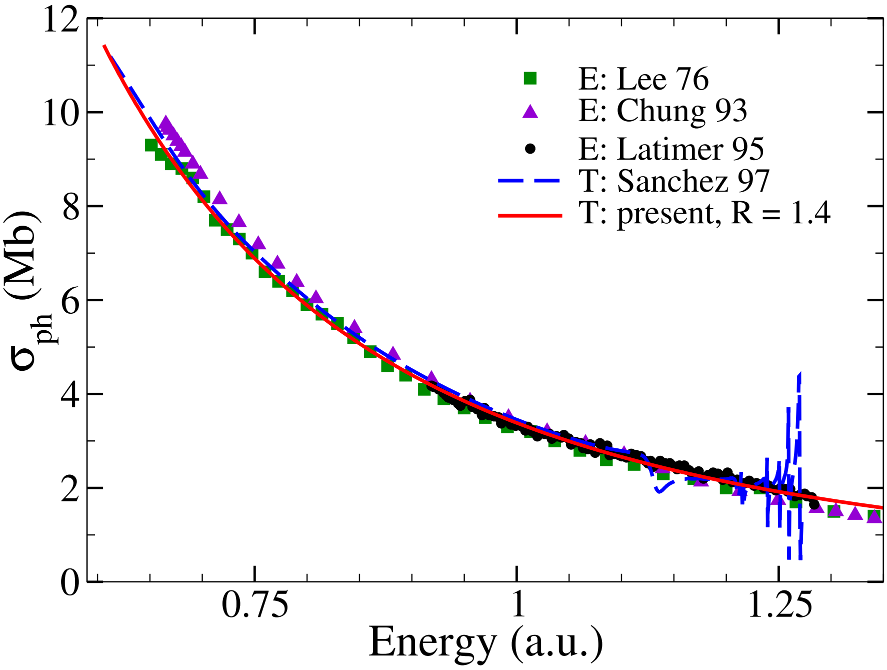

Figure 2.7.: *Total photoionization cross section of H_2 as a function of the photon energy for a fixed internuclear distance R_{nuc} = 1.4 a.u. Theory: red solid curve, present results with model potential V_{mod}; blue dashed curve, Sánchez and Martín [119]. Experiment: green squares, Lee et al. [120]; violet triangles, Chung et al. [121]; black circles, Latimer et al. [122]. Reproduced from [C].*

Photoionization cross sections

A calculation of the photoionization spectrum for the hydrogen molecule is used to demonstrate the applicability of the present model to interaction processes in which an H_2 molecule is ionized. In doing so, the representation of the continuum states is probed. Further applications of V_{mod} in order to describe ionization of H_2 in time-dependent processes can be found elsewhere [108, 123]. The photoionization cross section is given by

$$\sigma_{\text{p}h}(\epsilon) = \frac{4\,\pi^2}{c}\,(\epsilon - \epsilon_0)\;|\,M(\epsilon)\,|^2\;\rho(\epsilon)\,, \tag{2.39}$$

where ϵ is the positive energy of the ionized final state $|\,\epsilon\,\rangle$ with an angular momentum $l = 1$ and c is the speed of light. The transition matrix elements $M(\epsilon)$ are defined in the same way as in Eq. (2.38) except that the $|\,\epsilon\,\rangle$ are considered as final states. The density of continuum states $\rho(\epsilon)$ is used for energy-normalization of the cross section.

The present photoionization cross sections are calculated for $R_{\text{nuc}} = 1.4$ a.u. in order to compare the results with theoretical calculations from literature in which the fixed-nuclei approximation was used. Besides the theoretical results by Sánchez and Martín [119] also experimental photoionization cross sections are shown in Fig. 2.7 which were measured by Lee *et* al. [120], Chung *et* al. [121] and Latimer *et* al. [122].

It can be seen that the experimental photoionization cross sections are well described by the present model. At low energies, however, the results by Chung *e*t al. and Lee *e*t al. lie slightly above and below the present curve, respectively. The measurements by Latimer *e*t al. where performed between approximately 0.9 and 1.3 a.u. on a dense energy grid searching for resonances above 1.1 a.u. which they did not find. Their data match very well with the present curve which is, of course, free of any resonance caused by doubly-excited states. The clearly visible resonances in the theoretical data calculated by Sánchez and Martín around 1.12 and 1.25 a.u. were explained by Martín in [124] as being only visible within the fixed-nuclei approximation. In a further calculation which includes nuclear motion [124] the resonance effects are, in accordance with experimental results, practically invisible. This was explained by the broadening of the resonances, if the nuclear degrees of freedom are included. For energies below 1.1 a.u. where no resonances occur in the data of [119] their calculation agrees well with the present curve.

2.3. Model potential for alkali-metal atoms

A full description even of atomic targets of the same group as hydrogen in the periodic table of elements, the alkali-metal atoms, is much more demanding than for the hydrogen atom due to the fact that they are many-body systems with a large number of electrons. However, a large energy separation between the electrons of the closed inner shells and the outer valence electron is given for alkali-metal atoms. This electron structure suggests the application of a single-active electron (SAE) description, that is a separation of the electrons in frozen inner-shell electrons and a loosely-bound outer valence electron. In this work the valence electron of the alkali-metal atoms is exposed to a model potential,

$$V_{\mathrm{K}}(r) = -\frac{1}{r} - \frac{1}{r}\left[(Z-1)\,e^{-\gamma_1 r} + \gamma_2\, r\, e^{-\gamma_3 r}\right] - \frac{\alpha_d}{2r^4}\left(1 - e^{-\left(\frac{r}{\rho}\right)^4}\right)\,, \tag{2.40}$$

where Z is the nuclear charge, α_d the static dipole polarizability, ρ is a cut-off radius and $\gamma_{i=1,2,3}$ are atom-dependent model parameter. It is suitable for alkali-metal atoms describing the interaction of the valence electron with the nucleus as well as with the remaining inner-shell electrons. Additionally, core polarization effects are included. The employed model potential in Eq. (2.40) was proposed by Klapisch [125] and is therefore often referred to as *Klapisch potential.* The used potential parameters are given in Table I of Ref. [126]. The effect of the spin-orbit coupling is not included in the present approach.

The eigenstates and energies of the alkali-metal atoms are obtained with the approach presented in Sec. 2.1.2 by replacing the potential $V(r)$ in Eq. (2.7) with $V_{\mathrm{K}}(r)$ as given in Eq. (2.40). The energies of the states with principal quantum number $n < 6$ for the alkali metal atoms Li, Na and K are presented in Table 2.1 together with compiled values of the NIST (National Institute of Standards and Technology) data bank [110]. In the case of energy level splitting due to spin-orbit coupling the present energies are compared to the lower lying reference energies. The largest relative energy splittings

Table 2.1.: *Calculated binding energies in Rydberg for Li, Na and K using the Klapisch-model potential. All reference data are taken from the NIST data tables [110]. In the case of energy-level splitting due to spin-orbit coupling only the energetically lower lying reference energy is given.*

$n\,l$	Li calc.	Li [110]	Na calc.	Na [110]	K calc.	K [110]
2s	-0.396953	-0.396284				
2p	-0.260964	-0.260472				
3s	-0.148723	-0.148364	-0.378325	-0.377715		
3p	-0.114727	-0.114471	-0.223520	-0.223199		
3d	-0.111210	-0.111212	-0.112141	-0.111873	-0.123192	-0.122794
4s	-0.077388	-0.077230	-0.143507	-0.143155	-0.320210	-0.319032
4p	-0.064072	-0.063949	-0.102149	-0.101902	-0.200867	-0.200703
4d	-0.062547	-0.062547	-0.063061	-0.062884	-0.069908	-0.069372
4f	-0.062507	-0.062485	-0.062534	-0.062536	-0.062673	-0.062713
5s	-0.047354	-0.047273	-0.075312	-0.075168	-0.128242	-0.127425
5p	-0.040815	-0.040748	-0.058530	-0.058404	-0.094374	-0.093937
5d	-0.040025	-0.040025	-0.040319	-0.040211	-0.044316	-0.043965
5f	-0.040004	-0.039938	-0.040019	-0.040021	-0.040096	-0.040124

of the reference data due to the spin-orbit coupling of the energies given in Table 2.1 are 0.002 %, 0.1 % and 0.4 % for the energetically lowest lying p ($l = 1$) states of Li, Na and K, respectively. Particularly for Li there is a very good agreement with the data provided by NIST. But also for the other two atoms the deviation from the literature values remains at maximum around 1 %. The results for the Rb atom are of comparable accuracy (cf. Table 1 in Ref. [127]). However, due to the larger nucleus the hyperfine interaction becomes stronger leading to larger level splittings.

3. Close-coupling method

In ion-collision theory relativistic effects enter from two directions [94]. If the nuclear charge Z is sufficiently large, the mean velocity of an electron in a bound state can become comparable with the velocity of light c. Accordingly relativistic corrections, which are negligible for small Z ($\alpha Z \lesssim 0.1$) where $\alpha = 1/137.036$ is the fine structure constant, become significant for large Z and the employed orbitals must be based on solutions of the Dirac equation, or approximations to these. A different source of relativistic effects arises if the order of magnitude of the relative velocity in the collision becomes comparable with c. Relativistic kinematics must then be employed, and, in addition, even for small values of Z, relativistic orbitals must be used since the momentum distribution of the bound electron is very different in the relativistic and non-relativistic cases. In this work mostly small nuclear charges with $Z \leq 2$ are considered except for the alkali-metal atoms. For the latter, however, only the valence electron, which is exposed to a screened nucleus, is treated explicitly using a non-relativistic one-electron model description. The maximal velocity of the projectiles considered in this work is of the order of $0.1c$ and can therefore still be described without relativistic kinematics.

In this work the theoretical study of ion collisions with atoms and molecules shall be performed by solving the (non-relativistic) time-dependent Schrödinger equation (TDSE) of the collision system. The solution of the TDSE may be achieved by employing the close-coupling method. Here, an expansion of the time-dependent electronic scattering wave function in eigenstates of the atomic or molecular target is chosen. The according coupled equations are derived in the first section 3.1 of this chapter, while the eigenstates are obtained as described in the previous Chapter 2. The central ingredients in the close-coupling approach are the coupling or interaction matrix elements. These matrix elements are obtained by expressing the interaction potential between the projectile and the target in a basis of electronic eigenstates of the target. They contain all information about the considered collision system. They are derived in Sec. 3.2 where atomic and molecular targets as well as one- and two-electron molecules are separately discussed in some detail. Finally, in Sec. 3.3 there is a brief introduction to the first Born approximation which is a commonly used perturbative first-order approach to solve the TDSE.

3.1. Coupled equations

The time-dependent, non-relativistic, Schrödinger equation of a many-body system consisting of an ionic projectile[a] A^{Z_p} with charge Z_p, the positive core of the target B^{Z_T}, and N_e electrons e^- is

$$H\,\Psi = E\,\Psi\,, \tag{3.1}$$

with the Hamiltonian

$$H = i\,\frac{\partial}{\partial t} = T + V\,, \tag{3.2}$$

where E is the total energy and T and V are the kinetic and potential energy operators, respectively.

In the case of energetic projectiles, it is convenient to work in the framework of the impact-parameter method, i.e, the SCA as it is introduced in Sec. 1.3, where the position of the projectile is given by $\mathbf{R}(t)$. Then the kinetic energy operator T takes the form

$$T = -\frac{1}{2}\sum_{t=1}^{N_e}\nabla_t^2\,, \tag{3.3}$$

in which only the N_e electrons are considered. The potential energy operator V is the sum of the interparticle interaction energies

$$V = V_n(R) + \sum_{t=1}^{N_e}\left[V_e(r_t) + V_{int}(\mathbf{r}_t,\mathbf{R}) + \sum_{s>t}^{N_e} V_{ee}(\mathbf{r}_s,\mathbf{r}_t)\right], \tag{3.4}$$

where the $\mathbf{r}_s$ and $\mathbf{r}_t$ are the position vectors of the electrons. The interactions are considered to be solely Coulombic (spin-orbit coupling being neglected) with

$$V_e(r_t) = -\frac{Z_T}{r_t}\,, \tag{3.5}$$

$$V_{ee}(\mathbf{r}_s,\mathbf{r}_t) = \frac{1}{|\mathbf{r}_t - \mathbf{r}_s|}\,, \tag{3.6}$$

$$V_{int}(\mathbf{r}_t,\mathbf{R}) = -\frac{Z_p}{|\mathbf{r}_t - \mathbf{R}|}\,, \tag{3.7}$$

$$V_n(R) = \frac{Z_p\,Z_T}{R}\,. \tag{3.8}$$

Thereby, the Coulombic interaction potential between an electron and the nucleus B is given by V_e, between two electrons by V_{ee}, between an electron and the projectile A by V_{int}, and between the projectile A and the nucleus B by V_n.

More generally, V_e, V_{ee}, V_{int}, and V_n may also be effective potentials chosen to represent the interaction between the 'active' electron(s) and the ion cores A and B, and the interaction between the cores. It is assumed that these effective potentials are central.

---

[a] The ionic projectiles are considered to have no electrons which actively participate in the collision process.

For example, if B^+ represents a Na^+ ion, V_e represents an effective central potential between an electron and Na^+ and consequently V_{ee} would be zero. Usually, a specific form is chosen for a potential such as V_e depending on parameters which are adjusted so that on diagonalizing the Hamiltonian H_B of the atom ($B^+ + e^-$), where $H_B = -\frac{1}{2}\nabla^2 + V_e$, the energy spectrum obtained represents the observed energy spectrum of the atom as accurately as possible. The effective model potentials used in this work are presented in Secs. 2.2 and 2.3.

The time-dependent electronic scattering wave function in Eq. (3.1),

$$\Psi = \sum_j c_j \, \psi_j \, e^{-i\epsilon_j t} \,, \tag{3.9}$$

may be expanded in a complete basis set of target-centered eigenstates ψ_j of the time-*independent* Schrödinger equation

$$H_T \, \psi_k = \epsilon_k \, \psi_k \,, \tag{3.10}$$

where ϵ_k is the corresponding energy of the eigenstate ψ_k and the Hamiltonian H_T describes the unperturbed target system,

$$H_T = \sum_{t=1}^{N_e} \left[-\frac{1}{2} \nabla_t^2 + V_e(r_t) + \sum_{s>t}^{N_e} V_{ee}(\mathbf{r}_s, \mathbf{r}_t) \right] , \tag{3.11}$$

consisting of the kinetic and potential operators given in Eqs. (3.3), (3.5), and (3.6). Since all ψ_j and ϵ_j are time-independent the whole time dependence is included in the expansion coefficients c_j except for an explicitly time-dependent phase factor. A substitution of Ψ in Eq. (3.1) by its expansion given in Eq. (3.9) results in

$$i \, \frac{\partial}{\partial t} \sum_j c_j \, \psi_j \, e^{-i\epsilon_j t} = \sum_j \left[V_n(R) + V_{\text{int}}^{(N_e)}(\mathbf{R}) + \epsilon_j \right] c_j \, \psi_j \, e^{-i\epsilon_j t} \,, \tag{3.12}$$

with

$$V_{\text{int}}^{(N_e)}(\mathbf{R}) = \sum_{t=1}^{N_e} V_{int}(\mathbf{r}_t, \mathbf{R}) \,. \tag{3.13}$$

The projection on the state ψ_k yields

$$\begin{aligned} i \, \frac{dc_k}{dt} \, e^{-i\epsilon_k t} + i \, c_k \, (-i\epsilon_k) \, e^{-i\epsilon_k t} &= V_n(R) \, c_k \, e^{-i\epsilon_k t} + \epsilon_k \, c_k \, e^{-i\epsilon_k t} \\ &+ \sum_j \left\langle \psi_k \left| V_{\text{int}}^{(N_e)}(\mathbf{R}) \right| \psi_j \right\rangle \, c_j \, e^{-i\epsilon_j t} \end{aligned} \tag{3.14}$$

which can be easily rewritten into the usual form for the coupled equations

$$i \, \frac{dc_k}{dt} = V_n(R) \, c_k + e^{i\epsilon_k t} \sum_j \left\langle \psi_k \left| V_{\text{int}}^{(N_e)}(\mathbf{R}) \right| \psi_j \right\rangle \, c_j \, e^{-i\epsilon_j t} \,. \tag{3.15}$$

Note, it has been used that the time-independent eigenstates ψ are all orthogonal and also diagonalize $V_n(R)$ which does not depend on any electronic coordinate. Hence the term $V_n(R)\, c_k$ in Eq. (3.15) only leads to a phase shift and it can be therefore neglected in the case that only the transition probabilities

$$p_k = |c_k|^2 \tag{3.16}$$

into the states ψ_k are considered. Note, for a more differential analysis of the collision process, e.g., the extraction of angular-resolved electron-emission spectra, interference terms are important and the change of the phases by $V_n(R)$ is relevant.

The expression in Eq. (3.15) includes a sum over infinitely many states which is not possible to solve numerically in a finite time interval. Therefore, the close-coupling (CC) approximation is usually employed in which only a finite number N_{CC} of coupling matrix elements is considered. The name *close-coupling* originates from the idea that only the most relevant couplings are taken into account which are usually between (energetically) closely lying states ψ. In the present work, however, the coupling matrix elements between *all* N states ψ_j of the employed *finite* basis set are considered, i.e., $N_{CC} = N$. This results in a set of $N \times N$ complex or $2N \times 2N$ real coupled differential equations which have to be propagated in time.

The derived formulation of the coupled equations is also meaningful for molecular targets in the case that the Born-Oppenheimer (BO) approximation is employed. In the BO approximation it is assumed that the motion of the fast electrons and the slow nuclei of molecular targets can be decoupled (see, e.g., Ref. [89] for an introduction to the BO approximation and Secs. 2.1.3 and 2.1.4 for further comments). Accordingly, the Schrödinger equation for the electronic part of the molecular wave function can be solved for a fixed internuclear distance. Electronic potential curves are obtained, if the electronic part is solved for different internuclear distances.

The electronic part of the scattering wave function Ψ is expanded, like in Eq. (3.9), in a basis consisting of electronic eigenstates of the target molecule which are, however, obtained with the BO approximation. Hence, the coupled equations for molecules are formulated for a fixed internuclear distances vector $R_{\mathbf{n}uc}$ which becomes an (additional) parameter in the calculations. The dependence of the coupling matrix elements on the internuclear distance and the relative orientation of the molecular axis with respect to the projectile trajectory is explicitly discussed in Sec. 3.2.2.

3.2. Coupling matrix elements

In order to solve the coupled differential equations (3.15) and determine the expansion coefficients $c(t, b)$ the matrix elements [given in Eq. (3.7)]

$$V_{kj}(t, b) = \langle \psi_k \, | V_{\mathrm{int}}(\mathbf{R}(t, b)) | \, \psi_j \rangle \tag{3.17}$$

of the interaction potential V_{int} between the states ψ_k and ψ_j have to be known at every instant of time for the motion of the projectile along different trajectories $\mathbf{R}(t, b) =$

$(b, 0, vt)$, i.e., for different impact parameters b and velocities v. Since the time dependence of the coupling elements is not given by a (simple) time-dependent factor they have to be calculated in principle for all considered time steps explicitly. The required time steps are, however, not known in advance since a routine for solving the coupled differential equations is employed which chooses adaptively the size of the time steps in order to meet the requested accuracy. The coupling matrix elements are therefore calculated in advance on a grid along a given trajectory, i.e., for certain $\mathbf{R}_\nu = \mathbf{R}(t_\nu, b)$. The step size and functional behavior of the grid can be chosen where the expansion has either a linear, a quadratic, or a $(1 - \cos(x\,\pi/2))\,x$ form with $x = R/R_{\mathrm{max}}$. The functional form and step size of the grid expansion of the coupling matrix elements are further parameters which are of course subject to a convergence investigation. It turns out that a small step size in the vicinity of the nuclei and larger steps at larger distances, as provided by the $(1-\cos(x\,\pi/2))\,x$ shaped grid, are best suited due to the $1/R$ behavior of the Coulomb interaction. This choice reduces therefore the number of matrices which have to be calculated in advance. The coupling elements at the time t with $t_\nu \leq t < t_{\nu+1}$ needed for solving the coupled equations are obtained by interpolation of the in advance calculated matrix elements at $\mathbf{R}_\nu$ and $\mathbf{R}_{\nu+1}$.

As has been argued in the previous paragraph, first the coupling matrix consisting of $N \times N$ complex matrix elements has to be calculated several times for a large number of different time steps. Second, practically every state ψ_k is coupled via V_{int} with all other ψ_j of the basis due to the Coulomb interaction. This is in contrast to, e.g., the dipole interaction matrix elements which obey selection rules which strongly restrict the number of symmetry subspaces which are coupled. Due to these two facts which lead to a large number of coupling matrix elements to be calculated an efficient implementation for the calculation of the coupling matrix elements is required.

Finally, it should be emphasized that the development and implementation of the coupling matrix elements for one-electron and two-electron atoms and molecules, which are discussed in some detail in this section, are one of the central achievements of this work.

3.2.1. Atomic one-electron targets

The time-dependent matrix elements of the interaction potential $V_{int}(t; b)$ between the electronic basis functions $\psi_{n'l'm'}$ and ψ_{nlm} (obtained according to Sec. 2.1.2),

$$\begin{aligned} V_{n'l'm',nlm}(t; b) &= \langle \psi_{n'l'm'} \,| V_{int}(t; b) |\, \psi_{nlm} \rangle && (3.18) \\ &= \langle \psi_{n'l'm'} \,| 1\,/|\mathbf{r} - \mathbf{R}(t; b)| \,|\, \psi_{nlm} \rangle \ , && (3.19) \end{aligned}$$

depend on the position of the projectile $\mathbf{R}(t; b)$ and therefore, on the considered trajectory of the projectile. Due to the cylindrical symmetry of the collision process in the case of atomic targets (see the sketch on the cylindrical symmetry in Fig. 4.1) the matrix elements depend in particular on the impact parameter b. As was discussed before (see Sec. 2.1.3 also for notations and definitions) the (potential) term $1\,/|\mathbf{r} - \mathbf{R}|$ can be expanded in different ways,

$$\frac{1}{|\mathbf{r}-\mathbf{R}|} = \frac{1}{\sqrt{r^2+R^2-2rR\cos\gamma}} \tag{3.20}$$

$$= \sum_{s=0}^{\infty} \tilde{V}_s(r,R)\, P_s(\cos\gamma) \tag{3.21}$$

$$= \sum_{s=0}^{\infty} \sum_{q=-s}^{+s} \frac{4\pi}{(2s+1)} \tilde{V}_s(r,R)\, Y_s^{*q}(\Theta,\Phi)\, Y_s^q(\vartheta,\varphi)\,, \tag{3.22}$$

where ϑ, φ and Θ, Φ are the angular coordinates of the position vectors of the electron and the projectile, respectively. The coordinate system is chosen in such a way that the target nucleus is situated at the origin and the projectile moves parallel to the z axis from positive to negative z values. This means that the azimuthal angle Θ of the projectile decreases from values smaller than π to values close to 0 during its traversal. The impact-parameter vector $\mathbf{b}$ points along the x axis and thus the collision plane is perpendicular to the y axis. This coordinate frame is usually referred to as *space-fixed* or *laboratory* frame.

In what follows the expansion in spherical harmonics in Eq. (3.22) is considered to express the coupling matrix elements

$$\left\langle \rho_{n'l'} Y_{l'}^{m'} \left| \sum_{s=0}^{\infty} \sum_{q=-s}^{+s} \frac{4\pi}{(2s+1)} \tilde{V}_s(r,R) Y_s^{*q}(\Theta,\Phi) Y_s^q(\vartheta,\varphi) \right| \rho_{nl} Y_l^m \right\rangle . \tag{3.23}$$

in the eigenstates of the target. The matrix elements in Eq. (3.23) can be written as integrals over the spherical coordinates of the electron r, ϑ, and φ,

$$\begin{aligned} &\int dr\, r^2 \sum_{s=0}^{\infty} \sum_{q=-s}^{+s} \rho_{n'l'}^*(r)\, \tilde{V}_s(r,R)\, \rho_{nl}(r) \\ &\times \frac{4\pi}{(2s+1)} \iint \sin\vartheta d\varphi\, d\vartheta \Big(Y_{l'}^{*m'}(\vartheta,\varphi) \\ &\quad \times [\, Y_s^{*q}(\Theta,\Phi)\, Y_s^q(\vartheta,\varphi)\,]\, Y_l^m(\vartheta,\varphi) \Big) = \sum_{s=0}^{\infty} J_s(R) \sum_{q=-s}^{+s} I_s^q(\Theta,\Phi)\,. \end{aligned} \tag{3.24}$$

Thereby, the radial and the angular parts J_s and I_s^q, respectively, can be integrated separately. The integrals J_s and I_s^q are defined in the following way [b]

$$I_s^q = \frac{4\pi}{(2s+1)} Y_s^{*q}(\Theta,\Phi) \int_0^{\pi} \int_0^{2\pi} \sin\vartheta\, d\varphi\, d\vartheta\, Y_{l'}^{*m'}(\vartheta,\varphi)\, Y_s^q(\vartheta,\varphi)\, Y_l^m(\vartheta,\varphi)\,, \tag{3.25}$$

$$J_s = \int dr\, r^2 \rho_{n'l'}(r)\, \tilde{V}_s(r,R)\, \rho_{nl}(r)\,. \tag{3.26}$$

---

[b] In what follows the $*$ for $\rho_{n'l'}^*(r)$ is omitted since the $\rho(r)$ are all real functions.

The angular integration in I_s^q over the triple product of the spherical harmonics can conveniently be expressed with the help of the *Clebsch-Gordan-coefficients* (CGC) $C_{Jj_1j_2}^{Mm_1m_2}$ which are related to the *Wigner-3j-symbol* in the following way [128]:

$$C_{Jj_1j_2}^{Mm_1m_2} = (-1)^{j_1-j_2+M}\sqrt{2J+1}\begin{pmatrix} j_1 & j_2 & J \\ m_1 & m_2 & -M \end{pmatrix}. \tag{3.27}$$

The angular integral reads then [128]

$$\int_0^\pi \int_0^{2\pi} \sin\vartheta \, d\varphi \, d\vartheta \, Y_{l'}^{*m'} \, Y_s^q \, Y_l^m = \sqrt{\frac{(2s+1)(2l+1)}{4\pi(2l'+1)}} C_{l'sl}^{m'qm} C_{l'sl}^{000}. \tag{3.28}$$

The (complex) φ integration is only nonzero if $m' = q + m$ which results in a reduction of the sum over n in Eq. (3.24). Only for a value of $q = \bar{q} \equiv m' - m$ the integral remains nonzero. The CGC also fulfill the relation

$$C_{Jj_1j_2}^{Mm_1m_2} = (-1)^{J+j_1+j_2} \, C_{Jj_2j_1}^{Mm_2m_1} = (-1)^{J+j_1+j_2} \, C_{Jj_1j_2}^{-M-m_1-m_2}. \tag{3.29}$$

Furthermore, the CGC and therefore the integral I_s^q is only nonzero, if the sum of $l'+s+l$ is an integer and the triangular condition

$$|s-l| \leq l' \leq s+l$$

is fulfilled. Additionally, the sum $l' + s + l$ has to be even, since the CGC $C_{l'sl}^{000}$ is zero otherwise[c] [128, 129]. These three conditions lead to a limited number of s values given by

$$s = |l-l'|, |l-l'|+2, \ldots, l+l'-2, l+l'$$

for which the angular integrals I_s^q in Eq. (3.24) can be nonzero. Therefore, the number of different radial integrals J_s, which have to be explicitely calculated, is also limited to these s values. Of course, the condition $s \geq |\bar{q}|$ with

$$\bar{q} = m' - m \tag{3.30}$$

has also to be fulfilled. Although it is possible to solve the angular integration fully analytically, here the CGC are determined by employing existing numerical methods. An efficient recursive calculation of the CGC is, e.g., demonstrated in Ref. [130].

The integral I_s^q is finally expressed in the form

$$I_s^q(\Theta, \Phi) = \sqrt{\frac{4\pi(2l+1)}{(2s+1)(2l'+1)}} C_{l'sl}^{m'qm} C_{l'sl}^{000} \, Y_s^{*q}(\Theta, \Phi). \tag{3.31}$$

---

[c] From the relation $C_{Jj_1j_2}^{Mm_1m_2} = (-1)^{J+j_1+j_2} \, C_{Jj_1j_2}^{-M-m_1-m_2}$ given in Eq. (3.29) it can be easily seen that in the case $m_1 = m_2 = M = 0$ the CGC can only be nonzero, if the factor $(-1)^{J+j_1+j_2}$ is positive, i.e., the sum $J + j_1 + j_2$ is even.

In the case of atomic targets it is convenient to use trajectories which result in a collision plane perpendicular to the y axis (as defined before).[d] In that case the angle Φ of the projectile can always be set to $\Phi \equiv 0$ due to the spherical symmetry of atomic targets and the expression for I_s^q,

$$I_s^q(\Theta) = \begin{cases} 0 & \textit{for } q \neq \bar{q} \\ \sqrt{\frac{(2l+1)}{(2l'+1)} \frac{(s-\bar{q})!}{(s+\bar{q})!}}\, C_{l'\,s\,l}^{m'\,\bar{q}\,m}\, C_{l'\,s\,l}^{000}\, P_s^{\bar{q}}(\cos\Theta) & \textit{for } q = \bar{q} \end{cases}, \tag{3.32}$$

where P_l^m is an associated Legendre polynomial, simplifies since it becomes independent of Φ. Consequently, all coupling matrix elements are real numbers. After the angular part of the coupling matrix elements is solved the following facts can be concluded:

1. There is no dependence on R in I_s^q.
2. The angular part of V_{int} can be determined easily since it can be represented by CGC.
3. The CGC can be calculated efficiently using existing methods.
4. The sum $\sum_s$ has only a (small) finite number of nonzero summands according to the selection rules for CGC, if a finite basis expansion (in l) is used.
5. The sum $\sum_q$ has only one nonzero summand with $q = \bar{q} = m' - m$.
6. Matrix elements in Eq. (3.23) which differ only by the signs of m' and m are related by $I_s^{(m'-m)} = (-1)^{(m-m')}\, I_s^{(-m'+m)}$.

Now the radial integral $J_s(R)$ is considered in more detail,

$$\begin{aligned} J_s(R) = {} & \frac{1}{R^{s+1}} \int_0^R \rho_{n'l'}(r)\, r^s\, \rho_{nl}(r)\, r^2\, dr \\ & + R^s \int_R^{R_B} \rho_{n'l'}(r)\, \frac{1}{r^{s+1}}\, \rho_{nl}(r)\, r^2\, dr\,, \end{aligned} \tag{3.33}$$

where the explicit form of $\tilde{V}(r,R)$ is used which is given in Eq. (2.24). The radial functions $\rho_{nl}(r)$ which are determined as discussed in Sec. 2.1.2 are expanded on a dense sine-like spatial grid with N_g grid points in the entire interval $[0, R_B]$ of the (radial) box. The integration of Eq. (3.33) is then performed with an extended closed 14 points quadrature routine. The according weights were found once by fitting polynomials of order 13 through successive groups of 14 points.[e] This way of integration is efficient, since it is basically a summation of the integrand in Eq. (3.33) at all N_g grid points. It is at the same time rather precise [131] with an error that scales as $(1/N_g)^{14}$. The

---

[d] For atoms there is the freedom to choose a relative orientation of the trajectory due to their spherical symmetry.

[e] An introduction to simple quadrature routines and their implementation can be found in [131]. Therein also the derivation of the weight function is explained.

two integrals in Eq. (3.33) depend on R only by the upper or lower integration limit, respectively.

The coupling matrix elements in Eq. (3.18) expressed in eigenstates of the target can be formulated using the results of the radial and angular integrals in Eqs. (3.33) and (3.31), respectively, by

$$V_{n'l'm',nlm}(t;b) = \langle \psi_{n'l'm'} \left| V_{int}(t;b) \right| \psi_{nlm} \rangle \tag{3.34}$$

$$= \sum_{s=s_{\min}}^{*\, s_{\max}} J_s(R)\, I_s^{(m'-m)}(\Theta) \tag{3.35}$$

where $s_{\min}$ is given by $s_{\min} = \max(|l'-l|, |m'-m|)$. A restricted s summation, indicated by the * at the summation symbol $\sum^*$, is used in which either only even or odd values of s with $s_{\min} \leq s \leq l'+l = s_{\max}$ contribute depending on whether $l'+l$ is even or odd, respectively. Finally, it should be emphasized that the quality of the total interaction matrix elements is in principle determined by the accuracy of the radial functions ρ_{nl}.

3.2.2. Molecular one-electron targets

Molecular orientations

In contrast to atomic targets which are spherically symmetric, one set of trajectories, in which only the impact parameter b is varied, is not sufficient for molecular targets. In the case of a molecular collision, besides different b, also different angular orientations between the trajectory of the projectile and the molecular axis have to be considered explicitly in order to account for the anisotropy of the target. This leads to a three-dimensional set of trajectories of the projectile which can be characterized by the spherical coordinates $\{b, \Theta, \Phi\}$, where Θ, Φ give the relative orientation of the molecular axis.

For the description of the collision with a molecule two coordinate systems may be considered, namely the space-fixed frame and the molecule-fixed one. In the *space-fixed* frame, in which the x axis points along $\mathbf{b}$ and the z axis is parallel to $\mathbf{v}$ (cf. Fig. 1.2), the position vector of the projectile is given by $\mathbf{R}(t;b) = (R_x, R_y, R_z) = (b, 0, v\,t)$ and the spherical coordinates of one molecular nucleus are given by $(R_{nuc}/2, \Theta, \Phi)$.

The electronic wave functions ψ of the two-center molecular target in Eq. (2.21) are, however, defined in the *molecule-fixed* frame in which the z' axis is chose to be parallel to the internuclear axis (cf. Fig. 3.1). Therefore, also the time-dependent close-coupling calculations of the collision process are performed in the molecule-fixed frame. The position vector of the projectile $\mathbf{R} = (R_{x'}, R_{y'}, R_{z'})$ in the molecule-fixed space can be written as (cf. Refs. [73] and [G])

$$R_{x'} = b\,\cos\Theta\,\cos\Phi - v\,t\,\sin\Theta\,, \tag{3.36}$$

$$R_{y'} = -b\sin\Phi\,, \tag{3.37}$$

$$R_{z'} = b\,\sin\Theta\,\cos\Phi + v\,t\,\cos\Theta\,, \tag{3.38}$$

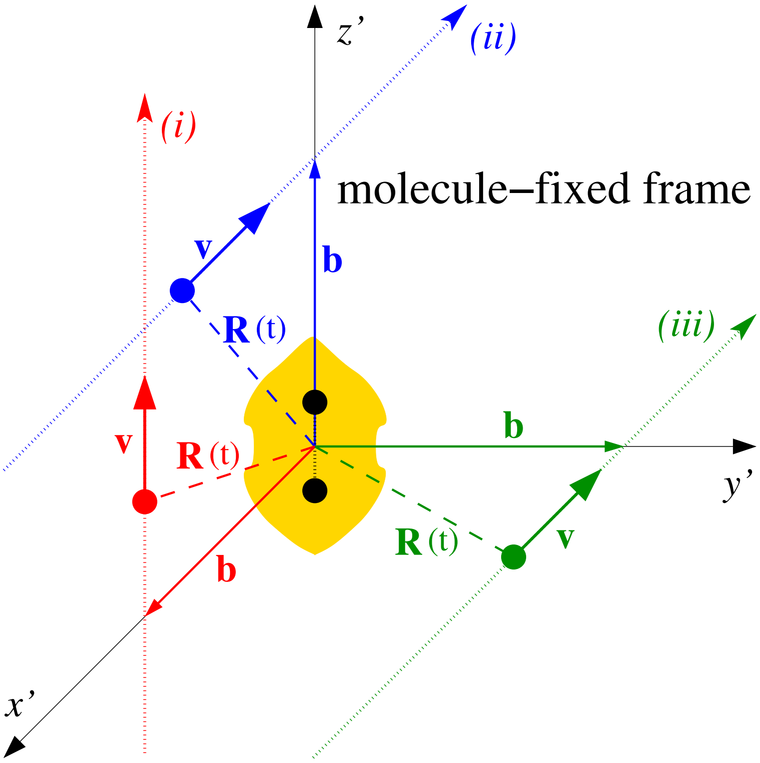

Figure 3.1.: Sketch of the molecule-fixed frame. The z' axis is parallel to the internuclear axis of the molecule. Shown are three trajectories of the projectile and their corresponding impact parameters **b** *for the orientations (i), (ii), and (iii), which are further explained in the text.*

or can be expressed in the *molecule-fixed spherical* coordinates

$$R = \sqrt{R_{x'}^2 + R_{y'}^2 + R_{z'}^2} = \sqrt{b^2 + v^2 t^2}\,, \tag{3.39}$$

$$\theta = \arccos\left(\frac{R_{z'}}{R}\right) = \arccos\left(\frac{b\,\sin\Theta\,\cos\Phi + v\,t\,\cos\Theta}{\sqrt{b^2 + v^2 t^2}}\right), \text{ and} \tag{3.40}$$

$$\phi = \arctan\left(\frac{R_{y'}}{R_{x'}}\right) = \arctan\left(\frac{-b\,\sin\Phi}{b\,\cos\Theta\,\cos\Phi - v\,t\,\sin\Theta}\right) \tag{3.41}$$

where ϕ [f] can take all values within the interval $[0, 2\pi]$. Note, in Eqs. (3.39)–(3.41) all three spherical coordinates are explicitly dependent on the time as well as on the impact parameter b. The angular coordinates θ and ϕ depend also on the relative orientation between the trajectory and the internuclear axis given by Θ and Φ. $R = |\mathbf{R}|$ is obviously the same in both frames.

---

[f] Care has to be taken that ϕ can take values within the interval 0 to 2π. Numerical programs often return values of arctan in the interval $[0, \pi]$. However, certain numerical programs provide a special function which returns ϕ usually within $-\pi \leq \phi \leq \pi$: Mathematica: ArcTan2, Fortran: ATAN2.

Molecular coupling elements

The coupling matrix elements of the time-dependent interaction potential induced by the moving projectile for a molecular one-electron target are similar to those for atomic targets discussed in the previous section. However, two major differences exist due to the loss of the spherical symmetry of the target. First, different orientations of the molecular axis with respect to the trajectory exist and lead to orientation-dependent coupling matrix elements. Second, the reduction of symmetries results in other (good) quantum numbers (m, π) characterizing the electronic states. Therefore, a different scheme for calculating the matrix elements is needed.

The coupling matrix elements of the interaction potential between the two states $\psi^{m'}_{n'\pi'}$ and $\psi^{m}_{n\pi}$, which are defined according to Eq. (2.21), are given by

$$\begin{aligned}
\left\langle \psi^{m'}_{n'\pi'} \middle| V_{\text{int}} \middle| \psi^{m}_{n\pi} \right\rangle &= \left\langle \psi^{m'}_{n'\pi'} \middle| \sum_{s=0}^{\infty} \sum_{q=-s}^{+s} \frac{4\pi}{(2s+1)} \tilde{V}^s \mathrm{Y}_s^{q*}(\theta,\phi) \mathrm{Y}_s^{q}(\omega) \middle| \psi^{m}_{n\pi} \right\rangle \\
&= \left\langle \sum_{l'=l'_{\min}}^{l'_{\max}} \rho^{m'}_{n'l'} \mathrm{Y}^{m'}_{l'} \middle| \sum_{s=0}^{\infty} \sum_{n=-s}^{+s} \frac{4\pi}{(2s+1)} \tilde{V}^s \mathrm{Y}_s^{*n}(\theta,\phi) \mathrm{Y}_s^{n}(\omega) \right| \\
&\quad \times \left| \sum_{l=l_{\min}}^{l_{\max}} \rho^{m}_{nl} \mathrm{Y}^{m}_{l} \right\rangle \qquad (3.42) \\
&= V^{(\phi)}_{m',m} \sum_{l'=l'_{\min}}^{l'_{\max}} \sum_{l=l_{\min}}^{l_{\max}} \sum_{s=s_{low}}^{s_{\text{up}}} V^{(R)}_{m'n'l',mnl,s} \, V^{(\theta)}_{m'l',ml,s} \, . \qquad (3.43)
\end{aligned}$$

Using the knowledge gained in the derivation of the atomic coupling elements the three terms $V^{(\phi)}_{m',m}$, $V^{(R)}_{m'n'l',mnl,s}$, and $V^{(\theta)}_{m'l',ml,s}$, which depend on ϕ, R and θ, respectively, are defined as [G]

$$\begin{aligned}
V^{(\phi)}_{m',m} &= e^{-i(m'-m)\phi} \, , \qquad (3.44) \\
V^{(R)}_{m'n'l',mnl,s} &= \left\langle \rho^{m'}_{n'l'} \middle| \tilde{V}_s(r,R) \left| \rho^{m}_{nl} \right\rangle \right. , \qquad (3.45) \\
V^{(\theta)}_{m'l',ml,s} &= \sqrt{\frac{(2l+1)}{(2l'+1)} \frac{(s-[m'-m])!}{(s+[m'-m])!}} \\
&\quad \times C^{m'(m'-m)m}_{l'sl} \, C^{000}_{l'sl} \, \mathrm{P}_s^{(m'-m)}(\cos\theta) \, . \qquad (3.46)
\end{aligned}$$

Due to the appearance of the CGC in Eq. (3.46) s only takes even or odd values depending on whether $s_{\text{up}} = l'_{\max} + l_{\max}$ is even or odd. The lower limit of s is determined by $s_{low} = \max(|m'-m|, |l'_{\max} - l_{\max}|)$. As in the atomic case in the summation over q only a single term with $q = m'-m$ has to be considered. Note, the expression (3.43) factorizes into two parts which can be determined independently, i.e., $V^{(\phi)}_{m',m}$ and a second term depending on R and θ in which different $V^{(R)}$ and $V^{(\theta)}$ are mixed by the summations over l', l and s. The possibility of this factorization is exploited in the time propagation, i.e., the integration of the coupled differential equations. During the (pre)calculation of the coupling matrix elements the term $V^{(\phi)}$ is not considered. Afterward, when the (complete) matrix elements are needed in the time propagation, the factor $V^{(\phi)}$ which is complex, is just multiplied.

From Eqs. (3.45) and (3.46) it can be seen that the form of the $V^{(R)}$ and the $V^{(\theta)}$ is similar to that of J and I, respectively, for atomic targets due to the one-center expansion of $\psi^{m'}_{n'\pi'}$ in Eq. (2.21). While $V^{(\theta)}$ and $V^{(\phi)}$ can be determined analytically, the radial part $V^{(R)}$ is integrated numerically using quadrature in the same way as discussed in the previous section for atomic systems. The number of different $V^{(R)}$ is much larger than those of $V^{(\theta)}$ and $V^{(\phi)}$, since the former depends on all seven parameters m', n', l', m, n, l, and s. Note, the number of radial integrals $V^{(R)}$ is also larger by approximately a factor l^2_{max} compared to the number of J in the atomic case, if the same number of basis states is considered. This is due to the employed one-center expansion of the molecular potential and the according expansion of the eigenstates in l dependent radial functions. Consequently, $V^{(R)}$ has to be evaluated efficiently. Furthermore, the behavior of the expressions in Eqs. (3.44)–(3.46) under exchange of the initial and the final state as well as under a simultaneous change of the signs of m' and m

$$V^{(\phi)}_{m',m} = V^{(\phi)*}_{m,m'} = V^{(\phi)*}_{-m',-m} = V^{(\phi)}_{-m,-m'}\,, \tag{3.47}$$

$$V^{(R)}_{m'n'l',mnl,s} = V^{(R)}_{-m'n'l',-mnl,s} = V^{(R)}_{mnl,m'n'l',s} = V^{(R)}_{-mnl,-m'n'l',s}\,, \tag{3.48}$$

$$\begin{aligned} V^{(\theta)}_{m'l',ml,s} &= (-1)^{(m'-m)} V^{(\theta)}_{-m'l',-ml,s} = V^{(\theta)}_{ml,m'l',s} \\ &= (-1)^{(m'-m)} V^{(\theta)}_{-ml,-m'l',s}\,, \end{aligned} \tag{3.49}$$

can be exploited to reduce the computational efforts.

Symmetries and selection rules

One aim of the present work is to drastically reduce the computational efforts in a theoretical treatment of collisions with molecules. This permits the description of more detailed cross sections in general, but is even more a prerequisite in view of full two-electron calculations for the demanding system $\bar{p}$ + H$_2$. Therefore, in what follows the three orthogonal orientations of the molecular axis $(\Theta, \Phi) = (i)\ (0, 0)$, $(ii)\ (\pi/2, 0)$, and $(iii)\ (\pi/2, \pi/2)$ are considered in more detail in order to discuss their properties and symmetries and the related selection rules of the according coupling matrix elements in Eq. (3.43). The resulting trajectories in the molecule-fixed frame for the parallel orientation (i) and the two perpendicular orientations (ii) and (iii) are sketched in Fig. 3.1. It should be emphasized that the presented method is more general and of course capable of arbitrary angular orientations.

In (i) the molecule- and space-fixed frame coincide resulting in the same kind of problem as for atomic targets, that is the angular coordinates in Eqs. (3.40) and (3.41) of the molecule-fixed frame become $\cos\theta = (v\,t)/R$ and $\phi \equiv 0$, respectively. In (ii) the molecular axis is oriented parallel to the impact parameter which gives ϕ equal to 0 or π for $R_{x'} > 0$ or $R_{x'} < 0$, respectively, and for θ one gets $\cos\theta = b/R$. Finally, in (iii) the molecular axis is oriented perpendicular to the collision plane given by $\mathbf{v}$ and $\mathbf{b}$ resulting in a time-dependent $\phi = \arctan(b/(v\,t))$ while θ is constant with $\cos\theta = 0$.

For (*i*) and (*ii*) the azimuthal angle ϕ can be considered as constant.[g] As a consequence, the system of coupled equations in Eq. (3.15) with the coupling elements given in Eq. (3.43) can be transformed in such a way that only positive m quantum numbers have to be treated explicitly when solving the coupled differential equations. Such a transformation was demonstrated explicitly, e.g., in Ref. [132] for atomic targets for which it is always possible to set $\phi \equiv 0$. Alternatively, the angular part of the basis states can be described with a combination of spherical harmonics $[(-1)^m Y_l^m + Y_l^{-m}]$ which is solely real as has been done for atomic targets (cf. Refs. [94] and [A]).

In (*iii*) these simplifications are not possible since ϕ is time-dependent. Consequently, positive as well as negative m quantum numbers have to be considered. However, the fact that $\cos\theta \equiv 0$ holds can be exploited. Accordingly, all odd associated Legendre polynomials — that is, $s + m' + m$ being odd — are zero and the interaction matrix elements of $V^{(\theta)}$ in Eq. (3.46) vanish. This results in a selection rule. Only those transitions are allowed in which either the parities of the initial and final state differ and the difference of the initial and final m is odd or both parities are equal and the difference of the m is even. In the case of an $\mathrm{H_2}^+$ molecular ion initially in its ground state, only transitions among the symmetry subspaces $(m, \pi) = (0, g)$, $(1, u)$, $(2, g)$, $(3, u)$, $(4, g)$,... are allowed.

Due to the mentioned symmetries for (*i*) and (*ii*) as well as for (*iii*) the employed expansion coefficients c_j separate into two sets which can be treated independently in the close-coupling calculations since they are not coupled by the matrix elements of the Coulomb interaction (Eq. (3.43)). Due to this decoupling the numerical effort can be reduced by nearly a factor 4. Note, although the time propagation in (*i*) and (*ii*) has only to be performed for either $m \geq 0$ or $m \leq 0$ the matrix elements in Eq. (3.43) have to be computed for negative and positive m which, however, differ only in $V^{(\theta)}$ and $V^{(\phi)}$.

3.2.3. Two-electron targets: He and H$_2$

The potential $V_{int}^{(N_e)}$ for the interaction between the projectile and N_e electrons of the target consists of N_e one-electron interaction potential terms V_{int}, as given in Eqs. (3.18)–(3.22), one for each electron. Therefore, it can be expressed in a sum of N_e one-electron terms,

$$V_{int}^{(N_e)} = \sum_{t=1}^{N_e} \frac{1}{|\mathbf{R} - \mathbf{r}_t|} = \sum_{t=1}^{N_e} V_{int}(\mathbf{r}_t)\,. \tag{3.50}$$

Although the following considerations are in general valid for N_e electrons the coupling matrix elements are derived explicitly only for two-electron targets. The two-electron

---

[g] In (*ii*) $V^{(\phi)}$ changes at $R_{x'} = 0$ from 1 discontinuously to $(-1)^{m'-m}$ what has to be taken into account during the calculation.

basis states

$$\begin{aligned}
\Phi_j^{\Omega}(\mathbf{r}_1,\mathbf{r}_2) &= \sum_{i'=1}^{N_C} C_{ij}\,\Upsilon_i^{\Omega}(\mathbf{r}_1,\mathbf{r}_2) && (3.51)\\
&= \sum_{i=1}^{N_C} C_{ij}\,\frac{1}{\sqrt{2}}\Big[\psi_\gamma(\mathbf{r}_1)\psi_\delta(\mathbf{r}_2) + (-1)^S\,\psi_\delta(\mathbf{r}_1)\psi_\gamma(\mathbf{r}_2)\Big] && (3.52)
\end{aligned}$$

are expanded according to Eqs. (2.32) and (2.31) in configurations Υ_i^{Ω} consisting of products of one-electron basis states ψ, where $i = (\gamma,\delta)$ labels a configuration. In what follows the configurations for $\Phi_{j'}^{\Omega'}$ may accordingly be denoted by $i' = (\alpha,\beta)$.

Utilizing Eqs. (3.50) and (3.52) a sum of one-electron matrix elements, which are determined as in the previous Secs. 3.2.1 and 3.2.2, can be used to express the coupling matrix elements between the two-electron states $\Phi_{j'}^{\Omega'}$ and Φ_j^{Ω},

$$\begin{aligned}
\Big\langle\, \Phi_{j'}^{\Omega'} \,\Big|\, V_{int}^{(2)} \,\Big|\, \Phi_j^{\Omega} \,\Big\rangle &= \sum_{t=1}^{2} \Big\langle\, \Phi_{j'}^{\Omega'} \,\Big|\, V_{\text{int}}(\mathbf{r}_t) \,\Big|\, \Phi_j^{\Omega} \,\Big\rangle && (3.53)\\
&= \sum_{t=1}^{2}\sum_{i'=1}^{N_C'}\sum_{i=1}^{N_C} C_{i'j'}\,C_{ij}\,\Big\langle\, \Upsilon_{i'}^{\Omega'} \,\Big|\, V_{\text{int}}(\mathbf{r}_t) \,\Big|\, \Upsilon_i^{\Omega} \,\Big\rangle && (3.54)\\
&= \frac{1}{2}\sum_{i'=1}^{N_C'}\sum_{i=1}^{N_C} C_{i'j'}\,C_{ij}\\
&\times \Big(V_{\alpha\gamma}\,\delta_{\beta\delta} + (-1)^{S'}\,V_{\alpha\delta}\,\delta_{\beta\gamma}\\
&\quad + V_{\beta\delta}\,\delta_{\alpha\gamma} + (-1)^{S'}\,V_{\beta\gamma}\,\delta_{\alpha\delta}\\
&\quad + (-1)^{S}\,V_{\beta\gamma}\,\delta_{\alpha\delta} + (-1)^{S+S'}\,V_{\beta\delta}\,\delta_{\alpha\gamma}\\
&\quad + (-1)^{S}\,V_{\alpha\delta}\,\delta_{\beta\gamma} + (-1)^{S+S'}\,V_{\alpha\gamma}\,\delta_{\beta\delta} \Big) && (3.55)\\
&= \delta_{S'S}\sum_{i'=1}^{N_C'}\sum_{i=1}^{N_C} C_{i'j'}\,C_{ij}\,\Big(V_{\alpha\gamma}\,\delta_{\beta\delta} + V_{\beta\delta}\,\delta_{\alpha\gamma}\\
&+ (-1)^{S}\,[\,V_{\alpha\delta}\,\delta_{\beta\gamma} + V_{\beta\gamma}\,\delta_{\alpha\delta}\,]\Big), && (3.56)
\end{aligned}$$

where $V_{\mu\nu}$ is the one-electron interaction matrix element,

$$V_{\mu\nu} = \langle \psi_\mu \,|\, V_{\text{int}} \,|\, \psi_\nu \rangle\,, \tag{3.57}$$

between the one-electron states ψ_μ and ψ_ν and $\delta_{\mu\nu}$ is the Kronecker delta due to the orthogonality of all ψ. Since the two-electron interaction matrix elements are basically obtained by performing a summation, the main work has to be done in advance, i.e. the calculation of the $V_{\mu\nu}$ and the C_{ij}. Consequently, the quality of the two-electron coupling matrix elements is mainly determined by the precision in the calculations of the one-electron coupling matrix elements and the CI coefficients. Note, the performed derivation is in principle the same for targets with atomic and molecular symmetry which differ only in the orbitals used for the configurations in Eq. (3.52).

The two-electron coupling matrix elements are only non-zero, if the spins of the initial and final state are the same due to the $\delta_{S'S}$ in Eq. (3.56). This means that in the case of a $S = 0$ singlet initial state — which is, e.g., the case for the ground states of H_2 and He — the interaction process can be described using a basis which only consists of singlet states.

3.3. The first Born approximation

A commonly used approach is the Born series, which is a perturbative expansion of the scattering wave function (or the scattering amplitude) in powers of the interaction potential. In a simple physical picture the Born series for the scattering amplitude can be regarded as a multiple scattering series in which the projectile interacts repeatedly with the interaction potential and propagates freely between two subsequent interactions. Thereby, the number of terms, i.e. the order of the approximation, corresponds to the number of considered interactions between the projectile and the potential. On the basis of this interpretation, the Born series can be expected to converge for non-relativistic scattering, if the incident particle is fast enough so that it cannot interact too many times with the potential and (or) if the interaction is sufficiently weak.

A remarkable progress in atomic collision theory was already made about 80 years ago in 1930 by Bethe who derived and applied the concept of the Born approximation for *the theory of the passage of fast corpuscle radiation through matter*[h] [74]. He was already at that time able to calculate first Born results for ionization and energy loss which are for fast particles in good agreement with experimental data. An extensive discussion of the whole framework of the Born approximation and its application to ion collisions is beyond the scope of this work. Rather, it is briefly shown how one can obtain results with the present method which correspond to the first Born approximation, that is how to treat the interaction in first-order perturbation. In this way first Born results are generated in this work.

An approximation of the coupled channels can be obtained by retaining a number of terms on the right-hand side of Eq. (3.15) and solving the resulting equations numerically. A perturbative first-order, i.e. first Born, solution is found as follows. If the system was originally in the state ψ_i with coefficient c_i, the initial conditions are given by

$$c_j(t) \to \delta_{ij}, \qquad t \to -\infty\,. \tag{3.58}$$

If the perturbation is small, all the amplitudes, i.e. expansion coefficients, $c_j(t)$ for $j \neq i$ will remain small and $c_i(t)$ will stay close to 1. The coupled equations (3.15) can then

---

[h] Original German title: *Zur Theorie des Durchgangs schneller Korpuskularstrahlen durch Materie.*

be approximated by

$$i\,\frac{dc_k}{dt} = \left\langle \psi_k \left| V_{int}^{(N_e)}(\mathbf{R}) \right| \psi_i \right\rangle \, e^{i(\epsilon_k - \epsilon_j)t} \,, \tag{3.59}$$

where the coupling is reduced to only the initial state. Due to the decoupling they can be solved (for $k \neq i$) by direct integration

$$c_k(t) = -i \int_{-\infty}^{t} \left\langle \psi_k \left| V_{int}^{(N_e)}(\mathbf{R}(t')) \right| \psi_i \right\rangle \, e^{i(\epsilon_k - \epsilon_j)t'} \, dt' \,. \tag{3.60}$$

The transition amplitude of finding the system after the collision in the state k is given by Eq. (3.60) in the limit $t \rightarrow \infty$. The matrix elements needed for the integration in Eq. (3.60) are the same as for the fully coupled equations. However, only coupling matrix elements including the initial state are required, that is only $N - 1$ complex coupling elements in contrast to $N \times N$ matrix elements in the general case, where N is again the number of basis states.

4. Cross sections

The probabilities for populating certain final channels after the collision may be preferably discussed in terms of cross sections. Cross sections are measurable quantities which are accessible in experiments. This chapter deals with the question how cross sections can be extracted from the results obtained in the present close-coupling calculations.

The relation between the final scattering wave function after the collision and the transition amplitudes as well as probabilities is shown in Sec. 4.1. Section 4.2 elaborates on the calculation of various cross sections for, e.g., ionization, excitation, electron-energy spectra, and energy loss. In the case that many-electron systems are described with effective one-electron model potentials a suitable interpretation of the transition amplitudes and probabilities is necessary. Accordingly, basic concepts of independent-electron and single-active-electron models are introduced in Sec. 4.3. Finally, in Sec. 4.4 the differences in the calculation of cross sections for molecular targets are discussed and partly compared with atomic targets.

4.1. Transition amplitudes and probabilities

The Hamiltonian H of the time-dependent Schrödinger equation (TDSE) in Eq. (3.1) describes the electrons of a target atom or molecule which are additionally exposed to a time-dependent Coulombic potential induced by a charged projectile moving on a given trajectory $\mathbf{R}(t)$. Due to its Coulombic nature, this interaction scales with $1/R$, that is, it decreases with increasing R but becomes 0 only in the limit $R \to \infty$.

In this work, the approximation is made that already for a large but finite $R = R_i$ the time-dependent interaction with the projectile is considerably small and can be set to zero. Therefore, it is possible to perform the integration of the TDSE, i.e. the time-propagation, within a finite time interval. This approximation leads for $R \geq R_i$ to an H which reduces to the time-independent target Hamiltonian H_T given in Eq. (3.11), that is, an unperturbed target system with the eigenstates ψ and eigenenergies ϵ which are determined as described in Sec. 2.1. Obviously, an appropriate radius R_i is not known *a priori* and it has to be shown that an increase of R_i does not change the outcome of the calculations significantly. Thus, it becomes a parameter in the numerical calculations. An appropriate R_i depends in particular on the specific collision system under consideration, e.g., on the charges Z_p and Z_T of the particles, the velocity of the projectile, and the spatial extension of the target.

Using this approximation, it is possible to have for a finite initial time t_i clearly defined initial conditions at $R(t_i) = R_i$. The target may, e.g., be initially in the state ψ_i, which can be the ground or an excited state, resulting in expansion coefficients $c_j(t_i) = \delta_{ji}$ in the expansion of the initial wavefunction $\Psi(t_i)$ in Eq. (3.9).[a]

The same approach is used for the final time t_f with $R(t_f) \geq R_i$, that is, for $t \geq t_f$ the target eigenstates ψ_j are again also eigenstates of the total Hamiltonian H. Then the amplitudes for a transition into a target eigenstate ψ_k after the collision,

$$a_k(t_f) = \langle \psi_k \,|\, \Psi(t_f) \rangle = c_k(t_f)\, e^{-i\epsilon_k t_f} \,, \tag{4.1}$$

can easily be determined by projecting on this state. The transition amplitudes are equal to the complex expansion coefficients c_k times a phase which depends on t_f. The theoretical description of the ion collision using the SCA is based on the impact-parameter formalism. Therefore, all transition amplitudes depend on the impact parameter $\mathbf{b}$ which is perpendicular to the incident direction of the projectiles. The probability for a transition into the state ψ_k is given by

$$p_k(t_f, \mathbf{b}) = |a_k(t_f, \mathbf{b})|^2 = |c_k(t_f, \mathbf{b})|^2 \,. \tag{4.2}$$

While the amplitude a_k in Eq. (4.1) is complex, p_k is a real number. Since p_k is a probability it satisfies the two conditions,

$$p_j(t) \,\epsilon\, [0,1] \quad \forall\, j \quad and \quad \sum_j p_j(t) = 1 \,, \tag{4.3}$$

for all t. The second condition corresponds to the conservation of the norm of the scattering wavefunction Ψ. The condition is checked throughout the time propagation and is usually always fulfilled, i.e., the norm remains unity with a variance of about 10^{-10}.

4.2. Calculation of cross sections

In the scattering example given in Sec. 1.1, which is used to illustrate the concept of a cross section σ, the number of particles scattered in the solid angle $d\Omega$, i.e. between θ and $\theta + d\theta$, is given [according to Eq. (1.5)] by

$$dN' = N_p \, n_T \, \frac{d\sigma}{d\Omega} \, d\Omega \,, \tag{4.4}$$

where N_p and n_T are proportional to the number of incident particles and scattering centers, respectively. The number of particles scattered in the impact parameter interval between b and $b + db$,

$$dN'' = N_p \, n_T \, P(\mathbf{b}) \, d\mathbf{b} \,, \tag{4.5}$$

is on the other hand proportional to an impact-parameter-dependent transition probability $P(\mathbf{b})$. Due to the conservation of the (scattered) particle number the equality

---

[a] Of course, the target can initially also be in any valid coherent superposition of the states ψ_j with according $c_j(t_i)$.

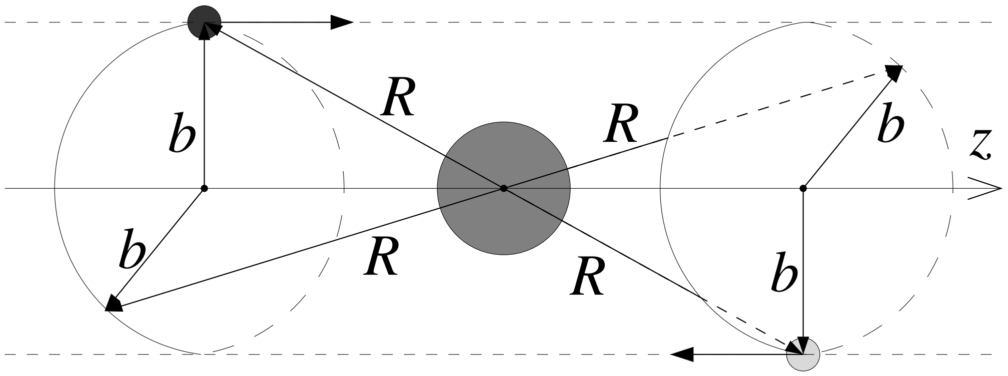

Figure 4.1.: *Schematic sketch of the cylindrical symmetry of the projectile trajectories and therefore transition probabilities and cross sections, respectively, in a collision with a spherically symmetric target (circle in the center). The projectile may approach the target parallel (black) or anti-parallel (gray) with respect to the z axis.*

$$\int dN' = \int dN'' \tag{4.6}$$

holds. Inserting Eqs. (4.4) and (4.5) into Eq. (4.6) yields

$$\int \frac{d\sigma}{d\Omega}\, d\Omega = \int P(\mathbf{b})\, d^2\mathbf{b}\,, \tag{4.7}$$

and the impact-parameter-dependent probability can therefore also be defined as

$$P(\mathbf{b}) \equiv \frac{d\sigma}{d^2\mathbf{b}}\,. \tag{4.8}$$

Finally, a cross section corresponding to the considered transitions may be defined as an integral of the corresponding transition probability P in the plane perpendicular to the incident direction which is spanned by the polar coordinates (b, ϕ),

$$\sigma = \int P(\mathbf{b})\, d^2\mathbf{b} = \int_0^{2\pi} d\phi \int_0^{\infty} db\, b\, P(b,\phi) \tag{4.9}$$

$$= 2\pi \int_0^{\infty} db\, b\, P(b)\,, \tag{4.10}$$

where Eq. (4.10) denotes the special case that the collision system has azimuthal symmetry ($\int_0^{2\pi} d\phi = 2\pi$) as, e.g., in the case for an atomic target.[b] The azimuthal symmetry in a collision with a spherically symmetric target is sketched in Fig. 4.1. Note, in this case there is of course no difference observed whether the projectiles moves parallel or anti-parallel to the z axis.

The probabilities are calculated in a finite impact-parameter interval $[b_{\mathrm{m}in}, \ldots, b_{\mathrm{m}ax}]$

---

[b] The general case without azimuthal symmetry is discussed in more detail in the context of molecular targets in Sec. 4.4.

which limits also the range of the b integration in Eq. (4.9). However, it is not sufficient to choose an interval in which the probability under consideration, $P(b,\phi)$, vanishes numerically for $b \to b_{\mathrm{max}}$. Instead it has to be assured that the term $b\,P(b,\phi)$ vanishes numerically for $b \to b_{max}$. The actual choice of a certain interval depends very much on the collision system, the collision process, and especially the impact energy of the projectile. The calculation of the probabilities for one specific $\mathbf{b}$ corresponds to a full solution of the TDSE in Eq. (3.1) for that $\mathbf{b}$. Therefore, the set of different $\mathbf{b}$ should be chosen in a way which is suited best to resolve the dependence of the probabilities on the impact parameter with a small but sufficient number of different $\mathbf{b}$ values. Usually the density of b points should be large in the vicinity of the target and can decrease for increasing b. Furthermore, the higher the impact energy, the larger $b_{\mathrm{m}ax}$ has to be chosen and at the same time the density of b points can be reduced. According to Eqs. (4.7) and (4.10) the calculated probabilities are weighted with the impact parameter b and are, after a spline interpolation, integrated with a standard quadrature routine.

4.2.1. Ionization and excitation

In the case of one-electron targets the probabilities for ionization and excitation[c] can be obtained easily and unambiguously by summing up all transition probabilities into ionized and excited states, respectively. As a criterion the energies ϵ of the target states can be used to define the probability for ionization,

$$P_{\mathrm{i}on} = \sum_{\epsilon_j > I_p} p_j \,, \tag{4.11}$$

and excitation,

$$P_{\mathrm{e}xc} = \sum_{\epsilon_0 < \epsilon_j < I_p} p_j \,, \tag{4.12}$$

where I_p is the ionization potential of the target and ϵ_0 is the ground-state energy. The probability for an excitation into a specific bound state ψ_k is obviously given by p_k in Eq. (4.2). Beside the probabilities for the sum of the total ionization $P_{\mathrm{i}on}$ and excitation $P_{\mathrm{e}xc}$ also other more differential probabilities might be considered, e.g., the sum of transitions into all bound-excited states within the same shell, i.e., the same n, or into all bound-excited or continuum states with quantum number l or m and so on. In these cases only the summations in Eqs. (4.11) and (4.12) have to be restricted accordingly.

For two-electron targets a larger variety of final channels exists. Using the same definitions as given in Eqs. (4.11) and (4.12) with I_p being the first ionization potential the interpretation is changed with respect to the one-electron case. $P_{\mathrm{e}xc}$ is the probability to find the target in a singly-excited bound state, that is one electron is considered to be in the ground state and the other in a bound excited state. $P_{\mathrm{i}on}$ on the other hand is the probability to find the target in a singly-ionized state, with one ground- or excited-state electron and one electron being ejected. Furthermore, $P_{\mathrm{i}on}$ includes the probability for

---

[c] Here the term *excitation* refers to transitions into bound states excluding the ground state. It is implied that the initial state is a non-degenerate ground state.

transitions into doubly-excited states whenever these states lie in the continuum and are therefore autoionizing as in the case of helium and hydrogen molecules[d] as well as for transitions into doubly-ionized states, in the case that they are included in the employed basis expansion. In order to differentiate further among these three channels the according two-electron eigenstates Φ_j have to be analyzed in more detail. This could be done in an approximate way by analyzing the leading, that is dominant, configurations for every Φ_j and attributing their properties to the total state. However, this kind of analysis for the two-electron states has not been implemented so far in this work.

In the case of positively charged projectiles the transition probability P_{ion} as given in Eq. (4.11) has to be considered more carefully since an electron of the target can be lost in two ways. First, there is, like for negative projectiles, ionization as given in Eq. (1.3). Second, there is additionally the channel for electron capture as given in Eq. (1.4), that is an electron is transferred during the collision from the target to the projectile reducing the projectile charge by one. Due to the employed one-center expansion of the scattering wavefunction Ψ centered on the target these two channels cannot be distinguished easily and enter both in P_{ion} which is therefore the total probability that an electron is lost by the target in the collision. Accordingly, the sum of both channels is more properly referred to as *electron loss* in the case of positive projectiles.

Finally, the cross sections for excitation into the bound state ψ_k, for total excitation, and total ionization of the target are obtained by replacing the probability P in Eq. (4.7) by p_k, P_{exc}, and P_{ion}, respectively.

4.2.2. Differential cross sections

The following discussion deals only with one-electron basis states ψ. Consistent with the previous sections the differential cross section for a transition into a specific (bound) state ψ_k of the target is simply given by

$$\sigma_k = \int_0^{2\pi} d\phi \int_0^{\infty} db\, b\, p_k(b, \phi) \tag{4.13}$$

where p_k is the transition probability given in Eq. (4.2). Obviously, the total excitation cross section is retrieved by the summation of all partial σ_j with $\epsilon_0 < \epsilon_j < I_p$.

In contrast to the case of discrete bound states this definition of a differential cross section cannot be used directly to obtain an observable quantity for ionized states which are continuous with respect to the electron energy ϵ. The differential cross section for ejecting one electron with an energy ϵ,

$$\mathfrak{s}(\epsilon) = \frac{d\sigma_{\text{ion}}(\epsilon)}{d\epsilon}\,, \tag{4.14}$$

---

[d] In hydrogen molecules the properties of the doubly-excited states can depend significantly on the internuclear distance R_{nuc} [133]. Around and below the ground-state expectation value $\langle R_{\text{nuc}} \rangle$, however, all doubly-excited states are autoionizing.

also referred to as electron-energy or electron-emission spectrum is rather obtained by

$$\mathfrak{s}(\epsilon) = \sum_{\mu} \sigma^{(\mu)}(\epsilon)\, \rho^{(\mu)}(\epsilon)\,, \tag{4.15}$$

that is the sum of all cross sections $\sigma^{(\mu)}(\epsilon)$ into a final ionization channel denoted by μ weighted with the density of continuum states $\rho^{(\mu)}(\epsilon)$ of that channel at the considered electron energy ϵ. Within one channel all states $\psi_\nu^{(\mu)}$ have the same electronic quantum numbers which may be comprised by μ, while ν in the index of the state $\psi_\nu^{(\mu)}$ within channel μ.

In practice, i.e. in any numerical approach, the ϵ_ν are discrete rather than continuous for $\epsilon_\nu > I_p$ due to the finite number of states in the expansion of Ψ. The quantities $\sigma^{(\mu)}(\epsilon)$ and $\rho^{(\mu)}(\epsilon)$ are therefore determined in the following way. For each symmetry subspace μ the value of the function $\sigma^{(\mu)}(\epsilon)$ for a specific electron energy ϵ may be achieved by interpolating the cross sections for transitions into the states $\psi_\nu^{(\mu)}$ and $\psi_{\nu+1}^{(\mu)}$ of this subspace where $\epsilon_\nu \leq \epsilon \leq \epsilon_{\nu+1}$. The $\sigma_\nu^{(\mu)}$ for a transition into the state $\psi_\nu^{(\mu)}$ is attained according to Eq. (4.13) by replacing p_k with $p_\nu^{(\mu)}$.

The density of states $\rho^{(\mu)}(\epsilon)$ of channel μ for a specific electron energy ϵ is approximated by interpolating the densities $\rho^{(\mu)}(\epsilon_\nu)$ and $\rho^{(\mu)}(\epsilon_{\nu+1})$ at the discrete electron energies ϵ_ν and $\epsilon_{\nu+1}$, respectively. In this work the density of states of channel μ for the electron energy ϵ_ν is obtained as

$$\rho^{(\mu)}(\epsilon_\nu) = \frac{2}{\epsilon_{\nu+1} - \epsilon_{\nu-1}} \tag{4.16}$$

where the condition $\epsilon_{\mu-1} < \epsilon_{\mu+1}$ has to be fulfilled. Note, in general the discrete energies ϵ_ν differer for different channels μ.

The total ionization cross section may be regained from the differential quantities in two ways. On the one hand, according to Eq. (4.14), by integration of the electron-energy spectrum $\mathfrak{s}(\epsilon)$ over the electron energy ϵ. this way can be used for a consistency check of the calculated differential cross section. But also by a simple summation of all partial σ_j obtained as in Eq. (4.13) for transitions into states ψ_j with electron energy $\epsilon_j > I_p$.

The extraction of doubly-differential cross sections is also possible and probably most simple in the framework of the impact-parameter method using the eikonal approximation. Derivations of the according transition amplitudes are performed, e.g., in Refs. [94, 132, 134] providing also further references. Recent applications of this approach for doubly-differential cross sections in collisions with protons and antiprotons are, e.g., [132, 134]. The extraction of doubly-differential cross sections is in principle also implemented in this work. However, no final results have been obtained so far, since the focus of this work is the development of a numerical method which is capable of the description of ion collisions on molecular two-electron targets. This is especially of importance for a precise characterization of low-energy antiproton collisions on molecular hydrogen which were required for the facility design of antiproton-storage rings. Therefore, the

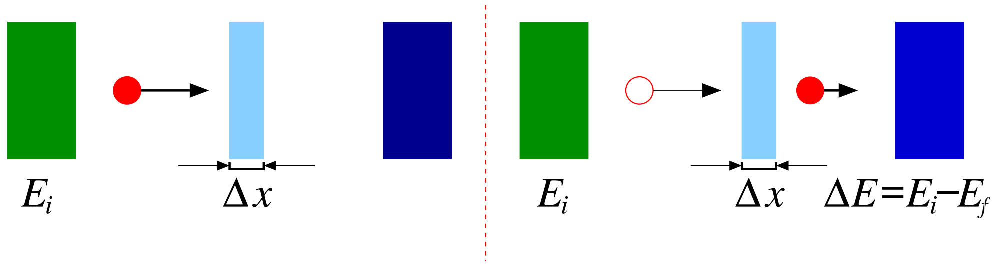

Figure 4.2.: *Schematic sketch of an energy-loss experiment. Left panel: A particle (red circle) is prepared (green box) with an initial energy* E_i *and encounters a medium (light blue) of thickness* Δx*. Right panel: After the traversal of the medium the particle is slowed down and reaches the detector (dark blue) with the final energy* E_f*. The energy loss of the particle is* $\Delta E = E_i - E_f$*. The stopping power is then given by* $S(E) = \Delta E/\Delta x$ *for* $\Delta x \to 0$.

extraction of doubly-differential cross sections has been postponed to future work, since it is considered as an application rather than a further development of the method. In this context it should be emphasized that much more (numerical) effort has to be spent in order to obtain converged doubly-differential results especially in comparison to total cross sections. This is due to the fact that for the extraction of doubly-differential cross sections transition *amplitudes* are required and the knowledge of transition *probabilities* is not sufficient (see the derivation in the above-mentioned references).

4.2.3. Stopping power

It can be assumed that the total stopping power of a heavy particle consists of an electronic and a nuclear part. The nuclear stopping power is of importance for very small impact velocities. For not too slow collisions it is, however, fully dominated by the electronic stopping power, that is $E > 10$ keV for antiproton collisions with hydrogen and helium targets [84–86, 135]). In what follows, only the electronic part of the stopping power S is determined.

A natural approach to measure the stopping power of a medium is to quantify the energy difference of the projectiles before and behind the target medium of a certain thickness and density which may be variable. This kind of experiment is sketched schematically in Fig. 4.2. Instead of looking at the energy which is lost by the projectile it is on the other hand also possible to consider the energy gain of the stopping medium due to inelastic interactions with the projectile. Both perspectives are equivalent since the sum of the energy loss by the projectile and the energy gain by the medium has to be zero.[e] In the present work the latter point of view is used to determine the

---

[e] The energetic equivalence of both perspectives is of course only given in a closed system. In the case, that only a finite target volume is considered, e.g. in experiments and applications, the projectile may deposit a certain amount of energy in this volume which may partly be transported to the surrounding by ejected particles. In a theoretical consideration, however, it is possible to assume a closed system.

stopping power

$$S = \sum_{\epsilon_j < I_p} (\epsilon_j - \epsilon_i)\, \sigma_j + \int_{I_p}^{\infty} d\epsilon\, (\epsilon - \epsilon_i)\, \mathfrak{s}(\epsilon)\,, \tag{4.17}$$

where σ_j and $\mathfrak{s}(\epsilon)$ are obtained as given in Eqs. (4.13) and (4.15), respectively. The ϵ_i and ϵ_j are the energies of the initial states i and the state j, respectively. They express the energy transfer from the projectile to the target needed for the transition and therefore the energy which is lost by the projectile. Obviously, the upper limit of the integration is reduced in a numerical approach to the maximal electron energy contained in the employed basis expansion.

4.3. Probabilities for one-electron models

Two different concepts can be used when describing many-electron targets with model potentials. Depending on the electronic structure of the target it might be advantageous to treat the electrons either on equal footing, e.g. for hydrogen molecules using an independent-electron model or to have one active electron in the field of the remaining (passive) electrons, e.g. for alkali-metal atoms with a closed inner shell structure and one outer valence electron, using the single-active-electron (SAE) model. The model potentials for hydrogen molecules[f] and alkali-metal atoms employed in this work are introduced in Secs. 2.2 and 2.3, respectively.

4.3.1. Independent-electron models

Using the assumption of independent electrons different ways have been suggested how to extract the transition probabilities of interest. Here only descriptions of two-electron targets with an independent-electron model are presented since only these are applied for molecular hydrogen and helium in this work. There are three common models using the idea of independent electrons which are presented in the following, namely, the *factor-2 model*, the *independent-particle model*, and the *independent-event model*.

The factor-2 model

The easiest way how to approximate single-electron transition probabilities for two-electron targets with an independent-electron model is the multiplication of all inelastic transition probabilities P with a factor 2,

$$P^{(2)} = 2\,P\,. \tag{4.18}$$

It is motivated by the idea that both electrons are independent and either electron A can be excited and electron B stays in the ground state or vice versa and therefore the probability for a certain process has to be doubled. This approach is known to work well

---

[f] The description of helium atoms is realized using the limit of the distance $R_{nuc} \rightarrow 0$ between the molecular nuclei.

when the probabilities for two-electron transitions as double ionization, ionization excitation, or double excitation are small. That is, in the case of ionization the probability for producing an ion is of the order of 10 % or less as has been observed, for example, for the ionization of an H_2 molecule by short intense laser pulses [136].

The independent-particle model

A more general way how to extract transition probabilities in the picture of two independent electrons is the independent-particle model (IPM). It is frequently employed in calculations of collisions with two-electron targets using an effective one-electron description, e.g., Refs. [137, 138]. It respects the two conditions for probabilities given in Eq. (4.3) and requires in particular for the independent electrons

$$1 = P_{\mathrm{g}r} + P_{\mathrm{ex}c} + P_{\mathrm{i}on} \tag{4.19}$$

where $P_{\mathrm{g}r}$ is the probability for staying in the ground state after the collision. Although the electrons are considered as independent it is furthermore required that the sum of all products between the transition probabilities of both electrons is also equal to unity,

$$\begin{aligned} 1 &= (P_{\mathrm{g}r} + P_{\mathrm{ex}c} + P_{\mathrm{i}on})\,(P_{\mathrm{g}r} + P_{\mathrm{ex}c} + P_{\mathrm{i}on}) \qquad (4.20)\\ &= {P_{\mathrm{g}r}}^2 + 2\,P_{\mathrm{g}r}\,P_{\mathrm{ex}c} + 2\,P_{\mathrm{g}r}\,P_{\mathrm{i}on} + 2\,P_{\mathrm{ex}c}\,P_{\mathrm{i}on} + {P_{\mathrm{ex}c}}^2 + {P_{\mathrm{i}on}}^2\,. \qquad (4.21)\end{aligned}$$

The six terms in Eq. (4.21) which are made up of the three one-electron probabilities $P_{\mathrm{g}r}$, $P_{\mathrm{ex}c}$, and $P_{\mathrm{i}on}$ are used to define the probabilities of the two-electron target. The following quantities might be defined as,

$$\begin{aligned} P_{\mathrm{g}r}^{(\mathrm{I}PM)} &= {P_{\mathrm{g}r}}^2\,, \qquad (4.22)\\ P_{\mathrm{ex}c}^{(\mathrm{I}PM)} &= 2\,P_{\mathrm{g}r}\,P_{\mathrm{ex}c}\,, \qquad (4.23)\\ P_{\mathrm{i}on}^{(\mathrm{I}PM)} &= 2\,P_{\mathrm{g}r}\,P_{\mathrm{i}on} + 2\,P_{\mathrm{ex}c}\,P_{\mathrm{i}on} = 2\,P_{\mathrm{i}on}\,(1 - P_{\mathrm{i}on})\,, \qquad (4.24)\end{aligned}$$

where $P_{\mathrm{g}r}^{(\mathrm{I}PM)}$ is the probability for staying in the ground state, $P_{\mathrm{ex}c}^{(\mathrm{I}PM)}$ for excitation of one electron into a bound state, and $P_{\mathrm{i}on}^{(\mathrm{I}PM)}$ for producing a singly-charged target. Accordingly, the two transition probabilities

$$\begin{aligned} P_{\mathrm{de}}^{(\mathrm{I}PM)} &= {P_{\mathrm{ex}c}}^2\,, \qquad (4.25)\\ P_{\mathrm{d}i}^{(\mathrm{I}PM)} &= {P_{\mathrm{i}on}}^2\,, \qquad (4.26)\end{aligned}$$

describe double excitation and double ionization, respectively. Note, in the case of helium and for molecular hydrogen with not too large internuclear distances [133] all doubly-excited states are autoionizing, i.e., they have a finite lifetime after which they decay into an ionic state.

As can be seen from Eqs. (4.22)–(4.24) the probabilities $P^{(\mathrm{I}PM)}$ go over to those of the simple factor-2 model $P^{(2)}$ described before, if

$$P_{\text{gr}} \to 1 \quad \wedge \quad P_{exc}\,,\, P_{\text{ion}} \to 0\,, \tag{4.27}$$

that is, in the case of weak interactions. Furthermore, the probabilities for transitions of both electrons, i.e. in particular $P_{\text{de}}^{(\text{I}PM)}$ and $P_{\text{d}i}^{(\text{I}PM)}$, vanish in this limit due to their quadratic dependence.

The independent-event model

A further simple model is the independent-event model (IEV) in which low-energy double-ionization is treated as a two-step *sequential* process. The first step is the removal of an electron from the neutral target. It takes place at a relatively large distance to the core. In the model the residual ion is assumed to relax to the ground state of the *ionic* target while the projectile is moving close enough to ionize in a second step the other electron, since the collision velocity is much lower than the target electrons' orbital velocity. Furthermore, the two steps are considered as being completely uncorrelated. Different implementations of the IEV have been proposed as mentioned in [50]. The way as the IEV is implemented in [50] is presented and used in this work.

In the IEV the probability of double ionization of the target B after a collision is given by

$$P_{\text{d}i}^{(\text{I}EV)} = P_{\text{i}on}^{\text{B}}\, P_{\text{i}on}^{\text{B}^+}\,, \tag{4.28}$$

where $P_{\text{i}on}^{\text{B}} = P_{\text{i}on}$ is, as described before, the ionization probability for one electron from the effective one-electron calculation using a model for B. $P_{\text{i}on}^{\text{B}^+}$ is on the other hand the single-ionization probability for a collision with the ionic target B^+. Furthermore, in this model the probability of neither of the two electrons being ionized, i.e. staying neutral, is

$$P_{\text{neu}}^{(\text{I}EV)} = (1 - P_{\text{i}on}^{\text{B}})\,(1 - P_{\text{i}on}^{\text{B}})\,, \tag{4.29}$$

the same as in the IPM above. The probability for one and only one electron to be ionized must then be

$$P_{\text{i}on}^{(\text{I}EV)} = 1 - P_{\text{neu}}^{(\text{I}EV)} - P_{\text{d}i}^{(\text{I}EV)}\,, \tag{4.30}$$

where the conditions for probabilities given in Eq. (4.3) have been used. This gives for the single ionization probability

$$P_{\text{i}on}^{(\text{I}EV)} = P_{\text{ion}}^{\text{B}}\,(1 - P_{\text{i}on}^{\text{B}^+}) + (1 - P_{\text{i}on}^{\text{B}})\,P_{\text{i}on}^{\text{B}} \tag{4.31}$$

$$= 2P_{\text{i}on}^{\text{B}} - P_{\text{i}on}^{\text{B}}\,P_{\text{i}on}^{\text{B}^+} - (P_{\text{i}on}^{\text{B}})^2\,. \tag{4.32}$$

The expression in Eq. (4.31) has a simple interpretation. The first term is the probability that one electron is ionized and that the remaining one (now in a B^+ potential) is not ionized. The second term is the probability that the first electron is not ionized times the probability that the second one (which is still in a neutral potential of B) is ionized. The difference between the IPM and the IEV is exactly given by the middle term of Eq.

(4.32), i.e., $P^{\mathrm{B}}_{ion}\,P^{\mathrm{B}^+}_{ion}$.

4.3.2. The stopping power of two independent electrons

In an independent-electron model it is assumed that both electrons have the same transition probabilities given by the single-electron probabilities in Eq. (4.2) and that they are independent of each other. As a consequence the total stopping power due to one electron is — in contrast to certain cross sections obtained with the IPM — independent from and equal to the one of the other electron. Therefore, in the case of targets with N electrons the final stopping power given in Eq. (4.17) computed for a single electron has to be multiplied with the factor N in order to sum up the contributions from all N independent electrons.

This argument can also be expressed in a more formal way starting in accordance with Eq. (4.3) with the relation

$$1 = \sum_j p_j = \sum_j p_j \sum_k p_k = \sum_{j,k} p_j\, p_k\,, \tag{4.33}$$

where the indices j and k are meant to indicate one of the electrons. In view of the stopping power [cf. Eq. (4.17)] the transition probabilities are multiplied with the sum of energies $\tilde{\epsilon}_j + \tilde{\epsilon}_k$ needed for the transitions of one electron into state ψ_j and the other into ψ_k with $\tilde{\epsilon_j} = \epsilon_j - \epsilon_i$. This yields

$$\begin{aligned}
\sum_{j,k} p_j\, p_k (\tilde{\epsilon}_j + \tilde{\epsilon}_k) &= \sum_{j,k} p_j\, p_k\, \tilde{\epsilon}_j + \sum_{j,k} p_j\, p_k\, \tilde{\epsilon}_k && (4.34)\\
&= 2 \sum_{j,k} p_j\, p_k\, \tilde{\epsilon}_j && (4.35)\\
&= 2 \sum_j p_j\, \tilde{\epsilon}_j \underbrace{\sum_k p_k}_{=\,1} && (4.36)\\
&= 2 \sum_j p_j\, \tilde{\epsilon}_j = \sum_j p_j\, (2\tilde{\epsilon}_j)\,. && (4.37)
\end{aligned}$$

It should be noted that the use of the sum of single-electron energies for both electrons is an approximation which seems, however, to be consistent within the employed independent-electron model. This approximation is reasonable, if one-electron transitions are dominating the electronic energy loss. Finally, the last line can be interpreted in the way that the total single-electron stopping power is multiplied with a factor 2 which accounts for the two electrons as mentioned above. Note, that the sum of all probabilities is still unity and is therefore conserved as it should be.

A similar derivation as in Eqs. (4.34)–(4.37) can be used in the case that the summation runs only over a limited number of final states as has been done in Ref. [F]. As example the contribution to the stopping power due to double ionization shall be considered first. Then the indices j and k only take continuum states into account leading to a restricted summation indicated by an asterisk above the sum

$$2 \sum_{j,k}^{*} p_j p_k \, \tilde{\epsilon}_j = 2 \sum_{k}^{*} p_k \sum_{j}^{*} p_j \, \tilde{\epsilon}_j \tag{4.38}$$

$$= 2 \quad P_{\text{ion}} \sum_{j}^{*} p_j \, \tilde{\epsilon}_j \, . \tag{4.39}$$

Accordingly, the contribution to the stopping power from all electron transitions into the continuum is obtained by relaxing the restriction on the sum over k in Eq. (4.38) to all possible final states. That is, the stopping power for the sum of all one-electron transitions into the continuum independent of the state of the other electron. The relaxation of the sum over k,

$$2 \sum_{k} \sum_{j}^{*} p_j p_k \, \tilde{\epsilon}_j = 2 \sum_{k} p_k \sum_{j}^{*} p_j \, \tilde{\epsilon}_j = 2 \sum_{j}^{*} p_j \, \tilde{\epsilon}_j \, , \tag{4.40}$$

yields a factor one instead of P_{ion} in Eq. (4.39). Thus, the same result as in the one-electron case is obtained which is just multiplied with a factor two. However, in the case of two-electron targets this is the sum of contributions due to single and double ionization. Finally, the contribution to the stopping power from all (independent) electron transitions into bound states is given by

$$2 \sum_{k} \overline{\sum_{j}} p_j p_k \, \tilde{\epsilon}_j = 2 \sum_{k} p_k \overline{\sum_{j}} p_j \, \tilde{\epsilon}_j = 2 \overline{\sum_{j}} p_j \, \tilde{\epsilon}_j \, , \tag{4.41}$$

where the bar above the sum indicates that the summation is restricted to bound states only. The sum of the contributions due to ionization in Eq. (4.40) and excitation in Eq. (4.41) obviously yields the correct total result as given in Eq. (4.37).[g]

The results in Eqs. (4.37)–(4.41) for the stopping power seem to contradict with the way how two-electron cross sections are extracted from single-electron probabilities employing the IPM. For cross sections it is important that the probability for double excitation or ionization is only counted once — compare Eqs. (4.25) and (4.26) — and not twice in order to preserve the sum of probabilities being unity. The factor two in the case of the stopping power, however, appears not due to an increase of the probability for double transitions but because of the fact that in these transitions both electrons

---

[g] A different classification can be used for contributions to the electronic stopping power due to ionization and excitation. If the contribution from all two-electron transitions leading to a continuum or bound final state is used the according expressions are given by

$$2 \left(P_{\text{ion}}^{(IPM)} \overline{\sum_{j}} p_j \, \tilde{\epsilon}_j + \sum_{j}^{*} p_j \, \tilde{\epsilon}_j \right) \qquad and \qquad 2 \left(1 - P_{\text{ion}}^{(IPM)} \right) \overline{\sum_{j}} p_j \, \tilde{\epsilon}_j \, ,$$

respectively. This interpretation differs from that in Ref. [F] but sum of both still recovers the total energy loss as given in Eq. (4.37).

gain energy and the probability has therefore to be weighted with the double amount of energy by what the seeming contradiction is resolved.

4.3.3. The single-active-electron model

In the SAE approximation a many-electron target is described as if it consists of only one (active) electron and a core which comprises the nucleons as well as the inner (passive) electrons usually expressed together by an effective potential. Therefore, the extraction of observables like cross sections can be performed exactly in the same way as described in the previous sections for true one-electron targets like the hydrogen atom. Thereby, the SAE model is capable of describing single-electron processes like single-ionization or single-excitation. However, no two-electron effects are included and accordingly no two-electron cross sections can be obtained with the SAE. The SAE model is a natural choice for one-electron descriptions of alkali-metal atoms.

4.4. Cross sections for molecular targets

4.4.1. Molecular transition probabilities

In contrast to atomic targets which are spherically symmetric, one set of trajectories in which only the absolute value of the impact parameter b is varied is not sufficient for molecular targets. In the case of a molecular collisions, besides different b, also different angular orientations between the trajectory of the projectile and the molecular axis have to be considered explicitly in order to account for its anisotropy. Furthermore, the distance R_{nuc} between the nuclei is subject to changes due to vibrational motion during the collision process. This leads to a four-dimensional set of trajectories of the projectile which can be characterized by the impact parameter b together with the spherical coordinates $\mathbf{R_{nuc}} = \{R_{nuc}, \Theta, \Phi\}$, where Θ, Φ give the relative orientation.of the molecular axis with respect to the projectile trajectory which defines the laboratory frame. A discussion on different orientations of the molecular axis and their influence on the coupling-matrix elements can be found in Sec. 3.2.2.

The probability after the collision $t = t_f$ for a transition into the electronic final state ψ_k for a fixed configuration of the molecular nuclei $\mathbf{R_{nuc}} = (R_{nuc}, \Theta, \Phi)$ in the BO picture is given by

$$p_k(b, E; R_{\mathrm{nuc}}, \Theta, \Phi) = |c_k(b, v; R_{\mathrm{nuc}}, \Theta, \Phi, t_f)|^2 \, , \tag{4.42}$$

using the classical relation between E and v as given in Eq. (.1). In accordance with

[73], the transition probability

$$\begin{aligned} p_k(b,E) &= \int \Big(\Big|\chi_{\nu j}(R_{nuc})\, Y_j^m(\Theta,\Phi)\Big| \Big/ R_{\mathrm{nuc}} \Big)^2 \\ &\quad \times\, p_k(b,E;R_{\mathrm{nuc}},\Theta,\Phi)\, \sin\Theta\, R_{nuc}^2\, dR_{\mathrm{nuc}}\, d\Theta\, d\Phi \qquad (4.43) \\ &= \int \Big|\chi_{\nu j}(R_{\mathrm{nuc}})\, Y_j^m(\Theta,\Phi)\Big|^2 \\ &\quad \times\, p_k(b,E;R_{\mathrm{nuc}},\Theta,\Phi)\, \sin\Theta\, dR_{\mathrm{nuc}}\, d\Theta\, d\Phi\,. \qquad (4.44) \end{aligned}$$

becomes independent of the orientation and the nuclear distance by integration over $\mathbf{R_{nuc}}$. The $\chi_{\nu j_{\mathrm{n}}}$ are the eigenfunctions of the molecular vibration, $Y_{j_{\mathrm{n}}}^{m_{\mathrm{n}}}$ the spherical harmonics, and $(\nu, j_{\mathrm{n}}, m_{\mathrm{n}})$ the vibrational and rotational quantum numbers in accordance with Eq. (2.18). Consequently, a sufficient number of trajectories for different Θ and Φ as well as R_{nuc} have to be calculated in order to perform a (numerical) integration of Eq. (4.44) for every impact parameter b. This drastically increases the computational effort needed for the determination of transition probabilities of molecules in comparison to spherically symmetric targets where only one orientation is sufficient and no internuclear distance occurs. Therefore, a suitable two-dimensional and one-dimensions grid of the angular and internuclear coordinates have to be found which are sufficient to appropriately describe the transition probability by using only an acceptable number of different molecular orientations, i.e., different sets of coupled equations as given in Sec. 3.1.

Afterward, when p_k is known the evaluation of the cross sections can be performed in the way presented in the previous sections. The cross section for a transition, e.g., into state ψ_k,

$$\sigma_k(E) = 2\,\pi \int p_k(b,E)\, b\, db\,, \qquad (4.45)$$

can be obtained again by integration of p_k over b as is done for atomic targets which are spherically symmetric.

4.4.2. Franck-Condon approximation

If, for instance, R_{nuc} is always set to the mean internuclear distance $\langle\, R_{nuc}\,\rangle$ of the target molecule like a rigid rotor or if the dependence of the cross section on R_{nuc} is negligible, the cross section can be evaluated by a Franck-Condon-type approximation,

$$\sigma \approx \sigma_{\mathrm{FC}} = \sigma(\langle\, R_{\mathrm{nuc}}\,\rangle)\,. \qquad (4.46)$$

This Franck-Condon (FC) approximation is often used for the calculation of electronic excitation in molecular collisions [139]. For the special case of $j_n = 0$ one can integrate in a straightforward way over the orientations Θ and Φ according to [73] in order to obtain a cross section independent of $\mathbf{R_{nuc}}$.

In this work the FC approximation is preferably used in order to reduce the numerical costs and therefore in what follows the subscript FC indicating the use of the FC approximation is omitted. However, the dependence of the ionization and excitation cross sections on the internuclear distance R_{nuc} and therefore the accuracy and range of applicability of the FC approximation is examined thoroughly in Sec. 6.2.3 for $\bar{p}$ + H_2. The dependence on R_{nuc} for antiproton impact on $H_2{}^+$ cations has been studied by Sakimoto [73] and good agreement is observed using the FC approximation especially for high impact velocities.

4.4.3. Orientational-average approximation

One aim of the present study is to drastically reduce the computational effort for ion collisions with molecules. This is a precondition for the demanding full two-electron calculations including H_2 molecules and may finally even permit the calculation of differential cross sections. As can be seen from Eq. (4.42) a large number of calculations are necessary in order to perform an integration over the angles Θ and Φ in Eq. (4.44).

An alternative approach, though approximate, is to use for fixed R_{nuc}, b, and E an orientationally averaged transition probability defined by

$$p_k = \frac{1}{3}\left[p_k(0,0) + p_k\left(\frac{\pi}{2},0\right) + p_k\left(\frac{\pi}{2},\frac{\pi}{2}\right)\right] . \tag{4.47}$$

Thereby, only the three orthogonal orientations of the molecular axis with respect to the projectile trajectory $(\Theta, \Phi) =$ (*i*) $(0,0)$, (*ii*) $(\pi/2, 0)$, and (*iii*) $(\pi/2, \pi/2)$ (*i*), (*ii*), and (*iii*) — discussed in Sec. 3.2.2 and sketched in Fig. 3.1 — are considered instead of performing the integration in Eq. (4.44). An integration requires, on the other hand, a two-dimensional grid of different angles where each point of the angular grid corresponds to a set of trajectories for different impact parameters b. Therefore, the number of trajectories in the case of integration is certainly much larger than in the case of orientational averaging, where each trajectory requires the solution of the corresponding TDSE.

In this work the results for ionization in $\bar{p}$ + $H_2{}^+$ collisions obtained by Sakimoto [73] were further analyzed regarding their orientational dependence. Using his data it was found that the orientation-integrated ionization cross sections for $\bar{p}$ + $H_2{}^+$ — obtained according to Eq. (4.44) — can be nicely reproduced by the orientation-averaged cross section — according to Eq. (4.47) — using only his results for the three orthogonal orientations (*i*), (*ii*), and (*iii*). The relative difference of the ionization cross section obtained by integration and by averaging of the three orientations is around 1% for $E = 2$ keV and 2% for $E = 100$ keV. Additionally, it was proven by Errea *e*t al. in Ref. [140] that for ion collisions with H_2 the approximation of using only the three specific orientations, i.e. Eq. (4.47), is equivalent to Eq. (4.44), if the integration is performed with a six-point quadrature formula.

Part III.

Results

5. Atomic targets

Ion collisions with atomic targets have a long tradition and are therefore experimentally as well as theoretically well studied. In view of the scope of this work, they can be considered as a first and at the same time elementary step towards collisions involving the more complex molecular targets. In general, there are ample of literature data available for ion collisions on various atomic targets. This is in particular true for positively charged projectiles like protons, helium ions or partly also highly-charged ions. However, the literature dealing with atomic targets is still rather sparse in the case of heavy-negative projectiles like antiprotons. This may be explained with the incomparably higher experimental efforts in the production of slow antiprotons and therefore only a small number of experimental facilities.

In this chapter there are two main motivations to discuss in some detail proton as well as antiproton collisions with atomic targets. First, the already mentioned existence of a considerable amount of theoretical as well as experimental literature data allows for a rigorous testing of the developed method. In the special case of He targets even antiproton impacts are remarkably well studied. Second, the results obtained for antiproton impacts should complement the mostly sparse literature for this projectile and thus improve the understanding of the electron processes involved in atomic collisions.

Concerning the first point, the implementation of the basic atomic one-electron method is mostly tested by comparing proton collisions on (single-active electron) alkali-metal atoms in the following section 5.1. The extension of the present method to two-electron targets is tested in the second part using antiproton impacts on helium atoms in Sec. 5.2, where the latter is often considered as benchmark system. These testings include also convergence studies which are inevitable in a numerical calculation to assure a certain quality and degree of accuracy. They should reveal the dependence of the one- as well as two-electron calculations on various basis parameters. Thus, they also provide valuable information for the calculations dealing with molecular one- and two-electron targets which are performed with the same program package IMPACT (cf. Sec. 1.4). In view of the second motivation, i.e. complementing the literature, it might be expected that advances in the quantity but also quality are achieved especially for antiproton impacts on the alkali-metal atoms. However, to a certain extent new data and improved insights may also be obtained for proton impacts on the larger alkali-metal atoms as well as for the antiproton–helium system. Results for proton and antiproton collisions on alkali-metal and hydrogen atoms obtained in this work have been published in Refs. [A,D].

5.1. Alkali-metal and hydrogen atoms

Collisions with alkali-metal atoms as targets have been studied in numerous experimental and theoretical works over many years. Among these studies a number of efforts deal with proton–alkali-metal atom collisions [141–156] and a smaller number of attempts address collisions including antiprotons as projectiles [60, 61]. One reason for the attractiveness of alkali-metal atoms is that they are relatively easy to access experimentally as well as theoretically which opens up the possibility for detailed comparisons. The given shell structure of the alkali metals suggests in a theoretical description the application of a quasi-one-electron model for the outermost loosely bound electron. The electron is then described by means of a model potential formed by the Coulomb potential of the nucleus and an effective potential representing the frozen inner-shell electrons. In particular, Li and Na atoms colliding with protons and electrons have been in the focus of the investigations so far. On the other hand, the literature on antiproton collisions involving alkali-metal atoms is still sparse compared to the work which was done for proton and electron impacts. In order to obtain cross sections for ionization of Li by antiproton impact a continuum-distorted-wave eikonal-initial-state model has been used by McCartney and Crothers [61]. Furthermore, an optical-potential description has been provided by Stary *et* al. [60] for antiproton collisions with Li and Na. On the other hand, no experimental data are so far available for the antiproton–alkali-metal atom collisions due to the experimental difficulties arising basically from the limited amount of available low-energy antiprotons which also complicates the conditions for collisions with alkali-metal atoms [157]. This may also be the reason for the relatively small interest in antiproton–alkali-metal collisions compared to their proton counterparts until now. However, the upcoming facility FAIR [24] with its incorporated Facility for Low-energy Antiproton and Ion Research (FLAIR) [25] will provide the necessary experimental conditions in future and is therefore expected to attract further attention to the field of antiproton collisions.

It is one motivation of this work to shed more light on the antiproton–alkali-metal collision systems and to provide a consistent data base for Li(2s), Na(3s), and K(4s) atom collisions with antiprotons and protons in a large energy range. It starts at low energies ($E = 0.25$ keV) where the collision processes depend considerably on the projectile and ranges up to high energies ($E = 1000$ keV) where the antiproton and proton collision systems are supposed to show the same behavior due to the expected applicability of the first Born approximation. The calculations for collisions with proton projectiles are considered to be valuable for two reasons. On the one hand, the proton results — especially for Li targets — can be compared in detail with literature values. This way the proton results can be utilized in order to test the present method and its implementation which is the same for protons and antiprotons. Furthermore, new theoretical ionization and excitation cross sections for proton collisions — especially for K targets — are provided which to the author's knowledge were unknown in the considered energy range.

Besides the obvious similarities of protons and antiprotons as projectiles they differ mostly in their capture behavior. First, only antiprotons can annihilate with protons of the atomic nucleus. Since it is known that the process of annihilation is only likely to occur at very low energies [158] it is not included in this investigation. Second, in the case of proton collisions electron capture by the projectile from the target atom is possible. This process plays a dominant role for low-energy collisions. Hence, a two-center approach appears to be most promising for low-energy proton collisions. However, at low energies the present calculations concentrate on antiproton collisions only. Therefore, a basis expansion which is centered solely on the target alkali-metal atom for both antiproton and proton projectiles is used. Thereby, limitations pertinent to a molecular approach at high energies are avoided. Furthermore, the same method can be used for antiproton and proton collisions which may be confirmed by a detailed comparison of present proton results with literature data. A detailed analysis of the electron capture process for proton scattering lies, however, beyond the scope of this work.

In what follows, first the convergence behavior and second the dependence of the ionization and excitation probabilities on the impact parameter b for different impact energies is investigated. Thereafter, the results for proton and antiproton collisions with the alkali-metal target atoms Li, Na, and K are presented and the findings are compared with data from literature, if any exists. A comparison of the obtained data for antiproton collisions with all considered alkali-metal atoms also includes results for Rb. The antiproton results are furthermore contrasted to the cross sections for hydrogen atoms. Finally, the electron-energy spectra of the ejected electrons in antiproton collisions are explicitly shown for Rb targets.

5.1.1. Convergence studies and transition probabilities

In the case of antiproton collisions with lithium calculations for three different basis sets A4, A6, and A8 with maximum angular momenta $l_{\max} = 4$, 6, and 8, respectively, are considered. In Table 5.1 the maximum angular and magnetic quantum numbers as well as the total number of basis states are given for these basis sets. In order to discuss the convergence of the results with respect to these basis sets the behavior of the product $b\,P(b,E)$ is investigated. This quantity is according to Eq. (4.10) the integrand of the final cross section. The probability P for a certain transition depends on the impact parameter b and the impact energy E. In Figs. 5.1(a) and 5.1(b) the calculated

Table 5.1.: *Parameters of the basis sets used for the convergence studies. Basis sets beginning with A (P) are used in calculation with antiprotons (protons). For each basis set the maximum angular quantum number l_{max}, the maximum magnetic quantum number m_{max} and the total number of basis states are given.*

basis	l_{max}	m_{max}	states	basis	l_{max}	m_{max}	states
A4	4	4	810	P6	6	6	1188
A6	6	6	1512	P8	8	8	1620
A8a	8	8	2430	P10a	10	3	2052
A8b	8	3	1620	P14	14	3	2916
				P10b	10	6	3024

transition probabilities for total excitation and ionization, respectively, of antiproton collisions on Li atoms, i.e. $\bar{p}$ – Li(2s), are presented for three different energies. As can be seen from Fig. 5.1, in general a good convergence behavior is observed for all energies which is worst for low impact energies. The calculations using A4 and A6 yield for $E = 1$ keV in the case of ionization [in 10^{-16} cm^2] 7.08 and 7.10, respectively, and for excitation 14.69 and 14.67, respectively. Thus the outcome of the two basis sets A4 and A6 differs by less than 0.3% and is regarded as almost converged in l. The range of integration has been stepwise increased from $-z_{\mathrm{m}in} = z_{\mathrm{m}ax} = 60$ used in the calculations with A4 and A6 to $-z_{\mathrm{m}in} = z_{\mathrm{m}ax} = 180$ in the calculation using the basis set A8a. This results in higher ionization (7.38) and slightly lower excitation (14.55) probabilities at low energies, where the two values are again given for $E = 1$ keV. It is found that the results for the calculation using $l_{\mathrm{m}ax} = 8$ converge quickly with increasing maximum projection of the angular momentum $m_{\mathrm{m}ax}$. Consequently, for the subsequent calculations dealing with antiprotons as projectile the basis set A8b with $l_{\mathrm{m}ax} = 8$, $m_{\mathrm{m}ax} = 3$, and $z_{\mathrm{m}ax} = 180$ is chosen resulting in a set of 1620 basis functions.

In the case of proton collisions with lithium calculations for five different basis sets P6, P8, P10a, P14, and P10b with maximum angular momenta $l_{\mathrm{m}ax} = 6$, 8, 10, 14, and 10, respectively, are shown in Fig. 5.2 for the same energies as before for the antiprotons. The further parameters of these basis sets are given again in Table 5.1. In contrast to the antiproton calculations, much higher angular momenta are needed to achieve convergence, especially for low energies $E \leq 4$ keV. The results for the basis sets P10a and P14 both with $m_{\mathrm{m}ax} = 3$ are converged for $E = 8$ keV within 2% with respect to l. Hence, $l_{\mathrm{m}ax} = 10$ is chosen but m is increased to $m_{\mathrm{m}ax} = 6$ leading to the basis set P10b. Like in the case of antiprotons the integration range $z_{\mathrm{m}ax}$ is also enlarged to $z_{\mathrm{m}ax} = 180$. For all considered energies with $E > 4$ keV these parameters lead to results which are differing for $E = 8$ keV by less than 2% from the values achieved with P10a and P14. The basis set P10b with 3024 basis functions is therefore used for all proton collision calculations. Note, for 1 keV protons the ionization and excitation probabilities are obviously structured. While a two-maxima structure starts to converged with improved basis sets for excitation, the outcome of the different basis sets concerning ionization is rather diverse. However, in both cases a minimum around $E = 7$ keV is clearly visible.

From the previous analysis it can be concluded that in general convergence is achieved (i) much faster for antiprotons than for protons, (ii) faster for excitation than for ionization, and (iii) faster at higher than at lower energies. Figures 5.1 and 5.2 also provide insight into the physics of the collision process. For high energies the same behavior for antiproton and proton collisions can be observed. For energies below the expected validity regime of the first Born approximation ($v \lesssim v_0$) the transition probabilities for antiproton collisions are shifted towards smaller impact parameters with respect to those for protons. For close encounters, i.e. trajectories with small b, which are relatively more important for low energies, the advent of the projectile inside the orbit of the target electrons creates in the case of protons an increased or for antiprotons a decreased binding of the electrons. This situation leads to a decrease (p) or increase ($\bar{p}$) of the transition probability $P(b)$ for small b [23] and a relative shift of the $P(b)$ curves to larger b in the case of protons. The ionization probability is, compared to excitation, for p and $\bar{p}$ more

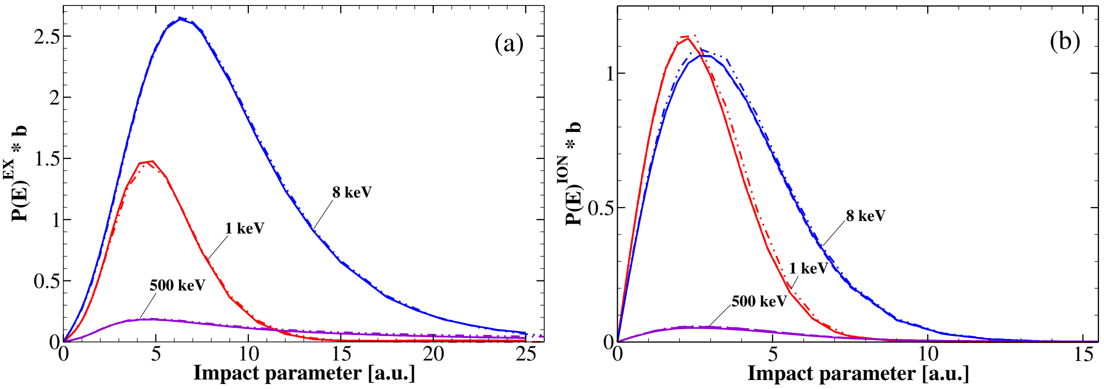

Figure 5.1.: *$\bar{p}$ – Li(2s) collision: The convergence behavior at different impact energies is shown for the three basis sets A4 (–), A6 (- -), and A8 (· – ·) with maximum angular momenta $l_{max} = 4$, 6, and 8, respectively. (a) Total excitation probability $P_{exc}(E)$ weighted with the impact parameter b as a function of b. (b) The same as (a), but for the ionization probability $P_{ion}(E)$. Reproduced from [A].*

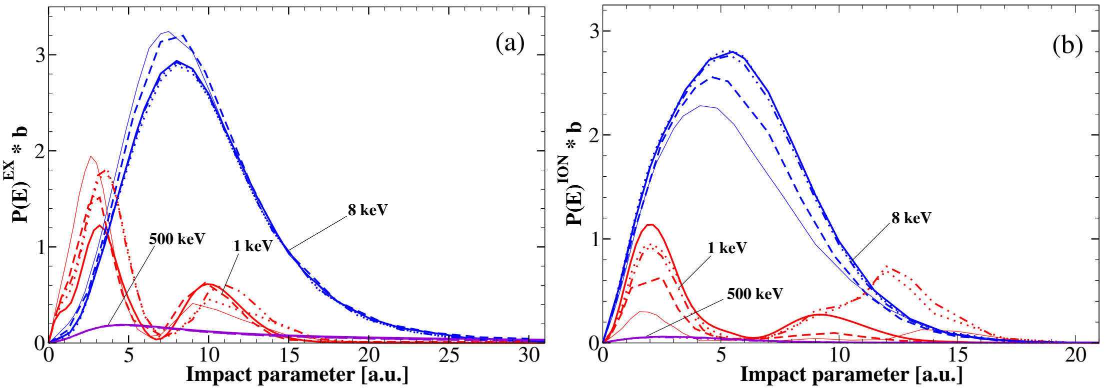

Figure 5.2.: *p – Li(2s) collision: The convergence behavior at different impact energies is shown for the five different basis sets P6 (-), P8 (- -), P10a (· – ·), P14 (· · ·), and P10b (-) with maximum angular momenta $l_{max} = 6$, 8, 10, 14, and 10, respectively. (a) Total excitation probability $P_{exc}(E)$ weighted with the impact parameter b as a function of b. (b) The same as (a), but for the ionization probability $P_{ion}(E)$. Reproduced from [A].*

concentrated in the vicinity of the nucleus. This can be made plausible using the simple picture that the mean velocity of the electrons close to the nucleus is higher than at larger distances. Therefore, for small b less energy has to be transferred to the electrons in order to obtain an electron energy which is larger than the ionization potential. On the other hand the excitation probability has a longer tail for large b compared to ionization. On the other hand, particularly at high energies care has to be taken that the calculations converge in the considered impact parameter range, i.e. $b_{\max}$ is sufficiently large, since the integrand for a cross section, $b\,P(b)$, includes a weighting with b due to geometrical reasons (cf. Sec. 4.2).

In the investigation on alkali-metal atoms the time propagation has been carried out for about 30 to 40 different impact parameters b for every collision system. The computational effort of a time propagation for one b is approximately 4 to 10 hours CPU time on a single 2.4 GHz processor with 2 GB core memory.

5.1.2. Cross sections for proton collisions

In contrast to antiproton collisions, for proton impacts, especially for Li atoms but also for Na, a number of theoretical and experimental results as well as derived fits exist in literature. Thereby these two proton collision systems become good candidates to test the developed method. Additionally, the results of different theoretical approaches and by that their applicability can be compared. The achieved understanding of the proton systems may be used for the discussion of the antiproton collisions later on for which a thorough comparison is not possible due to the sparseness of literature dealing with antiproton impacts on alkali-metal atoms. The present results for proton collisions with K complement the sparse literature data for this collision system.

Ionization

In Figs. 5.3, 5.4, and 5.5 the results of the calculations for proton collisions with Li(2s), Na(3s), and K(4s), respectively, are presented. The cross sections for the ionization of alkali-metal atoms A,

$$\mathrm{p} + \mathrm{A}(n_i\mathrm{s}) \rightarrow \left\{ \begin{array}{l} \mathrm{H} + \mathrm{A}^+ \\ \mathrm{p} + \mathrm{A}^+ + \mathrm{e}^- \end{array} \right. , \tag{5.1}$$

where A stands for either Li, Na or K initially in their ground states n_is, for example Li(2s), are shown in the Figs. 5.3(a), 5.4(a), and 5.5(a), respectively. According to Eq. (5.1) the ionization cross section for proton collisions includes two processes. These are the ionization of the alkali-metal atom due to the capture of an electron by the proton and the ejection of the electron into the continuum. The sum of both cross sections is also referred to as electron-loss cross section. The electron capture by the projectile is the dominant process for low energies, but vanishes rapidly with increasing energies and becomes negligible for $E > 100$ keV. For intermediate and high energies the ionization into the continuum is the dominant electron loss process. Therefore, in the following discussion the present ionization calculations are also compared with electron capture cross sections from the literature at low energies and with literature results for ionization excluding electron capture by the proton at high energies.

The present ionization cross section for proton impacts on Li(2s) in Fig. 5.3(a) matches perfectly with the 2s contributions of the theoretical ionization cross section by McCartney and Crothers [61] and also with the experimental results by Shah *e*t al. [141]. The ionization cross section by Schweinzer *e*t al. [147] is somewhat smaller at high energies. The contribution of the 1s electrons to the ionization cross section which is not included in the present calculations has been determined theoretically by Sahoo *e*t al. [159] as well as McCartney and Crothers [61] and experimentally by Shah *e*t al. [141]. For energies smaller than 100 keV the contribution of the inner shell becomes negligible compared to

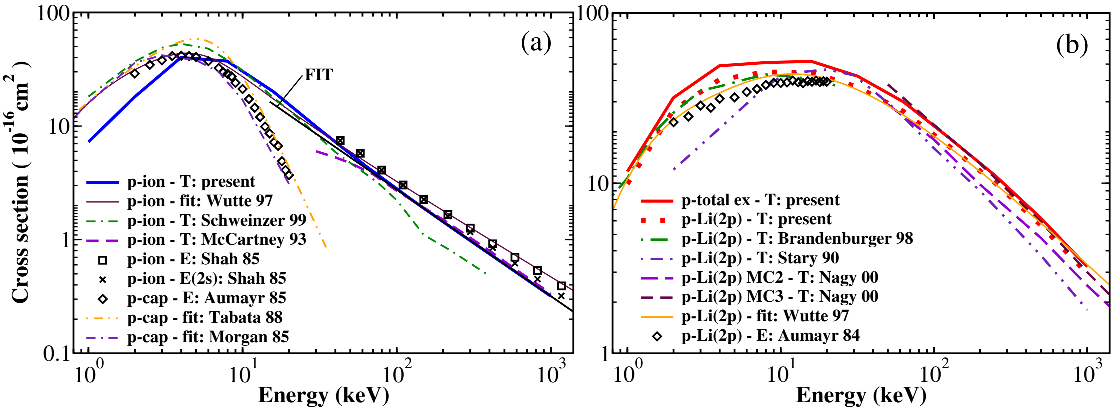

Figure 5.3.: *p – Li(2s): (a) Ionization and capture. Theory(ionization): solid curve, present results; doubly-dashed dotted curve, Schweinzer et al. [147]; dashed curve, McCartney and Crothers [61] (Li(2s)). Fit(ionization): thin solid curve, Wutte et al. [148]. Experiment(ionization): squares, Shah et al. [141]; crosses, Shah et al. [141] (Li(2s)). Fit(capture): dashed doubly-dotted curve, Tabata et al. [149]; dashed dotted curve, Morgan et al. [150]. Experiment(capture): diamonds, Aumayr and Winter [142]. (b) Total excitation and excitation into Li(2p). Theory(total excitation): solid curve, present results. Theory(excitation into Li(2p)): dotted curve, present results; dashed dotted curve, Brandenburger et al. [151]; dashed doubly-dotted curve, Stary et al. [60]; long-dashed curve, MC2 Nagy and Fritzsche [152]; short-dashed curve, MC3 Nagy and Fritzsche [152]. Fit(Li(2p)): thin solid curve, Wutte et al. [148]. Experiment(Li(2p)): diamonds, Aumayr et al. [143]. Reproduced from [A].*

the one of the outer shell. For high energies the 1s contribution is in accordance with the difference between the present 2s results and the Li electron ionization cross section. For energies smaller than 10 keV the electron capture by the proton becomes the dominant ionization process. Down to 4 keV the present findings are in good agreement with literature results shown in Fig. 5.3(a) for capture and ionization. However, for energies smaller than 4 keV the present ionization cross section is clearly smaller than all other shown results. This is in accordance with the difficulty to achieve convergence in the energy range $E \leq 4$ keV for proton collision already discussed in the previous section 5.1.1. It is known that a one-center expansion of the scattering wave function around the target is in comparison to an expansion around projectile and target not well suited, if the electron capture becomes the dominant process. Accordingly, the convergence using the one-center approach is much slower for a proper description of the electron-capture process.

In Fig. 5.4(a) the results for the ionization of the Na atom initially in the ground state are shown. Again, the present ionization cross section for proton collisions has smaller values for $E \leq 4$ keV. For $E \geq 4$ keV, the findings are in good agreement with the recent results by Zapukhlyak *et* al. [144]. Here, especially their experimental values match the present curve except for their three last data points with $E \geq 17$ keV which show an unexpected behavior. Their theoretical ionization cross section agrees for energies higher

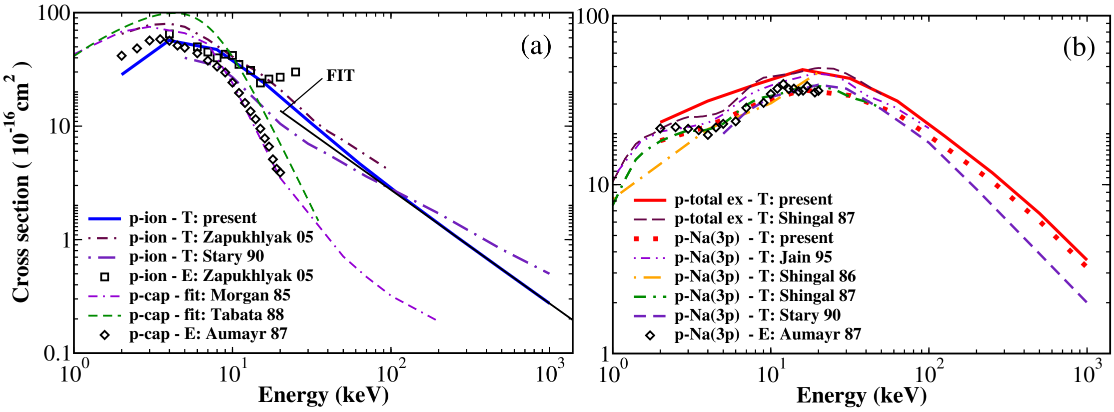

Figure 5.4.: *p – Na(3s): (a) Ionization and capture. Theory(ionization): solid curve, present results; long-dashed dotted curve, Stary et al. [60]; short-dashed dotted curve, Zapukhlyak et al. [144]. Experiment(ionization): squares, Zapukhlyak et al. [144]. Fit(capture): dashed curve, Tabata et al. [149]; doubly-dashed dotted curve, Morgan et al. [150]. Experiment(capture): diamonds, Aumayr et al. [145]. (b) Total excitation and excitation into Na(3p). Theory(total excitation): solid curve, present results; long-dashed curve, Shingal and Bransden [153]. Theory(excitation into Na(3p)): dotted curve, present results; dashed doubly-dotted curve, Jain and Winter [154]; dashed dotted curve, Shingal et al. [155]; doubly-dashed dotted curve, Shingal and Bransden [153]; short-dashed curve, Stary et al. [60]. Experiment(Na(3p)): diamonds, Aumayr et al. [145]. Reproduced from [A].*

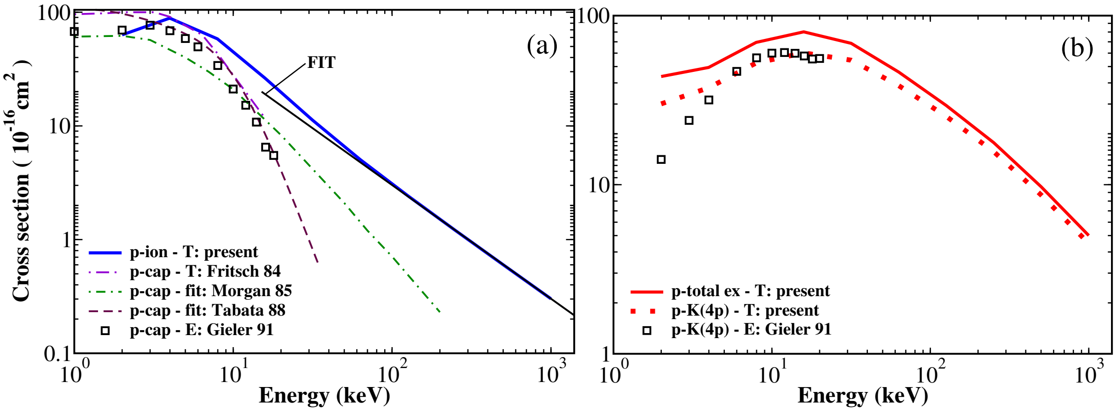

Figure 5.5.: *p – K(4s): (a) Ionization and capture. Theory(ionization): solid curve, present results. Theory(capture): long-dashed dotted curve, Fritsch [156]. Fit(capture): dashed curve, Tabata et al. [149]; dashed dotted curve, Morgan et al. [150]. Experiment(capture): squares, Gieler et al. [146]. (b) Total excitation and excitation into K(4p). Theory(total excitation): solid curve, present results. Theory(excitation into K(4p)): dotted curve, present results. Experiment(K(4p)): squares, Gieler et al. [146]. Reproduced from [A].*

than 6 keV with the present one but is larger for smaller energies. The cross section of Stary et al. [60], which also covers the range from low to high energies, differs from the present findings as well as from the other literature results. The data for electron capture by the proton are in general consistent with the present findings for the ionization cross section. However, the maximum of the fit by Tabata *e*t al. [149] has a clearly higher value.

In Fig. 5.5(a) the results of the proton – K(4s) collision calculations are presented. For potassium targets the literature data on proton cross sections are sparse. To the best of the author's knowledge no other experimental or theoretical ionization cross sections for proton collisions exists. Therefore, the present ionization cross section may be compared with results for electron capture. However, this is only meaningful for low energies $E < 10$ keV where electron capture is the dominant ionization process. The calculations by Fritsch [156], the experimental data measured by Gieler *e*t al. [146] as well as the fit provided by Tabata *e*t al. [149] of the electron capture cross section are in accordance with the present ionization cross section for $E > 4$ keV. The fitted capture cross section by Morgan *e*t al. [150] results in lower values in the relevant energy range between 4 and 10 keV. In the high-energy regime the present cross section shows the same qualitative behavior which already has been observed for Li and Na. Note, the absolute value of the maximum for K is considerably higher than for the other two alkali-metal atoms. A direct comparison of the alkali-metal targets is presented in Sec. 5.1.5 for antiproton impacts.

Excitation

In the Figs. 5.3(b), 5.4(b), and 5.5(b) the proton excitation cross sections for Li(2s), Na(3s), and K(4s) are shown. The total excitation of an alkali-metal atom A initially in its ground state n_is,

$$p + \mathrm{A}(n_i\mathrm{s}) \rightarrow p + \mathrm{A}(nl)\,, \tag{5.2}$$

is presented, which is the sum of transitions into excited bound states nl ($\neq n_i s$) with the according probability P_{exc}, cf. Eq. (4.12). Additionally, the cross section for the excitation process into the first excited state n_ip of A,

$$p + \mathrm{A}(n_i\mathrm{s}) \rightarrow p + \mathrm{A}(n_i\mathrm{p})\,, \tag{5.3}$$

is given, too. In the case of alkali-metal atoms the transition from the ground state into the first excited state is dipole-allowed and within the same shell and accordingly the oscillator strength for this transition is large compared to the other excitations. As a consequence, the excitation into the first excited state n_ip is the dominant excitation process, especially at high energies where the interaction is relatively weak. Therefore, there are experimental data for this specific excitation transition. It is found in the present investigation that it is essential, in particular for high energies, to extend the range of the impact parameter b to values up to 90 a.u. in order to achieve excitation cross sections which are converged with respect to b. The curves in Figs. 5.1 and 5.2 for 500 keV already indicate that the transition probabilities for excitation vanish slowly with increasing b.

The proton excitation cross sections for Li(2s) are shown in Fig. 5.3(b). To the best of the author's knowledge for p – Li collisions there are no data to compare the present total excitation cross section with. For the excitation into Li(2p) the present results are in good agreement with literature data also shown in Fig. 5.3(b), except with the calculations by Stary et al. [60]. Their findings differ for $E < 6$ keV and $E > 100$ keV from all results shown here. The experimental data by Aumayr [143] lie for all energies below the present calculations. On the other hand, the calculations by Brandenburger et al. [151] and also the fit provided by Wutte et al. [148] match with the present data in the whole energy range. Wutte et al. based their fit in the high-energy range on experimental and theoretical scaled-electron-impact excitation cross sections. The calculations for excitation by Nagy and Fritzsche [152] were performed with multi-configuration wave functions with an orbital basis up to $n = 2$ (MC2) and up to $n = 3$ (MC3).

In Fig. 5.4(b) p – Na(3s) collision cross sections for the total excitation and excitation into the 3p state of the sodium atom initially in the ground state are shown. The theoretical data for the total excitation cross section by Shingal and Bransden [153] agree well with the present results although they show a feature around 4 keV which is not reproduced by the present findings. Their excitation cross section into the Na(3p) state follows almost completely the present results, even around 4 keV. The structure at low energies is believed to be an interference effect due to the two positive nuclei which occurs at low energies and is discussed in [134]. Consequently, a two-center approach, as employed by Shingal and Bransden, is supposed to be able to better describe this two-center interference effect. The earlier calculation by Shingal et al. [155] agrees reasonable in the energy range 4−14 keV but shows a different behavior for higher and lower energies. Although the calculations of Jain and Winter [154] lead for all energies to higher values their qualitative behavior is comparable to the present results. The findings of Stary et al. [60] show the same behavior as their results for p – Li collisions in Fig. 5.3(b), namely, a cross section which is agreeing around the maximum but falls off much more rapidly for higher and lower energies than the other shown data. The experimental data provided by Aumayr et al. [145] is in line with the present cross section for excitation into Na(3p). It also shows a dip around 4 keV which is, however, more pronounced than for the present data.

In Fig. 5.5 the results of the present p – K(4s) collision calculations are presented. For excitation into the K(4p) state the experimental findings of Gieler et al. [146] are in good agreement with the present calculations around the maximum but then start to differ for $E \leq 4$ keV. Their data points fall off faster while the present result shows a behavior which has been already observed for p – Na collisions in Fig. 5.4(b). For Na the slope of the curve changes characteristically around $E = 4$ keV. However, there is no comparable feature for p – Li(2s) collisions. Although the excitation results for Li and Na collision seem to be reasonable also for low energies — in contrast to ionization including capture — it is not possible to quantify how reliable the p – K(4s) excitation cross sections for $E \leq 4$ keV are. The splitting of the energy levels due to spin-orbit coupling which is neglected in the present investigation is supposed to be most relevant for the 4p state of K. However, the good agreement of the present results with the experimental data by Gieler et al. for $E > 4$ keV suggests that the effect due to spin-orbit coupling does not play a major role at the level of accuracy which is achieved by the present method.

Conclusions for proton impacts

In conclusion, the comparison of the present proton ionization and excitation cross sections with literature data results in a good overall agreement in the energy range $4\ keV < E < 1000$ keV. Thereby, the applicability of the present method is confirmed even for positive projectiles. For small impact energies $E \leq 4$ keV two-center effects become important in the case of positive projectiles. Consequently, for these energies a two-center description is clearly preferable, since the convergence becomes very slow, if a one-center approach is employed.

In view of the following discussion for antiproton collisions in Sec. 5.1.3 the comparison of the two approaches from literature, which both provide data for proton as well as antiproton impact, with the present results should be kept in mind. The ionization cross section calculated by McCartney and Crothers for proton impact on Li [61] is in good agreement with the present results. Though, they provide data only for high energies. The findings by Stary *e*t al. [60] calculated for Li and Na, however, differ qualitatively in comparison with the present results as well as with the literature data. While their excitation cross sections are smaller for energies below and above the maxima, their ionization cross section is larger for high energies. Furthermore, the present calculations for $p-$K collisions complement the data provided by the sparse literature on this collision system.

5.1.3. Cross sections for antiproton collisions

Only very few data for antiproton–alkali-metal atom collisions exist in the literature. Theoretical cross sections are available for the ionization of Li(2s) and Na(3s) as well as for excitation into Li(2p) and Na(3p) by Stary *e*t al. [60]. Furthermore, there are ionization cross sections for $\bar{p}-$Li collisions calculated by McCartney and Crothers [61]. These two publications also provide results for proton impact which are discussed in some detail in the previous section 5.1.2. However, no cross section exists for ionization or excitation into K(4p) for K targets. Also, in the case of total excitation the present results are seemingly the first data for all three targets. The present data for antiproton impact on Rb atoms are discussed later in the context of comparing the alkali-metal atoms among each other and with the hydrogen atom in Sec. 5.1.5.

Ionization and excitation

The ionization cross sections for antiproton collisions with the target atoms Li(2s), Na(3s), and K(4s) are shown in Figs. 5.6(a), 5.7(a), and 5.8(a), respectively, and for excitation accordingly in Figs. 5.6(b), 5.7(b), and 5.8(b). The theoretical results for ionization in $\bar{p}-$ Li collisions by McCartney and Crothers [61] agree well with the present findings though, they only cover the high-energy regime $E > 30$ keV. The calculated antiproton ionization cross sections for Li and Na targets by Stary *e*t al. [60] differ both from the present findings. They have a less steep slope at high energies but do not show

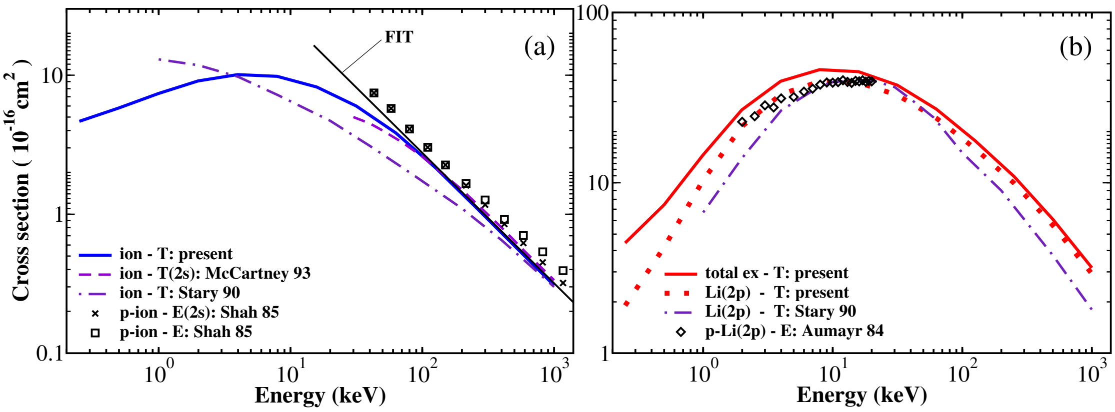

Figure 5.6.: *$\bar{p}$ – Li(2s): (a) Ionization. Theory: solid curve, present results; dashed dotted curve, Stary et al. [60]; dashed curve, McCartney and Crothers [61]. Experiment: crosses (p–Li(2s)), Shah et al. [141]; squares (p–Li(2s) and p–Li(1s)), Shah et al. [141]. (b) Total excitation and excitation into Li(2p). Theory(total excitation): solid curve, present results. Theory(excitation into Li(2p)): dotted curve, present results; dashed dotted curve, Stary et al. [60]. Experiment(excitation into Li(2p)): diamonds (p-Li(2s)), Aumayr et al. [143]. Reproduced from [A].*

a pronounced maximum. Their $\bar{p}$ – Li ionization cross section behaves differently for low to intermediate energies but seems to converge to the present findings for high energies. On the other hand, their $\bar{p}$ – Na ionization cross section shows a different behavior compared to the present curve in the whole energy range.

The cross sections for the excitation into the first excited state for Li and Na target atoms calculated by Stary *et* al. [60] both share the same features. Their cross sections agree with the present curves around the maxima at $E \approx 10$ keV and $E \approx 15$ keV for Li and Na, respectively, but fall off faster for lower and higher energies. The same behavior has been observed in the case of proton collisions in Figs. 5.3(b) and 5.4(b) for excitations into Li(2p) and Na(3p), respectively. Therefore, their results differ once more from the outcome of the present investigation.

The aim of Stary *et* al. was to obtain results comparable to literature data but using smaller basis sets within an optical potential approach adapted to this problem. A Feshbach projector formalism for the solution of the time-dependent Schrödinger equation leading to a finite set of coupled-channel equations with complex potentials was used. Thereby, two conditions were assumed to be fulfilled. First, the interactions occur instantaneously and second, the energy distribution of the Q-space which is the complement of the finite model space has a peak leading to the assumption of an average Q-space energy $\bar{\epsilon}$. Furthermore, a scaling factor is used which restores the correct energy dependence of the optical potential and which is determined at high impact energies. Since the present results for the proton case seem to be more in accordance with literature data than their one-center calculations the present results for antiproton collisions with Li and Na are also considered to be more reliable. If their solutions are converged as it was claimed by Stary *et* al. then either not both of the above mentioned conditions

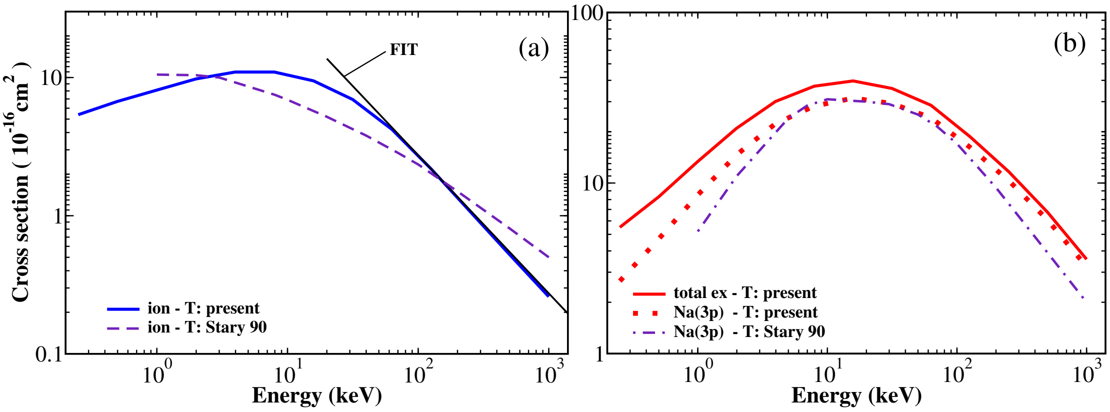

Figure 5.7.: *$\bar{p}$ – Na(3s) (a) Ionization. Theory: solid curve, present results; dashed curve, Stary et al. [60]. (b) Total excitation and excitation into Na(3p). Theory(total excitation): solid curve, present results. Theory(excitation into Na(3p)): dotted curve, present results. Reproduced from [A].*

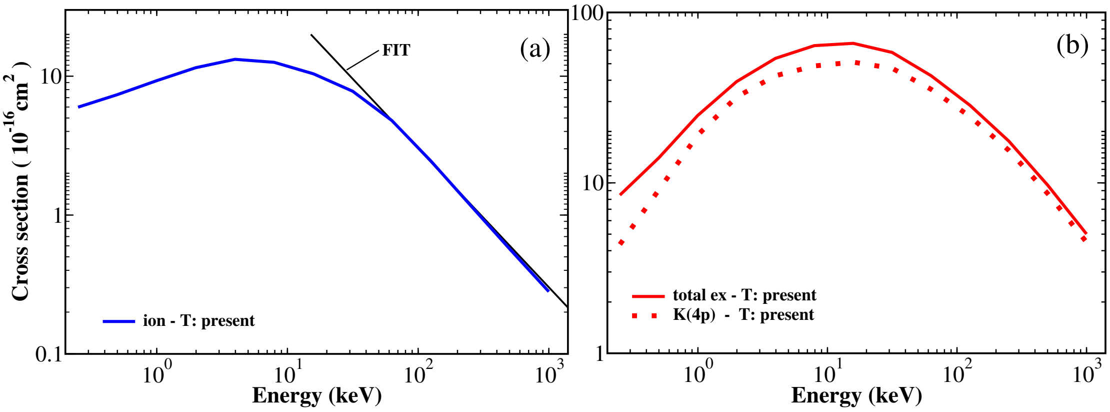

Figure 5.8.: *$\bar{p}$ – K(4s) (a) Ionization. Theory: solid curve, present results. (b) Total excitation and excitation into K(4p). Theory(total excitation): solid curve, present results. Theory(excitation into K(4p)): dotted curve, present results. Reproduced from [A].*

are fulfilled or the introduced scaling factor has a different functional behavior.

To the best of the author's knowledge no literature data on $\bar{p}$ – K cross sections exist for the considered energy range. The present cross sections for excitation and ionization of K in Fig. 5.8 show a qualitatively similar behavior like for $\bar{p}$ – Na collisions in Fig. 5.7 but with higher values throughout the energy range.

Until now, experimental results for the antiproton–alkali-metal atom collision systems are completely missing in the considered energy range. It may be noted that the experimental data of Aumayr [143] for excitation into Li(2p) by proton collisions fits better to the present antiproton than proton data.

5.1.4. Comparison of antiproton with proton cross sections

While for sufficiently high energies a similar behavior for proton and antiproton cross sections is to be expected (cf. Sec. 3.3 on the first Born approximation) the collision processes should differ for lower energies. In contrast to the proton collisions no electron capture by the projectile is possible for antiprotons. Since the electron capture is the dominant ionization channel for low-energy proton collisions noticeable differences especially for the antiproton ionization cross sections can be expected in the low-energy regime. In what follows the antiproton and proton cross sections are compared in some detail for high, intermediate and low impact energies. In Fig. 5.9(a) the ratios of proton to antiproton cross sections for ionization and excitation are given for the three considered target atoms.

High impact energies

The high-energy behavior of the antiproton and proton cross sections is considered first. In the validity range of the first Born approximation no differences in the cross sections for different projectiles like electrons, protons, and antiprotons with the same velocity are expected because in this approximation the cross sections only depend on the absolute value of the projectile charge. It is a high-energy approximation. A linear decrease of the ionization cross sections for all three alkali metal atoms can be observed on a doubly-logarithmic scale for high energies $100\ keV < E < 1000\ keV$ for protons as well as for antiprotons. Therefore, a general fit formula

$$\sigma_{\text{ion}}(E) = \sigma_{\text{ion}}(E_0)\left(\frac{E}{E_0}\right)^a \tag{5.4}$$

for the ionization cross sections in this energy range may be proposed, where $\sigma_{\text{ion}}(E_0)$ is the ionization cross section for an arbitrary E_0 in the range $100\ keV < E_0 < 1000\ keV$ and a is a fit parameter which yields the slope of the linear curve on a doubly-logarithmic scale. The fit parameters which may be proposed for the three alkali metals colliding with protons are given in Table 5.2. The fits for Na and K reveal a direct proportionality

Table 5.2.: *Parameters for the description of the ionization cross section for the energy range $100\ keV < E_0 < 1000\ keV$ using the fit formula in Eq. (5.4), where a is a dimensionless fit parameter. The energy E_0 is given in keV and the cross section $\sigma_{ion}(E_0)$ for E_0 in units of $10^{-16}\ cm^2$.*

Atom	E_0	$\sigma_{\text{ion}}(E_0)$	a
Li(2s)	141.3	2	-0.9386
Na(3s)	138	2	-1
K (4s)	151	2	-1

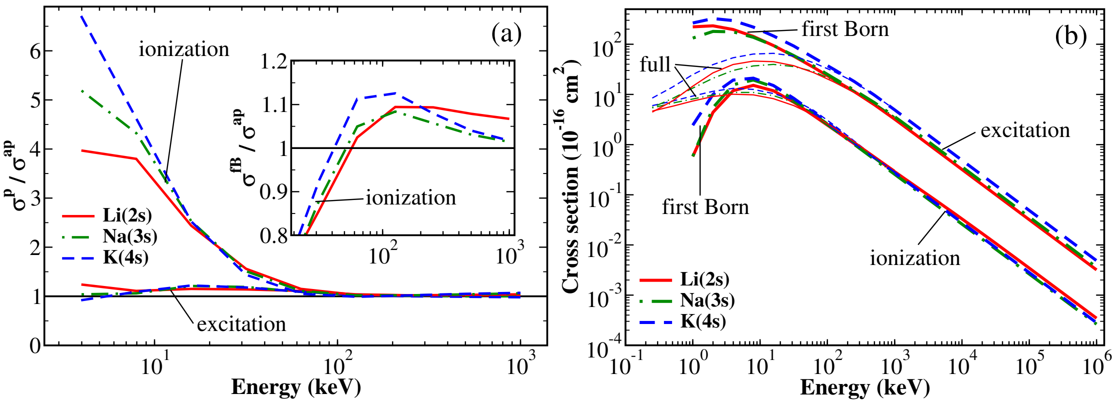

Figure 5.9.: *(a) Ratio of proton to antiproton cross sections σ^{p} / σ^{ap}. The ratios of the ionization and excitation cross sections for the target atoms Li(2s), solid curve, Na(3s), dashed dotted curve, and K(4s), dashed curve, are given. In the inset the ratios of the first Born to antiproton ionization cross section $\sigma^{fB} / \sigma^{ap}$ are shown. (b) Results of the first Born cross sections for ionization and excitation by antiproton impact (thick lines) in the energy range 1 keV $\leq E \leq$ 1 GeV for the target atoms Li(2s), Na(3s), and K(4s). Nonperturbative antiproton cross sections (thin lines) are also given for* 0.2 *keV* $\leq E \leq$ 1000 *keV. Reproduced from [A].*

between the ionization cross section and the inverse of the energy,

$$\sigma_{\text{ion}}(E) = \frac{\sigma_{\text{ion}}(E_0)\, E_0}{E} \propto \frac{1}{E}\,, \tag{5.5}$$

in the considered high-energy regime. This proportionality holds approximately also for the present Li ionization cross section. The proposed fits which are also shown in Figs. 5.3(a), 5.4(a), and 5.5(a) match well with the calculated ionization cross sections for $E \geq 150$ keV. These fits obtained for the proton case are also shown in Figs. 5.6(a), 5.7(a), and 5.8(a) in order to compare them with the antiproton ionization cross sections. It can be seen that the proton fits match remarkably well with the antiproton ionization results for energies higher than 150 keV. Therefore, the antiproton ionization cross sections also decrease as E^{-1}, which again holds only approximately for Li targets. This means that for energies higher than 150 keV no specific features are expected for antiproton ionization cross sections with the considered alkali-metal atoms.[a] In turn, for these energies the treatment of proton collisions should be sufficient which is especially in the case of experimental studies less demanding and costly.

In order to make this statement sound, first Born calculations, as described in Sec. 3.3, using the same description of the atomic electron systems (Klapisch potential) and basis sets as in the full calculations are performed for energies 1 *keV* $\leq E \leq$ 1 GeV. The

---

[a] Note, differences may still appear for differential cross sections or in the case of double-ionization. For example, the double-ionization of helium by antiproton impact has been found to be about two times larger than for protons even for energies above 1 MeV [23].

results are shown in Fig. 5.9(b). The ionization cross sections for $E \rightarrow 1$ GeV confirm nicely the behavior $\sigma_{\text{ion}}(E) \propto 1/E$. It should be mentioned that this proportionality also holds in the case of the Li ionization cross section which only showed an approximate $1/E$ behavior for $E \leq 1000$ keV in the full calculation. Using the first Born results as a basis for a high-energy formula of the ionization cross sections the parameter a can be set for the three alkali-metal atoms to $a = -1$. This leads to the simple formula for high energies

$$\sigma_{\text{ion}}(E) = \frac{C}{E}\,, \tag{5.6}$$

where $C = \sigma_{\text{ion}}(E_0)\,E_0$ is an atom-dependent constant taking the values $C^{\text{Li}} = 3.465 \times 10^{-14}\ cm^2$ keV, $C^{\text{Na}} = 2.640 \times 10^{-14}\ cm^2$ keV, and $C^{\text{K}} = 2.818 \times 10^{-14}\ cm^2$ keV. It should be emphasized that for these high energies the contribution of the inner electrons to the cross sections cannot be neglected and the presented results can be considered as partial cross sections. However, the cross sections which take only the valence electron into account can be extracted from the experimental data as was done, e.g., in [141]. The ratios of the cross sections determined with the first Born approximation and with the full calculation for antiprotons $\sigma_{\text{f}B}/\sigma_{\text{ap}}$ are given in the inset of Fig. 5.9(a). It can be seen that the largest deviation from unity of this ratio for $E = 1000$ keV is found for Li. Taking both the deviation of the ratio $\sigma_{\text{f}B}/\sigma_{\text{ap}}$ from unity and the deviation from the proportionality $\sigma_{\text{ion}} \propto 1/E$ for $E = 1000$ keV in consideration one may conclude that these two criteria are connected. Namely, the better the first Born results agree with the full calculation the closer is the value of the exponent a to -1 and therefore to a high-energy behavior of the ionization cross section proportional to $1/E$.

Intermediate to low impact energies

For energies lower than 100 keV antiproton and proton systems differ strongly regarding ionization due to the electron capture process which is only possible for protons. The proton cross section is strongly enhanced as can also be seen in Fig. 5.9(a). The maxima of the proton and antiproton ionization cross sections approximately at 45 and 10 [in $10^{-16}\ cm^2$], respectively, for Li targets differ by a factor 4.5. The ionization maxima for Na and K targets differ approximately by a factor 5.5 and 6.5, respectively. The maxima are all located between 4 and 6 keV. The proton maxima tend to occur at lower energies than the corresponding antiproton maxima.

A comparison of the present excitation cross sections for proton and antiproton collisions shows that they also agree for high energies $E > 150$ keV. The antiproton maximum for Li targets lies around 10 keV and is 10% lower than for proton collisions. The antiproton maxima for Na and K are situated at approximately 15 keV with ≈ 20% smaller values than for the proton case. But below their maxima the Na and K excitation curves for antiprotons and protons have comparable values.

The most striking feature of Fig. 5.9(a) is that the ratios of the proton to antiproton ionization cross sections increase strongly for low-energy collisions while the ratios for excitation only vary comparably weakly around 1. In the case of ionization the electron capture channel becomes important for low-energy proton collisions leading to large ionization cross sections compared to antiproton collisions. On the other hand, in the case of excitation the same channels are open for both projectiles.

Conclusions of the comparison

It can be concluded for the antiproton cross sections that the present results complement and improve the existing data on antiproton impacts on alkali-metal atoms. While the excitation cross sections are comparable for proton and antiproton projectiles the proton ionization cross sections are strongly enhanced at low energies due to electron capture. For high energies $E > 150$ keV proton and antiproton collisions with Li, Na, and K result in the same ionization cross sections which decrease proportional to E^{-1}.

5.1.5. Comparing alkali-metal and hydrogen atoms

In contrast to the alkali-metal atom targets, antiproton collisions with a hydrogen atom, which is also a member of the first group in the periodic table of elements, are studied in much more detail concerning theory but even experimental data were measured. Clearly, the hydrogen atom is considered as the most basic atom. Therefore, the present results for hydrogen atoms are compared to the findings for the alkali-metal atoms. Note, the results obtained for the rubidium atom (cf. Refs. [127] and [D]) are also considered. In what follows, differences of the ionization as well as excitation cross sections among the different targets are discussed and possible explanations are proposed.

Ionization

The ionization cross sections for antiproton collisions on H, Li, Na, K, and Rb are compared in the upper panel of Fig. 5.10. It can be seen that the curves for all alkali-metal atoms share the same qualitative behavior. They differ, however, in the magnitudes of the maxima which increase with the atomic size. While this ordering is also prominent at low energies, the differences between the atoms vanish at high impact energies.

For comparison also the present ionization cross sections for $\bar{p}$ + H collisions are given in Fig. 5.10 together with the experimental data measured by Knudsen *e*t al. [39] which are in good agreement. Similar results as for the alkali-metal atoms might be expected for H, since they are members of the same group in the periodic table. However, there are also obvious differences. Namely, the magnitudes of the cross sections for the alkalis and the H atom differ considerably and become only comparable at high impact energies $E \geq 500$ keV. Also the position of the maximum is shifted from $\approx$ 5 keV for the alkalis to ≈ 25 keV for H.

The differences of the magnitudes and the ordering of the ionization curves among the alkalis as well as between the alkalis and the H atom in Fig. 5.10 can be explained with the different ionization potentials of the target atoms (Table 1 of Ref. [A]) [all in a.u.]:

$$\mathrm{H} = 0.5\ , \quad \mathrm{L}i = 0.198\ , \quad \mathrm{N}a = 0.189\ , \quad \mathrm{K} = 0.160\ , \quad \mathrm{R}b = 0.156\,.$$

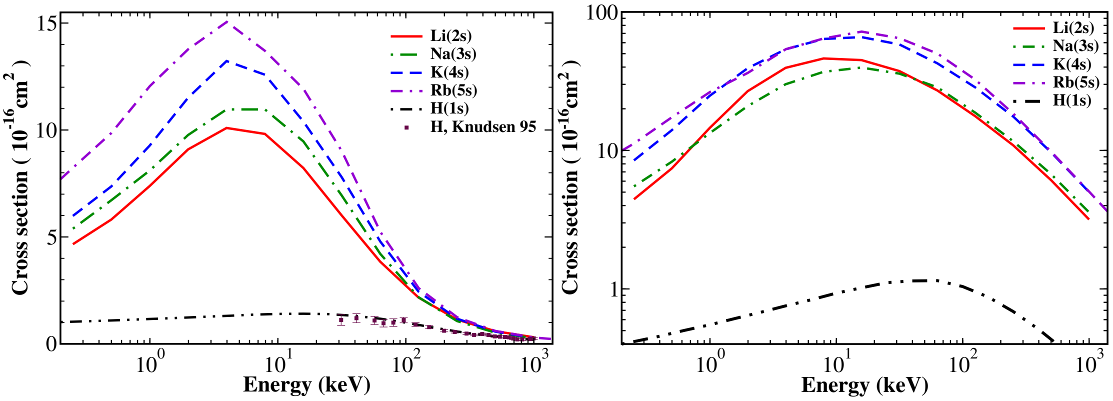

Figure 5.10.: *Cross sections for antiproton collisions with Rb compared with Li, Na, K as well as H targets as a function of the impact energy E. Solid curve, Li; dash–dotted curve, Na; dashed curve K; double-dash–dotted curve, Rb; dash–doubly-dotted curve, H. Experiment: squares, H, Knudsen et al. [39]. Upper panel: ionization. Lower panel: excitation. Reproduced from [D].*

Thereby, especially the large differences between alkali-metal and hydrogen atoms become understandable.

Excitation

In the lower panel of Fig. 5.10 the excitation cross sections for antiproton collisions with Rb are shown together with the results for Li, Na, K as well as H. Again, all curves for the alkali-metal atoms share the same qualitative behavior but differ in the magnitudes of their maxima. The maxima are, however, not ordered by the periods of the chemical element, since Li lies above Na. The maxima of the excitation curves are, compared to ionization, situated at higher impact energies: Na, K, Rb $\approx$ 15 keV and Li $\approx$ 8 keV. In absolute values all alkali curves for excitation lie clearly above the results for ionization — note the logarithmic scale for the cross sections — whereas the curves for Li and Na as well as for K and Rb are close to each other. On the other hand, the slope of the curve for Li is more similar to that of K and the one of Na more similar to that of Rb.

A comparison of the alkali excitation results to the H atom, which has a maximum around 50 keV, shows that the difference is even larger than in the case of ionization. The absolute values of the antiproton excitation maxima for the five atoms differ considerably [in 10^{-16} cm^2]:

$$\mathrm{H} = 1.15\ ,\quad \mathrm{L}i = 46.2\ ,\quad \mathrm{N}a = 39.7\ ,\quad \mathrm{K} = 65.9\ ,\quad \mathrm{R}b = 72.3\ ,$$

that is, the maximum for K is 66% higher than that for Na and the maximum of H is only of the order of 1.6% of the one for Rb. The differences for excitation among the alkalis as well as between the alkalis and the H atom can be explained with their excitation energies, especially for the transition into the lowest dipole-allowed p state ($l = 1$), which is clearly the dominant transition into bound excited states at high and intermediate E (see previous sections). The according energy differences between the ground and the first excited states are [in a.u.]:

$$\mathrm{H} = 0.375\ , \quad \mathrm{L}i = 0.068\ , \quad \mathrm{N}a = 0.089\ , \quad \mathrm{K} = 0.059\ , \quad \mathrm{R}b = 0.057\ .$$

The excitation energy for the 1s – 2p transition in H with 0.375 a.u. is in particular large compared to, e.g, the 5s – 5p with 0.057 a.u. for Rb. Note, the similarity of the excitation curves for K and Rb and the changed ordering for Li and Na are in particular consistent with the different excitation energies into the first excited states.

5.1.6. Electron-energy spectra

Besides total cross sections for ionization and excitation also differential information can be extracted from the collision process as is described in Sec. 4.2.2. In Fig. 5.11 the electron-energy spectrum, i.e., the cross section that an electron is emitted with the energy ϵ is presented for a Rb atom target. The spectra of the other alkali-metal atoms Li, Na, and K were also determined. They are qualitatively comparable to that of Rb and are therefore not shown or discussed explicitly here. Spectra for seven different $\bar{p}$ impact energies E, 1 k$eV \leq E \leq$ 4000 keV, are exemplarily presented in Fig. 5.11. All curves are smooth, fall off with increasing ϵ and no resonance structures can be seen for $\bar{p}$ impact which is also the case for $\bar{p}$ + H_2 collisions discussed in the next chapter in Sec. 6.2.4. This is in contrast to the spectra for electron loss in the case of p collisions where a pronounced resonance can be observed for $\epsilon = E/M_p = v_p^2/2$. The resonance originates from the electron capture process by the p. Thereby, the electron, which is transferred from the target to the projectile, moves with approximately the velocity v_p of the proton. Note, the appearance of the electron transfer as a resonance in the electron-energy spectrum is due to the employed one-center approach which is centered on the target. From a perspective centered on the projectile the electrons with energies around the capture peak can be in a bound state of the positively charged projectile.

For small electron energies $\epsilon \to 0$ the curves in Fig. 5.11 are ordered according to their impact energy E. The maxima of the spectra at $\epsilon \to 0$ are higher for lower impact energies E — see the inset of Fig. 5.11 — and the decrease of the curves with increasing ϵ becomes steeper. For larger electron energies $\epsilon > 0$ the spectra all share the same behavior. Always the uppermost curve starts at a certain ϵ to cross all lower-lying curves belonging to larger E. This is nicely illustrated in the inset of Fig. 5.11; first for the spectrum for $E = 1$ keV and afterward for $E = 4$ keV. Consequently, the mean kinetic energy of the ejected electrons $\bar{\epsilon}$ increases for larger impact energies E of the $\bar{p}$. This also means that in the description of high-energy collisions a basis set has to be chosen with a sufficiently large cutoff energy and density of states of the discretized continuum.

The steep fall-off of the electron-energy spectra can be made plausible using a classical argument. The energy in a classical two-body collision which can be maximally transferred is

$$\epsilon_{\mathrm{max}}^{(cl)} = \frac{1}{2}\,(2\,\frac{M_p}{M_p+1}\,v_p)^2 \lesssim 2\,v_p^2 \propto E \tag{5.7}$$

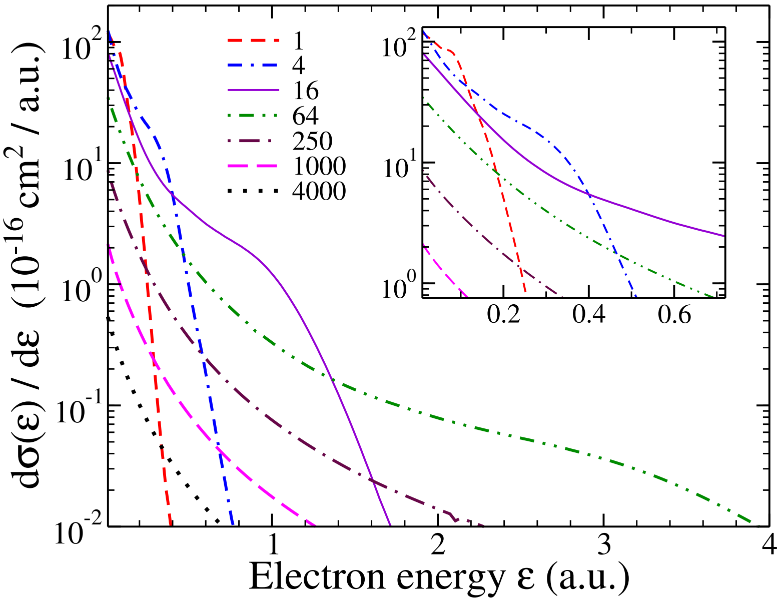

Figure 5.11.: *Electron-energy spectra for antiproton impact on Rb as a function of the emitted-electron energy ϵ. Spectra are shown for seven different antiproton impact energies [keV]: 1, 4, 16, 64, 250, 1000, and 4000. The inset shows the region of small ϵ enlarged. Reproduced from [D].*

where it is assumed that the initial velocity of the electron is zero and the projectile mass is much larger than than an electron, e.g., for protons and antiprotons. This results in the classically allowed values [in a.u.] $\epsilon_{max}^{(cl)} = 0.08$, 0.32, and 1.28 for the impact energies [in keV] $E = 1$, 4, and 16, respectively. These three values of $\epsilon_{max}^{(cl)}$ agree quite well with the ϵ regions where the corresponding energy spectra start to decrease strongly as can be clearly seen in Fig. 5.11. Note, the (classical) cutoff of the spectra increases according to Eq. (5.7) linearly with the impact energy E of the projectile.

5.2. Helium atom

In the beginning of the last century, with the invention of quantum mechanics, it became possible to properly describe the structure of the simplest atoms hydrogen and helium. It was, however, difficult to calculate accurate results for the states of helium due to the electron-electron correlation in that atom. Since then, it has become possible to perform calculations on many atoms to a high degree of accuracy using advanced methods together with computational resources which have been developed enormously.

It turned out that it is a much more difficult task to perform similar calculations on atomic systems which are not static but dynamic, such as atomic collisions or also the interaction with short intense laser pulses. Again one of the difficulties lies in the electron correlation inherent to many of these time-dependent interactions, which are, however, dynamic. At an early stage it was clear that benchmark data for the simplest atomic systems were needed to compare experiment with calculations. One of the simplest and basic of such systems — at least form the view of a theoretician — is the ionization of helium by antiproton collisions. One reason is that the projectile is heavy, allowing for a semiclassical theoretical approach. Additionally, the large mass of this projectile allows for the investigation of "slow" ionizing collisions, a feature which is not possible with electron impact. Furthermore, there is no complication from charge transfer due to the negative charge of the antiproton which is the case for collisions of positive ions. In contrast to the interaction with short intense laser pulses, the experimental parameters are usually much better under control and known with a higher accuracy in ion-collision experiments.

At the LEAR (Low-Energy Antiproton Ring) facility at CERN single and double ionization cross sections for antiprotons colliding with helium were measured from MeV energies down to 13 keV. These data led to much theoretical activity that resulted in the development of advanced models which selectively are discussed in brief below. Almost all of these calculations coalesce at projectile energies above 100 keV, where the interaction with the projectile might be considered as a low order perturbation of the target. However, at low energies it was most difficult to produce the experimental as well as the theoretical data and not surprisingly, there the disagreement between the different findings turned out to be largest. To discriminate between these theories and to clarify the obvious disagreement between experiment and theory, it was necessary to measure under improved conditions at considerably lower energies as well as to improve the theoretical description for these energies below the maximum. Using the AD (Antiproton Decelerator) facility at CERN together with an advanced technique for the creation of an intense beam of very slow antiprotons, single ionization cross sections of helium were very recently measured down to an impact energy of 3 keV [160].

The motivation in this work to deal with antiproton impacts on helium atoms is twofold. First, it is a benchmark system for the theoretical description of dynamic electron-electron correlation effects where a lot of effort has already been spent to increase the achieved accuracies. Therefore, the capability of the present method applied to two-electron targets can be checked thoroughly. Second, in this work the results for helium are obtained with the same method which is used for the more complex H_2 molecules using the limit of a vanishing internuclear distance $R_{nuc} \rightarrow 0$. Therefore, the calculations for helium can be very valuable with respect to the present studies on H_2 molecules where literature data is comparably sparse, since the implementation of the method and its applicability can be tested by an extended comparison to literature data. Furthermore, convergence studies performed for helium are, together with those for ${H_2}^+$ molecules, extremely beneficial for the studies performed for H_2 molecules. Consequently the two following sections deal with a rather detailed convergence study and a comparison to experimental data and a number of calculations.

Note, results are presented using the full two-electron method as well as the model potential V_{mod} introduced in Secs. 2.1.4 and 2.2.2, respectively. The discussion of double-ionization cross sections lies, on the other hand, beyond the scope of this work and is therefore the subject of a future study. The main reason is that an appropriate scheme has still to be implemented which unambiguously extracts the contribution from double

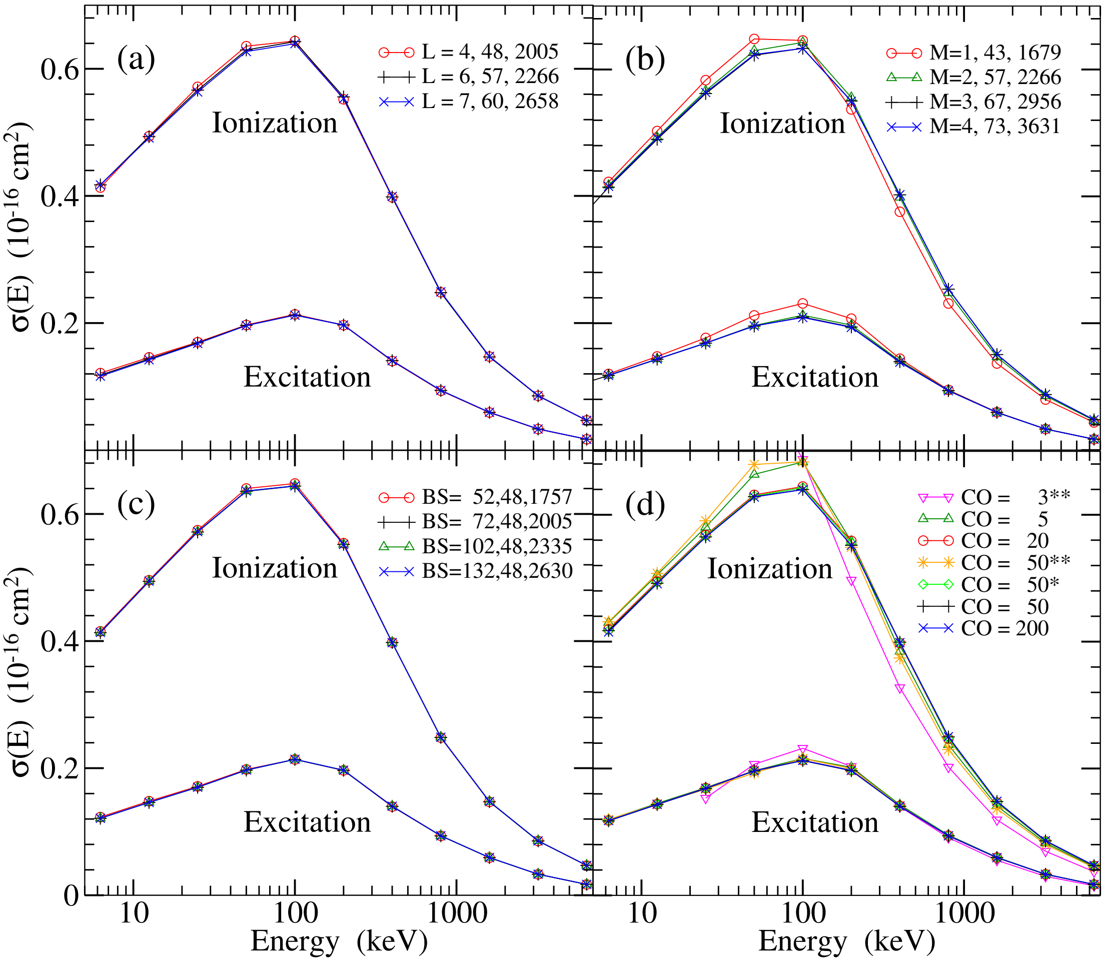

Figure 5.12.: *Convergence studies of the ionization and excitation cross sections σ_{ion} and σ_{exc}, respectively in $\bar{p}$ + He collisions as a function of the antiproton energy E varying four different basis parameters. (a) Maximal angular momentum l, (b) maximal azimuthal quantum number M, (c) number of B splines N, (d) cutoff energy of the orbitals in Rydberg. In (a), (b), and (c) also the total number of bound and continuum states are indicated for every basis set. For further details see text.*

ionization out of all transitions into the continuum. Consequently, in this work all transitions into the continuum are attributed to single ionization and no products of two continuum orbitals are used as configurations in the CI calculation.

5.2.1. Convergence study

In the following the convergence behavior of the ionization and excitation cross sections for antiproton impact on He atoms using the full two-electron description is discussed for the variation of four decisive basis parameters. These are

(a) the maximal angular momentum l of the *orbitals* entering in the configuration of the CI calculation,

(b) the maximal azimuthal quantum number M of the *two-electron basis states*,

(c) the number of B splines N per angular momentum used for the *orbitals*,

(d) the maximal energy of the *orbitals* used in the CI calculation.

The results of the convergence study are presented in Fig. 5.12. An emphasis in the discussion is put on the ionization cross sections.

Figure 5.12(a) indicates a good convergence behavior of the ionization and excitation cross sections with increasing l. No deviations for the different maximal l can be observed for high energies. The differences between the results for $l = 6$ and $l = 7$ around the maximum are minimal. The deviations for $l = 4$ are a little bit more pronounced. In general, an increase of l leads to (slightly) larger and smaller values of the ionization cross sections for energies below and around the maximum, respectively, while no effect is observed for high energies.

The variation of the maximal M in Fig. 5.12(b) reveals that $M = 1$ and around the maximum also $M = 2$ are not sufficient for ionization and excitation. The curves for $M = 3$ and $M = 4$ seem on the other hand to be converged. Note, the smaller the value of M the higher are the ionization cross sections around and below the maximum while they are lower for high energies.

The convergence with the number of B splines N used for the description of the orbitals per angular momentum is shown in Fig. 5.12(c) and can be considered as excellent. Around the maximum the curve for $N = 52$ only slightly deviates from all other curves with larger N. That is, already $N = 72$ can be considered as converged in N. However, it might be advantageous to use a basis expansion with $N = 52$ in order to further increase other basis parameters which may have a much stronger effect on the calculations. This kind of basis optimization seems to be reasonable due to the comparably small deviation for the results with $N = 52$.

Finally, in Fig. 5.12(d) the convergence with the maximal energy, in units of Rydberg, of the orbitals which enter the construction of the two-electron configurations Υ is examined. Obviously, a dependence on this energy cutoff CO can be observed. The cutoff energies CO = 3 a.u. and CO = 5 a.u. are clearly insufficient, where the former curve lies for $E < 100$ keV even outside of the graph. Results obtained with a value of CO = 20 a.u. on the other hand seem to be almost converged. In the construction of the two-electron states the leading series of the configurations $\Upsilon^{\Omega}_{(n\eta,n'\eta')}$ consist of one orbital in the ionic ground (and possibly also the first excited) state and the other orbital has a symmetry η' in accordance with the two-electron symmetry Ω. In these leading series either all n' with an orbital energy below the cutoff or a smaller number of orbitals are considered. Results for basis sets which have such a long series *only* for the symmetry Ω which includes the ground state are denoted by **. The basis set denoted by * has only for the dominant two-electron symmetries long series which include all orbitals $n'\eta'$ up to the cutoff. Considering these curves in Fig. 5.12(d) it can be concluded that at least one long configuration series is needed per symmetry block Ω. In general, with increasing cutoff energy the ionization results converge towards smaller values for impact energies

E around and below the maximum while they converge towards larger values for high E.

According to the presented studies for the two-electron description of the helium atom the subsequent calculations on $\bar{p}$ + He collisions are performed with a basis set including orbitals with angular momenta up to $l = 6$, $N = 72$ B splines per angular momentum, and a maximal energy of CO $= 25$ a.u. as well as two-electron states with azimuthal quantum numbers up to $M = 3$. Finally, an improvement of the two-electron basis for helium atoms usually leads to larger ionization cross sections for high energies above the maximum while the results obtained with an improved basis decrease for low energies and around the maximum.

Note, the results are sensitive to the choice of the included configuration series. A systematic discussion of the dependence on the chosen two-electron configuration in the CI basis is of course much more complex than a linear variation of parameters like l and M and is therefore only partly presented here. While the obtained results seem to be converged with respect to the three parameters l, M, and the number of B splines, it cannot be excluded that a more appropriate choice of configurations may lead to improved results. However, it is always possible to improve a basis set, if the existing states are kept unchanged and further basis states are added.

5.2.2. Total cross sections

The ionization cross sections σ_{ion} for antiproton impact on helium atoms using the model potential $V_{\mathrm{m}od}$ and the full two-electron description is compared in Fig. 5.13 to the data of the only existing three experiments in the considered energy range [34, 35, 160] all performed at CERN basically by the same group. During the last two decades the main effort has been spent to decrease the minimal impact energy of the antiprotons for which the extraction of experimental data was still possible.

Full description versus experiment and model $V_{\mathbf{m}od}$

The comparison of the present data obtained with the full two-electron description reveals an excellent agreement with the experimental data for $E \geq 200$ keV. For 40 $\mathrm{k}eV <$ $E < 300$ keV the data of the two experiments [34, 35] (slightly) separate from each other and the calculated curve lies either in-between both or at least fully within the error bars of one data set for all impact energies $E \geq 40$ keV. While the experimental data for the three lowest energies $E < 6$ keV are compatible with the present calculations, the data show a behavior for energies 7 $\mathrm{k}eV \leq E \leq 30$ keV which is clearly different from the present findings. Thereby, also the slopes of the two experiments (indicated in Fig. 5.13 by the dashed and dash–dotted straight lines) differ considerably in this energy range. That is, some kind of step or knee structure is suggest by the experimental data around $E = 30$ keV which is, however, not at all reproduced by the present findings. The experimental group proposes a re-measurement at these low energies in the near future [65], since no theorist, despite numerous attempts, has come up with a suggestion to explain this feature. Note, the data points for the two lowest impact energies by

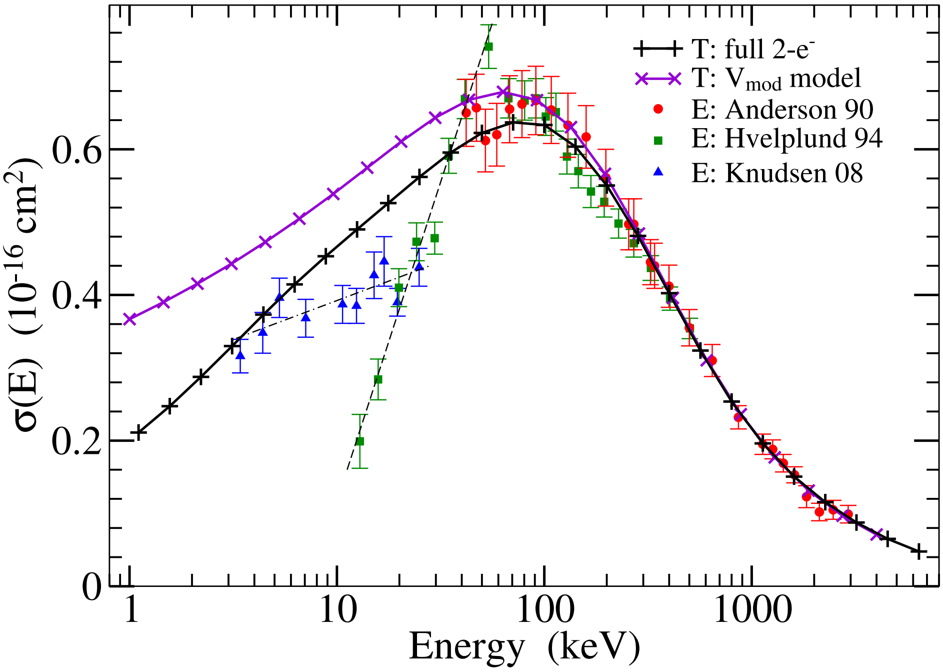

Figure 5.13.: *Ionization cross section σ_{ion} for $\bar{p}$ + He as a function of the impact energy E. Theory: Black curve with pluses, two-electron results; violet curve with* x*, model potential V_{mod}. Experiment: red circles, Anderson et al. [34]; green squares, Hvelplund et al. [35]; blue triangles, Knudsen et al. [160] .*

Hvelplund *et* al. [35] have been withdrawn by the experimental group in view of the recent measurement [160].

The present σ_{ion} curve obtained with the model potential V_{mod} nicely agrees with the full calculations and therefore also the experimental data for high energies $E > 200$ keV. While good agreement with experimental results still persists down to $E = 40$ keV for energies smaller than 300 keV the curves of both calculations start to deviate. Thereby, the results from the full two-electron description always stay below those of the model with an increasing difference for decreasing impact energy. Obviously, for these energies the dynamic electron-electron correlation effects become important and definitely have to be included in calculations aiming for high precision. They lead to a reduction of the cross section since the electron cloud can, especially in slow collisions, better adapt in a dynamic way to the approaching projectile. For high energies where the interaction is only short-lasting the dynamic electron-electron correlation effects, which require a finite interaction time [161], are of course less important.

In conclusion the model potential V_{mod} might be considered as a good approximation for energies $E > 40$ keV. Results obtained with V_{mod} for lower energies still reproduce the qualitative trend to some extent. However, they have to be interpreted with some caution considering the fact that they are obviously too large.

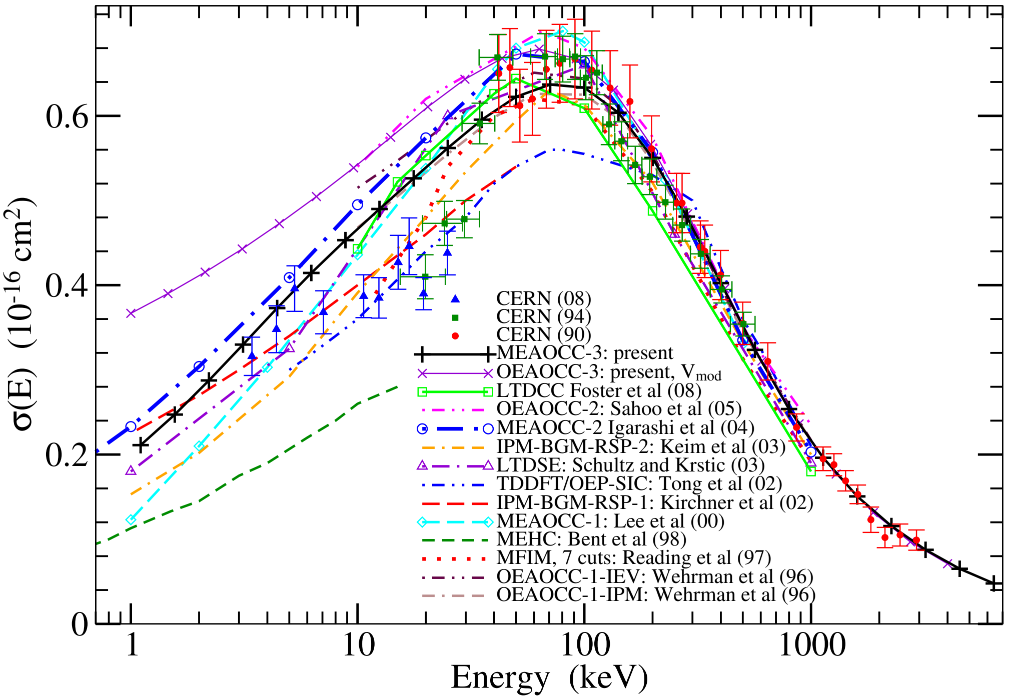

Figure 5.14.: *Comparison of various ionization cross section σ_{ion} for $\bar{p}$ + He as a function of the impact energy E. **Theory**: Black solid curve with pluses, two-electron results; violet solid curve with* x, *model potential V_{mod}; green solid curve with squares, [162]; magenta dash–double-dotted curve, [59]; blue dash–dotted curve with circles, [58]; orange double-dashed–dotted curve, [57]; violet long-dashed–dotted curve with triangles, [56]; blue dash–double-dotted curve, [55]; red long-dash curve, [54]; cyan long-dash curve, [53]; green dash curve, [52]; red dotted curve, [51]; maroon dash–double-dotted curve, [50]; brown long double-dash–dotted curve, [50]; **Experiment**: red circles, [34]; green squares, [35]; blue triangles, [160].*

Comparison to other calculations

In Fig. 5.14 the ionization cross section obtained with the present full two-electron and model description together with the experimental results are compared with a selection of various theoretical calculations by other groups using different methods. Since these calculations have already been compared elsewhere, e.g. in Ref. [160] and to a certain extent also in the cited references [50–59, 162], only some additional notes with respect to the present findings shall be made here.

The one-electron atomic-orbital close-coupling (OEAOCC) calculation performed in this work with the model V_{mod} agrees with the OEAOCC-2 results by Sahoo *et* al. [59], both using the IPM (cf. Sec. 4.3 for the introduction of different independent electron models), while the latter is slightly too high around the maximum. The IPM results by Wehrman *et* al. [50] differ, however, from the former two for energies around and below the maximum, but agree, on the other hand, remarkably well with the present two-electron calculations. The main difference between the three OEAOCC calculations is that they use different effective single-electron potentials. While the potential employed by Sahoo *e*t al. [59] is rather similar to the present model, Wehrman *e*t al. employ a qualitatively different potential in [50]. The latter one was developed to reduce the correlation correction on K-vacancy production by fast protons incident on light ions [163]. This effective nonlocal potential is identical to the Hartree-Fock potential when it operates on occupied virtual orbitals but is different when it operates on unoccupied virtual orbitals. By this means the defect of the Hartree-Fock potential for scattering-state solutions at large distances [50] should be improved.

The recent lattice time-dependent close-coupling (LTDCC) calculations by Foster *e*t al. [162], which have been considered as state of the art, are in some agreement with the present many-electron atomic-orbital close-coupling (MEAOCC-3) results for energies below the maximum. Their high-energy results are, however, remarkably poor. They are too low at high energies, that is below the error bars, and higher than the present findings for low energies. This qualitative behavior reminds on results obtained in this work in the attempt to study the convergence behavior discussed before (cf. Fig. 5.12) where the curves originating from insufficient basis sets usually approach the converged results in the same way, i.e., from below for high and from above for low impact energies, respectively. Therefore, the lattice calculations are probably not fully converged with the grid size or the spacing of the grid points. These parameters may be determined by the maximally available computational resources necessary for this kind of large-scale calculations. Note, the number of eight data points for different energies is rather small for a detailed comparison but also due to the very demanding grid approach. An earlier attempt to solve the TDSE on a lattice (LTDSE) was performed by Schultz and Krstic [56]. However, they performed the calculations only in reduced dimensionality, i.e. 2×2D instead of the full 2×3D description. This was mainly motivated by the limited available computational resources. The accuracy of this approximation is not fully known. While their curve also seems to be too low for high energies, although better than the LTDCC calculations, it alternates around the present two-electron data for energies around and below the maximum. Very recently a new attempt to calculate $\bar{p}$ + He collisions on a grid was performed [164]. Besides differential results for both electrons also total ionization cross sections were calculated. For high energies the single ionization cross section, lying below the LTDCC results, does not agree with the experimental results. For energies below the cross-section maximum it is comparable with the present two-electron results.

The method employed in the calculations of the MEAOCC-2 data by Igarashi *e*t al. [58] is closest to the present MEAOCC-3 approach. Accordingly, both curves are qualitatively similar. The cross sections of the former approach are, however, larger around and below the maximum. This may also indicate that their calculations using a rather restricted basis set are not fully converged at these energies.

Very recently time-dependent density functional theory (TDDFT) calculations have been presented by Henkel *e*t al. [165] for this collision system. Their main purpose is, however, to compare different models within the TDDFT and contrast them with the available literature. They concluded that the functional and dynamic correlation of the electrons are of comparable importance for single ionization and that the exchange-only approximation should be preferred for calculations within TDDFT.

Finally, one may conclude that it is possible to obtain converged results with the full two-electron description concerning the studied parameters. Second, excellent agreement of these results are achieved with the experimental data for high energies and within the error bars for the very-low energies and around the maximum. A possible knee structure around $E = 30$ keV suggested by the measurements is, however, neither reproduced by the present findings, nor by any other theoretical work. The differences among the various calculations may partly be caused by the fact that they are probably not fully converged in all relevant parameters. Finally, the model potential is in good agreement with experiment around and especially above the ionization maximum. Below, however, the quantitative agreement with the two-electron description including dynamic electron-electron correlation effects becomes worse with decreasing impact energy. For energies below the maximum, an advanced model description, like the one used in [50], might be more appropriate.

6. Molecular targets

Considering antiproton impacts on molecules the most basic targets are molecular hydrogen cations and hydrogen molecules. In contrast to atoms they consist of two nuclei and have one and two electrons, respectively. The increased complexity caused by the nuclear degrees of freedom may be described by vibration and rotation of the molecular axis. Accordingly, using the BO approximation, the transition probabilities depend in particular on the internuclear distance and the relative orientation of the internuclear axis with respect to the projectile trajectory. It is a central goal of this work to finally provide a full description of collisions with H_2 targets including effects due to the two electrons as well as the two nuclei, i.e. in contrast to atoms the non-spherical symmetry.

In order to achieve this demanding aim several steps are completed on that way with increasing complexity. First, an atomic one-center approach has been developed, tested, and also applied to alkali-metal atoms which is discussed in Sec. 5.1. Second, a molecular one-electron two-center approach is implemented as a self-contained extension of the atomic code and it is applied to molecular hydrogen cations in the following section. Thereby, the two-center description of the nuclei allows for the study of different internuclear distances and orientations of the molecular axis. Finally, the latter approach together with a CI procedure is used to obtain a full two-electron two-nuclei description of the target which is therefore also well suited for H_2 molecules and is discussed in Sec. 6.2. As an intermediate step calculations are also performed with the atomic one-electron approach employing the model potential V_{mod}. They are of course much less demanding than the full description. They provide, however, also information on the dependence the internuclear distance.

In numerical calculations which necessarily are only capable of finite dimensions rigorous convergence studies are crucial to assure the quality and accuracy of the results. However, the investigation of the atomic targets can be considered as a general testing of the convergence behavior for the one- and two-electron approaches using the alkali-metal and helium atoms, respectively. Together with additional convergence studies for the $H_2{}^+$ cation a sound understanding of the convergence behavior is obtained which finally can be applied to efficiently find sufficient basis sets for H_2 molecules.

For $\bar{p}$ collisions with molecules experimental $\bar{p}$ + H_2 data for ionization cross sections [35, 38] as well as for the stopping power [76, 79] were measured. As for the double ionization of helium targets, a considerable difference in the production of H^+ ions was observed between $\bar{p}$ and p [67, 68] impacts. Theoretically, however, only little has been investigated for $\bar{p}$ impacts on molecular targets. Actually, there is one calculation for $H_2{}^+$ [73] and one for H_2 [72] targets. While the former might be considered as substantial contribution the results of the latter are unsatisfactory with respect to experiment. The results obtained in this work for $H_2{}^+$ and H_2 molecules are therefore of considerable interest to complement the rather incomplete insight provided by the literature so far.

In the following section the molecular one-electron approach is tested for H_2^+ targets including detailed convergence studies, verifying the orientation averaged cross sections, and providing the first data on excitation. In Sec. 6.2, first the model potential V_{mod} is applied to calculate cross sections for proton and antiproton collisions. Afterward, the full two-electron two-nuclei description of H_2 is employed and the results are compared to the experimental data and the model description. Additionally, the dependence on the orientation and even more detailed on the internuclear distance is studied. Finally, electron-energy spectra for proton and antiproton impacts are provided. The last section 6.3 deals briefly with the H^+ production in antiproton collisions. Thereby, the applicability of a two-step model is critically examined.

6.1. Hydrogen molecular ion

An elaborate calculation of the *ionization* process for a molecular target was performed recently by Sakimoto [73] being a pioneering work on $\bar{p} + H_2^+$ collisions. The calculations were performed using a discrete variable representation (DVR) method in which the wave function is directly calculated on grid points constructed from the zeros of orthogonal polynomials. Sakimoto examined closely the dependence of the ionization cross section on the internuclear distance of both nuclei. Furthermore, he investigated the dependence on the relative orientation of the molecular axis with respect to the trajectory of the antiproton. Thereby, it was possible to present cross sections for ionization independent of a fixed orientation of the molecular axis and of the internuclear separation. However, Sakimoto considered the effort for these calculations using the DVR method due to the many degrees of freedom as being extremely time-consuming especially in the case that also excitation cross sections should be considered. Consequently, the calculation of results for excitation was postponed although the employed method is in principle capable of describing excitation.

It is therefore one aim of the present work to reduce the amount of time needed for the computation of $\bar{p}$ collisions with molecules. This is not only important in order to be able to determine H_2^+ excitation cross sections but is even more a prerequisite for calculations of more complex systems like $\bar{p} + H_2$ which are in the focus of the ongoing research, since they are experimentally better accessible and at the same time of relevance in applications. In order to decrease the computational effort a number of different actions are taken into account in the present work. These are, first, an appropriate basis representation of the time-dependent scattering wave function using eigenstates of the unperturbed H_2^+ ion. Second, the use of the symmetry of the collision system decreases the number of coupled equations which have to be considered explicitly. Finally, the number of different orientations of the molecular axis that have to be calculated is reduced using an appropriate scheme for orientational averaging. The implementation of these operations is mainly discussed in Secs. 2.1.3 (generation of the appropriate basis set), 3.2.2 (exploiting symmetries and selection rules), and 4.4 (approximation of an appropriate orientational average). It should be emphasized that all mentioned actions contribute in the same way to the full two-electron molecular H_2 target and thus become even more expedient.

Another issue which is qualitatively similar for the ${H_2}^+$ and the H_2 targets, within the chosen description, is the convergence behavior considering the maximal included azimuthal quantum number m, angular momentum l, which is an expansion parameter rather than a quantum number (cf. Sec. 2.1.3), and the number of B splines per l. Therefore, the convergence of the ionization and excitation results with respect to these quantities is discussed in some detail in the following section. The computational effort to do a broad testing of the dependencies on these parameters is of course favorable in the case of the one-electron target ${H_2}^+$. Once a certain qualitative understanding is gained this can be directly used for the H_2 calculations drastically reducing the number of calculations for checking convergence.

The understanding gained for an efficient description of antiproton collisions with molecular targets as well as excitation and ionization cross sections for antiproton impacts on ${H_2}^+$ molecules have been published in Ref. [G].

6.1.1. Convergence study

In Tables 6.1–6.3 the variations of the quantities $\sigma_{\text{i}on}(\Theta,\Phi)$ and $\sigma_{\text{e}xc}(\Theta,\Phi)$ with respect to the basis set parameters N, m, and Δl are presented considering the three different orientations $(\Theta,\Phi) = (i)\ (0,0)$, $(ii)\ (\pi/2,0)$, and $(iii)\ (\pi/2,\pi/2)$. These orientations and their symmetries as well as the meaning of the angles Θ and Φ are discussed in Sec. 3.2.2 and the corresponding trajectories in the molecule-fixed frame are sketched in Fig. 3.1. The cross sections $\sigma_{\text{i}on}(\Theta,\Phi)$ and $\sigma_{\text{e}xc}(\Theta,\Phi)$ are defined in accordance with Eq. (14) of Ref. [73] by

$$\sigma_{\text{i}on}(\Theta,\Phi) = 2\pi \int P_{\text{i}on}(b;\Theta,\Phi)\, b\, db\,, \tag{6.1}$$

$$\sigma_{\text{e}xc}(\Theta,\Phi) = 2\pi \int P_{\text{e}xc}(b;\Theta,\Phi)\, b\, db\,, \tag{6.2}$$

where $P_{\text{i}on}$ and $P_{\text{e}xc}$ are the probabilities for ionization and excitation, respectively. A fixed internuclear distance is used which is chosen to be $R_{nuc} = 2.0$ a.u. throughout the convergence study. This is the equilibrium distance of an ${H_2}^+$ molecule. Note, $\sigma_{\text{i}on}(\Theta,\Phi)$ and $\sigma_{\text{e}xc}(\Theta,\Phi)$ as given in Eqs. (6.1) and (6.2) are also experimentally meaningful, if only aligned molecules are considered all having the relative orientation (Θ,Φ) of the internuclear axis with respect to the projectile trajectory (i.e. in the laboratory frame). However, in this work they are primarily used in order to learn more about the convergence behavior and the orientational dependence.

Table 6.1 shows the excellent convergence behavior of $\sigma(\Theta,\Phi)$ with respect to the number N of target states per m, π, and l used in the expansion of the scattering wavefunction Ψ. Note, this favorable convergence behavior is independent of the impact energy, angular orientation, or whether ionization or excitation is considered. The value of N depends on the number of B splines and the chosen energy cutoff (25 a.u.) which eliminates the highly oscillating states in the basis expansion. In this work N is usually equal to approximately 2/3 of the number of B splines. A relatively small value of $N = 35$ — corresponding to 52 B splines— yields already relative errors $|\Delta\sigma(\Theta,\Phi)/\sigma(\Theta,\Phi)| < 0.1\%$ for all considered $\sigma_{\mathrm{ion}}(\Theta,\Phi)$ and $\sigma_{\mathrm{exc}}(\Theta,\Phi)$ in Table 6.1.

The variation of $\sigma_{ion}(\Theta,\Phi)$ and $\sigma_{exc}(\Theta,\Phi)$ with respect to m in Table 6.2 yields relative errors for $m = 3$ which are smaller than 0.5% except for (*iii*), where these are 2.5% for $\sigma_{\mathrm{ion}}(\pi/2,\pi/2)$ at $E = 250$ keV and 1.1% for $\sigma_{\mathrm{ex}}(\pi/2,\pi/2)$ at $E = 250$ keV. The need for larger m for orientation (*iii*) is plausible, if the symmetries of the three orientations are considered as is done in Sec. 3.2.2. In order to have a similar number of coupled equations after exploiting the symmetries and selection rules of the matrix elements, m should be the same for (*i*) and (*ii*) but has to be larger for (*iii*).

Table 6.1.: *Variation of $\sigma_{ion}(\Theta,\Phi)$ and $\sigma_{exc}(\Theta,\Phi)$, in units of 10^{-16} cm^2, for $\bar{p}$ + $H_2{}^+$ with respect to N, the number of B splines, while $m = 3$ and $\Delta l = 2$ are kept constant and $R_{nuc} = 2.0$ a.u.*

	$\sigma_{\mathrm{ion}}(\Theta,\Phi)$			$\sigma_{\mathrm{exc}}(\Theta,\Phi)$		
E (keV)	2	50	250	2	50	250
N			$(\Theta,\Phi) = (0,0)$			
14	0.0737	0.4065	0.1867	0.8755	1.4922	0.7251
21	0.1194	0.4064	0.1856	0.8443	1.4633	0.7172
30	0.1383	0.4053	0.1869	0.8247	1.4638	0.7177
35	0.1396	0.4059	0.1872	0.8226	1.4651	0.7187
50	0.1396	0.4058	0.1871	0.8228	1.4651	0.7186
65	0.1396	0.4059	0.1871	0.8228	1.4651	0.7187
N			$(\Theta,\Phi) = (\pi/2,0)$			
14	0.0340	0.4574	0.1980	0.3165	2.1410	1.2231
21	0.0447	0.4453	0.2023	0.2994	2.1068	1.2137
30	0.0476	0.4433	0.2031	0.2973	2.1074	1.2127
35	0.0480	0.4439	0.2032	0.2980	2.1072	1.2127
50	0.0480	0.4438	0.2031	0.2979	2.1073	1.2127
65	0.0480	0.4438	0.2031	0.2979	2.1073	1.2127
N			$(\Theta,\Phi) = (\pi/2,\pi/2)$			
14	0.0280	0.2982	0.1661	0.1892	0.7161	0.5202
21	0.0393	0.2787	0.1615	0.1709	0.7013	0.5159
30	0.0439	0.2786	0.1619	0.1670	0.7034	0.5169
35	0.0444	0.2793	0.1622	0.1675	0.7061	0.5182
50	0.0444	0.2792	0.1621	0.1675	0.7059	0.5181
65	0.0444	0.2792	0.1621	0.1675	0.7061	0.5182

A somewhat worse convergence behavior can be observed in Table 6.3 for the variation of $\Delta l = (l_{\max} - l_{\min})/2$ which is the number of different l per symmetry subspace (m, π). $\Delta l = 3$ gives relative errors less than 1%, 1.5%, and 2.5% for the orientations (*i*), (*ii*), and (*iii*), respectively. Increasing Δl to a value of 4 decreases the maximal relative error to 0.6%. In general larger Δl are required for lower impact energies. This trend is also known from atomic targets (cf. Sec. 5.1 and Ref. [48])

Overall, one may conclude that the employed method shows already an expedient convergence behavior for a comparably small basis expansion. This should help in the calculations for the two-electron H_2 molecule. In the calculations of the $\bar{p}$ + H_2^+ results the basis set parameters are chosen to be $(N, m, \Delta l) = (35, 3, 3)$ for the orientations (*i*) and (*ii*) and $(N, m, \Delta l) = (35, 4, 3)$ for (*iii*). The size of the basis is in general given by $N \times (2m + 1) \times 2\Delta l$. Exploiting the symmetries discussed in Sec. 3.2.2 a total number of $N_{CC} = 840$, 840, and 945 coupled differential equations have to be solved for (*i*), (*ii*), and (*iii*), respectively. The obtained results should be converged within 3%, while the convergence for energies $E \geq 50$ keV should in general be much better. A further increase of one of the parameters N, m, or Δl leads for nearly all energies and orientations to decreasing $\sigma_{\text{ion}}(\Theta, \Phi)$ and $\sigma_{\text{exc}}(\Theta, \Phi)$. Therefore, the present results obtained with fixed

Table 6.2.: *Variation of $\sigma_{ion}(\Theta, \Phi)$ and $\sigma_{exc}(\Theta, \Phi)$, in units of 10^{-16} cm^2, for $\bar{p}$ + H_2^+ with respect to m while $N = 50$ and $\Delta l = 3$ are kept constant and $R_{nuc} = 2.0$ a.u.*

	$\sigma_{\text{ion}}(\Theta, \Phi)$			$\sigma_{\text{exc}}(\Theta, \Phi)$		
E (keV)	2	50	250	2	50	250
m	$(\Theta, \Phi) = (0, 0)$					
1	0.1371	0.4118	0.1547	0.8046	1.4858	0.7184
2	0.1353	0.4045	0.1839	0.7936	1.4404	0.7062
3	0.1350	0.4004	0.1889	0.7916	1.4367	0.6998
4	0.1354	0.3999	0.1894	0.7923	1.4366	0.6982
m	$(\Theta, \Phi) = (\pi/2, 0)$					
1	0.0497	0.4447	0.2047	0.2787	2.1237	1.2262
2	0.0465	0.4435	0.2138	0.2875	2.0899	1.2144
3	0.0458	0.4413	0.2194	0.2890	2.0856	1.2096
4	0.0460	0.4404	0.2203	0.2898	2.0851	1.2092
m	$(\Theta, \Phi) = (\pi/2, \pi/2)$					
1	0.0472	0.2019	0.1149	0.1496	0.7817	0.4905
2	0.0426	0.2573	0.1501	0.1537	0.6984	0.4991
3	0.0411	0.2704	0.1617	0.1552	0.6666	0.4964
4	0.0410	0.2711	0.1659	0.1552	0.6592	0.4949

sets of $(N, m, \Delta l)$ might be considered as upper bounds to the exact values. An energy cutoff of 25 a.u. is used, i.e., only (continuum) states ψ_k with $\epsilon_k < 25$ a.u. are considered in the expansion of Ψ in Eq. (3.9).

6.1.2. Total cross sections

The dependence of the ionization cross section on the internuclear distance R_{nuc} for $\bar{p}$ + $H_2{}^+$ was examined in [73] for the range 1.5 a.u. $\leq R_{\rm nuc} \leq 3$ a.u. in which the radial distribution $|\chi^{(k)}_{\nu j_{\rm n}}|^2$ of the vibrational ground state χ^0_{00} is non-negligible. It was shown that the dependence of the cross sections on R_{nuc} is approximately linear. A similar dependence of the cross sections on R_{nuc} around the expectation value $\bar{R}_{\rm nuc} \equiv \langle R_{\rm nuc}\rangle$ is also obtained in the calculations for $\bar{p}$ + H_2 as is discussed in Sec. 6.2 below. Under the assumption that $|\chi^{(k)}_{\nu j_{\rm n}}|^2$ is an even function of $(R_{nuc} - \bar{R}_{\rm nuc})$, which is fulfilled to a

Table 6.3.: *Variation of $\sigma_{ion}(\Theta, \Phi)$ and $\sigma_{exc}(\Theta, \Phi)$, in units of 10^{-16} cm^2, for $\bar{p}$ + $H_2{}^+$ with respect to $\Delta l = (l_{max} - l_{min})/2$ while $N = 50$ and $m = 3$ are kept constant and $R_{nuc} = 2.0$ a.u.*

	$\sigma_{\rm ion}(\Theta, \Phi)$			$\sigma_{\rm exc}(\Theta, \Phi)$		
E (keV)	2	50	250	2	50	250
Δl			$(\Theta, \Phi) = (0, 0)$			
1	0.2010	0.3311	0.1716	0.7733	1.5828	0.7971
2	0.1396	0.4058	0.1871	0.8228	1.4651	0.7186
3	0.1349	0.3977	0.1901	0.7917	1.4374	0.6986
4	0.1338	0.3938	0.1900	0.7847	1.4314	0.6929
5	0.1332	0.3929	0.1900	0.7827	1.4295	0.6912
Δl			$(\Theta, \Phi) = (\pi/2, 0)$			
1	0.0672	0.3594	0.1252	0.3312	2.0894	1.0544
2	0.0480	0.4438	0.2031	0.2979	2.1073	1.2127
3	0.0457	0.4382	0.2213	0.2891	2.0859	1.2070
4	0.0450	0.4344	0.2243	0.2859	2.0822	1.2023
5	0.0449	0.4334	0.2248	0.2848	2.0809	1.2007
Δl			$(\Theta, \Phi) = (\pi/2, \pi/2)$			
1	0.0855	0.4475	0.1944	0.2809	1.1539	0.7686
2	0.0444	0.2792	0.1621	0.1675	0.7059	0.5181
3	0.0411	0.2701	0.1616	0.1552	0.6666	0.4960
4	0.0401	0.2664	0.1601	0.1513	0.6559	0.4898
5	0.0399	0.2656	0.1599	0.1503	0.6529	0.4881

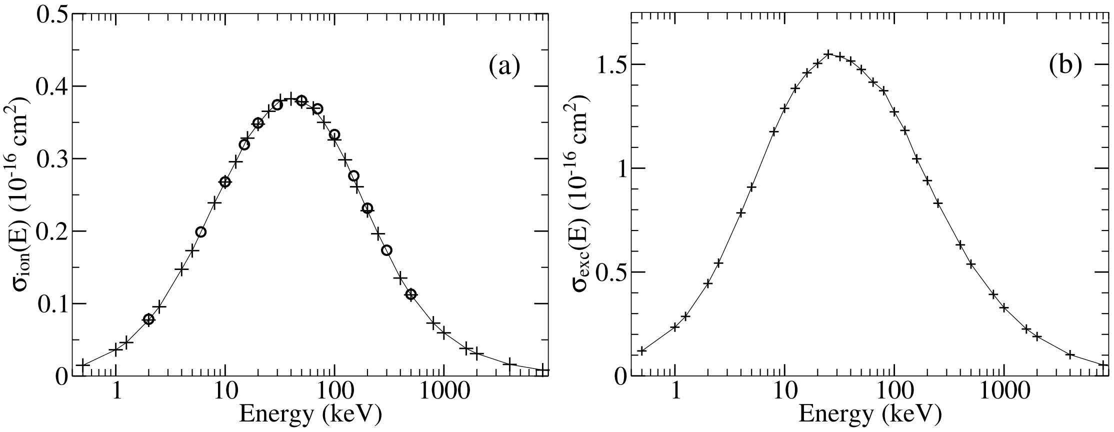

Figure 6.1.: *Cross sections for $\bar{p}$ + H_2^+ as a function of the antiproton impact energy. Solid curve with pluses, present (orientation-averaged) results; open circles, (orientation-integrated) calculation by Sakimoto [73]. (a) Ionization, (b) excitation. Reproduced from [G].*

high extent for the ground state, and $\sigma(R_{nuc})$ is linear in R_{nuc} around $\bar{R}_{nuc}$ the Franck-Condon (FC) approximation becomes accurate as discussed, e.g., in Refs. [111, 112]. Consequently, in Ref. [73] the FC results for $\bar{p}$ + $\mathrm{H_2}^+$ were found to be very close to the exact cross sections obtained by an integration over R_{nuc} as given in Eq. (4.44). In what follows the FC approximation is used, i.e., the calculations of the ionization and excitation cross sections are performed for $R_{\mathrm{nuc}} = \bar{R}_{\mathrm{nuc}} = 2.05$ a.u. which is the expectation value for the ground state. Note, the expectation value $\bar{R}_{\mathrm{nuc}}$ differs from the minimum of the ground-state potential curve of $\mathrm{H_2}^+$ at $R_{\mathrm{nuc}} = 2$ a.u. used in the convergence studies.

Calculations for $\bar{p}$ collisions with $\mathrm{H_2}^+$ are performed within a broad energy range of 0.5 keV $\geq E \geq$ 10 MeV. The three orientations of the molecular axis in the space-fixed frame (Θ, Φ)=$(0, 0)$, $(\pi/2, 0)$, and $(\pi/2, \pi/2)$ are considered. Trajectories for these three directions in the molecule-fixed frame are sketched in Fig. 3.1. An orientation-averaged transition probability $p_k(b, E)$ is gained from the results for the three orientations according to Eq. (4.47). Subsequently, the total ionization and excitation cross sections are obtained as prescribed in Sec. 4.2. The present data for the total ionization and excitation cross sections $\sigma_{\mathrm{i}on}$ and $\sigma_{\mathrm{e}xc}$, respectively, are listed for a selection of energies in appendix IV in Table .3.

Ionization

The *orientation-averaged* FC cross sections for ionization $\sigma_{\mathrm{i}on}$ are shown in Fig. 6.1(a) and are compared to the *orientation-integrated* results — employing Eq. (4.44) — calculated by Sakimoto [73]. The present calculations reproduce the latter results almost perfectly. From Table .3 it can be seen that for $E \leq 50$ keV the agreement is better than 1%. For $E = 100$ keV, 200 keV, and 500 keV, the difference is of the order of 2.1%, 1.7%, and 0.9%, respectively. The increased differences between the two calculations for the latter three energies might be caused by a reduction of the basis size in Ref. [73] for $E > 50$ keV while it is kept the same in the present work. As intended by Sakimoto [73] this reduction seems to have less influence on the results with increasing E but is still visible for $E \leq 200$ keV. He also mentions that for $E = 100$ keV and $(\Theta, \Phi)=(0, 0)$ the relative convergence error is largest and not below 2%.

Due to the good agreement between both calculations the following conclusions can be drawn. First, the results by Sakimoto [73] are confirmed by the use of a substantially independent approach. Second, the use of only three orthogonal orientations of the molecular axis seems to be sufficient for the description of the total ionization cross section in $\bar{p}$ + $H_2{}^+$ collisions. Consequently, the effort is reduced drastically, since no two-dimensional integration over the angles Θ and Φ has to be performed. Such an integration as given in Eq. (4.44) requires a sufficient number of points in Θ and Φ direction, each of these points corresponds to a full time-dependent calculation. The number of points needed for a numerical two-dimensional integration is obviously much larger than three as used in the present approach applying the simple averaging in Eq. (4.47). Note, the total computational effort scales linearly[a] with the number of calculated orientations, since each orientation corresponds to the full solution of the set of N_{CC} coupled differential equations.

Excitation

The orientation-averaged FC cross sections for excitation σ_{exc} are shown in Fig. 6.1(b). To the best of the author's knowledge there are no literature data for excitation in $\bar{p}$ + $H_2{}^+$ collisions available to compare to. Converged excitation cross sections especially for high E require an extended range of the impact parameter b in comparison to ionization as can be seen in Fig. 6.2. In contrast to [73], the extension of the b range is well feasible with the present approach due to its seemingly higher efficiency. In all calculations 30 different b values are considered whereas the maximal b increases from 15 a.u. to 30 a.u. from the lowest to the highest impact energies. The spacing between the b values increases with b in order to sufficiently resolve the inner region. Figure 6.2(b) shows for example that a range of $b \leq 10$ a.u. is not large enough for calculating the excitation cross section for an impact energy of $E = 125$ keV. On the other hand in the case of ionization a range of $b \leq 5$ a.u. can according to Fig. 6.2(a) already be considered as sufficient.

The shape of $\sigma_{\rm exc}$ in Fig. 6.1(b) is similar to that of $\sigma_{{\rm i}on}$ in Fig. 6.1(a), although a little less symmetric. The absolute height of the maximum is, however, about a factor of 4 larger for excitation than for ionization. This factor is actually minimal around the maximum and enlarges to about 6.5 towards the smallest and largest impact energies covered in the present work. The positions of the maxima are around 40 keV and 25 keV for ionization and excitation, respectively. This is similar to the findings for hydrogen atoms but larger than for alkali-metal atom targets (see Sec. 5.1).

---

[a] In practice a small deviation from a purely linear scaling occurs, since the convergence is orientation-dependent as discussed in the previous section 6.1.1.

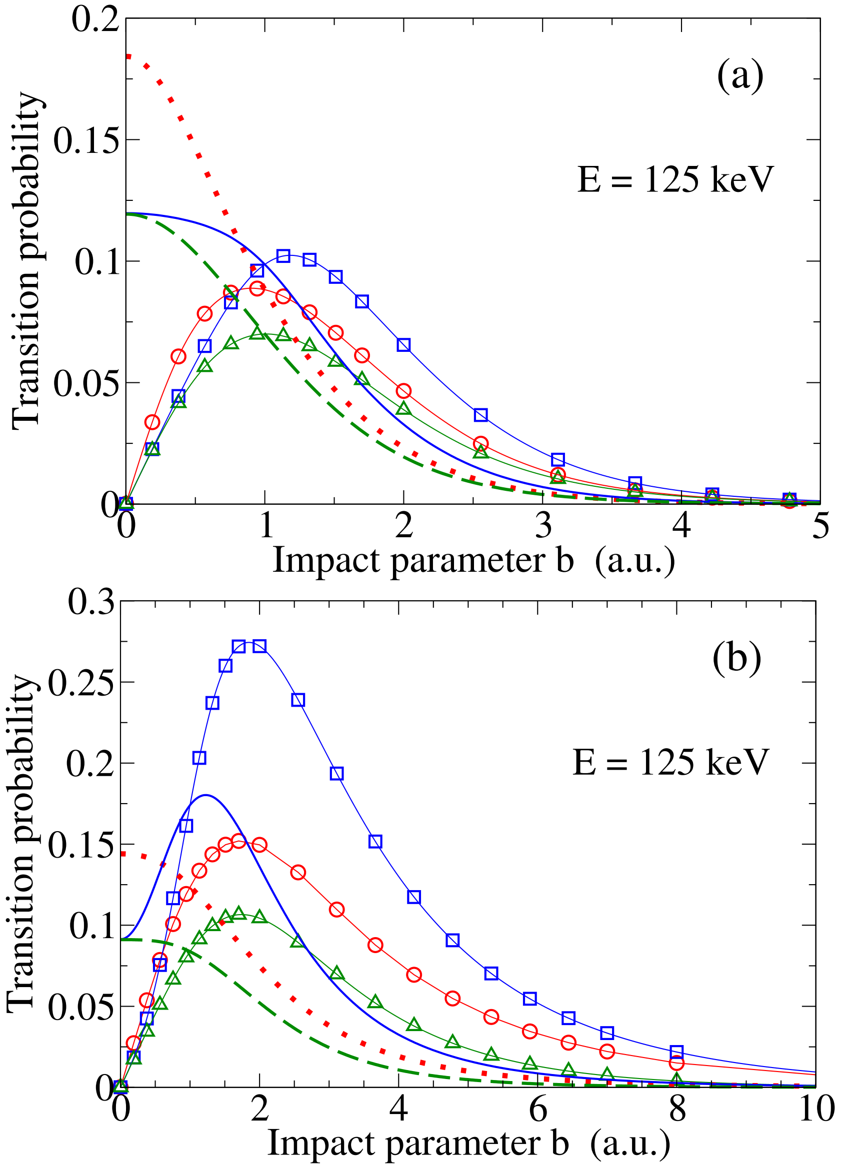

Figure 6.2.: *The transition probability $P(b)$ and $b\,P(b)$ — weighted with b — for $\bar{p}$ + H_2^+ collisions as a function of the impact parameter b for different molecular orientations and $E = 125$ keV. $P(b)$: red dotted curve, $(\Theta, \Phi) = (0, 0)$; blue solid curve, $(\pi/2, 0)$; green dashed curve, $(\pi/2, \pi/2)$. $b\,P(b)$: red circles, $(0, 0)$; blue squares, $(\pi/2, 0)$; green triangles, $(\pi/2, \pi/2)$. (a) Ionization, (b) excitation. Reproduced from [G].*

6.1.3. Dependence on the molecular orientation

The cross sections $\sigma_{\text{ion}}(\Theta, \Phi)$ and $\sigma_{exc}(\Theta, \Phi)$ as defined in Eqs. (6.1) and (6.2) are presented in Figs. 6.3(a) and 6.3(b), respectively, as a function of the impact energy together with the orientation-averaged FC cross sections for comparison. The three perpendicular orientations (*i*), (*ii*), and (*iii*), which enter in the orientation-averaged cross sections, are considered.

It can be said that in general the curves differ considerably for different orientations as well as from the orientation-averaged curve for both ionization and excitation. Similarities in the dependence on E, however, can be found for the same orientation between curves for ionization and excitation. Thereby, the two curves for the orientations (*ii*) and (*iii*), which are both perpendicular to the trajectory, share qualitatively a similar behavior, while quantitatively the latter is for most energies clearly larger than the former.

For very low energies the curves for (*ii*) and (*iii*) seem to coincide for ionization ($E < 2$ keV) as well as for excitation ($E < 1$ keV). For these low energies the transition probability in Eq. (4.42) is only non-vanishing for very small b. The differences between the trajectories of the $\bar{p}$ for (*ii*) and (*iii*) increase with b but become negligible for small b. This can be seen from Eqs. (3.36)–(3.38) which go for both orientations (*ii*) and (*iii*) in the limit $b \to 0$ over to $R_{x'} = -vt$, $R_{y'} = 0$, and $R_{z'} = 0$. Consequently, the curves of the transition probabilities in Figs. 6.2(a) and 6.2(b) for (*ii*) and (*iii*) merge for $b \to 0$. These two curves are, on the other hand, most different around $b \approx 1$ a.u. where the trajectories of orientation (*ii*) encounter the position of the $\mathrm{H_2}^+$ nuclei.

For high energies $E > 100$ keV, on the other hand, the equality

$$2\sigma_{\mathrm{ion}}(0,0) = \sigma_{\mathrm{ion}}(\pi/2,0) + \sigma_{\mathrm{ion}}(\pi/2,\pi/2) = 2\sigma_{\mathrm{ion}} \tag{6.3}$$

holds with only about 1% deviation. In the case of excitation another equality,

$$\sigma_{exc}(\pi/2,0) = \sigma_{\mathrm{exc}}(0,0) + \sigma_{exc}(\pi/2,\pi/2) = 1.5\sigma_{\mathrm{exc}}\,, \tag{6.4}$$

holds already for $E \geq 50$ keV with the same accuracy as the one for ionization except for the energies 160 $keV \leq E \leq 250$ keV where the deviation is of the order of 5%. Thereby, $\sigma_{exc}(0,0)$ shows some structures for energies above the maximum in contrast to the orientations (*ii*) and (*iii*).

For even higher energies $E \geq 2000$ keV all ionization curves seem to coincide. In the case of excitation $\sigma_{exc}(0,0) \approx \sigma_{exc}(\pi/2,\pi/2)$ holds for $E \geq 4000$ keV. The behavior at high energies can be explained by the fact that the relative contribution to excitation and ionization from distant encounters, i.e., larger b values, increases with E. At larger distances from the center the electron is exposed to a quasi-central potential and the near-field details including the spatial distribution of the nuclei are not that much resolved any more. This is especially true for the orientations (*i*) and (*iii*), as can be nicely seen in Fig. 6.3(b), for which the molecular axis lies in the plane perpendicular to $\mathbf{b}$ (cf. the sketch in Fig. 3.1 in order to gain a three-dimensional insight of the collision geometry). This is in contrast to (*ii*) where the molecular axis is parallel to $\mathbf{b}$ and therefore the minimal distance between the antiproton and one of the $\mathrm{H_2}^+$ nuclei is smaller.

The observed dependence on the orientation at high energies suggests that ionization and excitation for $\bar{p}$ + $\mathrm{H_2}^+$ can be described in accordance with Eqs. (6.3) and (6.4) surprisingly well with only one orientation, i.e., for ionization and $E \geq 100$ keV by

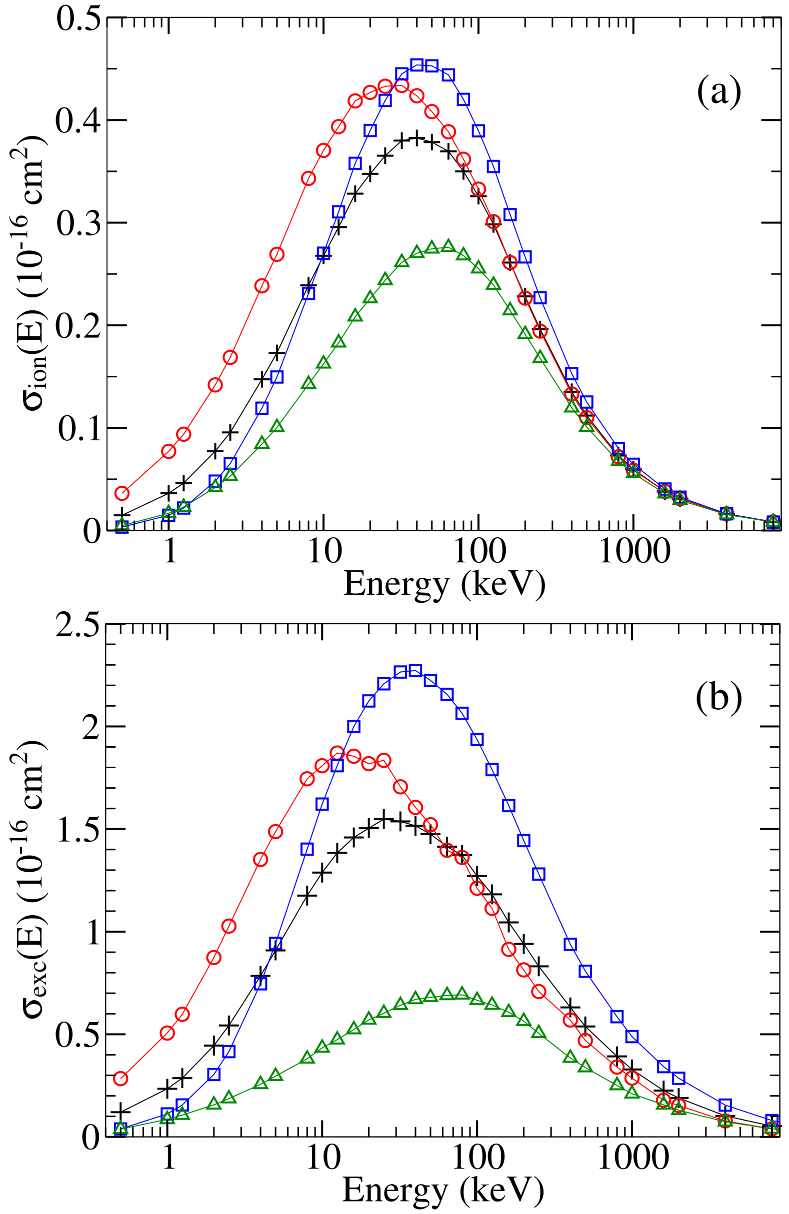

Figure 6.3.: *Ionization cross section σ_{ion} and excitation cross section σ_{exc} for $\bar{p}$ + H_2^+ as a function of the antiproton impact energy for different molecular orientations. Black pluses, orientation-averaged; red circles, $(\Theta, \Phi) = (0, 0)$; blue squares, $(\pi/2, 0)$; green triangles, $(\pi/2, \pi/2)$. (a) Ionization, (b) excitation. Reproduced from [G].*

$\sigma_{\mathrm{ion}} = \sigma_{\mathrm{ion}}(0, 0)$ and for excitation and $E \geq 50$ keV by $\sigma_{\mathrm{exc}} = 2/3\, \sigma_{\mathrm{exc}}(\pi/2, 0)$. This also means that for $E \geq 100$ keV an appropriate one-center model potential might be sufficient in particular for the description of the ionization process. For these high energies satisfactory results are obtained in calculations for $\bar{p}$ + H_2 collisions (cf. the following section on H_2, using a one-center one-electron model for the description of the H_2 molecule as described in Sec. 2.2. The calculations reproduce the experimental data [35, 38] for $E \geq 90$ keV. For lower energies the mentioned $\bar{p} + H_2$ results resemble qualitatively those for the orientation (i), which separate from the orientation-averaged curves in Fig. 6.3 for $E < 100$. Note, only one kind of trajectory is possible with the employed H_2 model potential due to its atomic (spherically symmetric) character. This kind of trajectory is practically the same as the one for the orientation (i) in the molecule-fixed frame.

Finally, it is interesting to note that the knowledge of the results for maximally three perpendicular orientations appears to be sufficient to accurately reproduce the total angular-integrated ionization cross section, although the three curves differ considerably among each other.

6.2. Hydrogen molecule

For molecular targets measurements were made for ionization in $\bar{p} + H_2$ collisions [35, 38]. However, there is a notable difference between the number of studies on H_2 molecules interacting with protons and antiprotons. While detailed work has been done for proton impacts, e.g. [67–71], little is investigated for ionization of molecules by antiproton impact and even nothing has been documented considering excitation. In the case of $\bar{p} + H_2$ collisions a single calculation was performed by Ermolaev [72], who used an atomic hydrogen target with a scaled nuclear charge $Z_\mathrm{n} = 1.09\, Z_{proton}$ in order to mimic the H_2 ionization potential. This model, which is referred to as H_{scal} in this work, is discussed in Sec. 2.2.1.

The aim of the present work is to examine the $\bar{p} + H_2$ collision process in some detail and to improve the existing theoretical cross sections. Therefore, the target molecule is described with the improved model potential V_{mod} as introduced in Sec. 2.2.2 in comparison to the simple model H_{scal} used by Ermolaev. Prior to this, the applicability of the model potential V_{mod} in ion collisions is demonstrated in proton collisions in order to compare to a larger variety of experimental and theoretical literature data.

The accurate description of antiproton collisions with H_2 molecules is one of the central goals of this work. Therefore, besides the model description of the H_2 target, calculations are also performed with the developed full two-electron two-center description of the hydrogen molecule. The latter results depend on the relative orientation of the molecular axis to the projectile trajectory and an appropriate orientational averaging is used for a comparison to the experimental and model results. This orientational averaging is rather successful for the molecular hydrogen cation $H_2{}^+$ and is introduced in Sec. 4.4.

The results for total ionization and excitation presented in this section are discussed for the expectation value of the internuclear distance in the rovibrational ground state $R_{nuc} = \langle\, R_{nuc} \,\rangle = 1.4487$ a.u. while the dependence of the cross sections on the internuclear distances of the H_2 molecule is examined afterward for the model and the full description in order to examine the applicability of the frequently employed Franck-Condon approximation. Finally, electron-energy spectra of the ejected electrons are considered and compared for proton and antiproton impact on H_2 molecules.

6.2.1. Model description of H_2

As has been discussed in the context of alkali-metal atom targets in Sec. 5.1.1 in some detail much more effort is needed to bring cross sections for proton compared to antiproton impact to convergence using the present method. This is in particular true for low proton impact energies where electron capture becomes the dominant loss channel for the target electrons. The difficulties in the description of the electron capture are mainly due to the use of a spherically symmetric one-center expansion of the scattering wave function around the target. The two-center character of the electron transfer process has to be compensated with an enlarged basis set, i.e., especially by an increased angular resolution. The main motivation for the present calculations of proton results is given by the need for a comparison of the employed method with an extended amount of literature, since the experimental and theoretical data on antiproton collisions with H_2 molecules are still sparse. A one-center expansion around the target seems, however, to be justified for antiproton collisions in which electron capture is absent and which are in the focus of this investigation.

Ionization of H_2 by p impact

The present results for the electron loss[b] of molecular hydrogen obtained with the model potential $V_{\mathrm{m}od}$ in collisions with protons are shown in Fig. 6.4 together with the electron-loss cross sections for *atomic* hydrogen in a p + H collision multiplied by a factor of 2. The present data are compared with experimental results by Rudd *e*t al. [69, 70] and by Shah and Gilbody [67, 68] and calculations by Elizaga *e*t al. [71]

The present findings for H_2 match the experimental data by Rudd *e*t al. in the whole energy range. The agreement with the measurements of Shah and Gilbody is also good except for $E < 20$ keV where their data start to be smaller than the results of the present work as well as those of Rudd *e*t al. The electron-loss cross sections for an *atomic* hydrogen target in p + H collisions multiplied by a factor 2 agree well with the experimental and present data for $E > 300$ keV. With decreasing impact energies the dependence of the cross sections on the internuclear distance $R_{\mathrm{n}uc}$ increases.[c] Accordingly, for lower energies the results for p + H, which might be interpreted as $R_{\mathrm{n}uc} \to \infty$, get considerably too large.

In the theoretical work by Elizaga *e*t al. [71] a similar model potential was used which can be obtained by integrating an effective hydrogen atom-like charge distribution with Gauss's theorem. This model potential was also proposed by Hartree in [166] for He atoms ($R_{\mathrm{n}uc} = 0$). Cross sections for the electron loss were calculated for $R_{\mathrm{n}uc} =$ 1.4 a.u. Thereby, the three methods molecular orbitals (MO), optimized dynamical pseudostates (ODP), and eikonal classical trajectory Monte Carlo (ECTMC) were used in the calculations and the results of the former two are also shown in Fig. 6.4. The

---

[b] For positive-ion, e.g. proton, impact the ionization of the target may be further subdivided in the ejection of an electron into the continuum and the capture of an electron by the positive projectile, i.e. charge transfer. The sum of both channels is also referred to as electron loss.

[c] See the discussions on the R_{nuc} dependence in Ref. [73] and in Sec. 6.2.3 for ${H_2}^+$ and for H_2, respectively.

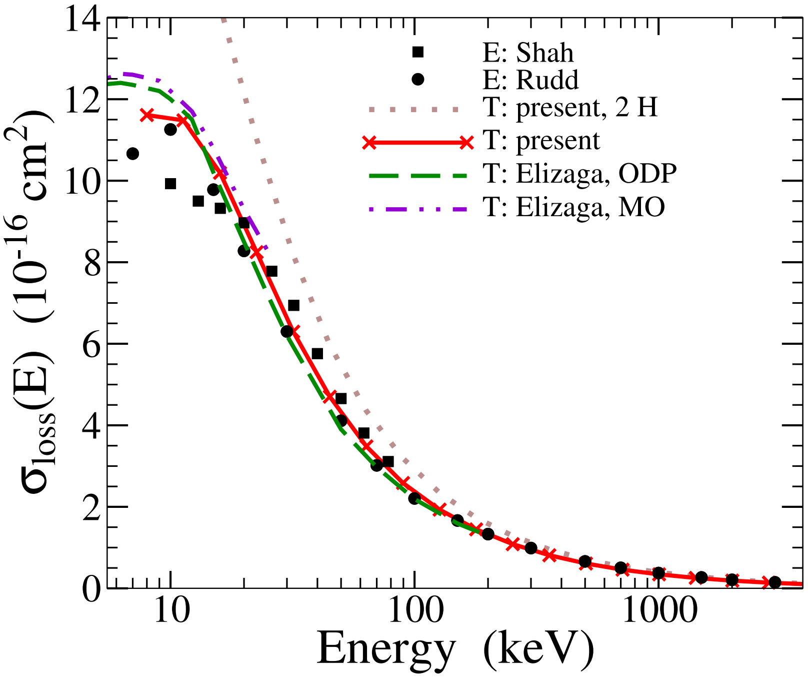

Figure 6.4.: *Electron-loss cross sections σ_{loss} for $p + H_2$ obtained with the model potential V_{mod} as a function of the impact energy E. Theory. Present results: solid curve, $p + H_2$; dotted curve, $p + H$ multiplied by 2; Elizaga et al. [71]: dashed curve, optimized dynamical pseudostates (ODP) method; dash–doubly-dotted curve, molecular orbitals (MO) method; Experimental results: filled circles, Rudd et al. [69, 70]; filled squares, Shah and Gilbody [67, 68]*

cross sections obtained with ODP are very similar to the present ones. Only for $E < 10$ keV they are larger than the present data and those by Rudd *et* al. The MO approach was applied only at low energies $E < 25$ keV and leads throughout to similar, though, slightly larger results than those obtained with ODP. Exactly in the latter energy range the outcome obtained with ECTMC differs considerably from all other curves whereas it matches the experimental and the present results very well for $E > 25$ keV. It may be concluded that the present approach is capable of describing collisions with H_2 targets quite accurately within the employed approximations in the considered energy range, i.e., for $E \geq 10$ keV in the case of proton impacts.

Ionization of H_2 by $\bar{p}$ impact

The present results for ionization of molecular hydrogen by antiproton impact using the model potential V_{mod} are shown in Fig. 6.5 as solid curve. Also shown are the ionization cross sections for antiproton collisions with *atomic* hydrogen multiplied by two. The results are compared with calculations by Ermolaev [72] and experimental data for non-dissociative ionization by Anderson *et* al. [34] as well as data of a subsequent measurement by Hvelplund *et* al. [35]. As has been suggested by Hvelplund *et* al. in

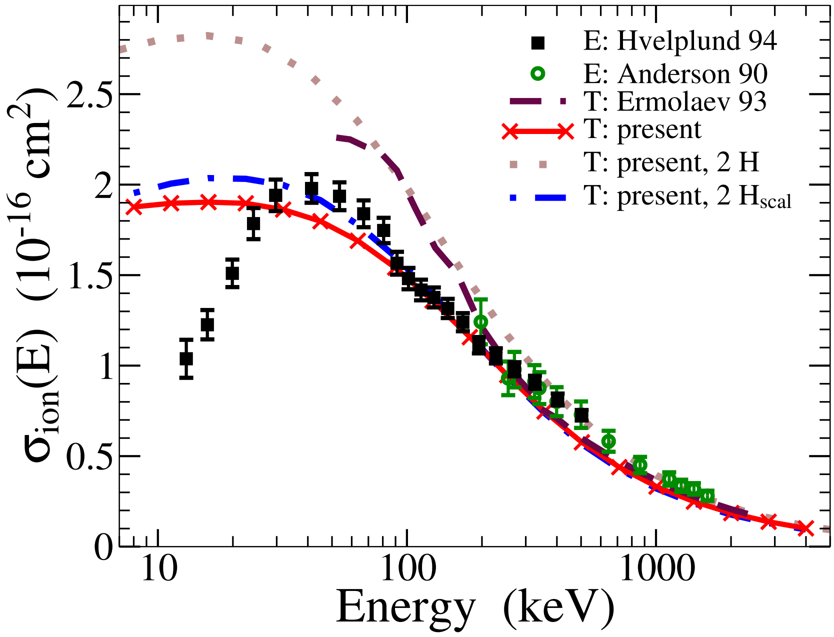

Figure 6.5.: *Ionization cross section σ_{ion} for $\bar{p}$ + H_2 as a function of the impact energy E. Theory: solid curve, present results; dotted curve, present results for $\bar{p}$ + H multiplied by 2; dash-dotted curve, present results for $\bar{p}$ + H_{scal} multiplied by 2; dashed curve, results for $\bar{p}$ + H_{scal} multiplied by 2, Ermolaev [72]. Experiment: circles, Anderson et al. [38]; squares, Hvelplund et al. [35].*

[35] the data for impact energies below 200 keV of their earlier measurement [34] are omitted in Fig. 6.5. The data for $E < 200$ keV of their first experiment are generally some 10% larger than those in the second [35] but have a considerably lower accuracy than the latter.

For high impact energies $E \geq 1000$ keV all theoretical curves coincide and also agree with the experimental data. For lower energies ($400\,keV < E < 1000$ keV) the ionization cross sections for atomic hydrogen start to differ from both theoretical results for a hydrogen molecule. However, at these energies the atomic results seem to describe better the experimental data. In the energy regime from 250 keV down to 90 keV the theoretical cross sections by Ermolaev approach those of the $\bar{p}$ + H calculation which differ significantly from the measured cross sections. Note, the present results using the same model as Ermolaev, i.e., $\bar{p} + \mathrm{H}_{scal}$, differ clearly from his findings, too. The present cross sections for H_{scal} are, on the other hand, more in accordance with the experimental data and the present results using V_{mod}. This observation may lead to the conclusion that the cross sections calculated by Ermolaev may be not fully converged for $E \leq 200$ keV.

The experimental data are, however, well described by the present $\bar{p}$ + H_2 cross section in this energy regime (250 keV down to 90 keV). Though, the strong variation of the experimental data around 85 keV is not followed by the smooth curve of the present results. While the magnitude of the present cross sections is comparable to the

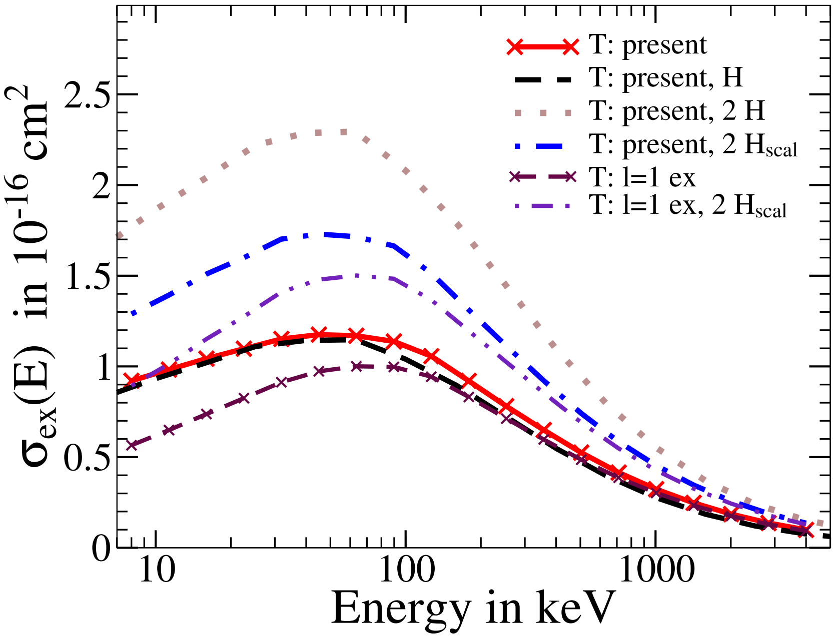

Figure 6.6.: *Excitation cross section σ_{exc} for $\bar{p}$ + H_2 as a function of the impact energy E. Theory: solid curve, present results; long-dashed curve, results for $\bar{p}$ + H; dotted curve, same results for $\bar{p}$ + H multiplied by 2; dash-dotted curve, results for $\bar{p}$ + H_{scal} multiplied by two. Cross sections for excitation into $l = 1$ states. Theory: thin short-dashed curve, present results; thin dash-double-dotted curve, results for $\bar{p}$ + H_{scal} multiplied by 2. Reproduced from [B].*

experimental data down to 20 keV the functional behavior of both, experimental and present curve, starts to differ for $E < 50$ keV. Here, the present $\bar{p} + \mathrm{H}_2$ curve possesses a similar characteristic as 2 times the cross sections of the hydrogen *atom* but with a smaller magnitude because of the larger ionization potential of the molecule. The experimental data show on the other hand a behavior very similar to that of the single ionization of helium also measured with the same experimental set-up by Hvelplund *et* al. [35]. Very recently the same authors published another measurement of the single ionization cross section for $\bar{p}$ + He in the energy range 3 $keV < E <$ 25 keV [160] which revealed that their earlier helium single ionization cross sections in [35] are too small for the lowest measured energies. It may be an interesting question whether the same is true in the case of the $\bar{p} + \mathrm{H}_2$ ionization cross sections, originating from the same experimental effort, as suggested by the present results. The currently, basically by the same experimental group, produced $\bar{p} + \mathrm{H}_2$ cross sections at low antiproton energies might help to solve this open issue.

An effective one-electron description with a fixed internuclear distance seems to be sufficient to describe non-dissociative ionization cross sections for $\bar{p} + \mathrm{H}_2$ at high energies. But without a comparison to a molecular two-electron description it is unclear how strong the influence of two-electron effects and the dependence on the molecular orientation is at intermediate and low energies. Since the energy regime around and below the maximum of the ionization cross section is believed to contain interesting physical effects a full quantum mechanical treatment of the target molecule is desirable and presented in this work in the following section 6.2.2. It should be mentioned, however, that such an advanced approach is of course much more demanding and a simplified description of the H_2 molecule might be preferred where applicable.

Excitation of H_2 by $\bar{p}$ impact

The present excitation cross sections for $\bar{p}$ + H_2 obtained with the model potential $V_{\mathrm{m}od}$ are shown in Fig. 6.6 as solid curve. Also shown are results for antiproton collisions with *atomic* hydrogen and the same *atomic* cross sections multiplied by a factor of 2. To the best of the author's knowledge there are no antiproton data in the literature to compare these results with.

Due to the experiences with the ionization cross sections one may estimate the range of validity of the excitation cross sections presented here to be about $100\,\mathrm{k}eV \leq E \leq 4000$ keV. Comparing the results for ionization and excitation in $\bar{p}$ + H_2 collisions one can say that $\sigma_{\mathrm{e}xc}$ is smaller than $\sigma_{\mathrm{i}on}$ for impact energies $E <$ 1000 keV and that both are practically the same for larger energies. The maximum of $\sigma_{\mathrm{e}xc}(E)$ lies around $E = 58$ keV and therefore at a higher energy than the maximum for ionization.

The excitation cross sections for molecular hydrogen can also be compared with the results for *atomic* hydrogen. Fig. 6.6 clearly shows that the naive assumption that an H_2 molecule is essentially composed of two *independent* hydrogen atoms (2 H; dotted curve) yields excitation cross sections which are obviously different from those which are obtained with the model potential $V_{\mathrm{m}od}$ given in Eq. (2.36). Only for high impact energies both curves get closer to each other. On the other hand, it is interesting to observe that the excitation cross sections for a *single* hydrogen atom seem to be much more in accordance with the present molecular $\sigma_{\mathrm{e}xc}$. Both cross sections show the same behavior and have practically the same values in the considered energy range. This similarity for atomic and molecular hydrogen targets is evidently not found in the case of ionization in Fig. 6.5. The results for $\bar{p}$ + H_{scal} lie in-between the cross sections for H_2 obtained with $V_{\mathrm{m}od}$ and for 2 times atomic hydrogen. However, the bound-state properties of H_{scal}, including the oscillator strengths for dipole-allowed transitions, are clearly worse than those of $V_{\mathrm{m}od}$ as discussed in detail in Sec. 2.2.3.

Note, especially for high energies $E >$ 100 keV the excitation process is clearly dominated by the transition into dipole-allowed excited bound states with angular momentum $l = 1$ as is observed for the alkali-metal atoms. Thereby, the cross section for the transition into the energetically lowest p state is of the order of 2/3 of the total excitation cross section throughout the considered energy range.

6.2.2. Full two-electron description of H_2

Until now only spherically symmetric one-electron models for the description of the hydrogen molecule (cf. Sec. 2.2) have been employed in order to calculate ionization and excitation cross sections and stopping powers for antiproton impact presented in the previous section and below in Sec. 7.1, respectively. They can mostly reproduce the experimental ionization results for antiproton impact energies $E \geq 90$ keV, while the experimental electron loss for proton impact is reasonably described for $E \geq 20$ keV. The findings together with the experiences from He targets (cf. Sec. 5.2 and Ref. [160]) suggest, however, that for lower energies molecular as well as electron-electron correlation effects are important and have to be considered. The only earlier theoretical work by Ermolaev [72], using H_{scal} as target, turned out to be unsatisfactory for $E \leq 200$ keV reproducing rather atomic than molecular hydrogen. Therefore, his results are also in clear disagreement with the present cross sections obtained with H_{scal} as discussed in Sec. 6.2.1.

In response to the limited theoretical understanding and renewed experimental activities [65] a full two-electron close-coupling method is developed in this work which is basically an extension of the tools used for the one-electron $\mathrm{H_2}^+$ targets to two-electron targets and is mainly described in Secs. 2.1.4 and 3.2.3. To the best of the author's knowledge no two-electron description for antiproton impacts on molecular targets has been introduced before in this energy range. Cross sections for single ionization and excitation of molecular hydrogen are provided over a wide energy range from 1 keV to 6.5 MeV on a dense energy grid. The experiences and insights achieved in previous convergence studies especially on He and $\mathrm{H_2}^+$ targets are extremely valuable. In the case of the molecular H_2 target the scattering wave function is expanded in a two-electron basis which includes $M \leq 3$ for orientations (i) and (ii) and $M \leq 4$ for (iii). For the orbital basis all angular momenta including $l = 6$ are used with $N = 52$ B splines per angular momentum. The energy cutoff of the orbitals is set to 25 a.u. The results for antiproton collisions on H_2 molecules obtained in this work using the full two-electron description have been published in Ref. [H].

The cross sections for different targets as well as within different levels of approximation can be used to figure out the differences between atomic and molecular targets as well as the importance, e.g., of a full two-electron description and of the molecular geometry including different orientations of the molecular axis. This means on the other hand that they indicate the range of applicability of the model descriptions which have been used so far. Furthermore, these benchmark data might be helpful for the development of models for collisions involving molecular targets.

In Fig. 6.7, the results of the time-dependent close-coupling calculations for (a) single ionization and (b) bound-state excitation of the hydrogen molecule by antiproton impact are presented. The numerical data are listed in the appendix in Table .4. The present results are compared to the $\bar{p} + \mathrm{H}_2$ data available in literature, which are basically those obtained in this work using the model potential V_{mod} and H_{scal}. The cross sections are obtained for a internuclear distance $R_{nuc} = \langle R_{\mathrm{nuc}} \rangle = 1.4487$ a.u. using an orientational averaging of the molecular orientations which is successfully employed for the case of $\mathrm{H_2}^+$ cation targets and is introduced in Sec. 4.4. The validity of the Franck-Condon approximation is discussed afterward in Sec. 6.2.3.

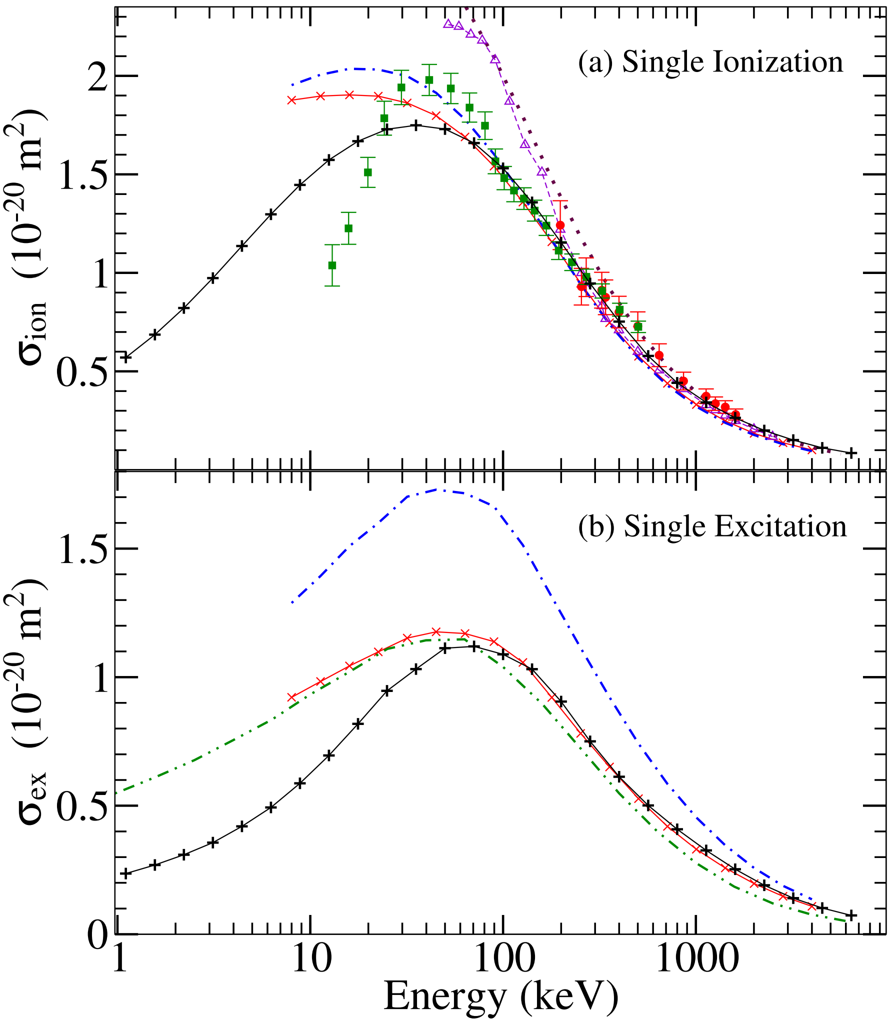

Figure 6.7.: *Cross sections for (a) single ionization σ_{ion} and (b) excitation σ_{exc} by antiproton impact on H_2. Black solid curve with pluses, molecular two-electron results for H_2; red solid curve with* x*, H_2 model potential V_{mod}; blue dashed–dotted curve, scaled hydrogen atom H_{scal}; green doubly-dotted–dashed curve, hydrogen atom; maroon dotted curve, two times hydrogen atom; violet dashed curve with triangles, H_{scal} by Ermolaev [72]; green squares, CERN 94 [35]; red circles, CERN 90 [38]. Reproduced from [H].*

Ionization

The single-ionization cross section in the top panel of Fig. 6.7 is in excellent agreement with the experimental measurements for energies above 85 keV except for the data points at 500 keV. Below 85 keV the experimental data show a small discontinuous step and increase to a higher maximum than the present results which is situated in both cases around 40 keV. Note, in the extensive convergence studies performed in this work an enlargement of the basis always led to smaller values of the maximum. This is nicely demonstrated in Sec. 5.2.1 for the case of helium atoms. Below the maximum the experimental data fall off steeply similar to the data for helium which were both measured at the same occasion [35]. For helium, however, the two lowest energy data points were withdrawn after a recent remeasurement [160]. Recent still unpublished experimental results for $\bar{p}$ + H_2 collisions, which are still preliminary, suggest that also for molecular hydrogen especially the two lowest energy data points might be too small [65]. However, these new measurements seem also to indicate that the experimental ionization cross sections around $E \approx 10$ keV might still be lower than the present results. The final experimental data together with their error bars, which are currently produced, may help to clarify the trend below the maximum.

The results obtained in this work using the model potential V_{mod} and a hydrogen atom with scaled nuclear charge $Z = 1.09$, i.e. H_{scal}, both explained in Sec. 2.2, are able to approximate the full two-electron calculations for energies above 50 and 100 keV, respectively. Though, they are throughout lower than the latter for these energies. For lower impact energies both models yield evidently too large cross sections and show in both cases rather an atomic than a molecular slope by what they reveal their atomic nature. Below the maximum also the lack of electron-electron correlation effects can be expected to become relevant as in the case of the helium atom [160] discussed in the previous chapter in Sec. 5.2. The only other calculation for $\bar{p}$ + H_2, performed by Ermolaev [72] using also a scaled hydrogen atom, is not satisfactory. His results follow for intermediate energies rather the data for a hydrogen atom multiplied by a factor of 2 and thus they even deviate from the present outcome using an H_{scal} target as discussed in the previous section.

Excitation

The lower panel of Fig. 6.7 compares the two-electron excitation cross sections for molecular hydrogen with the only existing literature, i.e., the two model calculations performed in this work. Obviously, the scaled hydrogen atom is not capable of reproducing the excitation cross section for molecular hydrogen despite its reasonable results for ionization for $E > 100$ keV. The model potential V_{mod}, on the other hand, is again an excellent approximation for energies above 50 keV. This might have been expected considering the detailed analysis of the two models done in Sec. 2.2. There, the bound state energies and oscillator strengths of the model potential are found to be in good agreement with those of the hydrogen molecule in contrast to the ones predicted by the scaled hydrogen atom. Note, for energies above the maximum the cross section for excitation of the hydrogen molecule is quite similar to that of atomic hydrogen while for ionization it is rather comparable to *twice* the cross section of the hydrogen atom.

Dependence on the molecular orientation

In Fig. 6.8 the dependence on the orientation of the molecular axis with respect to the antiproton trajectory is presented in a similar way as for $\bar{p}$ + H_2^+ collisions in Sec. 6.1.3. The cross sections $\sigma(\Theta, \Phi)$ for (a) ionization and (b) excitation are defined as in

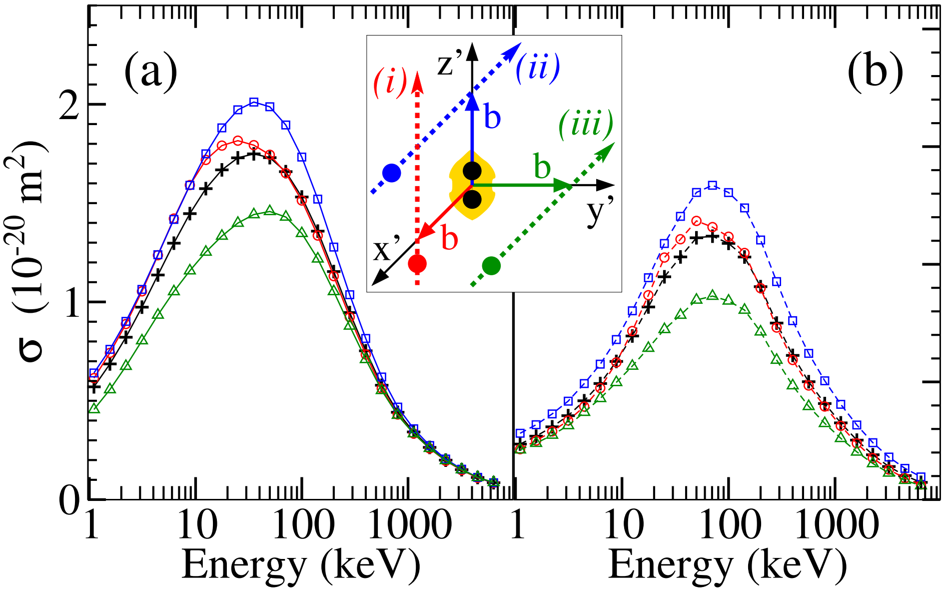

Figure 6.8.: *Cross sections for (a) single ionization and (b) excitation of molecular hydrogen by antiproton impact for different molecular orientations. Black pluses, orientationally averaged; red circles, (i); blue squares, (ii); green triangles, (iii). The inset shows a sketch of the three orientations in the molecule-fixed frame. Reproduced from [H].*

Eqs. (6.1) and (6.2), respectively. They are given for the three orthogonal orientations $(\Theta, \Phi) = (i)\ (0,0)$, $(ii)\ (\pi/2, 0)$, and $(iii)\ (\pi/2, \pi/2)$ which are sketched in the inset of Fig. 6.8 in the molecule-fixed frame and are discussed in some detail in Sec. 3.2.2. The results of these three orientations enter in the final orientation-averaged cross sections as is successfully performed and confirmed for H_2^+ targets in Sec. 6.1. The following three conclusions may be obtained.

First, the curves for the three different orientations differ in general and especially around the maximum. There also the orientation-averaged ionization curve in Fig. 6.7(a) differs most from the experimental data and additional orientations might, probably, improve the average curve. However, the experiences with the less spherically symmetric H_2^+ target, for which the three orientations perfectly reproduce the *orientation-integrated* cross sections, indicate that only a small modification can be expected due to an inclusion of additional orientations.

Second, the calculation of only the parallel orientation (i) reproduces for energies above the maximum the orientation-averaged results with less than 3% relative deviation. Thus, at high energies the parallel orientation (i) seems already to be sufficient to reproduce the total cross sections. This is exactly the energy range in which the model potential V_{mod} is applicable. Note, in the case of a spherically symmetric target, as the used model potentials, obviously only one orientation of the trajectories is possible which is basically the same as the one for parallel orientation (i).

Third, for energies around and below the maximum, for which close encounters, i.e.

small b, become dominant, the consideration of the molecular geometry is inevitable. The curves for orientation (i) are close to that for (ii) for ionization below the maximum and close to that for (iii) for excitation below 5 keV. This is in contrast to the findings for the molecular hydrogen ion, where for low energies the curves for orientations (ii) and (iii) are practically the same and the curves for (i) are clearly higher. In general, the differences among the cross sections for the three orientations are less pronounced than for the molecular hydrogen ion. This might be due to the smaller internuclear distance and the two electrons of the hydrogen molecule making it a more spherically symmetric target than ${H_2}^+$.

In Figs. 6.9(a) and 6.9(b) the excitation probabilities $P_{exc}(E, b)$ are shown as a function of the impact energy E in keV and the impact parameter b in a.u. for antiproton impact on molecular hydrogen with an internuclear distance $R_{nuc} = 1.4487$ a.u. for the orientations (i) and (ii), respectively. The general behavior is similar to the findings for atoms as helium or the alkali-metal atoms in Sec. 5.1.1. For low energies the probabilities at small b are more pronounced while for higher impact energies the transition probabilities at small b decrease and those at larger b become relatively more important. The latter fact leads to the need for a sufficiently large impact-parameter range for high energies in order to achieve convergence with b_{max}. On the other hand, a denser grid at small b is needed for low impact energies in order to resolve the relatively narrow structures. Remind, the integrand in the determination of the excitation cross section is the product $b\,P_{exc}(E, b)$. If the decrease of $P_{exc}(E, b)$ with b becomes less steep for higher energies, a b_{max} sufficient for converged results increases notably due to the scaling in the integrand with b. In this work a value of $b_{max} = 45$ a.u. is found to be sufficient for antiproton impact on H_2 molecules in the considered energy range.

A striking feature in Fig. 6.9 is the structure of the probability surfaces. This is not observed for atomic targets where the probability maximum — for the considered impact energies — is found at $b = 0$. For the H_2 molecule, however, the global maximum is observed for $b > 0$. Additionally, a second local maximum of $P_{exc}(E, b)$ is apparent in Fig. 6.9. These two maxima originate from the excitation into two dominant channels with differential probabilities which depend differently on E and b. For orientation (ii) the local maximum at $b = 0$ depends strongly on E and is much narrower than the global maximum at $b > 0$. For orientation (i) the global maximum clearly dominates the local maximum at $b = 0$ and is much more pronounced than the one in (ii). The main difference between atomic and molecular targets is that the latter have several charge centers which might also be reflected in the dependencies of the transition probabilities. The importance of different excitation channels in certain b intervals is discussed at the end of Sec. 6.2.3 in connection with the discussion on the resonant dependence of σ_{exc} on R_{nuc} which is observed especially for orientation (ii) in Fig. 6.12.

6.2.3. Dependence on the internuclear distance

The major difference between a He atom and an H_2 molecule from a theoretical point of view is the fact that the latter consists of two nuclei. The internuclear distance R_{nuc} between the two protons of the H_2 molecule parametrically determines the electronic

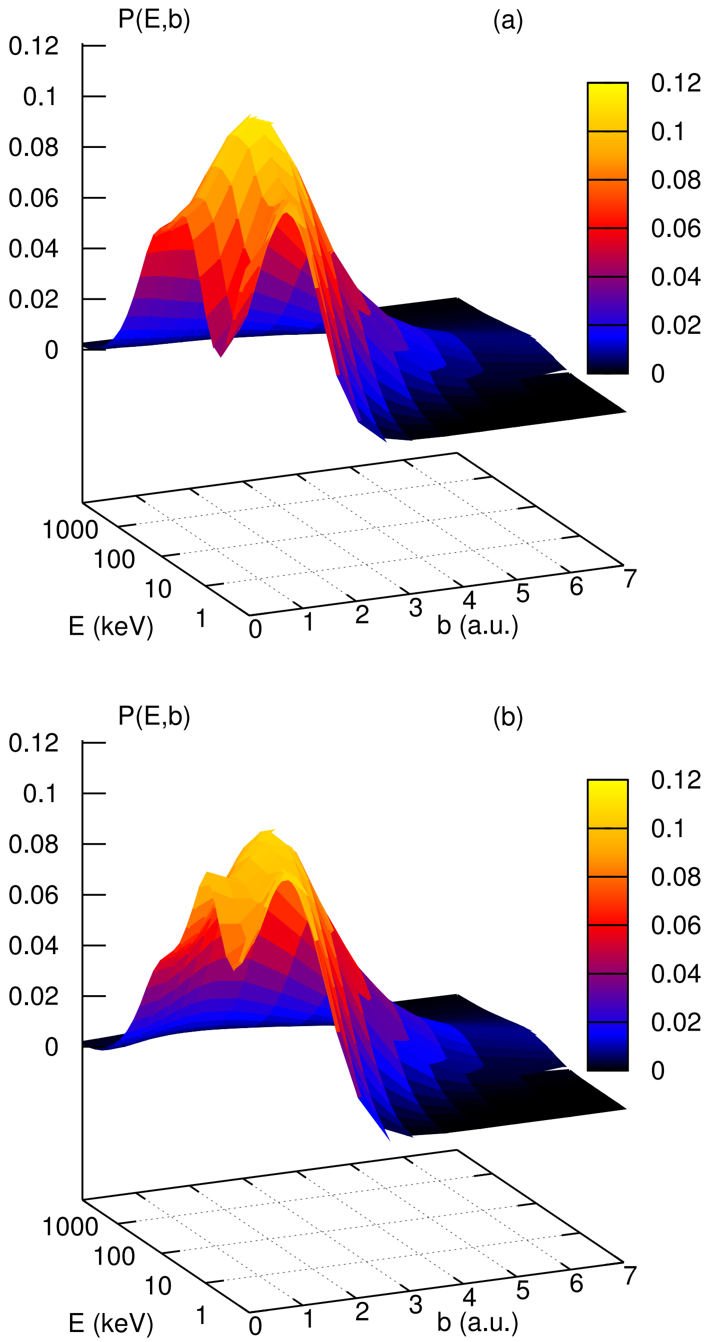

Figure 6.9.: *Excitation-probability surface $P_{exc}(E, b)$ as a function of the impact energy E in keV and the impact parameter b for antiproton impact on molecular hydrogen with internuclear distance $R_{nuc} = 1.4487$ a.u. (a) Orientation (i), (b) orientation (ii).*

wavefunction of the molecule in the BO approximation employed in Secs. 2.1.3 and

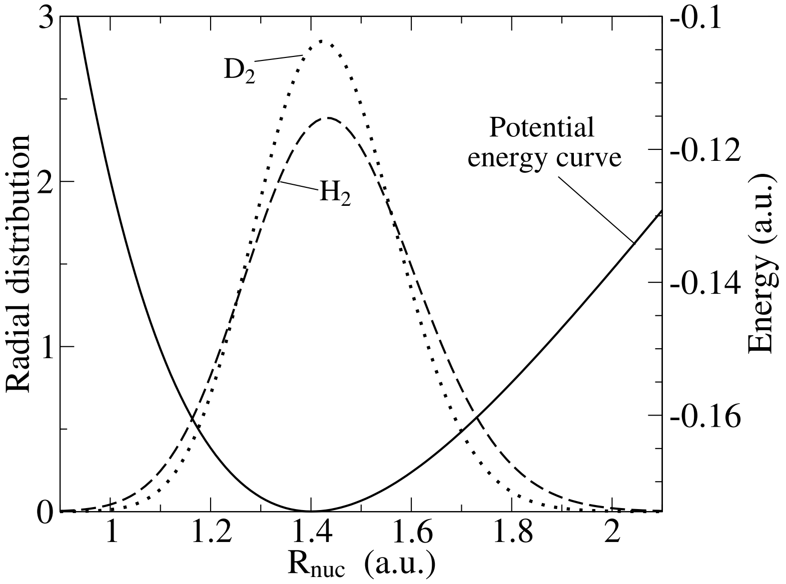

Figure 6.10.: *Radial distribution* $|\chi_0(R_{nuc})|^2$ *of the* H_2*(– –) and the* D_2 *(···) ground state of molecular vibration in a.u. [123]. Also shown is the potential-energy curve of the electronic ground state in Hartree (—).*

2.1.4. However, according to the fundamental concepts of quantum mechanics the two nuclei are always in motion even if they are in the vibrational and rotational ground state of the nuclei. Therefore, it is of importance to understand the dependence of the quantities obtained in this work, e.g., ionization and excitation cross sections, on the internuclear distance R_{nuc}. For example in the interaction of short intense laser pulses with H_2 molecules [123] the ionization yield can vary by several orders of magnitude within the R_{nuc} range in which the radial distribution of the ground state of the molecular distribution is non-negligible (cf. Fig. 6.10). In that case, a detailed understanding of the dependence on R_{nuc} is obviously of importance.

The description of the H_2 molecule is realized in this work in two ways using a one-center, one-electron model and a full two-center, two-electron description. The variation of the internuclear distance is therefore achieved in different ways for the two approaches. As described in Sec. 2.2 the dependence of the ionization potential $I_p[R_{\mathrm{nuc}}]$ of the H_2 molecule on R_{nuc} (cf. Fig. 2.2 and Table .2) is used to adapt the model description to different internuclear distances. A cross section $\sigma(R_{\mathrm{nuc}})$ which depends on R_{nuc} may therefore be defined in the context of the model potential straightforwardly as

$$\sigma(R_{\mathrm{nuc}}) \equiv \sigma\left(I_p[R_{\mathrm{nuc}}]\right) , \tag{6.5}$$

where the relation between the ionization potential $I_p[R_{\mathrm{nuc}}]$ of the H_2 molecule and R_{nuc} is presented in Fig. 2.2 and Table .2. In the case of the full molecular description the internuclear distance enters directly in the calculation of the $\mathrm{H}_2{}^+$ orbitals which are either used for $\mathrm{H}_2{}^+$ targets or as CI basis for H_2 molecules [cf., e.g., Eqs. (2.20) and (2.30)].

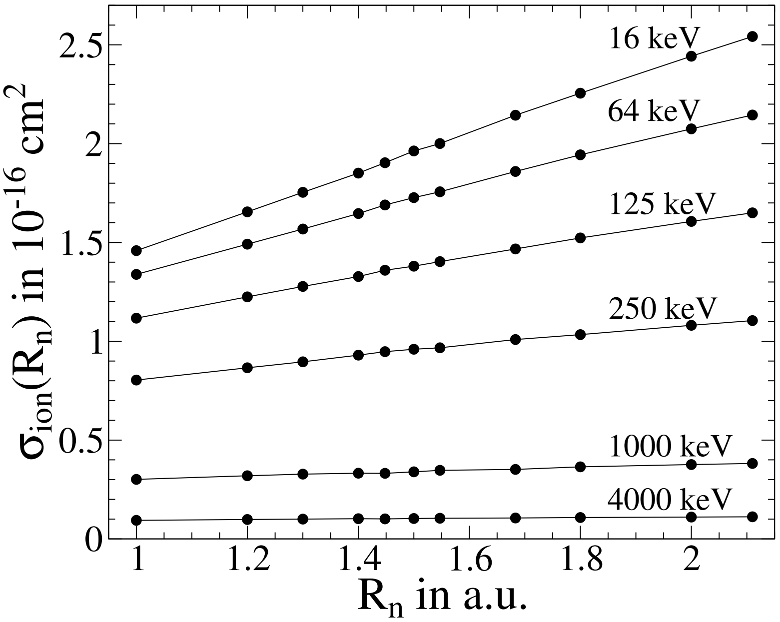

Figure 6.11.: *Ionization cross section $\sigma_{ion}(R_{nuc})$ for $\bar{p}$ + H_2 as a function of the internuclear distance R_{nuc} obtained with the model potential V_{mod} for $E = 16$, 64, 125, 250, 1000, and 4000 keV. Reproduced from [B].*

Note, in both cases, the model and the full description, an independent calculation has to be performed for every internuclear distance R_{nuc}. Consequently, the computational effort to obtain results for N_R different internuclear distances is N_R times larger than for only one R_{nuc}, e.g., the equilibrium distance or the expectation value of R_{nuc} in the vibrational ground state which are most frequently used. An elaborate study on the R_{nuc} dependence is therfore quite often postponed to future work.

It has been shown for $\bar{p}$ + $\mathrm{H_2}^+$ collisions by Sakimoto [73] — who used a molecular description of the target ion — that the dependence of $\sigma_{\mathrm{ion}}(R_{\mathrm{nuc}})$ on R_{nuc} in the range 1.5 a.*u.* $\leq R_{\mathrm{nuc}} \leq$ 3.0 a.u. differs for the parallel (*i*) and the two perpendicular orientations (*ii*) and (*iii*). Especially for the orientation of the molecular ion perpendicular to the collision plane (*iii*) the dependence on R_{nuc} is rather weak. Whereas for an orientation of the internuclear axis parallel to the trajectory of the projectile (*i*) the ionization cross sections increase approximately linearly with R_{nuc} by more than a factor two in the given R_{nuc} range. Especially at low energies the ionization cross section for orientation (*ii*) increases faster than linear with R_{nuc}. A stronger orientational dependence may be expected for $\mathrm{H_2}^+$ cations compared to the $\mathrm{H_2}$ molecule because of their larger equilibrium internuclear distance. In this work, necessarily, no molecular-orientation dependence is taken into account in the case that the spherically symmetric model potential V_{mod} is used. Since the cross sections obtained with the model depend according to Eq. (6.5) on the ionization potential which is orientation-independent the present results are interpreted as orientation-averaged. On the other hand, in the case of the full description of the $\mathrm{H_2}$ molecule every calculation is performed for a specific orientation. Results are presented for the three orthogonal orientations (*i*), (*ii*), and (*iii*).

Dependence on R_{nuc} using the model potential V_{mod}

In Fig. 6.11 the $\bar{p}$ + H_2 ionization cross sections $\sigma_{ion}(R_\mathrm{nuc})$, obtained with the model potential and defined according to Eq. (6.5), are shown as a function of R_nuc. Six different impact energies E = 16, 64, 125, 250, 1000, and 4000 keV are considered. Thereby, the ionization cross sections are calculated for eleven different internuclear distances in the range 1.0 a.*u.* $\leq R_\mathrm{nuc} \leq$ 2.11 a.u. corresponding according to Fig. 6.10 to the R_{nuc} range in which the radial distribution of the ground state of the molecular distribution χ_0 of the H_2 as well as D_2 molecules are non-negligible. It can be seen that for all impact energies shown here the ionization cross sections increase with larger R_nuc. This can be explained with the decrease of the ionization potential for an increasing internuclear distance also shown in Table .2. The dependence of σ_{ion} on R_{nuc}, however, diminishes with higher impact energies. For energies $E \geq$ 1000 keV $\sigma_{ion}(R_\mathrm{nuc})$ depends only weakly on R_{nuc} and increases by about a factor 1.2 in the whole R_{nuc} range. For smaller energies $E \leq$ 125 keV the dependence on the internuclear distance is much stronger and for E = 16 keV $\sigma_{ion}(R_\mathrm{nuc})$ increases by more than a factor 1.7 in the considered R_{nuc} range. Furthermore, for all considered impact energies the cross sections show an approximately linear dependence on R_nuc. Therefore, one may assume that for all impact energies E considered in the present investigation the simple relation

$$\sigma_{ion}(R_\mathrm{nuc}) = \sigma_{ion}(\,\bar{R}_\mathrm{nuc}\,) + \left(R_\mathrm{nuc} - \bar{R}_\mathrm{nuc}\right) \left.\frac{d\sigma_{ion}(R_\mathrm{nuc})}{dR_\mathrm{nuc}}\right|_{\bar{R}_{nuc}} \tag{6.6}$$

holds approximately in the examined interval, where $\bar{R}_{nuc}$ might be any fixed internuclear distance within this interval.

A comparison of the ionization probabilities $P_{ion}(b)$ weighted with the impact parameter b as a function of b is performed for different internuclear distances and impact energies (see Fig. 2 of Ref. [B]). In accordance with Fig. 6.11 the $b\,P_{ion}(b)$ curves for the higher impact energies differ much less for different R_nuc than those for the lower energies. All maxima of the $b\,P_{ion}(b)$ curves for $E = 1000$ keV lie around b = 1.3 a.u. while the maxima of the curves for $E = 125$ keV slightly shift from b = 1.0 a.u. for R_nuc = 1.2 a.u. towards b = 1.3 a.u. for R_{nuc} = 2.11 a.u. and also slightly increase in height. However, no qualitative change of the $b\,P_{ion}(b)$ curves is observed.

In order to determine results which include the rovibrational motion of the H_2 molecule one may use a summation over all rovibrational states belonging to a specific electronic final state. Closure with respect to all possible final rovibrational states of the final electronic states as described in Ref. [111] results in

$$\sigma = \int_0^\infty \sigma(R_\mathrm{nuc}) \left| \frac{\chi_0(R_\mathrm{nuc})}{R_{nuc}} \right|^2 (R_\mathrm{nuc})^2 \, dR_\mathrm{nuc}\,, \tag{6.7}$$

where $\chi_0(R_\mathrm{nuc})/R_\mathrm{nuc}$ is the radial nuclear wave function of an H_2 molecule in its rovibrational ground state which is considered as the initial state. It should be mentioned that the integration in Eq. (6.7) leads to a loss of the information of the electron-energy distribution. The energy information is, however, not relevant for integrated cross sections σ, but for differential cross sections like the electron-energy spectrum $\mathfrak{s}(\epsilon)$. A more detailed analysis of the validity of this approximation and a possible improvement for cases in which the electronic final state is dissociative is discussed in [111, 112].

Furthermore, it is always possible to express $\sigma(R_{nuc})$ in terms of an (infinite) polynomial in R_{nuc} with coefficients a_k and therefore to reformulate Eq. (6.7) as

$$\begin{aligned} \sigma &= \int_0^\infty \left(\sum_{k=0}^{\infty} a_k \, (R_{\rm nuc})^k \right) |\, \chi_0(R_{\rm nuc}) \,|^2 \; dR_{\rm nuc} && (6.8) \\ &= \sum_{k=0}^{\infty} a_k \int_0^\infty (R_{\rm nuc})^k \; |\, \chi_0(R_{\rm nuc}) \,|^2 \; dR_{\rm nuc} && (6.9) \\ &= \sum_{k=1}^{\infty} a_k \left\langle \, (R_{\rm nuc})^k \, \right\rangle + a_0 \, , && (6.10) \end{aligned}$$

where $\left\langle \, (R_{nuc})^k \, \right\rangle$ denotes the expectation value of $(R_{\rm nuc})^k$ for the rovibrational ground state of H_2. If the cross section $\sigma(R_{nuc})$ depends linearly on $R_{\rm nuc}$, which is here at least to a good extend the case, all a_k with $k \geq 2$ can be set to zero. Consequently, one finds, using Eqs. (6.6) and (6.10), by the relation

$$\sigma = a_0 + a_1 \, \langle \, R_{\rm nuc} \, \rangle = \sigma(\langle \, R_{\rm nuc} \, \rangle) + (R_{nuc} - \langle \, R_{nuc} \, \rangle) \, \frac{d\sigma(R_{\rm nuc})}{dR_{\rm nuc}} \bigg|_{\langle \, R_{nuc} \, \rangle} \qquad (6.11)$$

the coefficients a_0 and a_1. Finally, this means that it is sufficient to evaluate the cross section at the expectation value of the internuclear distance $\langle \, R_{nuc} \, \rangle$ of the H_2 molecule. The value $\langle \, R_{\rm nuc} \, \rangle = 1.4487$ a.u. has been reported by Kolos and Wolniewicz [167] and it is used in this work to determine ionization and excitation cross sections with the H_2 model potential which incorporates to a certain extend the rovibrational motion of the nuclei.

It may be mentioned that although vibration and rotation of the H_2 molecule are taken into account a distortion of the molecular vibration and rotation during the collision with the projectile may possibly lead to a change in the magnitude of the cross section. The effect of such a distortion (which is not accounted for in the present work) on σ may be largest for small impact energies where the cross sections depend more strongly on R_{nuc} as shown in Fig. 6.11. In order to better understand collision processes involving slow antiprotons ($E < 100$ keV) it would be desirable to fully include, in an advanced approach though, the evolution of the internuclear distance during the collision. However, the total effect of such a distortion might probably be small, since the dependence on R_{nuc} is much weaker than compared to, e.g., the results for interactions of an H_2 molecule with short intense laser pulses [123]

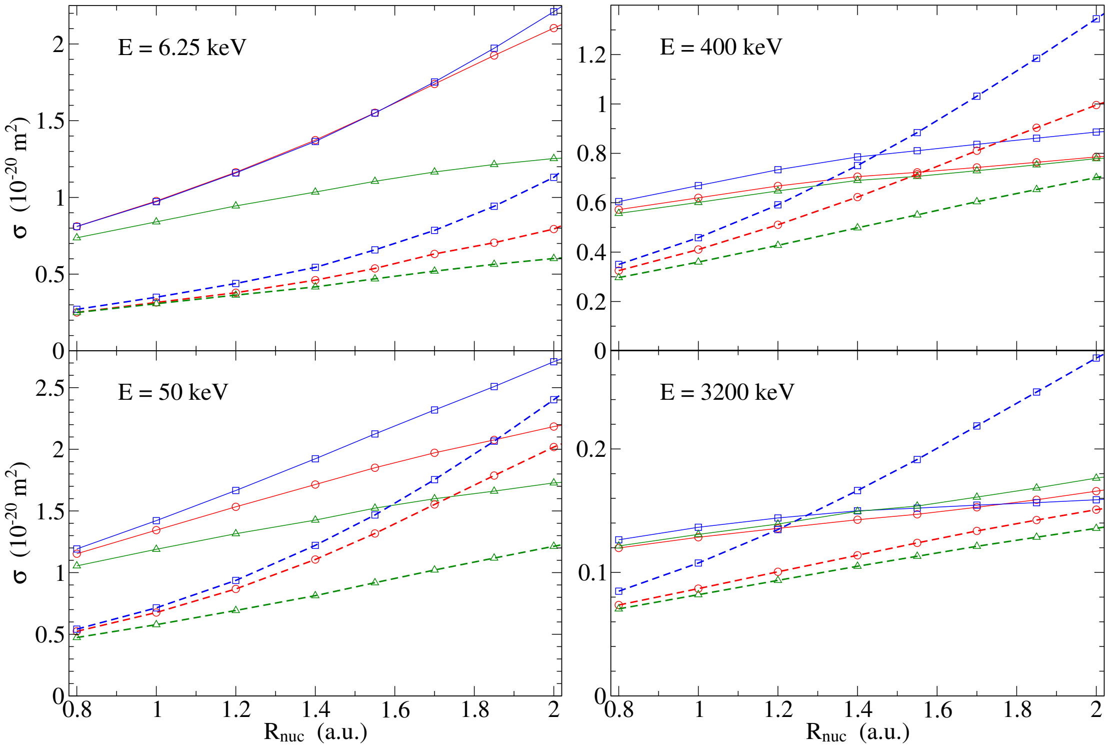

Figure 6.12.: *Cross sections $\sigma_{ion}(\Theta,\Phi)$ (—) and $\sigma_{exc}(\Theta,\Phi)$ (– –) as a function of the internuclear distance R_{nuc} in $\bar{p}+H_2$ collisions for four different impact energies $E = 6.25$, 50, 400, and 3200 keV. Results are shown for the three orthogonal orientations of the molecular axis (cf. Sec. 3.2.2): red circles, (i); blue squares, (ii); green triangles, (iii).*

Dependence on R_{nuc} using the full description

In Fig. 6.12 ionization and excitation cross sections $\sigma_{\rm ion}(R_{\rm nuc})$ and $\sigma_{\rm exc}(R_{\rm nuc})$, respectively, for antiproton impact on H$_2$ molecules obtained with the full two-center, two-electron molecular description, are shown as a function of R_{nuc}. The three orthogonal orientations of the molecular axis denoted in this work by (i), (ii), and (iii) are chosen. Four different impact energies E = 6.25, 50, 400, and 3200 keV are considered. The cross sections are calculated for eleven different internuclear distances in the range 0.8 a.$u.$ $\leq R_{nuc} \leq$ 3 a.u. while only the R_{nuc} regime corresponding — according to Fig. 6.10 — to the range in which the radial distribution of the ground state of the molecular distribution χ_0 of the H$_2$ as well as D$_2$ molecules are non-negligible is shown in Fig. 6.12 in order to improve the visibility. In general the differences among the different orientations decrease with smaller R_{nuc}. This is of course expected, since in the limit $R_{\rm nuc} \to 0$ the description of a He atom is achieved which is spherically symmetric. It can be observed that for all impact energies and orientations shown here the ionization and excitation cross sections increase with larger R_{nuc} as is the case for the description with the model potential V_{mod} for ionization (see Fig. 6.11). Also, as in the case of the model, the dependence on R_{nuc} decreases in general with higher impact energies. However, in contrast to the findings for ionization with V_{mod} in Fig. 6.11, here the dependence on R_{nuc} may not be considered as linear in all cases, especially at low energies and for excitation.

One motivation to study the internuclear-distance dependence of the ionization and excitation cross sections is the question regarding the validity of the Franck-Condon (FC) approximation introduced in Sec. 4.4.2. Therefore, the cross sections $\sigma_{int}(\Theta, \Phi) = \int |\chi_0|^2 \, \sigma(R_{nuc}, \Theta, \Phi) \, dR_{nuc}$ are considered. They are obtained according to Eq. (6.7) by an integration over R_{nuc} weighted with the radial distribution of the rovibrational ground state $|\chi_0(R_{nuc})|^2$ of the nuclei which is shown in Fig. 6.10. They are compared to the usually used FC cross sections $\sigma(\Theta, \Phi) \equiv \sigma(\Theta, \Phi; \langle R_{nuc} \rangle)$ obtained with the fixed internuclear distance $R_{nuc} = \langle R_{nuc} \rangle = 1.4487$ a.u. The numerical results of this comparison for the three orthogonal orientations (*i*), (*ii*), and (*iii*) are given in appendix B in Table .5.

The comparison of the obtained numbers ascertains that in general the use of the FC approximation is very well justified. It works best for high impact energies as well as for orientation (*iii*). The FC approximation works better for ionization than for excitation, since the cross sections for excitation depend less linearly on R_{nuc} as can be seen in Fig. 6.12. The largest deviations can be observed for low energies and orientation (*ii*). The maximal relative deviation occurs for orientation (*ii*) and energy $E = 6.25$ keV and is for excitation and ionization of the order of 3.7% and 1.9%, respectively. All other deviations are smaller. Furthermore, it can be stated that the values of the integrated cross sections are always larger than those from the FC approximation, i.e., the increase of all considered cross sections with R_{nuc} is (slightly) stronger than linear.

Additionally, the integrated cross sections $\sigma_{int}(\Theta, \Phi)$ are used to obtain orientation-

Table 6.4.: *Comparison of orientation-averaged cross sections for $\bar{p}$ + H_2 collisions obtained by using the Franck-Condon approximation, $\sigma \equiv \sigma(\langle R_{nuc} \rangle)$, and by an integration over R_{nuc}, $\sigma_{int} = \int |\chi_0|^2 \, \sigma(R_{nuc}) \, dR_{nuc}$, in units of 10^{-16} cm^2 for four impact energies E = 6.25, 50, 400, and 3200 keV. The relative deviations between both cross sections are given in percent.*

E (keV)	6.25	50	400	3200
		Ionization		
σ_{int}	1.3226	1.7482	0.7366	0.1492
$\sigma(\langle R_{nuc} \rangle)$	1.3043	1.7372	0.7319	0.1478
$\Delta\sigma/\sigma$	1.40	0.63	0.64	0.93
		Excitation		
σ_{int}	0.5133	1.1320	0.6597	0.1345
$\sigma(\langle R_{nuc} \rangle)$	0.5002	1.1069	0.6540	0.1330
$\Delta\sigma/\sigma$	2.62	2.27	0.89	1.16

averaged cross sections σ_{int} according to Eq. (4.47). The results for σ_{int} are also compared to orientation-averaged FC cross sections in Table 6.4. Obviously, the FC approximation is very well suited for the description of antiproton collisions with molecular hydrogen. The maximal relative error is, except for excitation at low-energies, below 2%, i.e., to a certain extent the larger deviations observed for the individual orientations in Table .5 average out.

Note, the integrated cross sections $\sigma_{int}(\Theta, \Phi)$ and therefore also σ_{int} are obtained using only a finite number of different R_{nuc}. Decreasing the spacing of the R_{nuc} grid may lead to slightly different and more accurate cross sections. Also, somewhat smaller basis sets have been used for the present study on the R_{nuc} dependence in order to reduce the computational demands. They include H_2 states with azimuthal quantum numbers $M \leq 2$ and $M \leq 3$ in the case of the orientations (i), (ii), and the orientation (iii), respectively, in contrast to $M \leq 3$ and $M \leq 4$ used in the calculations of the total ionization and excitation cross sections in Sec. 6.1.1. However, the deviations of the FC cross sections obtained with the different basis sets are only quantitative and smaller than 1% for the energies $E = 6.25$ keV and 50 keV and about 2–3% for the two higher energies $E = 400$ keV and 3200 keV. This is in accordance with the convergence behavior with the azimuthal quantum number observed for $\text{H}_2{}^+$ molecules and He atoms. The general conclusions obtained for the R_{nuc} dependence are obviously not expected to differ due to a small variation of the basis set.

Resonant dependence of the excitation on R_{nuc}

The strongest dependence on R_{nuc} can be observed in Fig. 6.12 for orientation (ii). Especially the excitation cross section for (ii) increases exponentially with R_{nuc} in the range 0.8 a.$u.$ $\leq R_{\text{nuc}} \leq 3$ a.u. with increasing slope for lower impact energies. In Fig. 6.13 the excitation probabilities $P_{\text{exc}}(b)$ as a function of the impact parameter for the orientation (ii) and $E = 6.25$ keV are given for the different internuclear distances R_{nuc}. One can clearly see that with increasing R_{nuc} a local minimum shapes around $b = 0.6$ a.u. and a maximum builds up which gets more pronounced and moves to larger b values. In the case of orientation (ii) the impact parameter b is parallel to the internuclear axis of the molecule (cf. the sketch in the inset of Fig. 6.7). Obviously, the position of one molecular nucleus moves from $b = R_{\text{nuc}}/2 = 0.4$ a.u. to 1.5 a.u. with increasing R_{nuc}. Therefore, the maximum of the excitation probability lies on the molecular axis but always clearly outside the internuclear distance in-between the two nuclei.

In order to better understand the shape of the probability curves one has to examine more closely the involved excitation channels. It turns out that only three final excitation channels contribute substantially to the total excitation which are the Σ_g, Σ_u, and Π_u symmetries and therein the energetically lowest excited states. While for $b \approx 0$ only Σ_g and Π_u contribute, the importance of the Σ_u channel is practically zero for $b \approx 0$ and increases with b up to the maximum of $P_{\text{exc}}(b)$. On the other hand, the contribution from the Π_u channel decreases with b while the sum of the excitation probabilities for all states of Σ_g is rather constant with b. This change of the importance of the symmetry of the final excited states is probably easiest to understand in the limit of small R_{nuc} recovering

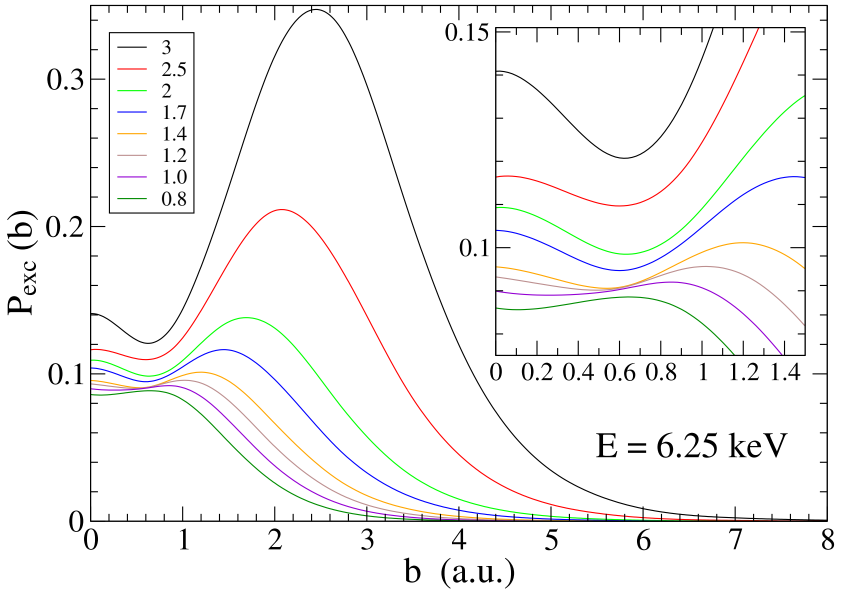

Figure 6.13.: *Excitation probability P_{exc} as a function of the impact parameter b in a $\bar{p}$ + H_2 collisions and orientation (ii) with impact energy $E = 6.25$ keV for different internuclear distances R_{nuc}. The inset shows the region of small b on an enlarged scale.*

basically the atomic symmetry. Therefore, atomic orbitals ($2\sigma_g \leftrightarrow 2\mathrm{s}_0$, $1\sigma_u \leftrightarrow 2\mathrm{p}_0$, and $1\pi_u \leftrightarrow 2\mathrm{p}_{\pm1}$) may be used to reformulate the dependence on b for the excitation into different symmetries. At small b the electrons are found to be mostly excited into $2\mathrm{s}_0$ and $2p_{\pm1}$ orbitals while for $2\mathrm{p}_0$ the electron density along the b axis — which is the z' axis for orientation (ii) — is small at b close to zero. For b values close to the probability maximum, however, the transitions into the $2\mathrm{p}_0$ orbital clearly dominate, gathering approximately 50% of the total excitation probability. The $\mathrm{p}_{\pm1}$ orbitals on the other hand do not extend so much in the direction of b, i.e., parallel to z'. Therefore, the local minimum of $P_{\mathrm{exc}}(b)$ results from the existence of two overlapping maxima. At small b the transitions into Π_u states dominate but decrease with b leading to a local maximum. With increasing b transitions into Σ_u states become relatively more important leading to a maximum for intermediate b which depends resonantly on the internuclear distance.

The increase of the height of the maximum of $P_{\mathrm{exc}}(b)$ with R_{nuc} may originate from the decreasing binding energy. However, the exponential dependence on R_{nuc}, which becomes according to Fig. 6.12 more pronounced for lower energies, might also indicate some kind of resonance behavior. Probably, it originates from a resonant electronic state of a trimer which is formed out of the two protons and the antiproton. The formation of moleculelike metastable states including antiprotons has been discussed in the literature for He atoms [93, 168]. For the case of H_2 molecules, however, quantum-chemistry calculations would clearly be of interest providing the potential surface and therefore possibly favorable geometries of an antiprotonic trimer, i.e., relations between R_{nuc} and b. Analogously, metastable configurations can also be expected for orientation (i).

6.2.4. Electron-energy spectra

The present method provides the full information of the electronic wave function after the collision. This allows for the determination of differential cross sections like the electron-energy spectra of the emitted electrons. They are obtained in this work as described in Sec. 4.2.2 using the model $V_{\mathrm{m}od}$ for the description of the H_2 molecule. As mentioned in Sec. 6.2.3, the disadvantage of the closure approach in the context of the R_{nuc} dependence lies in the loss of the full electron-energy information of the transition probabilities which is of relevance to the electron-energy spectra (cf. [112]). Therefore, the presented results may be interpreted as electron spectra for a fixed internuclear distance rather than including rovibrational motion of the nuclei as for the integrated cross sections which are discussed in Secs. 6.2.1 and 6.2.2.

Electron-energy spectra are calculated for a wide electron-energy range $0 < \epsilon < 12$ a.u. and for different impact energies of the antiproton ranging from 48 keV to 1015 keV. The electron-energy spectra $\mathfrak{s}(\epsilon, E) = \mathrm{d}\sigma(\epsilon, E) \,/\, \mathrm{d}\epsilon$ of ejected electrons in a $\bar{p}$ + H_2 collision are presented in Fig. 6.14(a) as a function of the electron energy ϵ and the impact energy of the antiprotons E. The contour plot on the bottom of Fig. 6.14(a) gives information on the gradient of the spectra surface. It can be seen that within the whole impact-energy range the electron spectra decrease smoothly and monotonically for increasing ϵ. Considering small electron energies $\epsilon < 2$ a.u., the spectra fall off strongly in view of the logarithmic scale for all impact energies. Within this ϵ interval, Fig. 6.14(a) shows that the smaller the impact energies E the larger the values of $\mathfrak{s}(\epsilon, E)$. However, for larger ϵ this uniform trend starts to cease. For $\epsilon > 4$ a.u. the overall decrease becomes weaker. Though, the electron spectra for small E start to decrease again very strongly and the fall-off of the spectra is the steepest for the smallest E. Consequently, in the intervals of ϵ and E considered here, the largest value of $\mathfrak{s}(\epsilon, E)$ for a given ϵ moves from $E = 48$ keV at $\epsilon = 0$ to $E \approx 200$ keV at $\epsilon = 12$ a.u. as can be seen from the contour plot in Fig. 6.14(a).

Cuts $\mathfrak{s}(\epsilon)$ through the same electron-spectra surface for ten different antiproton impact energies $E = 48$, 67, 95, 132, 186, 260, 367, 515, 723, and 1015 keV are presented in Fig. 6.15. The inset shows these $\mathfrak{s}(\epsilon)$ curves also in an interval of small electron energies $0 \leq \epsilon \leq 2$ a.u. Thereby, the scaling of the y axis of the inset is kept the same as in the main graph while the scaling of the x axis is enlarged. The ordering of the $\mathfrak{s}(\epsilon)$ curves in the inset is according to their impact energy E, i.e., the uppermost curve corresponds to the smallest (48 keV) and the lowest curve to the largest (1015 keV) impact energy E. It can be seen that no crossing of the electron-spectra curves $\mathfrak{s}(\epsilon)$ occurs in this low electron-energy regime.

In contrast to the behavior for small ϵ shown in the inset the $\mathfrak{s}(\epsilon)$ curves start to cross each other at higher electron energies. The curve for $E = 48$ keV starts to fall off much steeper than the other $\mathfrak{s}(\epsilon)$ curves for $\epsilon > 3$ a.u. and therefore crosses all lower-lying curves. Its first crossing takes place at $\epsilon \approx 3.19$ a.u. while its last crossing occurs at $\epsilon \approx 6.13$ a.u. with the curve for $E = 1015$ keV. The other electron-energy curves for higher antiproton impact energies share the same characteristics, namely, that the curve with the largest values of $\mathfrak{s}(\epsilon)$ in a certain ϵ range starts to fall off steeper than all other

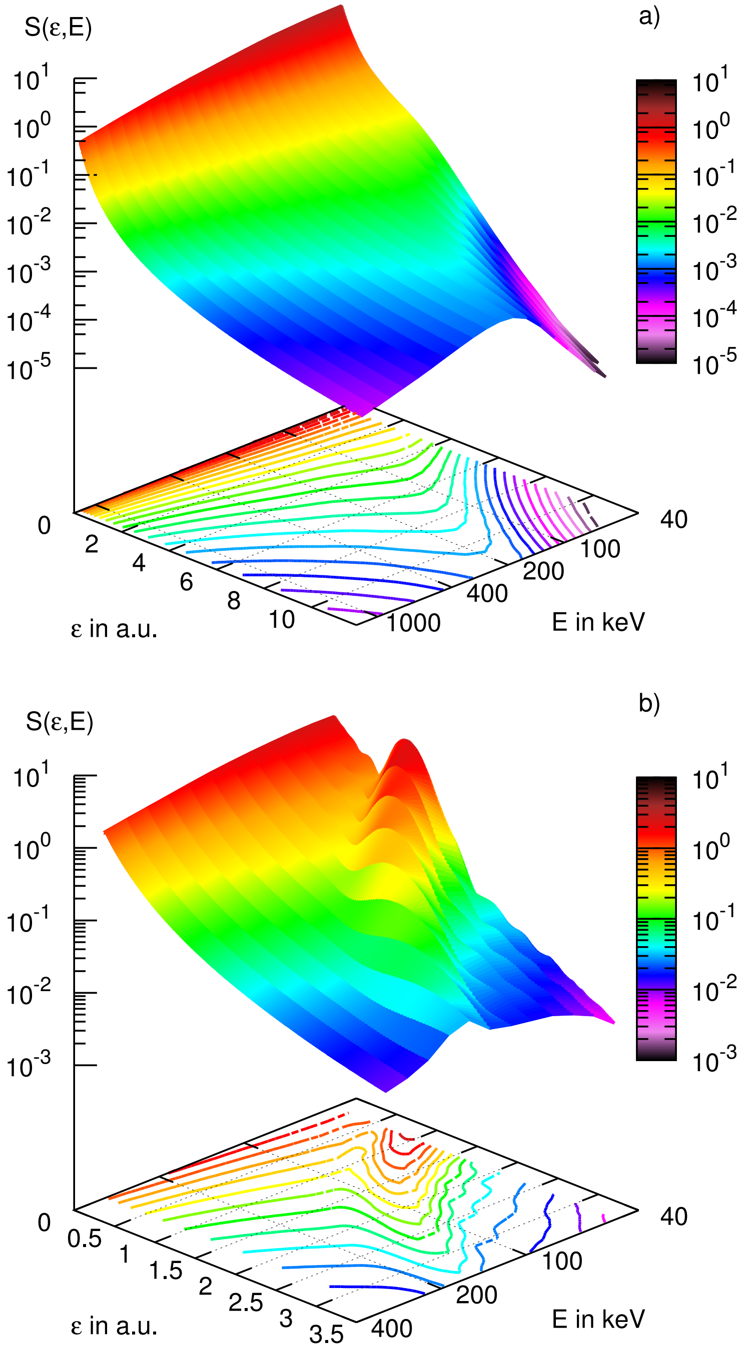

Figure 6.14.: *Electron-energy spectra surface $\mathfrak{s}(\epsilon, E) = d\sigma(\epsilon, E) \,/\, d\epsilon$ given in $10^{-16}\,\mathrm{cm}^2 \,/\, \mathrm{a.u.}$ as a function of the electron energy ϵ in Hartree and the impact energy of the antiproton E in keV. a) $\bar{p} + H_2$; b) $p + H_2$. Reproduced from [B].*

lower lying spectra curves which correspond to higher impact energies E. Though, with increasing impact energies E the decline of the $\mathfrak{s}(\epsilon)$ curves starts at larger ϵ and gets less

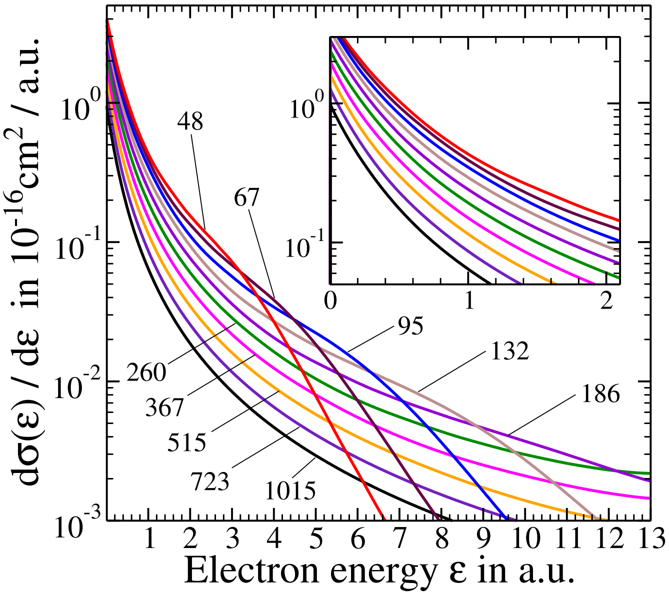

Figure 6.15.: *Electron-energy spectra curves $\mathfrak{s}(\epsilon) = d\sigma(\epsilon)\,/\,d\epsilon$ for $\bar{p}$ + H_2 as a function of the electron energy ϵ for the antiproton impact energies $E = 48$, 67, 95, 132, 186, 260, 367, 515, 723, and 1015 keV. The inset shows the spectra for the range $0 \leq \epsilon \leq 2$ a.u. with the same scaling of the y axis. The curves in the inset have the same color code and are order accordingly to the impact energy E. The uppermost curve corresponds to the smallest (48 keV) and the lowest curve to the highest (1015 keV) impact energy E. Reproduced from [B].*

steep.

The steep fall-off of the electron-energy spectra can be made plausible using the same classical argument as in Sec. 5.1.6. The energy in a classical two-body collision which can be maximally transferred is, according to Eq. (5.7), equal to $\epsilon_{\mathrm{max}}^{(cl)} = \frac{1}{2}\,(2\,v_p)^2 = 2\,v_p^2$ and therefore proportional to the impact energy of the projectile $E = \frac{M_p}{2} v_p^2$, where M_p is the mass of the projectile. This results for the four lowest impact energies [in keV] E = 48, 67, 95, and 132 in the classically allowed values [in a.u.] $\epsilon_{\mathrm{max}}^{(cl)}$ = 3.84, 5.36, 7.60, and 10.56, respectively. The behavior of the four corresponding electron-energy spectra in Fig. 6.15 for ϵ larger than these four $\epsilon_{\mathrm{max}}^{(cl)}$ values is the same, namely, a linear decrease of $\mathfrak{s}(\epsilon)$ with increasing ϵ on a logarithmic scale. The according exponential decrease of $\mathfrak{s}(\epsilon)$ is stronger for smaller E. Consequently, the influence of basis states with eigenenergies larger than $\epsilon_{\mathrm{max}}^{(cl)}$ in the expansion of the scattering wave function on the final cross sections is usually very small. The use of an energy cutoff in the basis expansion can be therefore justified, if the cutoff energy is chosen to be larger than the corresponding value of $\epsilon_{\mathrm{max}}^{(cl)}$.

For comparison to the antiproton results an electron-energy spectra surface $\mathfrak{s}(\epsilon, E)$ is also presented for p + H_2, i.e., for proton impact, in Fig. 6.14(b). The electron spectra are given within the electron-energy range $0 < \epsilon < 3.5$ a.u. and for proton impact

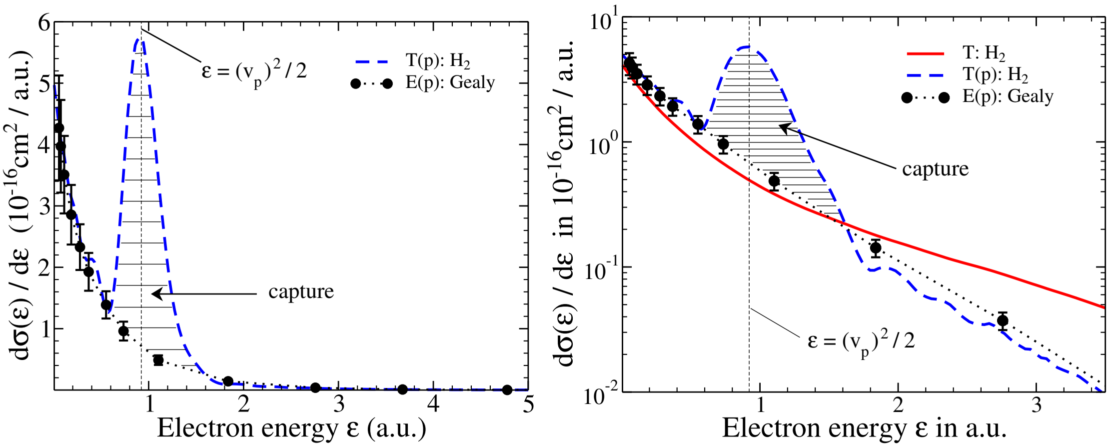

Figure 6.16.: *Electron-energy spectra curves $\mathfrak{s}(\epsilon) = d\sigma(\epsilon) \,/\, d\epsilon$ for p and $\bar{p}$ impact on H_2 as a function of the electron energy ϵ at $E = 48$ keV. Theory: dashed blue curve, p results for electron loss; solid red curve, $\bar{p}$ results for ionization. Experiment: filled circles, proton results for ionization only, Gealy et al. [169]. The energy ϵ of electrons with the velocity v_p is indicated by the vertical line. The hatched area corresponds to the capture cross section. The y axis of the left graph is linear while it is logarithmic in the right graph.*

energies from 48 keV to 310 keV. In general the values of $\mathfrak{s}(\epsilon, E)$ decrease for larger ϵ. However, the most striking feature of Fig. 6.14(b), in contrast to the case of antiproton impact, is the existence of local maxima of the curves $\mathfrak{s}(\epsilon)$ for a given impact energy E which are also visible in the contour plot on the bottom of the figure. The position of the peaks of $\mathfrak{s}(\epsilon, E)$ varies with the impact energy E. At the center of the maxima the ratios of the two energies E and ϵ are such that the classical velocities of the proton v_p and of the electron v_e are equal, i.e.,

$$\sqrt{\frac{2\,E}{M_p}} = v_p = v_e = \sqrt{2\,\epsilon}\,, \tag{6.12}$$

which can be reformulated in terms of energies as

$$\epsilon = \frac{E}{M_p} = \frac{1}{2}\,(v_p)^2\,, \tag{6.13}$$

where M_p is the proton mass. The accuracy of this statement is nicely demonstrated in Fig. 6.16 where the present $\mathfrak{s}(\epsilon)$ curve for protons with an impact energy $E = 48$ keV, i.e. $v_p = 1.3856$ a.u., is shown as dashed curve. The maximum of $\mathfrak{s}(\epsilon)$ is located at $\epsilon = \frac{1}{2}\,(v_p)^2 = 0.96$ a.u., also indicated by the vertical line.

The occurring maxima for proton impact can be explained with a simple picture of the electron-capture process where the electron is captured by the proton and moves basically with the momentum of the projectile. Therefore, the velocity of the captured electron relative to the H_2 molecule is given by the velocity of the projectile, namely the proton, as well as the electron velocity relative to the moving rest frame of the projectile. Since both contributions to the electron momentum can be oriented in different directions the peaks of the electron spectra $\mathfrak{s}(\epsilon)$ are centered around the energy ϵ which corresponds from the point of view of the ionized target to a free electron with the velocity of the projectile, cf. Eq. (6.13). It may be mentioned that the capture peaks get much less pronounced for higher impact energies. This is, first, due to the diminishing probability of capture for larger E and, second, due to a broader ϵ distribution of the captured electrons.

If the discussed maxima of $\mathfrak{s}(\epsilon, E)$ in Fig. 6.14(b) are removed one is left with a smoothly decreasing electron-spectra surface for increasing ϵ which is more similar to the one for antiproton impact in Fig. 6.14(a). This modified electron-spectra surface for proton impact may be interpreted as the one where the electron capture by the projectile is excluded. This issue is further examined in Fig. 6.16, where the present $\mathfrak{s}(\epsilon)$ curve for a proton impact energy $E = 48$ keV is compared with experimental data by Gealy *e*t al. [169] for which capture is excluded. The comparison shows that except for the ϵ regime where capture is a non-negligible process, i.e. $0.6 > \epsilon > 1.6$, the present results agree with the experimental data. The difference between the present and the experimental curve integrated over ϵ, i.e. the hatched area in Fig. 6.16, yields approximately 2.2×10^{-16} cm^2. It can be interpreted as an approximation of the capture cross section for $E = 48$ keV. Thereby, the theoretical capture cross section calculated by Shingal and Lin [170] of about $2 \times 10^{-16}\,\text{cm}^2$ is reproduced to a good extend. The reason for the structures of the present curve for energies close to the capture peak is not exactly known. Possibly, they originate from the finiteness of the numerical description.

For comparison the $\mathfrak{s}(\epsilon)$ curve for an antiproton with the same impact energy $E = 48$ keV is also shown in the right panel of Fig. 6.16. Obviously, no sign of electron capture is visible. The antiproton spectrum decreases more strongly for ϵ corresponding to electron velocities smaller than v_p and less strongly for larger ϵ in comparison to the experimental proton results. Clearly, it is energetically not favorable for the ejected electron to move in close vicinity to the antiproton, i.e. with the same velocity $\mathbf{v}_p$. Therefore, the use of a one-center expansion of the scattering wavefunction centered on the target is justified for antiproton collisions.

6.3. Production of H^+ in $\bar{p} + H_2^+$ and $\bar{p} + H_2$

The information on the H^+ production in $\bar{p}$ + $H_2{}^+$ collisions can be used for the interpretation of the H^+ production in $\bar{p}$ + H_2 collisions which was measured one and a half decades ago [35] but is still not understood theoretically. In Ref. [73], Sakimoto discussed the idea to use the concept of a two-step sequential ionization process to explain the measured $\bar{p}$ + H_2 data. This is in analogy to what was done by Janev *e*t al. [171] and Wehrman *e*t al. [50] in order to describe double ionization in $\bar{p}$ + He collisions using effective single-electron descriptions. The underlying idea is that in a first step the target is ionized and one electron is ejected. In a second step the projectile interacts with an ionic rather than a neutral target reducing the probability for double ionization.

It turned out that Wehrman *e*t al. were fairly successful with this independent-event model (IEV) [cf. Sec. 4.3.1] in reproducing the measured antiproton double-ionization cross section for He targets. As the probability for double ionization they used — in accordance with the IEV — the product of the single-electron ionization probabilities for He and He$^+$ P_{ion}^{He} and $P_{ion}^{\mathrm{He}^+}$, respectively.

Sakimoto, who proposed the possible use of a two-step model for the determination of H$^+$ production in $\bar{p}$ + H$_2$, was, however, not able to perform it quantitatively. As discussed in Sec. 6.1, he was lacking the excitation probabilities for $\bar{p}$ + ${H_2}^+$, since their "*calculation, requiring a wider range of impact parameters, would become extremely time consuming*" [73]. He argued that dissociative ionization, producing H$^+$ by ionization and excitation, also may occur. It is known to occur even much more frequently than double-ionization in electron and proton collisions with H$_2$ [172, 173]. With this argument he used his $\bar{p}$ + ${H_2}^+$ ionization data rather qualitatively in order to exclude for H$_2$ the simple interpretation of the two-step model used by Janev *e*t al. for He targets. In this work, however, a quantitative testing of the applicability of the two-step model, as used by Wehrman *e*t al. for double ionization of He, is performed with respect to the (measured) H$^+$ production in $\bar{p}$ impacts on H$_2$ molecules. Consequently, only transition probabilities from one-electron calculations are considered here.

6.3.1. $\bar{p}$ + H_2^+

In collisions of $\bar{p}$ with ${H_2}^+$ three main mechanisms lead to the production of H$^+$. First, ionization of the target,

$$\bar{p} + \mathrm{H}_2^+ \rightarrow \bar{p} + \mathrm{H}^+ + \mathrm{H}^+ + e^- \,, \tag{6.14}$$

second, electronic excitation followed eventually by dissociation,

$$\bar{p} + \mathrm{H}_2^+ \rightarrow \bar{p} + \mathrm{H} + \mathrm{H}^+ \,, \tag{6.15}$$

third, direct dissociation which is not included in the present approach. At very low energies the replacement of the electron by the $\bar{p}$ may also become important. However, these energies lie beyond the scope of the present work [158, 174]. As can be seen from Eqs. (6.14) and (6.15) two H$^+$ are produced in the ionization process while it is only one in the case of excitation. The cross section for H$^+$ production due to ionization and excitation is therefore given by the sum $2\sigma_{\mathrm{i}on} + \sigma_{exc}$. It follows from the present results (cf. Table .3 and Fig. 6.1) that the absolute contribution to this sum in $\bar{p}$ + ${H_2}^+$ collisions originates, however, only from a third to a quarter from ionization depending on whether the impact energy is close to or further away from the maximum, respectively.

6.3.2. $\bar{p}$ + H$_2$

While no experimental data are available for $\bar{p}$ + ${H_2}^+$ collisions, measurements of the ionization and the H$^+$ production cross sections have been performed for $\bar{p}$ + H$_2$ [35]. The present results obtained for $\bar{p}$ + ${H_2}^+$ collisions shall be used to learn more about the different production mechanisms of the measured H^+ cross section for $\bar{p}$ + H_2 which has not been explained theoretically so far. The analysis is done by applying the IEV as introduced in the introduction to this section. It was used by Wehrman *et* al. [50] for the description of double ionization in $\bar{p}$ + He collisions. In the IEV double ionization is considered as a two-step process and the cross section is obtained by using the product of transition probabilities from (effective) one-electron calculations only.

For the description of the first step the single-electron ionization probabilities $P_{\mathrm{i}on}^{\mathrm{H}_2}$ for $\bar{p}$ + H_2 are calculated using the one-center one-electron model potential $V_{\mathrm{m}od}$ for the description of the H_2 target which reproduces experimental and the two-electron calculation ionization and excitation data well for $E \geq 90$ keV and $E > 50$ keV, respectively.

In the second step $\bar{p}$ + $H_2{}^+$ collisions can contribute in two ways to the cross section for H^+ production (in contrast to $\bar{p}$ + He^+ in double ionization of helium). They are given in Eqs. (6.14) and (6.15) and are attributed to the probabilities $P_{\mathrm{i}on}^{\mathrm{H}_2^+}$ and $P_{\mathrm{e}xc}^{\mathrm{H}_2^+}$, respectively, where the probabilities are obtained as described in Sec. 6.1. Therefore, both cross sections, $\sigma_{\mathrm{d}i}$ for double ionization and σ_{ie} for ionization followed by excitation of an H_2 target,

$$\sigma_{\mathrm{d}i} = 2\,\pi \int P_{\mathrm{i}on}^{\mathrm{H}_2}(b)\, P_{\mathrm{i}on}^{\mathrm{H}_2^+}(b)\, b\, \mathrm{d}b\,, \tag{6.16}$$

$$\sigma_{\mathrm{ie}} = 2\,\pi \int P_{\mathrm{i}on}^{\mathrm{H}_2}(b)\, P_{\mathrm{e}xc}^{\mathrm{H}_2^+}(b)\, b\, \mathrm{d}b\,, \tag{6.17}$$

are considered in accordance with the IEV.

Furthermore, all doubly-exited electronic states of H_2 are in principle autoionizing. But it is also possible that the doubly-excited H_2 dissociates before an electron is ejected. The description of this channel is clearly very subtle and has been studied in detail with a considerable effort for the excitation of H_2 by photons [124, 175]. The double-excitation cross section σ_{de} for $\bar{p}$ + H_2 collisions,

$$\sigma_{\mathrm{de}} = 2\,\pi \int P_{\mathrm{e}xc}^{\mathrm{H}_2}(b)\, P_{\mathrm{e}xc}^{\mathrm{H}_2}(b)\, b\, \mathrm{d}b\,, \tag{6.18}$$

is approximated using the independent particle model (cf. Sec. 4.3.1 and Ref. [137]). The single-excitation probabilities $P_{\mathrm{e}xc}^{\mathrm{H}_2}$ for H_2 originate form the same calculations as the $P_{\mathrm{i}on}^{\mathrm{H}_2}$ used in Eqs. (6.16) and (6.17).

In Fig. 6.17 the results for $\sigma_{\mathrm{d}i}$ and σ_{ie} are presented together with the sum of these cross sections

$$\sigma_{\mathrm{H}^+} = 2\sigma_{\mathrm{d}i} + \sigma_{\mathrm{ie}}\,, \tag{6.19}$$

in which $\sigma_{\mathrm{d}i}$ is counted twice, since two H^+ are produced in the double ionization of H_2. Also given are the measured cross sections for the total H^+ production in $\bar{p}$ + H_2 by Hvelplund *et* al. [35] and for dissociative ionization for p + H_2 by Shah and Gilbody [67], where the latter includes besides $\sigma_{\mathrm{d}i}$, σ_{ie} also transfer ionization.

For all energies considered in Fig. 6.17 $\sigma_{\mathrm{d}i}$ lies below $\sigma_{\mathrm{i}e}$ by about a factor $\lessapprox 2$. Therefore, both mechanisms in the H^+ production as given in Eqs. (6.14) and (6.15) contribute with a comparable amount of H^+ in σ_{H^+}. Although the measured data for $\bar{p}$

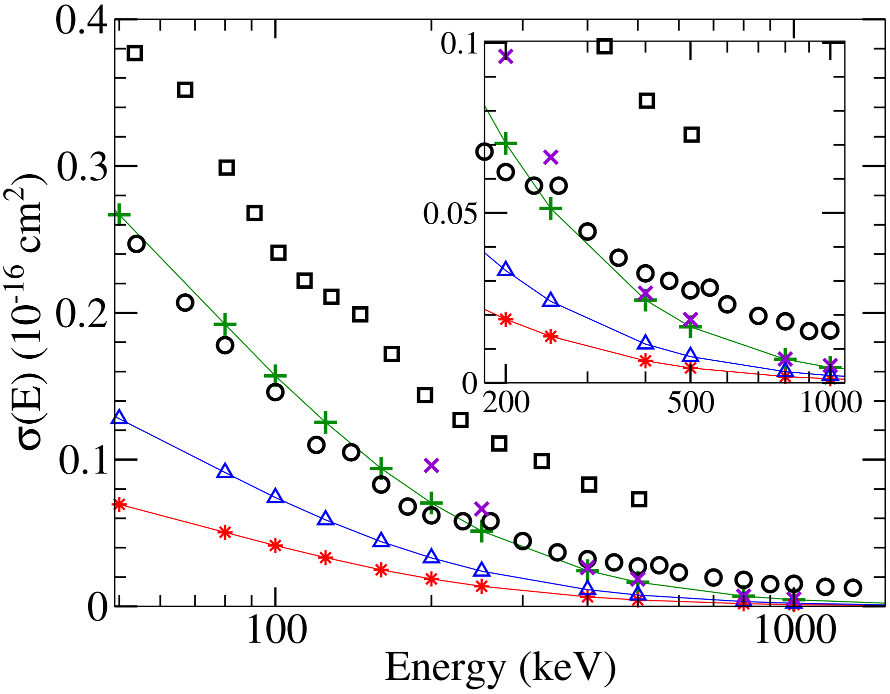

Figure 6.17.: *Cross sections leading to the production of H^+ in collisions with H_2 targets as a function of the projectile energy. $\bar{p}$ impact. Present results. $\bar{p}$: red stars, double ionization σ_{di}; blue triangles, ionization and excitation σ_{ie}; green plus, summed H^+ production $\sigma_{H^+}=2\sigma_{di}+\sigma_{ie}$. p: violet X, H^+ production σ_{H^+}. Experimental data: black squares, total H^+ production for $\bar{p}$ +H_2 [35]; black circles, dissociative ionization for p+H_2 [67]. The inset shows the high-energy part on an enlarged scale. Reproduced from [G].*

+ H_2 have a similar slope than the present σ_{H^+} the latter is shifted down relative to the experimental results by $\approx 10^{-17}$ cm^2 for the lowest and $\approx 6 \times 10^{-18}$ cm^2 for the highest energies in Fig. 6.17. The cross section for double excitation σ_{de} which is not included in σ_{H^+} is of the order of approximately 10% of σ_{H^+} in the whole energy range. This means that the three mechanisms for the production of H^+ described with the employed models are not sufficient in order to reproduce the experimental data of Hvelplund *et* al. [35]. The description of the dissociative ionization channel using additionally the product of the probabilities $P^{H_2}_{exc}(b)\,P^{H_2^+}_{ion}(b)$ in Eq. (6.18) increases σ_{ie} only by about a third (not shown here) and is therefore also not capable to resolve the discrepancy. Its inclusion may anyhow considered as an inappropriate interpretation of the examined model, since not every excitation of the H_2 molecule also results in an $H_2{}^+$ molecular cation in the first step.

Note, the curves given in Fig. 6.17 are calculated with the FC data presented before which implies that the internuclear distances of the $H_2{}^+$ is set to $R_{nuc} = 2.05$ a.u. Under the assumption that the time between the first and the second step in the IEV is too short to allow for a change of the internuclear distance the $\bar{p}$ + $H_2{}^+$ collisions are also calculated for $R_{\mathrm{nu}c} = 1.4478$ a.u. which is the expectation value of H_2. This leads to an increase of the binding energy and therefore to a decrease of the ionization and excitation cross sections of $\bar{p}$ + $\mathrm{H_2}^+$. Consequently, the results for $R_{\mathrm{nu}c} = 1.4478$ a.u., which are not shown in Fig. 6.17, become even smaller and reproduce those for $R_{\mathrm{nu}c} = 2.05$ a.u. from about 80% for $E = 50$keV to 90% for $E = 1000$ keV.

The experimental data for dissociative ionization in p + H_2 collisions by Shah and Gilbody also have a similar slope as the present results. Note, in contrast to the measured $\bar{p}$ data, their absolute values are comparable with those of the present σ_{H^+} for $\bar{p}$.

Additionally, σ_{H^+} results for p collisions with H_2 are calculated and shown in Fig. 6.17. They are obtained exactly in the same way as described for $\bar{p}$ impact only that the projectile charge Z_p in the interaction potential (cf. Eq. (3.7)) is set to +1 instead of -1 for $\bar{p}$. Although the present approach does not distinguish between ionization and electron capture by the proton, the p results are still meaningful for high energies, since the cross section for electron capture for p + H_2 is negligible for $E \geq 200$ keV [68, 69]. In general, the present data for $\bar{p}$ and p impact are very similar and practically the same for $E \geq 400$ keV both being close to the experimental proton results. This means that an obvious difference of the H^+ production between $\bar{p}$ and p impacts for high energies as measured experimentally and suggested by the double-ionization cross sections for He targets cannot be reproduced by the present study using the two-step model. An advanced treatment of the H^+ production in $\bar{p}$ + H_2 collision seems to be required. It should include at least a two-electron description of the target but also a more detailed consideration of the nuclear dynamics might be of importance especially in view of the important dissociative ionization channel.

Within the employed two-step model it might be crucial to consider an orientational dependence also for $P_{\mathrm{i}on}^{\mathrm{H2}}$ (as done in the present work for the two-electron calculations). That way, the probability $P_{\mathrm{i}on}^{\mathrm{H2}}$ should be multiplied first for each orientation individually with the probabilities for $\mathrm{H_2}^+$, as in Eqs. (6.16) and (6.17), and afterward orientationally averaged. Since the dependence on E of $P_{\mathrm{i}on}^{\mathrm{H2}}$ for the three orientations is similar to that of the $\mathrm{H_2}^+$ target as shown in Figs. 6.3 and 6.8 this might lead to a sizable effect on $\sigma_{\mathrm{d}i}$ and $\sigma_{\mathrm{i}e}$ and therefore also on σ_{H^+}.

Finally, it might be concluded that the application of the two-step IEV model as applied by Wehrman *e*t al. for double ionization of He in $\bar{p}$ collisions yields theoretical results which cannot reproduce the findings for H^+ production in $\bar{p}$ + H_2 collisions in a satisfactory way. Therefore, an advanced treatment of the $\bar{p}$ + H_2 collision seems to be necessary which includes at least a two-electron description of the target and might be performed with the present two-electron method in a future work. However, the dynamic motion of the nuclei allowing for dissociation during the collision may also be of relevance, which is only partly accounted for in the present method.

7. Stopping power

The passage of a particle through matter is determined by the stopping power of the medium. It is the change of the kinetic energy of the projectile per unit length in the stopping medium. The knowledge of the stopping power is needed in a number of applications concerning, e.g., cancer therapy, space exploration, radiation detectors and damage, etc. The stopping power is related to the energy loss of the projectile. Therefore, it is in principle well accessible in experiments by measuring the difference of the kinetic energy of the projectile before and after the target (see the schematic sketch in Fig. 4.2). The theoretical calculation of the stopping power is related to the determination of the ionization and excitation cross sections. However, the knowledge of the total cross sections is not sufficient. In fact, energy-resolved transition probabilities have to be weighted with the energies which are needed for the according transitions (see Sec. 4.2.3). This requires in particular a target description with a high density of continuum states. While this requirement can be fulfilled with moderate effort in the case of one-electron basis sets it becomes a rather challenging task in the case of two-electron descriptions. Therefore, in this work the calculation of the stopping power is performed employing only (effective) one-electron descriptions of the targets, i.e., using model potentials in the case of many-electron targets. The obtained results for the stopping powers are published in the Refs. [D-F]

The quantum mechanical formulation of the energy loss of fast charged particles in matter dates back to the theory by Bethe [74, 176]. He derived the so-called *stopping power* in the first-order Born approximation where it is proportional to the projectile charge squared Z_p^2. In Bethe's model, the stopping power $-dE/dx$ or energy loss per unit length of a charged particle with the velocity v can be written as

$$-\frac{dE}{dx} = n_T\, S(v) = n_T\, \frac{4\pi e^4 Z}{m} \frac{Z_p^2}{v^2}\, L(v) \tag{7.1}$$

where n_T is the density of atoms of atomic number Z in the stopping medium, m is the electron mass, and e is the elementary charge. $S(v)$ is the stopping cross section (related to the stopping power by n_T) and $L(v)$ is the velocity-dependent stopping number.

While Eq. (7.1), in which Z_p appears in quadratic form, works sufficiently well for high non-relativistic velocities, it was a surprise when it was found in an experiment that the range of negative pions was longer than that of positive pions of equal momentum. The existence of this phenomenon was later fully confirmed with negative and positive hyperons by Barkas *et* al. [177]. This so-called Barkas effect has been interpreted as a polarization effect in the stopping material depending on the charge of the projectile. It appears as the second term in the implied Born expansion of the energy loss and is proportional to Z_p^3. Following Lindhard [178], the stopping number may be expanded in a Born series in Z_p as

$$L(v) = \sum_{i=0}^{\infty} Z_p^i L_i(v)\,. \tag{7.2}$$

where L_0 ($S \propto Z_p^2$) is the Bethe term. The second term L_1 ($S \propto Z_p^3$) also referred to as Barkas correction is the first odd-order term in the Born series and reflects the asymmetry of the energy loss between charge-conjugated particles.

With the advent of the Low-Energy Antiproton Ring (LEAR) at CERN antiproton beams with improved quality at low energy became available, making an accurate comparison of stopping powers for antiprotons ($\bar{p}$) and protons (p) feasible. The first measurements were performed for solid silicon [75]. The $\bar{p}$ stopping powers $S^{\bar{p}}$ for various solid targets which where obtained in more recent experiments [179] at the Antiproton Decelerator (AD) were found to be smaller by 35-55% than those for p collisions and confirmed therefore an asymmetry between charge-conjugated projectiles. These measurements also strongly supported a proportionality of the stopping power to the velocity below the stopping maximum as expected for a point-like projectile.

Also at LEAR stopping powers for $\bar{p}$ in H_2 and He were measured by the OBELIX Collaboration [76, 79] for a kinetic-energy range of the $\bar{p}$ from about 0.5 keV to 1.1 MeV. In these experiments a focus was put on the investigation of the Barkas effect. The results indicate fundamental differences between $\bar{p}$ stoppings in the simplest gases (H_2, He) and in solid targets below some MeV [76–78] — calling for a thorough investigation of the involved stopping mechanism. Particularly, below the $\bar{p}$ stopping-power maximum no velocity proportionality could be observed. Above the maximum the stopping power $S^{\bar{p}}$ for $\bar{p}$ collisions was claimed to be even larger than for p impact (S^p) with a difference $S^{\bar{p}} - S^p$ of 21% ±3% and 15% ±5% around a kinetic energy of 600 keV for H_2 [77] and 700 keV for He [78], respectively. In a very recent effort [180] the measured He data [76] were reconsidered. After an extended analysis of the data it was claimed that a part of the antiprotons must have been reflected by the wall of the experimental gas vessel in order to bring the simulated results in accordance with the experimentally measured data. A sizeable influence of this newly considered reflection process on the previously analyzed stopping power is, however, not expected by these authors [181]. Although the data were taken more than a decade ago theoretical investigations have not been able to fully reproduce the experimental findings concerning the slowing down of the antiprotons; especially for H_2 targets.

Approximately at the same time experiments for negatively charged muons (μ^-) stopping in H_2 and He gases were performed at the PSI[a] [80–82]. In these experiments basically the excitation cross sections were determined by measuring the time-distribution of the scintillation light emitted from the excited targets during the slowing down of the projectile. In order to obtain the muon stopping power S^{μ^-} from the measured data also experimental $\bar{p}$ ionization cross sections and experimental and theoretical data for the mean energy transfer for ionization and excitation of the target were used. In contrast to the $\bar{p}$ results S^{μ^-} was found to stay below S^p for energies above the stopping maximum

---

[a] Paul Scherrer Institute, Switzerland

$E > E_{\mathrm{max}}$. However, in the analysis of the μ^- data it was assumed that for fast particles with a velocity $v \geq 0.1\,c$ (corresponding to an antiproton energy of approximately 4.7 MeV) the Bethe-Bloch stopping formula is valid. In a more recent measurement for μ^- in an H_2 gas target performed by the same authors the stopping power was measured directly [83]. The results also stay below the proton stopping power for $E > E_{max}$. Although the uncertainties of the latter experiment are considerably larger than those in [80–82] (and thus its results are not discussed quantitatively here) these uncertainties are caused by totally different systematic errors than in the earlier muon experiments providing therefore results which are independent of the earlier findings.

Except for deviations at small projectile velocities v the total $\bar{p}$ and μ^- stopping powers should be the same at a given v, $S^{\mu^-}(v) = S^{\bar{p}}(v)$. The deviations among the experimental results are, however, of the order of 20% indicating the experimental difficulties and uncertainties.

On the other hand, differences can be expected between projectiles with different charges Z_p as, e.g., antiprotons and protons [182, 183]. From Eqs. (7.1) and (7.2) as well as the discussed experimental evidence it is apparent that higher-order terms in Z_p will be present in an exact calculation of the stopping power. In order to highlight the Barkas effect and also higher-order terms L_i in S it is common to determine the relative stopping power for particles and their antiparticles defined as

$$\frac{\Delta S}{S} = \frac{S^p - S^{\bar{p}}}{S^p}\,. \tag{7.3}$$

Using Eqs. (7.1) and (7.2) Eq. (7.3) can be rewritten as

$$\frac{\Delta S}{S} = \frac{2Z_pL_1 + 2(Z_p)^3L_3 + \ldots}{L_0 + Z_pL_1 + (Z_p)^2L_2 + \ldots} \tag{7.4}$$

showing that the difference depends only on odd terms. In the case that higher-order terms are insignificant $\Delta S\,/\,S$ becomes approximately proportional to the Barkas term L_B. Then the first-order correction L_B can be approximated, using Eqs. (7.1) and (7.4), by

$$L_B = L_1\,(Z_p)^2 \approx \sum_{i=0}^{\infty} L_{2i+1}(Z_p)^{2i} = \frac{1}{8\pi(Z_p)^3Z}\,v^2\Delta S\,. \tag{7.5}$$

Strictly speaking, L_B as approximated in Eq. (7.5) is equal to the correction to the stopping number due to the sum of all odd terms L_{2i+1}, since the projectile charges considered in this work have the absolute value $|Z_p| = 1$. Therefore, L_B can also be considered, if the condition that L_1 is the dominant odd contribution is not fulfilled. Though, in that case it might not be appropriate to call L_B Barkas term.

7.1. Hydrogen and helium

A peculiarity in the context of antiproton scattering and in particular for the stopping power is the fact that in the case of hydrogen targets all experiments were done for *molecules* while the theoretical description on the other hand concentrates mainly on *atomic* targets [84–87]. The evident deviations between the theoretical atomic and experimental molecular hydrogen results for $S^{\bar{p}}$ were therefore claimed to origin from molecular effects [84–86]. The naive picture of an H_2 molecule as being basically the same as two individual H atoms has been shown in this work (cf. Refs. [B,H]) to be inadequate for the type of collision processes considered here. It is one aim of the present work to treat the *atomic* and *molecular* hydrogen targets separately in order to figure out the differences and also to compare directly to the experimental findings. The H_2 molecule and the He atom are described here with the effective one-electron model potential which is discussed in detail in Sec. 2.2 (see Ref. [C]) and already applied for the determination of ionization and excitation cross sections for $\bar{p}$ + H_2 collisions in Sec. 6.2.1 (cf. Refs. [B,E]). Also, the incongruity among the experimental results is discussed in view of the present findings. Possible deficiencies of the used model description in connection to the stopping power are discussed using the He target which is studied more rigorously theoretically as well as experimentally.

The present results are calculated with a basis set qualitatively similar to that used for alkali-metal atoms in Sec. 5.1 including orbitals with angular momenta up to $l = 7$. An energy cutoff for the continuum states of 250 a.u. was used leading to about 260 B-spline functions per angular momentum. The interaction potential V_{int} in Eq. (3.7) causes l and m_l mixing. However, in order to reduce the numerical effort only orbitals with magnetic quantum numbers $|m_l| \leq 3$ are taken into account as was systematically discussed in Sec. 5.1.1 and Ref. [A]. Exploiting the symmetries of the collision system the time-dependent scattering wavefunction Ψ was expanded in a total number of 6540 states. All parameters given above are checked thoroughly in convergence tests.

As a result of this study it is found that especially a sufficiently high energy cutoff and density of continuum states also at large state energies are of importance for converged results. This is somehow contrary to what is expected for ionization cross sections. However, an insufficient choice of both parameters influences the final stopping power

Table 7.1.: *Convergence with respect to the energy cutoff ϵ of the ionization cross section σ_{ion} and the contribution to the stopping power S_{ion} caused by ionization for 3.2 MeV antiproton collisions with H_2. Four different values for the energy cutoff are given which are sufficient to recover the final result (with a cutoff energy of 250 a.u.) within the given relative accuracy.*

degree of recovery of final value (%)	energy cutoff ϵ σ_{ion} (a.u.)	 S_{ion} (a.u.)
90	1.8	29.0
95	3.2	63.5
97	4.8	96.5
99	11.3	155

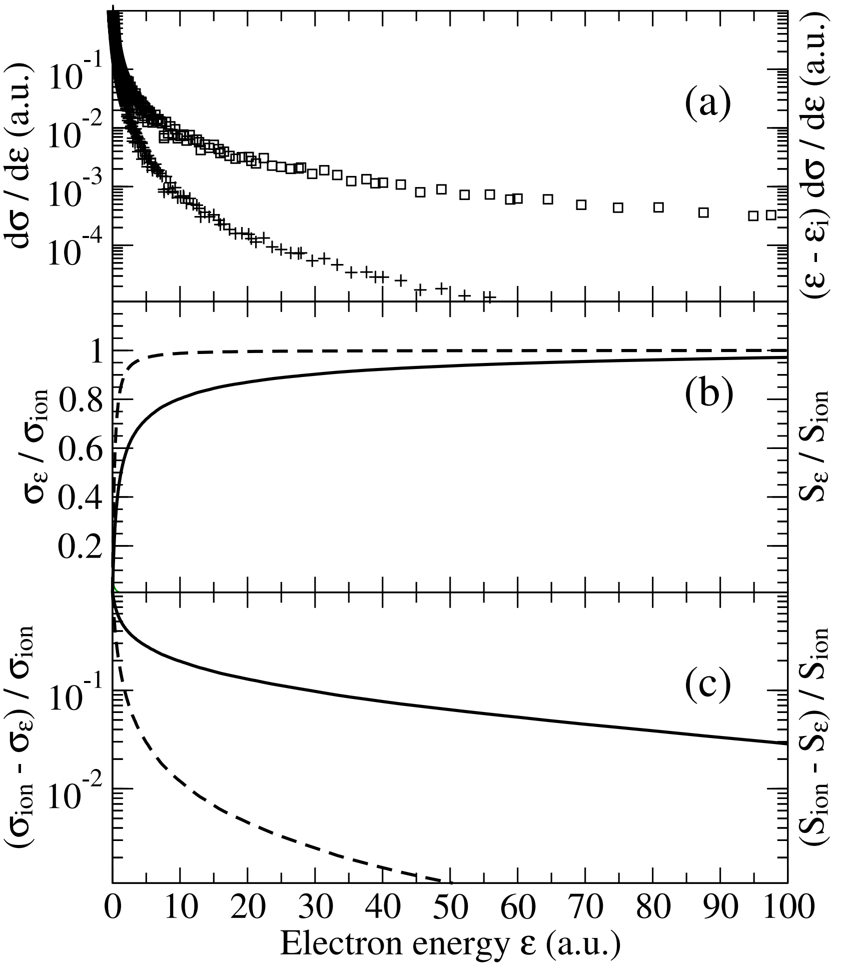

Figure 7.1.: *Convergence behavior of σ_{ion} and S_{ion} with respect to the energy cutoff of the basis. The results are given for 3.2 MeV antiproton collisions with H_2. (a) Electron energy spectrum $\mathfrak{s}(\epsilon) = d\sigma\,/\,d\epsilon$ [see Eq. (4.14)], pluses; electron energy spectrum multiplied with the energy required for the excitation $(\epsilon - \epsilon_i)\ d\sigma\,/\,d\epsilon$ [see Eq. (4.17)], squares. (b) Ratio $\sigma_\epsilon\,/\,\sigma_{ion}$ of the ionization cross sections with an energy cutoff ϵ to the one with the cutoff 250 a.u. (– –); ratio $S_\epsilon\,/\,S_{ion}$ of the stopping power caused by ionization with an energy cutoff ϵ to the one with the cutoff 250 a.u. (—). (c) Deviation from unity of the curves presented in (b).*

differently which may even lead to some kind of compensation. A too small energy cutoff results in a too small stopping power while an insufficient density of continuum states, on the other hand, led in the present study to a larger stopping power.

Figure 7.1 illustrates the convergence of, first, the contribution to the stopping power caused by ionization S_{ion} [cf. Eqs. (4.17) and (4.40)] and, second, the ionization cross section σ_{ion} with respect to the energy cutoff of the employed basis. The results are calculated for 3.2 MeV antiprotons colliding with H_2. In Fig. 7.1(a) it can be seen that the electron energy spectrum $\mathfrak{s}(\epsilon) = \mathrm{d}\sigma/\mathrm{d}\epsilon$ decreases much faster for increasing ϵ than the product $(\epsilon - \epsilon_i) d\sigma/d\epsilon$ which is the integrand of S_{ion} in Eq. (4.17). Therefore, the contribution to the stopping power caused by ionization converges much slower with respect to the cutoff energy of the basis than the ionization cross section, as becomes obvious from Fig. 7.1(b). Here, the quantities σ_ϵ and S_ϵ take all transitions into final states ψ_f of the used basis set with positive $\epsilon_f \leq \epsilon$ into account. Figure 7.1(c) shows how much σ_ϵ and S_ϵ deviate from their final value (obtained including all ψ_f with $\epsilon_f \leq 250$ a.u.), if the cutoff energy is chosen as ϵ. In table 7.1 those cutoff energies are given which recover the final values of σ_{ion} and S_{ion} obtained with a cutoff of 250 a.u. within 90, 95, 97, and 99%. Figure 7.1(c) and table 7.1 clearly show the different convergence behaviors of σ_ϵ and S_ϵ with respect to the cutoff energy. While the ionization cross section is converged within approximately 1% with a cutoff of 10 a.u. in the case of S_{ion} a convergence within 3% is only achieved with an cutoff of around 100 a.u.

Obviously, this slow convergence behavior of S_{ion} becomes more pronounced for higher impact energies, since the relative population of high-lying continuum states increases. This leads to a less steep fall-off of the electron energy spectra as is discussed in Sec. 2.2 and [B]. On the other hand, for lower impact energies a smaller energy cutoff is sufficient, since the electron energy spectra fall off steeply for $\epsilon \geq \frac{1}{2}(2v)^2$ corresponding to the maximally transferred energy in a classical collision [B].

Calculations are performed for $\bar{p}$ collisions with the three targets H, H_2, and He. The obtained data for the stopping power are given in numerical form in the appendix in Table .6. In the following the findings of all three targets will be separately discussed and compared with literature data.

7.1.1. Stopping power: $\bar{p}$ + H

The stopping power for atomic hydrogen is shown in Fig. 7.2 as a function of the equivalent antiproton impact energy. The equivalent antiproton energy can be obtained by multiplication of the impact energy with the factor $m_{\bar{p}}/M_p$, where $m_{\bar{p}}$ and M_p are the masses of an antiproton and the considered projectile, respectively. The factor for μ^- projectiles is accordingly $m_{\bar{p}}/m_{\mu^-} \approx 8.880$. Since no experiments have been performed for the stopping power of atomic hydrogen targets so far, the present results are compared to various theoretical calculations for $\bar{p}$ and μ^- impact. The stopping power for hydrogen atoms is preferably used for the testing of a theoretical approach, since the target description is well known and in principle no approximations are needed. A detailed analysis of S for H and He was done by Schiwietz *et* al. [84] comparing three different approaches, namely, an atomic-orbital (AO), a distorted-wave (DW), and an adiabatic-ionization (AI) description. Due to the inherent approximations of the AI — adiabatic collision — and the DW — interaction in first order — approaches they are basically low-energy and high-energy methods, respectively. Their advantage over the AO method, which treats the interaction in infinite order (cf. Secs. 3.1 and 3.3), is based on their comparably small numerical effort. The AI and DW results describe the stopping power reasonably for $E < 20$ keV and $E > 100$ keV, respectively. Note, the use of the DW method leads to a clearly different position and height of the stopping maximum compared to the AO method and the AI curve does not show any maximum

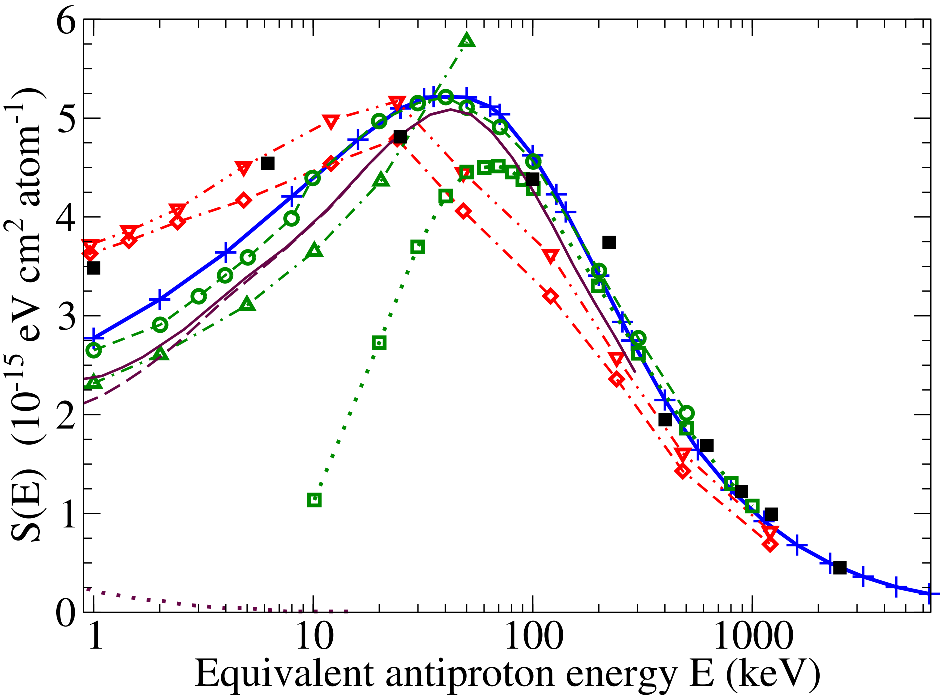

Figure 7.2.: *Energy-loss cross section $S(E)$ for H targets as a function of the equivalent antiproton impact energy E. **T**heory. Present results: blue solid curve with plus. Schiwietz et al. [84]: green dashed curve with circles, atomic orbital (AO); green dash–dotted curve with triangles up, adiabatic-ionization (AI); green dotted curve with squares, distorted wave (DW). Cabrera-Trujillo et al. [85]: violet thin solid curve, total S; violet long dashed curve, electronic S; violet dotted curve, nuclear S. Custidiano and Jakas [86]: black squares, CTMC for $\bar{p}$. Cohen [87]: red dash–doubly-dotted curve with triangles down, CTMC (CL) for μ^-; red doubly-dash–dotted curve with diamonds, quantum-classical CTMC (QC) for μ^-. Reproduced from [F].*

at all. The present findings, which are also based on an atomic-orbital approach, are in good agreement with the AO results, except for the regime 2 keV $< E <$ 8 keV where a small discrepancy exists. From the comparison to the AO results it is assumed that the present method is correctly implemented.

The electron-nuclear dynamics (END) theory, which is based on the application of the time-dependent variational principle to the Schrödinger equation using a coherent state representation of the wave function, was employed by Cabrera-Trujillo *et* al. [85]. This method allows for the simultaneous determination of the electronic and nuclear stopping power. The latter is small for all surveyed projectile energies and completely negligible for $E >$ 10 keV. The END results for the electronic stopping power show a similar behavior like both AO calculations but predict throughout lower values. These three curves share in particular the position of the maximum at around $E_{max} \approx 40$ keV and similar slopes for energies below and above E_{max}.

The Classical Trajectory Monte Carlo (CTMC) method was recently employed by Custidiano and Jakas [86] in order to determine $S^{\bar{p}}$ and earlier already by Cohen [87] for S^{μ^-}. Both calculations agree for high energies $E > 200$ keV with the AO, DW, and END results but differ from them below the stopping power maximum sharing the same slope. While the CTMC results for $S^{\bar{p}}$ follow the trend of the AO and END curves down to about 20 keV the S^{μ^-} results by Cohen show a different behavior in the energy range around E_{max}. Besides the purely classical CTMC (CL) Cohen also provided a quantum-classical analysis (QC) of his data. They differ mainly in the vicinity of E_{max} where the CL results are closer to the END and AO curves than those from the QC analysis. It was shown in [86] that for low impact energies $E < 30$ keV the CTMC stopping power depends considerably on the eccentricity of the initial classical electron orbits. The similar behavior of all CTMC results below 30 keV may be caused by the fact that Custidiano and Jakas followed a procedure for preparing initial conditions which had been described by Cohen.

Finally, it is possible to conclude that the present findings for H targets agree well with the other AO calculation and share the same behavior than the END results. For all other approaches considered here the energy range in which they are applicable is limited to energies around and above the stopping maximum $E \gtrapprox E_{max}$ except for the AI method which gives, on the other hand, reasonable results below the maximum.

7.1.2. Stopping power: $\bar{p} + H_2$

In Fig. 7.3 the $S(E)$ for H_2 targets is shown as a function of the equivalent antiproton impact energy. The present data are calculated for a fixed internuclear distance $R_{nuc} = \langle R_{nuc} \rangle = 1.4487$ a.u. of the two nuclei as proposed in Refs. [112] and [B]. The consideration of isotopes of hydrogen molecules leads to a slightly different $\langle R_{nuc} \rangle$ [167]. The effect on the stopping power for different R_{nuc} in the range 1.4 a.u. $\leq R_{nuc} \leq$ 1.5 a.u. has been found in this work to be only of quantitative form and largest around the stopping maximum where the deviation is of the order of 1.5%.

In contrast to the hydrogen atom four experiments have been performed for H_2 whereas the author is only aware of a single calculation in the molecular case by Schiwietz *et* al. [84] employing the AI method in which the H_2 molecule was described in a quasiatomic way with an effective scaled charge. Within an IPM the effective charge was chosen in such a way that the total electronic energy of the molecule at its equilibrium internuclear distance is reproduced.

It is evident from Fig. 7.3 that the experimental results for $S^{\bar{p}}$ by Adamo *e*t al. [79] and by Agnello *e*t al. [76] as well as for S^{μ^-} by Hauser *e*t al. [81] all differ considerably. For high energies $E > 200$ keV the findings for $\bar{p}$ impact by Adamo *e*t al. and μ^- impact are very similar. At energies below the maximum the S^{μ^-} are closer to the more recent $\bar{p}$ results by Agnello *e*t al. The maxima of the three experimental curves [79], [76], and [81] are situated approximately at the equivalent antiproton energies $E_{max} \approx 45$ keV, 100 keV, and 75 keV, respectively. While the maxima of both $S^{\bar{p}}$ curves are of comparable height the maximum of S^{μ^-} lies well below those two.

It should be noted that the experimental curves shown here are the best fit results

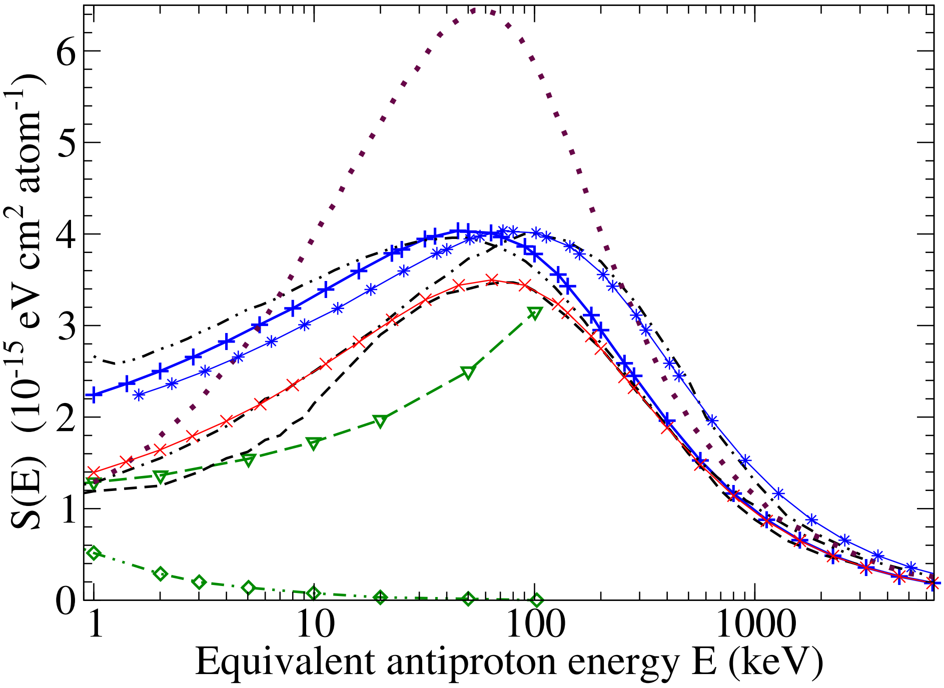

Figure 7.3.: *Energy-loss cross section $S(E)$ for H_2 targets as a function of the equivalent antiproton impact energy E.* ***T****heory. Present results: blue solid curve with plus, R_{nuc}=1.4487 a.u.; blue thin solid curve with stars, E scaled by a factor 1.6 (see text); red thin solid curve with x, double ionization excluded (see text). Schiwietz et al. [84]: green dashed curve with triangles down, adiabatic-ionization (AI); green dash–doubly-dotted curve with diamonds, nuclear stopping.* ***E****xperiment. $\bar{p}$: Agnello et al. [76], black dash–dotted curve; Adamo et al. [79], black dash–doubly-dotted curve. μ^-: Hauser et al. [81], black dashed curve. p: Andersen and Ziegler [182], brown dotted curve. Reproduced from [F].*

from an analysis of the measured data. The order of the uncertainties was estimated in [76] to amount to ±10%. In the case of the μ^- results the uncertainties vary from ±10% for impact energies in the vicinity and above $E_{\max}$ and increase up to ±50% for decreasing E. Furthermore, in the μ^- experiments basically only the excitation cross section was determined as stated already in the introduction of this chapter. The shown S^{μ^-} results depend therefore also on additional data which were taken from literature. The experimental $\bar{p}$ ionization cross sections σ_{ion} [38] used in order to determine S^{μ^-}, however, were later on found to be erroneous for $E < 200$ keV [35, 157].

Due to these substantial uncertainties it is one aim of this work to discriminate with the help of the present findings between the different experimental results. For $E > 200$ keV the present results are in good agreement with the μ^- data and the $S^{\bar{p}}$ by Adamo *et* al. While the latter curve has a similar behavior like the present calculations also in the vicinity and below the maximum the former S^{μ^-} curve deviates clearly for $E < 200$ keV. The $S^{\bar{p}}$ curve determined by Agnello *et* al. is on the other hand not compatible with the present data. While the heights of both maxima are very similar it appears as if the experimental curve is shifted to larger energies. A simple scaling of E by a factor of 1.6 between the present and the experimental $\bar{p}$ data by Agnello *e*t al. as suggested in [E] can, however, not be verified in view of this more detailed investigation. The scaled curve which is also shown in Fig. 7.3 clearly deviates from the measured data for the highest energies. On the other hand, it is the scaled curve which looks most similar to the one for $S^{\bar{p}}$ by Agnello *e*t al. for impact energies around and above the stopping maximum. The good agreement of the excitation and ionization cross sections determined with the model potential and the full two-electron calculations especially at high energies [H] makes it very likely that the experimental stopping curve by Agnello *e*t al. is too large for $E > E_{\max}$. Also, at these energies one-electron processes are clearly dominating which are mimicked well by the effective one-electron H_2 model.

On the other hand, it is known that the IPM overestimates the two-electron processes like double ionization (e.g., [50]). This is also observed in other application of the employed model potential [C]. Single excitation and single ionization are, however, reasonably well described in comparison to the full two-electron calculation especially for $E > 50$ keV (see Sec. 6.2.1 and Ref. [H]). Therefore, the present stopping power without the contribution from double ionization S^{sin} has also been analyzed by using the difference between Eq. (4.37) and Eq. (4.39) instead of the total S given by Eq. (4.37). The qualitative behavior of the present curves for S and S^{sin} is similar due to the fact that both curves originate from the same calculation. The quantitative difference on the other hand increases for low impact energies. While the relative difference is below 1% for $E > 1500$ keV it is larger than 10% for $E < 100$ keV and finally becomes as large as one third for $E = 2$ keV. In the validity range of the used model this curve can be interpreted as a lower bound to the stopping power. For $E > 40$ keV S^{sin} matches the experimental S^{μ^-} while for $E < 25$ keV the experimental data by Agnello *e*t al. are reproduced by S^{sin}. Unfortunately, the author is not aware of any independent and reliable data for double ionization cross sections for low-energy $\bar{p} + H_2$ collisions. These would allow for a rough quantitative estimate of the uncertainties due to the use of the IPM for impact energies below 100 keV. However, a further series of calculations of the stopping power at intermediate to low energies using the present molecular two-electron description would despite its computational demands obviously be of high value in order to clearly discriminate between the experimental curves at low energies. These calculations together with an extension of the extraction of stopping powers also for two-electron targets are therefore regarded as the most urgent future work to be done within the developed approach.

The other theoretical curve calculated by Schiwietz *e*t al. shows a similar dependence on E like the AI results in the case for atomic H targets. It agrees with the measurements of $S^{\bar{p}}$ by Agnello *e*t al. and of S^{μ^-} by Hauser *e*t al. for $E < 5$ keV but differs clearly for $E > 10$ keV from all other curves. The nuclear stopping power also calculated by Schiwietz *e*t al. [84] is again small in the considered energy regime but considerably larger than the END results in the case of atomic H.

A comparison to the stopping power for p impact shows a maximum at $E \approx 60$ keV which is about 60% larger than the present value for $S^{\bar{p}}$. Note that all curves in Fig. 7.3 lie below the p results for energies larger than E_{max} except for $S^{\bar{p}}$ determined by Agnello *e*t al. At high energies all curves converge to the p results showing a $1/v^2$ dependence of S as expected from Bethe theory [cf. Eq. (7.1)]. Below the maximum only the present curve and the one by Adamo *e*t al. cross the p curve for $E > 1$ keV resulting in a change of the sign of the Barkas term.

7.1.3. Stopping power: $\bar{p}$ + He

In contrast to hydrogen, data of more than one experimental *and* theoretical approach exist for He targets. They are shown in Fig. 7.4 together with the present findings and the experimental results for p impact. For $\bar{p}$ + He collisions also the ionization cross section $\sigma_{\mathrm{i}on}$ is experimentally and especially theoretically well studied (cf. [160] and references therein) making it a good candidate for the comparison of different approaches.

The experimental curves for $\bar{p}$ and μ^- stopping in He gases exhibit a behavior similar to the one of the H_2 target measured by the same groups which are shown in Fig. 7.3. The stopping maximum is approximately 25% higher for He than for H_2. Again the experimental $S^{\bar{p}}$ by Agnello [76] *e*t al. is larger than the p results by Andersen and Ziegler [182] above the stopping maximum while the measured S^{μ^-} by Kottmann [80] stays below the p curve for all energies considered here.

As for the atomic H target Schiwietz *e*t al. [84] applied the AI, AO, and DW methods to calculate the He stopping power. The AI curve shows a functional dependence on E analogous to the one observed for H and H_2 targets. That is, for small E it is generally in accordance with the two experimental $S^{\bar{p}}$ and S^{μ^-} curves while it seems not to be applicable for $E > 20$ keV. The DW results fully agree with the experimental S^{μ^-} for $E > 300$ keV but fall off much faster below the stopping maximum for $E < 50$ keV. Exactly the same behavior was observed for $\sigma_{\mathrm{i}on}$ calculated earlier by Fainstein *e*t al. [184] also using a DW method which again coincides with the $\sigma_{\mathrm{i}on}$ resulting from the DW calculations by Schiwietz *e*t al. [84]. Although first measurements of low-energy ionization for $\bar{p}$ + He collisions [34, 35] fully confirmed this steep fall off of $\sigma_{\mathrm{i}on}$ below the ionization maximum, a recent more accurate experiment was able to clearly contradict this trend [160] in favor of a less steep decrease of $\sigma_{\mathrm{i}on}$ below the maximum. The S results calculated by Schiwietz *e*t al. using the AO and the DW method fully agree with each other for $100\ keV < E < 200\ keV$ both having a maximum value lying in between the two experimental curves at $E \approx 100$ keV. This is somehow different from the case of atomic H targets where the height and position of the AO and DW stopping maxima clearly differ (see Fig. 7.2). Below the maximum, however, the two curves diverge with decreasing E. The AO results stay above the DW and the experimental data with deviations increasing to more than 50% for $E < 5$ keV. These deviations of the AO results were explained by the use of a model treating one active electron in the effective potential of the heavy nucleus and a static density distribution of the second inactive electron which screens the nucleus [84]. In the adiabatic limit of the AO model for He no ionization threshold exists for $R \to 0$ as is known for an H atom (also referred to as Fermi-Teller radius). This is, however, in contrast to a full two-electron treatment of a He atom which leads for $R \to 0$ to a finite ionization threshold of ≈ 0.7 eV due to the fact that the electron density is changed dynamically when the $\bar{p}$ approaches the

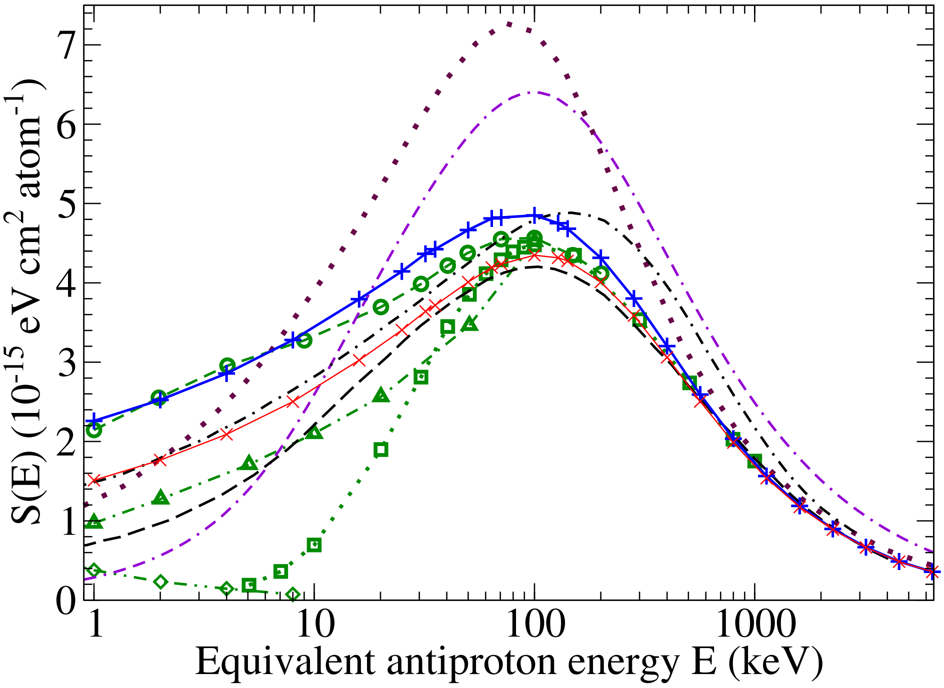

Figure 7.4.: *Energy-loss cross section $S(E)$ for He targets as a function of the equivalent antiproton impact energy E.* ***T****heory. Present results: blue solid curve with plus; red thin solid curve with x, double ionization excluded (see text). Schiwietz et al. [84]: green dashed curve with circles, atomic orbital (AO); green dash–dotted curve with triangles up, adiabatic-ionization (AI); green dotted curve with squares, distorted wave (DW); green dash–doubly-dotted curve with diamonds, nuclear stopping. Basko [185]: violet doubly-dash–dotted curve, low-velocity Bohr (LVB).* ***E****xperiment.* $\bar{p}$ *: Agnello et al. [76], black dash–dotted curve.* μ^- *: Kottmann [80]: black dashed curve. p: Andersen and Ziegler [182], brown dotted curve. Reproduced from [F].*

nucleus. Therefore, the AO results were expected to overestimate the ionization cross section and consequently also the stopping power for low E [84].

The present results for S coincide with the experimental S^{μ^-} and theoretical DW data for high energies $E > 500$ keV, but become considerably larger for $E < 200$ keV. As for the H_2 target the maximum of the present He curve has the same height as the $S^{\bar{p}}$ measured by Agnello *et* al. and it is situated around 100 keV as predicted by the AO and DW methods. Below the stopping maximum the present data are, however, much larger than the experimental $S^{\bar{p}}$ and S^{μ^-} and theoretical AI results. The present calculations are, on the other hand, basically in agreement with the AO data for low energies. Therefore, it may be concluded that the deviations of the present findings at low energies also originate from deficiencies of the employed effective one-electron model which leads to substantial changes of the ionization potential in the adiabatic limit as is the case for the AO model. Due to the existing uncertainties of experimental and theoretical results, especially for low energies, it is, however, not possible to finally conclude on the exact behavior of the stopping power in this energy range. On the other hand, the error of the measured S^{μ^-} curve could be reduced drastically, if a point at low energies could be fixed safely [80]. In this context it would be valuable to perform a calculation using a full two-electron description of the target, as already stated in the case of $\bar{p}$ + H_2 collisions, in order to eliminate the uncertainties connected so far with both AO approaches using effective one-electron models.

As has been done for H_2 the stopping power excluding double ionization S^{sin} has also been analyzed for He targets. The present S and S^{sin} curves are again qualitatively similar while quantitative differences increase for lower impact energies. For low impact energies the relative contribution from double ionization to S is slightly smaller than in the case of H_2 while it is the other way round for high energies. It is interesting to note that these relative contributions correspond roughly to the ratios of cross sections for double and single ionization in the IPM (e.g., [50]) multiplied by two. The factor two accounts for the energy of both electrons involved in the double ionization. The S^{sin} curve lies above the experimental data for μ^- for $E < 400$ keV indicating that the measured results might be too small. For $E < 25$ keV S^{sin} describes the experimental $\bar{p}$ data reasonably as is the case for H_2 pointing out that the contribution of double ionization in the present S data is too large especially at low energies.

As in the case of $\bar{p}$ + H_2, the two-electron approach in this work, but also a number of other advanced calculations, e.g. [51, 58, 162], for the ionization cross sections of $\bar{p}$ + He collisions allow for a rough estimate of some of the uncertainties of the presented He stopping results stemming from the target model and the use of the IPM. Furthermore, these calculations may also allow for an attempt to estimate an corrected value of S at low impact energies. According to Sec. 5.2 the cross section for single ionization obtained with the model potential V_{mod} is in good agreement with experiment for $E > 40$ keV but becomes increasingly too large for smaller impact energies due to the reasons discussed above. The cross section for double ionization depends quadratically on the single-electron ionization probability within the IPM. However, double-ionization cross sections obtained with the IPM are known to overestimate the measured data (cf., e.g., [50]). In the following, the averaged energy transfer is assumed to be described correctly. Then the stopping power depends linearly on the cross sections. Under this assumption the correct contribution to the stopping power due to double ionization may be roughly approximated as being only 50%, 43%, and 30% of the difference $S - S_{sin}$ for the three energies 200, 100, and 25 keV, respectively. For $E = 25$ keV the single-ionization cross section of the present full two-electron calculation is approximately 10% smaller than the one obtained with V_{mod}. For this energy a value of the present stopping power which includes all mentioned assumptions and corrections may be therefore roughly approximated with 3.3 10^{-15} eV cm^2 per atom. This value lies slightly below the curve for S_{sin} by what the significance of S_{sin} might be increased. Although no quantitative estimate has been done in the discussion for H_2 targets it might be expected that the correction is qualitatively similar to that performed for He. Note, the contributions due to excitation have not been changed in this simple estimate. The discussion on possible corrections obviously shows the need for further calculations of the stopping power using full the two-electron description of the H_2 and He targets in order to improve

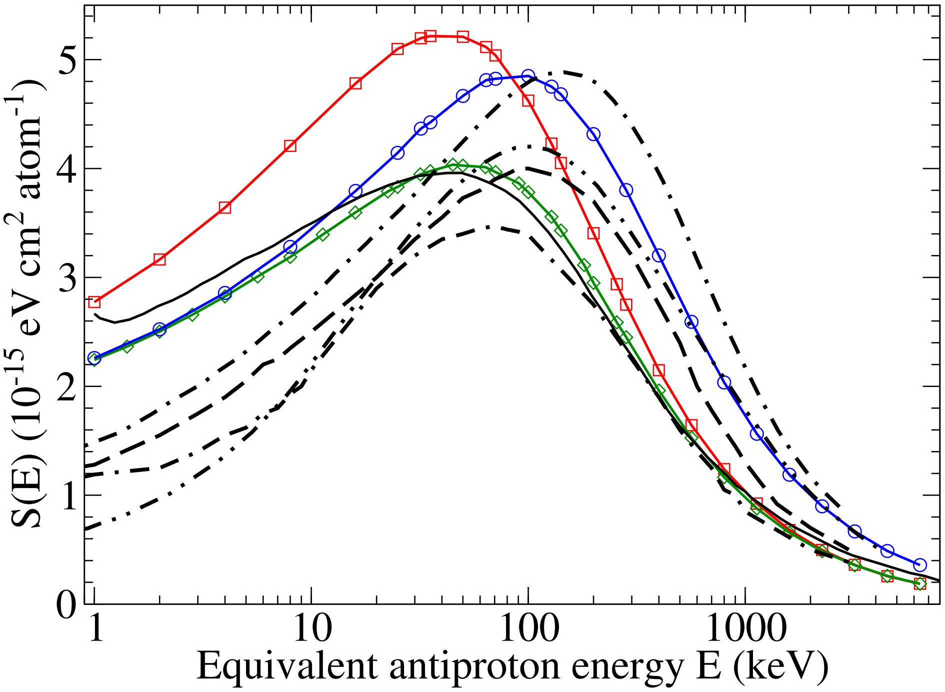

Figure 7.5.: *Comparison of the energy loss cross sections $S(E)$ for H, H_2, and He targets as a function of the equivalent antiproton impact energy E.* ***T****heory. Present results: red solid curve with squares, H; green solid curve with diamonds, H_2; blue solid curve with circles, He.* ***E****xperiment. H_2: black solid curve, Adamo et al. [79], $\bar{p}$; black dashed curve, Agnello et al. [76], $\bar{p}$; black doubly-dash–dotted curve, Hauser et al. [81], μ^-. He: black dash–dotted curve, Agnello et al. [76], $\bar{p}$; black dash–doubly-dotted curve, Kottmann [80], μ^-. Reproduced from [F].*

the quantitative description for impact energies below 100 keV.

Also shown in Fig. 7.4 is a calculation by Basko using a semi-classical low-velocity Bohr (LVB) stopping model [185] that extends the Bohr model to lower energies in which the stopping number L depends on the sign of the projectile. The shape of the LVB curve is similar to that for p but shifted to higher energies. Besides the $S^{\bar{p}}$ for H_2 and He measured by Agnello *e*t al. the LVB curve is the only one being larger than the curve for p impact for energies above the maximum. Below the stopping maximum the LVB results stay well below the p results and cross all other curves. Besides the position of the stopping maximum the outcome of the LVB method does not fit well any of the curves discussed here.

7.1.4. Comparison of H, H_2, and He

In Fig. 7.5 the present stopping power curves for all three targets H, H_2, and He are shown in one graph. For comparison also the experimental data for $\bar{p}$ and μ^- impact on H_2 and He targets are given. In the limit of high energies $E > 500$ keV the present results for atomic and molecular hydrogen coincide which is also obvious from Table .6.

For these energies the present findings for He stay clearly above those for hydrogen. For $E > 2000$ keV, however, the present S curve for He approaches the hydrogen results multiplied by a factor 2 (cf. Table .6).

The high-energy behavior can be made plausible by considering how the impact parameter region — and therefore also the distance r between the electron and the nucleus — where the main contribution to the energy loss originates from depends on the projectile energy. It is known that for large impact energies the relative importance of distant encounters is increasing for excitation and ionization and therefore also for the electronic stopping power (cf. previous chapters). The used model potential in Eq. (2.36) fulfills the requirement that it behaves for $r \to \infty$ as the potential of a hydrogen atom. Since at large distances the "outer" electron of the H_2 molecule and the He atom is practically only exposed to the field of the sum of the three remaining charges, the same stopping power for hydrogen atoms and molecules *p*er atom can be expected.

The doubled values for He for large E can be understood in the following way. For high impact velocities the collision process can be considered independently for both electrons of the He atom, since the projectile–electron interaction happens on a much shorter time scale than the mean electron motion and finally, the *d*ynamic electron-electron interaction only plays a minor role. Therefore, in the high-energy regime it is also meaningful to consider the stopping power per *electron* instead of per *atom* leading then to the same result for H, H_2, and He targets.

At low energies the present stopping power curves for H_2 and He coincide. For energies around and below the stopping maximum the results for hydrogen atoms obviously differ from those for the molecules lying clearly above the He and H_2 curves. This could have been expected, since all previous attempts to compare calculated S data for H atoms with experimental curves for H_2 turned out to be not satisfactory. The apparent differences have been ascribed to *m*olecular effects [84–86] but have not been further specified. A full treatment of the H_2 molecule has to account for a two-center description with two interacting electrons as well as vibrational and rotational motion of the nuclei. This leads, e.g., to a different ionization potential and an asymmetry of the charge distribution compared to an H atom, dynamic two-electron effects as well as the existence of different rotational and vibrational states.

The present calculations employ an atomic-like one-center model for the description of H_2. It provides an appropriate ionization potential which is, however, static, since the second electron is accounted for by a screening potential which does not allow for dynamic interaction effects. The nuclear motion is included to a certain extent using the linearity in R_{nuc} of the antiproton cross sections (cf. Sec. 6.2). The present findings seem to show that the cross sections and therefore also the stopping power are strongly determined by the correct ionization potential of the target. Thereby, ionization is the main energy loss channel for $\bar{p}$ collisions with H_2. Also, specific molecular effects due to the existence of two centers like rotational and vibrational motion of the nuclei, dissociation, or an asymmetric charge distribution seem to play a minor role for impact energies above the stopping maximum. On the other hand, dynamic electron-electron effects during the collision, which are excluded in the present approach, become important for energies below the stopping maximum due to the fact that (i) the longer time scales allow for interactions between the electrons and (ii) the inelastic collisions take place closer to the nuclei where the electron density is higher. Therefore, the explicit consideration of these effects is obviously inevitable in order to improve the understanding of the stopping power at low energies.

7.1.5. The Barkas effect

The present results for $\Delta S \,/\, S$ and L_B in antiproton and proton collisions with molecular hydrogen and helium atoms are discussed in detail in Ref. [F]. The proton data are thereby taken from experiments and at high energies $E > 200$ keV — where electron capture can be safely neglected — also from present calculations. The qualitative behavior of L_B is similar to that of the ratio $\Delta S \,/\, S$ but they differ in the scaling for different E. Thereby, L_B is suppressed at low energies but enhanced at high energies, since it is proportional to v^2 and therefore also to E. The difference between H_2 and He is of the order of a factor 2. Exactly this factor enters in Eq. (7.5) as the atomic number Z in the denominator being one for hydrogen and two for He. For the highest energies, $E > 1000$ keV, $\Delta S \,/\, S$ and therefore also the L_B curves evaluated only from the present results for $S^{\bar{p}}$ and S^p decrease with increasing E and, as expected, approach zero for $E > 1000$ keV. For small energies $E < 10$ keV, L_B is very small but nonzero except for $E \approx 6$ keV where it changes sign. However, for these small energies a sizable difference between the stopping power of $\bar{p}$ and p exists. Consequently, the often used condition,

$$L_{2i+1} \ll 1 \quad \text{for} \quad i \geq 0\,, \tag{7.6}$$

that is to assume that higher-order terms of the stopping number, which lead to different results for particles and antiparticles, are insignificant, is not sufficient to extract the leading odd term L_1 from $\Delta S \,/\, S$ in Eq. (7.4). While the sum of all odd corrections L_B — given here by Eq. (7.5), since $(Z_p)^{2i} \equiv 1$ holds for $\bar{p}$ and p — already fulfills this condition for small E, the findings for the stopping power of p and $\bar{p}$ impact clearly differ in Figs. 7.3 and 7.4. Therefore, it seems more appropriate to use stronger bounds for the condition given in Eq. (7.6), that is,

$$|L_{2i+1}| \ll |L_1| \quad \text{for} \quad i \geq 0\,. \tag{7.7}$$

7.2. Alkali-metal atoms

As for hydrogen and helium targets the obtained differential information on ionization and excitation of alkali-metal atoms in Refs. [A,D] and Sec. 5.1 is used for the determination of the cross section for electronic energy loss. Since the alkali-metal atoms are treated with a SAE model, the cross sections are extracted in the same way as for the hydrogen atom. Therefore, only one-electron transitions are considered and no difficulties with respect to possible many-electron excitations occur. Although the SAE model is in principle a limiting factor its applicability is impressively demonstrated in Sec. 5.1 and Ref. [A] proving the usefulness of the underlying concept of dividing the electrons

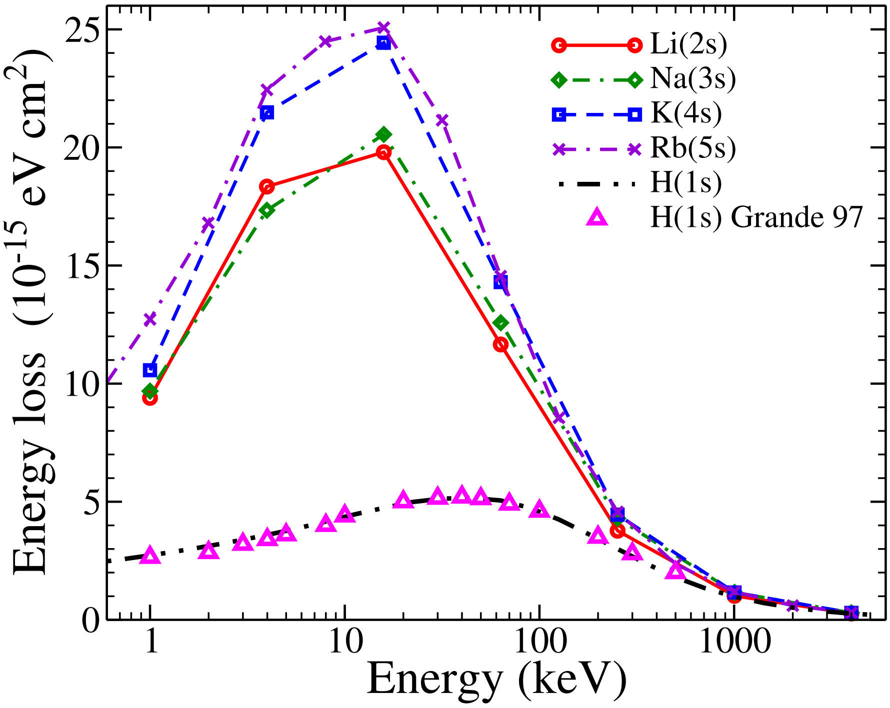

Figure 7.6.: *Theoretical energy-loss cross sections for $\bar{p}$ collisions with Li, Na, K, Rb and H as function of E. Red solid curve, Li; green dash–dotted curve, Na; blue dashed curve K; violet double-dash–dotted curve, Rb; black dash–double-dotted curve, H; magenta triangles, H, Grande and Schiwietz [186]. Reproduced from [D].*

into one loosely-bound outer valence electron and a core of the remaining passive inner electrons.

The present results for $\bar{p}$ collisions with Li, Na, K, Rb, and H atoms [D] are shown in Fig. 7.6, where all target atoms are initially in their ground state with $l = 0$. Also shown is a comparison of the present findings for $\bar{p}$ + H with an atomic orbital calculation by Grande and Schiwietz [186]. Good agreement between the two curves for H atoms is achieved (as discussed before in Sec. 7.1.1) confirming therefore the present implementation. To the best of the author's knowledge no data on the energy loss of antiprotons interacting with alkali-metal atoms have been provided in literature before neither theoretically nor experimentally.

As could have been expected from the results for ionization and excitation the electronic energy loss for H targets is in general smaller than for the alkali-metal atoms. On the other hand, the difference of $S(E)$ between alkali-metal and H atoms is, especially for high E, not very large. This can be understood qualitatively regarding Eq. (4.17) where the σ_j and $\mathfrak{s}(\epsilon)$ are weighted with the excitation energies $(\epsilon_j - \epsilon_i)$ which are clearly larger for excitations of an H atom.[b] That is, the comparably smaller excitation and

---

[b] For hydrogen atoms the ionization potential is considerably larger than for the alkali-metal atoms and excitations within the shell of the initial ground state are, in contrast to the alkali-metal atoms, not

ionization cross sections for collisions with H atoms are to a certain extent countervailed by the larger amount of transferred (average) energy. Consequently, the alkali-metal atoms also show the same behavior for large impact energies like the hydrogen molecule and helium atom.[c] They all have a hydrogen-like potential at large electron distances to the core r which become relatively more important for high energies. However, the alkali stopping power coincides with the hydrogen results only for comparably high energies $E > 4000$ keV for Na, K, and Rb and $E > 1000$ keV for Li, since the alkali-metal atoms are spatially more extended than is the case for hydrogen. The differences for Li and Na observed for ionization and excitation in Sec. 5.1 compensate each other for the electronic energy loss. Also, the results for K and Rb are very similar. The clear ordering of the magnitude of the cross sections by element number is not as pronounced as for ionization.

In general, it is possible to conclude that in the case of $\bar{p}$ impact the electronic stopping power of alkali-metal atoms is dominated by the excitation process. Therefore, a large stopping power can be found for all alkali-metal atoms around the maxima of the excitation cross section at $E \approx 15$ keV. Thereby, considered on a linear E scale, this big energy loss occurs in a narrow impact energy range. The discussed stopping behavior obviously leads to the fact that it is important to have practically no alkali-metal atoms as residual gas in an experimental setup dealing, e.g., with low-energy collisions on hydrogen and helium. The possible risk of polluting the experimental setting has lead to the fact that only few experiments have been performed for proton collisions with alkali-metal atoms and none for antiproton collisions, since alkali-metal atoms have the tendency to stick on the walls of the (vacuum) chambers of the experiment and it is difficult to completely remove them afterward.

---

possible.

[c] Confer the comparison of the stopping powers for H, H_2, and He in Sec. 7.1.4.

8. Conclusions and outlook

The objective of this chapter is threefold. First, the status of the five problems, specified at the end of the Introduction (p. 12 *et seq.*), which is achieved in this work should be highlighted. Second, additional conclusions may be provided which are based on findings obtained in a number of different chapters and are therefore not discussed in any of the previous chapters. Finally, an outlook is given comprising further applications of the method as well as further developments which are closely related with this work.

8.1. State of the specified problems

Implementation of a nonperturbative method

The method developed in this work for the calculation of ion collisions with one- and two-electron atomic as well as molecular targets using the impact-parameter method can be considered as state of the art close-coupling approach. The choice of a spectral expansion of the scattering wave function in eigenstates of the target instead of a spatial expansion on a grid leads to a rather efficient approach. Thereby, the calculation of the electronic structure of the target has to be done only once for a certain basis set. This is in particular of advantage for two-electron targets where the determination of the electron-electron interaction term is known to be most time-consuming. Therefore, its determination is a limiting factor for most grid-expansion methods where this term has to be calculated for every time-step. On the other hand, the main task in the case of the present (spectral) method is to find an appropriate basis set with a sufficient description of the continuum, especially in the case of two-electron basis sets. However, a central feature of the spectral approach is that the choice of a basis set is motivated by the physical process under consideration. This allows for an efficient convergence of those observables which are of interest.

While the employed codes for the calculation of the electron structure of the targets have already been existing and are only adapted or further developed to the specific needs, one central achievement of this work is the development and implementation of the coupling matrix elements. They are realized for atoms and (homo-nuclear dimer) molecules with one and two electrons. Thereby, arbitrary orientations of the molecular axis are possible. Although calculations can in principle also be performed for arbitrary internuclear distances the convergence behavior of the molecular basis states becomes less favorable for large internuclear distance due to the use of a one-center expansion of the potential of the two nuclei. In the case that electronic wave functions for internuclear distances are needed which are much larger than the equilibrium distance of H_2 molecules a two-center molecular basis should be employed as was developed by coworkers in Ref.

[187].

Due to the high efficiency in calculating the electronic structure and the coupling matrix elements the computational time is basically determined by the time propagation, that is the solving of the TDSE. Therefore, the computational effort is in principal comparable for one- and two-electron targets since for the solution of the TDSE only the number of coupled equations, i.e. the number of basis states is relevant. However, in the case of two-electron calculations usually more basis states are needed.

As a consequence of the efficiency, the computation can be performed on a number of standard PCs instead of using a large-scale computing facility as is normally the case for close-coupling expansions on a spatial grid. This allows for a considerable number of extensive calculations in order to confirm convergence. Note, the time required for the performed computation is clearly dominated by the convergence studies. Furthermore, the capabilities of the method can still be extended in order to enlarge the number of quantities extracted from the full scattering wave function after the collision. That is, also converged higher differential cross sections which are not in the focus of this work should be computationally within reach in a number of future applications, though, a considerable computational effort may be required to perform the according convergence studies and to achieve convergence.

Testing of the developed method

The developed method, and in particular its one-electron description, is rigorously tested with proton impacts on alkali-metal atoms and hydrogen molecules using model potentials for the target description. Good agreement with literature data is achieved for the proton–alkali metal cross sections for impact energies $E > 4$ keV. While in the case of proton impacts convergence is not achieved for lower energies, due to the one-center expansion of the scattering wave function, in the case of antiproton collisions the results are converged for all energies, $E > 0.5$ keV. The two-electron target description is tested by means of antiproton collisions with helium atoms. While convergence with the parameters of the one-electron orbitals is obtained rather easily, care has to be taken in the choice of configurations for an appropriate two-electron basis. The obtained ionization cross sections for antiproton collisions with helium agree with experimental data for energies beyond the cross-section maximum where the agreement is even excellent for high energies, $E > 100$ keV. For energies below the maximum, however, no rigorous comparison is possible due to the differences between the experimental and theoretical literature data. It may be concluded that the developed method is capable of providing theoretical data for antiproton and proton collisions discussed in the next item.

Providing theoretical collision data

Besides the ionization and excitation cross sections for antiproton collisions with hydrogen and helium atoms, which were discussed in detail in the literature already before, a large number of cross sections is calculated in this work for antiproton collisions with other, previously not studied, atomic and molecular targets. First, a systematic study of collisions with the alkali-metal atoms Li, Na, K, and Rb is performed, providing different cross sections for ionization, total and differential excitation, as well as electron-energy spectra. For these systems no experimental and only two theoretical studies of Li and Na targets with limited amounts of data were previously available in the literature. Even in the case of proton impacts the calculated cross sections for total excitation of the alkali-metal atoms and all cross sections for the K targets complement the sparse literature data. Furthermore, a large amount of theoretical data is obtained for collisions with molecular targets. While the ionization cross section for antiproton collisions with molecular hydrogen cations is in excellent agreement with the one calculation available in the literature, first results for excitation of this collision system are achieved in this work. On the other hand, a lot of theoretical data are calculated in this work for hydrogen molecules which are discussed in the next item.

Theoretical data for collisions with molecular hydrogen

The theoretical approach developed in this work is in particular appropriate for treating antiproton collisions with hydrogen molecules. It allows for the first time for a non-perturbative, two-electron, two-nuclei description of hydrogen molecules in antiproton collisions. The performed calculations provide ionization data which reproduce the experimental data for energies beyond the cross-section maximum, while they are slightly lower than the latter around the maximum. For energies below the maximum the present calculations provide the first theoretical data which lie, however, above the measurements. Recent unpublished experimental data suggest on the other hand, that for low energies the earlier measurements are too small. The dependence of the cross sections on the internuclear distance and on the orientation of the molecular axis with respect to the projectile trajectory are analyzed in detail. It is found that the Franck-Condon cross sections obtained for the expectation value of the internuclear distance agree within 2% with the cross sections obtained by integration of Franck-Condon cross sections over the internuclear distance, where the latter include the vibrational motion of the nuclei.

Besides the full description of the molecule, also simple one-electron model potentials are employed. They are computationally much less demanding and their use in calculations is therefore attractive, if their ranges of applicability are known. The comparison of the full with the model-potential description yields that in the case of antiproton collisions with molecular hydrogen the agreement of the ionization and excitation results is good for energies around the cross-section maximum (≈ 50 keV) and becomes even excellent for energies beyond the maximum. For low energies the simplified model descriptions yield too large cross sections due to the missing dynamic electron correlations. They also show an atomic rather than a molecular slope revealing their atom-like nature. The cross sections for proton impacts obtained with the model agree with literature data even for lower energies, $E > 10$ keV. Electron-energy spectra are calculated for antiproton and proton impact and compare well with literature data in the case of proton impact. The spectra for antiproton collisions together with differential excitation cross sections are used to obtain antiproton stopping powers discussed in the next item.

Improved understanding of stopping powers

In this work stopping powers for antiprotons in hydrogen atoms and molecules, helium and alkali-metal atoms are obtained from low to high impact energies where only (effective) one-electron descriptions of the targets are employed. A detailed study for hydrogen and helium targets is performed which distinguishes for the first time systematically between the stopping powers of atomic and molecular hydrogen. The present stopping power for antiprotons in atomic hydrogen agrees well with other advanced calculations and thus validates the present implementation. For high energies, where the cross sections of the model potential nicely agree with the full two-electron description, the present findings for the energy loss of antiprotons colliding with molecular hydrogen and atomic helium agree with all measurements except for the fundamentaly different experimental data which were found to be larger than those for proton impacts. Due to the limited accuracy of the employed model potential for low-energy antiproton impacts it is not possible to make a sound statement with the results obtained so far which of the differing experimental curves describes the stopping power correctly at these energies. However, an additional attempt is provided which tries to reduce the known deficiencies of the model potential at low energies. Furthermore, it should be emphasized that the full two-electron description developed in this work allows for a much more accurate calculation of the stopping powers for low energies. Since only a small extension in the extraction of the electron-energy spectra for two electrons has still to be implemented highly accurate data for hydrogen molecules and helium atoms for low impact energies can be expected soon in a future work. These calculations may resolve the open debate on the behavior of the antiproton stopping power.

8.2. Additional conclusions

In the previous chapters a considerable amount of results and data are presented. These results are discussed using the involved targets as a classification scheme for the collision systems. However, in the following a number of conclusions shall be highlighted which may primarily build on insights gained from findings all across this work.

8.2.1. Atomic and molecular targets

In this work collisions involving atomic as well as molecular targets are considered. In the following the obtained results shall be used in order to learn something about similarities and differences of these systems with a focus on the ionization process.

In Fig. 8.1 the single-ionization cross sections obtained in this work for antiproton collisions are compared for the helium and hydrogen atom as well as for the hydrogen molecule and the molecular hydrogen cation, where the latter is scaled by a factor of 4. The comparison shows that for the energy regime below the maxima the curve for molecular hydrogen decreases much faster with decreasing energy than is the case for the helium and even more for the hydrogen *atom*. For the latter atom a minimal ionization

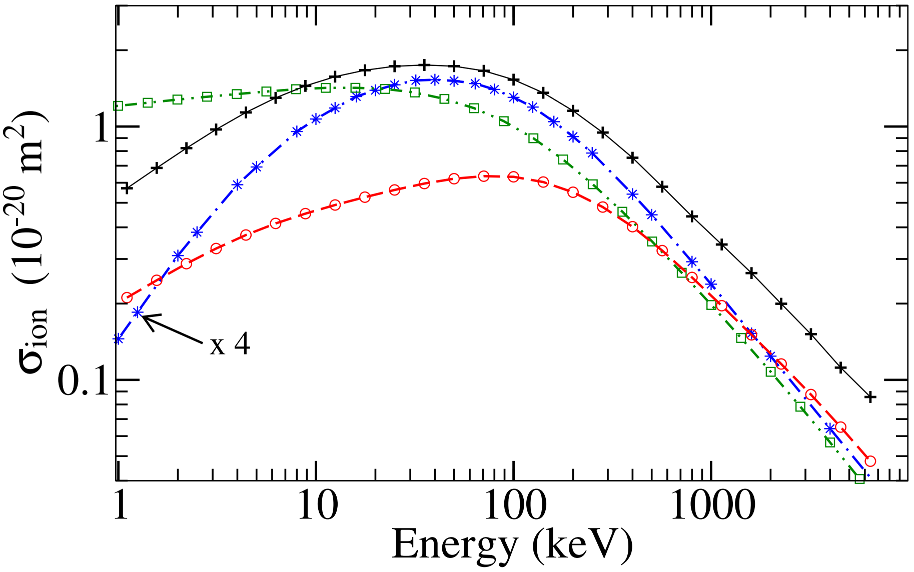

Figure 8.1.: *Comparison of single-ionization cross sections for antiproton impact on different targets obtained in this work. Black solid line with pluses, orientation-averaged results for molecular hydrogen; red dashed curve with circles, helium atom; blue dash–dotted curve with stars, molecular hydrogen ion (times 4); green double-dashed–dotted curve with squares, hydrogen atom.*

cross section at low energies is determined by the Fermi-Teller radius[a] [188], due to the fact that there are no bound states for the three-body system consisting of a proton, an antiproton, and an electron. The molecular hydrogen curve is on the other hand qualitatively more similar to that of the *molecular* ion, though less steep. That means, especially for these energies the qualitative shape of the ionization cross section seems to be different for atomic and molecular targets. At low energies ionization occurs mainly in a small b region close to the nuclei, as discussed, e.g., for the b-resolved transition probabilities in Secs. 5.1.1 and 6.2.2, where the electronic density and the expectation value of the electron velocity are high. In a close encounter of the antiproton on a molecular target the electron cloud might be more efficiently moved away from the projectile towards the other nuclei, especially for the molecular ion since there is in contrast to atoms always one positive particle which is not neutralized by the antiproton.

At high energies the single-ionization cross section for helium and 4 times the molecular hydrogen ion are both similar to the curve of the hydrogen atom while the results for molecular hydrogen are in good agreement with *twice* the curve for the hydrogen atom [cf. Fig. 6.7(a)]. For these energies distant encounters, i.e. trajectories with larger b, become relatively more important for the ionization process. Accordingly, details of the targets like the exact distribution of the positive charges become less crucial and the cross sections are mostly determined by the ionization potential. The latter statement is

---

[a] The adiabatic ionization energy as a function of the distance R between proton and antiproton vanishes for R smaller than the Fermi-Teller radius $R_{FT} = 0.639$ a.u. [188] and becomes 0.5 a.u. as $R \to \infty$.

confirmed by the outcome of the two model potential descriptions, $V_{\mathrm{m}od}$ and H_{scal}, which disagree in their short-range as well as long-range r behavior but agree in the ionization potential and for high energies in the cross sections for ionization.

8.2.2. Applicability of model potentials

There is no doubt that the use of models and approximations can be very helpful and may sometimes even be the only way to solve a complex problem. On the other hand it is crucial to know the range of applicability of each of the employed simplifications well in order to be able to use the obtained findings for sound statements.

Some effort is spent in this work to introduce and examine the model potential V_{mod} intended to be used for the description of H_2 molecules and He atoms. Basically, it is an atomic, i.e., a spherically symmetric, one-center, one-electron model which can be adapted in a unique way to different internuclear distances using the ionization potential as criterion. It turns out that quantities like excitation energies, dipole transition moments and photoionization cross sections agree astonishingly well with those of the H_2 molecule, also in the case of different internuclear distances. Furthermore, in a different work [123] the usefulness of the model potential V_{mod} is demonstrated in comparison to a full H_2 description for interactions with short intense laser pulses, especially when the results finally have to be convoluted in order to match the experimental conditions.

The applicability of the $V_{\mathrm{m}od}$ model for the description of He atoms and H_2 molecules in ion collisions is one of the main issues in this work. It can be summarized that agreement in the case of ionization of He and H_2 with experiment and the full two-electron description is excellent at high energies beyond the cross-section maximum and still acceptable for energies around the maximum. For excitation the agreement for H_2 is also good for energies around and beyond the excitation maximum. At energies below the maximum the model description results in too large cross sections in all cases where ionization is better described for He than for H_2. The comparison to another simple atomic model H_{scal}, i.e. a hydrogen atom with scaled charge, shows a comparable behavior for ionization but an obvious disagreement for excitation. From these findings it may be concluded that for ionization the ionization potential is relevant for high impact energies while at low energies the dynamic electron-electron correlation cannot be neglected. For excitation the ionization potential is not relevant. Instead the correct description of the bound states and excitation energies are of importance, where especially the energetically lowest-lying dipole-allowed bound states are crucial. Additionally, in the case of molecular targets molecular effects, due to the orientation of the internuclear axis and the two centers, become important for low energies. The dependence of the (orientation-averaged) cross sections on the internuclear distance can, however, be described satisfactory with the model potential V_{mod}. Thereby, it has to be emphasized that besides the term α, which is directly determined by the ionization potential and enables the modeling of different internuclear distances, no parameter is included in the potential in order to fit the energies or wave functions to those of the correct electronic states of H_2. On the other hand, not all effects which may be of increasing importance at low impact energies can be described by the model. First, the influence of a second electron is solely incorporated as a static screening, second, no dependence on the molecular orientation during the collision is allowed, and also vibrational excitation including dissociation is not considered in this approach.

From the comparison of model potentials for the description of antiproton impact on helium atoms it seems that the advanced potential proposed by Lindroth *e*t al. [163] is a better approximation for energies below the ionization maximum since it is in good agreement with the present full two-electron results. The model is intended to reduce the correlation corrections on K-vacancy production by fast protons incident on light ions.

In this work a model potential proposed by Klapisch [125] is employed for the description of the alkali-metal atoms. The overall good agreement of the obtained results with the literature data demonstrates the usefulness of the underlying single-active electron approach, that is, of the implied concept of an outer, loosely-bound valence electron and a core consisting of the nucleus and the remaining inner-shell electrons in the case of alkali-metal atoms. Note, especially for high impact energies the obtained results are, however, less meaningful due to the increasing probability for excitation and also ionization of inner-shell electrons. These transitions are necessarily not accounted for by the model. Consequently, the calculated data might rather be interpreted as differential cross sections originating only from the valence electron for these energies.

8.2.3. Comparison of proton and antiproton impacts

The developed method is in principle capable of handling an arbitrary projectile charge which enters only as a factor in the coupling elements. However, the physics of collision systems including positive or negative projectiles can differ considerably. The most striking difference for positive projectiles like protons, in the considered energy regime, is the existence of an electron-capture channel being obviously absent for negative projectiles like antiprotons which is nicely visible in the energy spectra of the ejected electrons for the two projectiles. This difference has also an influence on the calculations using the present method where a much faster convergence is observed for antiproton compared to proton impacts, especially at low energies.

The preference of the present method for negative projectiles originates from the employed one-center expansion of the scattering wave function centered on the target. In the case of electron capture a considerable part of the electron density moves with the positive projectile and is therefore rather localized which requires in a spherically symmetric one-center expansion a sufficient angular resolution, that is, a sufficient number of spherical harmonics with different l and m coefficients. Also the independent determination of cross sections for capture and ionization into the continuum for positive projectiles can only be performed using an analysis of the electron-energy spectra.

Obviously, a lot more literature data exist for proton than for antiproton collisions, especially when experiments are considered due to the high demands in producing low-energy antiprotons. Therefore, calculations including protons are preferable for comparing with the literature and for testing the implementation while the antiproton results may help to increase the amount of the still sparse literature data and improve the understanding of electronic effects which may be dominated by electron capture in the case of positive projectiles. Thereby, the relatively good agreement of proton calculations using the model potential V_{mod} compared with experimental results also for energies below the cross-section peak may be explained by the dominance of the capture process which is primarily a one-electron process. Most importantly, it may be concluded that the present method is appropriate of antiproton and proton collisions.

8.3. Outlook

In view of the method developed in this work and the understanding gained in the various applications it is of interest to give a short outlook which focuses on closely related future projects. In general, this should be done by distinguishing between further applications of the method which are possible with no or only small extensions and related further developments which require, however, some additional efforts. Clearly, a number of other projects are conceivable in connection with this work not being covered by the following small selection.

8.3.1. Further applications of the method

Here a selection of applications is presented concentrating on an extended use of the full two-electron description. Since in this work total cross sections for ionization and excitation are discussed in some detail a comparable degree of understanding in the case of differential quantities would be highly desirable.

Differential cross sections with full description

Differential cross sections, namely, differential excitation and electron-energy spectra, have been obtained and discussed in this work for the alkali-metal atoms and using the model description also for H_2 molecules. The electron-energy spectra and also further differential quantities of He atoms and H_2 molecules are of interest at low energies since they are planned to be measured by recycling the antiproton projectiles [65]. This would help to drastically improve the experimental statistics required for a differential resolution. At low energies, however, deviations can be expected from the results obtained so far with the used model potential description V_{mod}.

While differential cross sections for excitation are already accessible for the full description this is not the case for the electron-energy spectra. However, this requires only an appropriate normalization procedure for the two-electron continuum states which has to be formulated and implemented.[b] Different ways how to solve this problem are reviewed by Lambropoulos *e*t al. in [190]. Afterward, the spectra can be extracted in practically the same way as is done for the one-electron model description. Obviously, the extraction of differential information requires convergence not only for the total results. Thereby,

---

[b] When more than one continuum is open, continua associated with different thresholds have different discretization, and the necessary degeneracy for obtaining the correct outgoing wave functions is lost [189, 190].

the knowledge about appropriate basis sets obtained in this work is helpful. The efficient implementation of the collision process allows for larger two-electron basis sets and in addition also for an extended convergence study for the two-electron targets.

In this context it would be interesting to extent the extraction of cross sections from the scattering wave function after the collision also to angular-resolved double and total differential cross sections. Clearly, the demands on the basis description increase, the more differential the extracted data are. An efficient computation and a thorough knowledge of the choice of appropriate basis sets, both achieved in this work, become even more important. Still, the calculation of a number of differential cross sections can be expected to be a considerable numerical task. Also a comparison of results obtained with the model and the full two-electron description should be considered in order to determine the range of applicability of the model potential with respect to double and total differential cross sections.

Stopping power at low energies

The stopping cross sections are very much of interest at low energies since, especially at low energies, the experimental findings for He as well as those for H_2 targets differ considerably. However, the results obtained with the model description used in this work turn out to become less reliable at these energies. Since uncertainties in the experimental data analysis could not be fully excluded, it was stated by Kottmann in [80] that the error of the measured S curve would reduce drastically, if a point at low energies could be fixed safely. Therefore, improved theoretical results especially at low energies would limit the uncertainties still persisting at low impact energies and therefore present a stringent test of the accuracy of the $\bar{p}$ measurements of the stopping power. The elimination of the diversity for the stopping power results from different experiments (cf. Refs. [77] and [F]) is consequently one of the most urgent aims which may be achieved with the present method in the near future.

In order to improve the description of the stopping power a two-electron description of the H_2 and He targets shall be implemented. Once the electron-energy spectra are obtained for the two-electron description (see above) it is, together with the already accessible results for differential excitation, straightforward to obtain the electronic energy-loss cross sections in the same way as presented in this work. Consequently, the total effort required for reaching that goal may be regarded to be manageable.

Double ionization

One of the striking features in when comparing antiproton and proton collisions are the clearly differing cross sections for double ionization of helium but also the H^+ production from molecular hydrogen targets. However, the achieved understanding of the H^+ production from H_2 targets even with the improved attempts in this work is still not satisfying.

In order to use the presented two-electron method to improve the insight in the double-ionization process the basis sets should be extended including also configuration series where both electron orbitals are assumed as continuum states. Obviously, an advanced analysis of the final scattering wave function is required and has to be implemented such that it is able to clearly separate the ionization yield into single- and double-ionization channels. Possibly, it may be advantages to also consider an alternative approach described in Refs. [189, 190] which uses *free-boundary* conditions instead of the fixed-boundary approach used in this work. While in the latter case the discretized continuum wave functions are selected by the boundary condition that they are equal to zero at the boundary R_B of the radial box (see Sec. 2.1.2), in the free-boundary approach the continuum wave functions are selected according to their energy. This approach may be used first of all for helium targets and the obtained results may be compared with literature data. With the help of this comparison also the applicability of the approach can be checked. Afterward, the same kind of calculation can be performed for the H_2 molecule in order to try to explain the experimental findings for H^+ production.

8.3.2. Further developments

Very low impact energies for He

Low-energy antiproton collisions with helium atoms are identified due to the discussed fundamental properties as a preferable candidate for stringent tests with respect to theoretical descriptions of correlated many-electron systems. The competition concerning the applicability and accuracy of large-scale state of the art methods and numerical calculations, however, concentrates on impact energies larger than 1 keV while already the description of the collision process below 20 keV is not conclusive and partly even missing for $E < 1$ keV. On the other hand it is important to note that in the next years antiproton collision experiments will be performed especially at very low energies in the range of 10 eV to 500 eV [64] using the recently developed antiproton trap by the ASACUSA [10] collaboration at CERN [66]. These experiments should help to close the gap which exists in the description — theoretically as well as experimentally — between the very-low and low energy regimes where antiproton capture by a target and target ionization by the antiproton, respectively, are dominating. Finally, the intense experimental activities at CERN trying to obtain antihydrogen atoms in ground state are profiting from an improved understanding of antiproton interactions at low to very-low energies.

For these impact-energy regimes different descriptions of the collision system have to be considered. Two methods shall be implemented in order to achieve the proposed goal both having in common that they are close-coupling methods using a molecular orbital representation. They differ by the fact that one is a semiclassical time-dependent (SCTD) and the other, used for energies where the semiclassical approximation is no longer applicable, a full quantum-mechanical time-independent (QMTI) formalism. While the SCTD approach, e.g., in Refs. [92, 191], is conceptually closer to what has been done in this work with atomic orbitals, a kind of quantal perturbed-stationary-state (PSS) method shall be employed as QMTI approach. The latter method was originally proposed by Massey and Smith [192] and reviewed, e.g., in Refs. [92, 191].

Further developments concerning this approach have also been contributed in [193, 194].

Note, the existing techniques were mainly designed and employed for positive projectiles and have to be adjusted to the anticipated kind of collisions. Therefore, a further development might be required in order to account for the qualitatively different processes (e.g., antiproton capture) which occur in the presence of a heavy negatively-charged particle. This reveals a second aspect of the proposed future work, that is, the enhancements of methods used for low-energy collisions with the emphasis on heavy *negatively*-charged projectiles.

Larger target systems

The studies on helium atoms and hydrogen molecules can be considered as most fundamental to the understanding of the basic (many-electron) processes involved. However, in most applications concerning collisions larger target systems are of interest. Therefore, in a similar way as is done in the present study, model potentials for the description of various target systems may be used together with accordingly adapted coupling matrix elements. Obviously, also other ways of a target description can be employed as, e.g., the basis generator method [195] which very recently was used for collisions including water molecules [196] and should be extended to larger molecules. But also density functional theory may be applied for the description of a number of larger molecules. The latter is currently used by coworkers, also in terms of a spectral close-coupling approach, in order to perform time-dependent calculations of the interaction of intense short laser pulses with a number of different molecules. In order to transform this concept to the case of ion collisions, basically the operator in the matrix elements has to be exchanged accounting for the Coulomb interaction. This may be most conveniently done using again the impact-parameter method. That means, the basic concept of the method developed in this work would stay the same apart from the fact that the basis description and therefore the matrix elements would be determined differently.

The connection to the present work is given by two aspects. First, key ingredients of the present method may be, at least partly, used or appropriately adapted in order to describe also larger target systems. Second, the target descriptions used for larger systems may be directly tested for the two basic atomic and molecular systems, He and H_2, by means of the presented method in order to be able to estimate the accuracy of the newly developed approach.

Summary

Based on the state of the art for low-energy antiproton collisions and also motivated by requirements for the facility design of FLAIR five problems are specified for this thesis. These are the (i) implementation of a nonperturbative close-coupling method and the (ii) rigorous testing of the developed method. Furthermore, this method should be used for calculations providing a (iii) substantial amount of theoretical collision data, and in particular (iv) theoretical data for collisions with molecular hydrogen, as well as an (v) improved understanding of stopping powers for low-energy antiprotons.

Method

In this work a nonperturbative numerical method is developed for the time-dependent calculation of ion impacts on (effective) one- or two-electron atoms as well as molecules. The collision process is treated by applying the semiclassical impact-parameter method where the energetic projectile moves on a classical trajectory. The electrons of the targets are described fully quantum-mechanically. A spectral expansion is used for the time-dependent electronic scattering wave function which is expressed in terms of time-independent eigenstates of the target obtained by solving the time-independent Schrödinger equation. Thereby, the radial and the angular part of the orbitals are expanded in B splines and spherical harmonics, respectively, centered on the target. In the case of molecules a one-center expansion of the nuclear potential around the midpoint of the internuclear axis is employed in the calculation of the one-electron orbitals. The two-electron target eigenstates are obtained from a configuration-interaction (CI) calculation using products of ionic orbitals as two-electron configurations. Furthermore, a simple atom-like model potential $V_{\mathrm{m}od}$ is introduced in order to treat H_2 and He as effective one-electron targets. With this model different internuclear distances $R_{\mathrm{nu}c}$ are achieved by matching the ionization potential of H_2 for a certain R_{nuc}. Results obtained with the model for excitation energies and dipole transition elements as a function of $R_{\mathrm{nu}c}$, as well as for photoionization compare nicely with orientationally-averaged data for H_2 molecules. The Klapisch potential is used in order to treat alkali-metal atoms as single-active-electron targets.

The time-dependent Schrödinger equation of the collision process is solved with a close-coupling formalism leading to a set of N coupled linear differential equations where N is the number of basis states. The coupling matrix elements (CME) are time-dependent. They are calculated in advance on a grid along each trajectory. The angular and radial parts of the one-electron CME are solved analytically and numerically using quadrature, respectively. In the case of molecules different orientations of the internuclear axis with respect to the trajectory are considered and symmetries and selection rules for three orthogonal orientations are implemented. The CME for two-electron targets are constructed out of a sum of one-electron CME multiplied with the corresponding CI coefficients.

After the collision, i.e. for a sufficiently large distance between target and projectile, the transition probabilities are obtained by projecting the target eigenstates on the scattering wave function. The **b** dependent probabilities for a certain kind of transition are integrated over the impact parameter **b** in order to obtain the corresponding cross section. In the case of effective one-electron descriptions the many-electron transition probabilities are obtained with an independent particle model. For molecular targets the transition probabilities also depend on the internuclear distance R_{nuc} and the molecular orientation. Accordingly, an integration over these degrees of freedom is in general necessary. However, in this work simplified orientation-averaged transition probabilities are proposed using only three perpendicular molecular orientations which reduce the numerical effort drastically. Cross sections which include the rovibrational motion of the nuclei may be obtained by integration of Franck-Condon cross sections over the internuclear distance.

Atoms

Ionization and excitation cross sections for antiproton and proton collisions with the alkali-metal atoms Li, Na, K, and Rb are calculated in a wide energy range from 0.25 to 1000 keV. The calculations converge faster for collisions involving antiprotons than protons, faster for higher than for lower impact energies, and faster for excitation than for ionization. Good agreement with literature data is achieved for the proton–alkali-metal-atom cross sections for impact energies $E \geq 4\,\mathrm{keV}$. For antiproton–alkali-metal-atom collisions the sparse literature data are improved for Li and Na and extended for K and Rb. The ionization cross sections for protons and antiprotons differ considerably for energies smaller than 100 keV due to the electron capture process. Qualitatively, the ionization and excitation cross sections for antiproton impact are similar for all alkali-metal atoms, but their absolute values differ due to the atom-dependent ionization potentials and excitation energies, respectively. Similar characteristics are found for hydrogen atoms due to the common s-state (angular momentum $l = 0$) structure. However, the hydrogen-atom cross sections have much lower values because of the tightly bound 1s electron. For the proton–alkali-metal ionization cross sections a simple fit formula — decrease proportional with inverse of energy (E^{-1}) — is proposed for the energy range from 150 to 1000 keV which also describes the slope of the antiproton ionization cross sections well.

Excitation but especially ionization cross sections for antiproton impact on He atoms are considered in this work. They can be used for a critical testing of the present two-electron description as well as of the applicability of the model potential V_{mod}. Additionally, detailed convergence studies are performed being of direct use for the H_2 calculations. The results converge well with respect to one- and two-electron angular-momentum quantum numbers and converge fast with the number of B splines. A stronger dependence of the quality of the two-electron continuum description can be observed for the choice of orbitals entering the two-electron configurations. An insufficient basis set usually results in a too small ionization cross section for high energies and too large values for energies around and partly also below the ionization maximum. A comparison of the present two-electron description with experimental data reveals excellent agreement for high energies ($E \geq 200$ keV) and still good agreement around the cross-section peak ($E \gtrsim 40$ keV) as well as the lowest measured points ($E \leq 7$ keV). The agreement between the present findings and other advanced close-coupling methods is reasonable, though some of these calculations show deviations as observed in the convergence studies for insufficient basis sets. The results using the model potential $V_{\mathrm{m}od}$ fully agree with the full description for high energies but are larger than the experimental and the present two-electron data below the cross-section peak with increasing deviation for decreasing energy.

Molecules

Calculations for $\bar{p}$ collisions with molecular $\mathrm{H_2}^+$ cations are performed in a broad energy range ($0.5\,\mathrm{keV} \leq E \leq 10\,\mathrm{MeV}$). Extensive convergence studies assure that the final results are independent of the set of expansion parameters. The present ionization cross section nicely reproduces the *orientation-integrated* results calculated by Sakimoto [73] showing that the use of an *orientation-averaged* cross section including three perpendicular molecular orientations is sufficient. An extension of the range of the impact parameter b in comparison with [73] allows for the first excitation cross section. While in general the contributions from different orientations to an orientation-independent cross section differ considerably, for high energies, the cross sections for ionization ($E \geq 100$ keV) and excitation ($E \geq 50$ keV) can be approximated by results of only one molecular orientation.

The model potential $V_{\mathrm{m}od}$ is used in calculations of antiproton and proton collisions with molecular hydrogen for energies 8 to 4000 keV. The applicability of the method is validated with electron-loss cross sections for p + H_2 collisions which agree with experimental and theoretical literature data. The ionization cross sections for $\bar{p}$ + H_2 collisions agree well for $E > 90$ keV with the experimental data. While for $20\,\mathrm{k}eV < E < 80\,\mathrm{keV}$ the magnitudes of the present and experimental cross sections are still comparable, the slopes of both curves develop differently. The calculated excitation cross sections for antiproton collisions with atomic and molecular hydrogen are found to be very similar. Electron-energy spectra, $\mathfrak{s}(\epsilon, E)$, are presented as a function of the electron energy, $\epsilon \leq 12$ a.u., and the impact energy, $48 \leq E \leq 1015$ keV. While the electron-energy spectrum for antiprotons shows a smooth decay with the electron energy ϵ, which is more pronounced for slow collisions, in the case of protons electron-capture peaks can be found along $\epsilon = E/M_p = (v_p)^2/2$, where M_p and v_p are the mass and the velocity of the projectile, respectively. The spectra decrease steeply for $\epsilon \gtrsim 2\,(v_p)^2$, being an appropriate energy cutoff in the basis-set expansion. A comparison between the model potential $V_{\mathrm{m}od}$ and a scaled hydrogen atom H_{scal} with identical ionization potential shows that the ionization cross sections depend primarily on the ionization potential. The two excitation cross sections differ notably, due to the clear differences between the properties of the (dipole-allowed) bound states for both models.

The results for single ionization and excitation from antiproton impact on molecular hydrogen using the full two-electron description are presented for a wide energy range. The experimental data are in good agreement with the present calculations for high energies but are larger around the cross-section maximum. For energies below the maximum the ionization cross section decreases with decreasing energy much faster than in the cases of the hydrogen and helium atoms. On the other hand, the ionization cross section decreases in a similar way, though slower, as for the molecular hydrogen cation revealing the differences between atoms and molecules. The importance of the molecular geometry and the two-electron description is demonstrated by a comparison with the results from V_{mod} and $\mathrm{H}_{\mathrm{scal}}$. Both models reproduce the ionization cross section for $E >$ 50 keV and 100 keV, respectively, while for $E >$ 50 keV excitation is nicely described only by V_{mod} and $\mathrm{H}_{\mathrm{scal}}$ obviously fails. The present full two-electron H_2 data provide a benchmark for molecular collisions in general and for antiproton impact on molecular hydrogen, in particular, which might be useful for the development of molecular models.

The dependence of the cross sections on the internuclear distance R_{nuc} is found to be approximately linear in the R_{nuc} interval in which the probability density of the vibrational ground state is basically non-zero. The dependence on the internuclear distance is more pronounced for lower energies and for excitation compared to higher energies and ionization, respectively. Cross sections which account for the vibrational motion of the H_2 nuclei can be obtained by employing closure with respect to the vibrational states and performing an integration over the internuclear distance R_{nuc}. These results compare remarkably well with the FC cross sections obtained at $R_{\mathrm{nuc}} = \langle R_{\mathrm{nuc}} \rangle = 1.4487$ a.u. due to the linear dependence on R_{nuc}, where the largest deviation is about 2%. A resonant dependence (exponential increase) on the internuclear distance R_{nuc} is observed for orientation (*ii*) and excitation in the R_{nuc} interval 0.8 to 3 a.u. This behavior might indicate a metastable molecular configuration consisting of the antiproton and the H_2 molecule.

Cross sections for ionization followed by excitation and for double ionization are studied, as well as their contribution to the H^+ production in $\bar{p} + H_2$ collisions employing a sequential two-step model which uses (effective) single-electron transition probabilities. The present results for H^+ production in $\bar{p} + H_2$ collisions are smaller than the antiproton experiment, but similar to experimental data when $p + H_2$ collisions are considered. The implied independent two-step model is therefore not able to reproduce the experimental findings for H^+ production from antiproton collisions.

Stopping power

The present method is applied to calculations of the electronic energy-loss cross sections S for antiproton collisions which distinguish between atomic and molecular hydrogen targets, as well as for helium and the alkali-metal atoms Li, Na, K, and Rb in an impact-energy range from 1 keV to 6.4 MeV. The targets are treated as (effective) one-electron systems employing the model potential V_{mod} for He and H_2 and the Klapisch potential for the alkali-metal atoms. The calculated stopping cross sections for H compare well with other nonperturbative calculations confirming the implementation while the He and H_2 data provide, in the applicability range of the model potential, a reasonable description. The findings for He and H_2 seem, however, to overestimate the stopping power S for low impact energies in accordance with what is observed for ionization and excitation at low energies using the model potential V_{mod}. For high energies, where the cross sections of the model potential nicely agree with the full two-electron description, the present stopping powers for $\bar{p} + \mathrm{H}_2$ and $\bar{p} + \mathrm{He}$ collisions agree with all measurements except for the fundamentally different experimental data which were found to be larger than those for proton impacts. The energy loss of the projectile for the three targets H, H_2, and He is mainly caused by ionization in contrast to the alkali-metal-atom targets for which excitation is clearly the dominant loss process. Additionally, the absolute values of the stopping maxima for the alkali-metal atoms are larger by a factor of 5 to 7 compared to the three other targets. While the average energy transferred to excited targets depends only weakly on the impact energy E, the energy transfer increases with E in the case of ionized targets. Consequently, calculations for high impact energies require the inclusion of high-lying continuum states in the basis expansion and are therefore computationally more demanding.

Outlook

The efficency of the developed method allows for extended two-electron calculations for He and H_2 targets including also the extraction of differential cross sections, as well as the discussion of double ionization. Additionally, the number of possible targets can be extended rather easily by employing further effective one- or two-electron descriptions, e.g., for larger molecules.

Part IV.

Appendix

A note on units

Unless otherwise stated, theoretical quantities and formulae in this work are given in *atomic units* in which the mass of the electron (m), the magnitude of the electronic charge (e), and Planck's constant divided by 2π ($\hbar$) all have the value unity.

Measured cross sections are generally displayed in units of cm^2 or m^2. Usually the energy of the incident particles is stated for the laboratory system of coordinates, in which the target atom or molecule is at rest before the collision. Since the ion-atom cross sections depend primarily on the relative velocity v, rather than the incident energy, cross sections are generally shown as a function of laboratory energy measured in electron-volts (eV), or kilo-electron-volts (keV), divided by the mass of the incident particle in atomic mass units (a.m.u.). The relationship, valid at non-relativistic energies,

$$E = 25\, v^2 \ \mathrm{k}eV/a.m.u. \tag{.1}$$

Table .1.: *Atomic units.*

Quantity	Unit	Physical Significance	Value
Mass	m	Mass of the electron	9.10953×10^{-31} kg
Charge	e	Absolute value of the electron charge	1.60219×10^{-19} C
Length	a_0	Bohr radius for atomic hydrogen	5.29177×10^{-11} m
Velocity	v_0	Electronic velocity in the first Bohr orbit of atomic hydrogen	$2.18769 \times 10^{6}\ \mathrm{m\,s^{-1}}$
Time	a_0/v_0	Time an electron travels the distance a_0 in the first Bohr orbit of of atomic hydrogen	2.41889×10^{-17} s
Energy	$\frac{e^2}{4\pi\varepsilon_0 a_0}$	Twice the ionization potential of atomic hydrogen (with infinite nuclear mass)	4.35981×10^{-18} J (27.2116 eV)
Angular momentum	$\hbar$	Planck's constant divided by 2π	1.05459×10^{-34} Js

should be noted, where v is the relative velocity of the colliding particles in atomic units. When v is comparable with c, the velocity of light, the corresponding relationship is

$$E = 50\,(\gamma - 1)\,c^2 \ \mathrm{k}eV/a.m.u. \tag{.2}$$

where $\gamma = (1 - v^2/c^2)^{-\frac{1}{2}}$ and both v and c are expressed in atomic units.

Table .1 summarizes the quantities used in this work. They are listed with their basic unit and the corresponding values in the standard SI units. Additionally, the physical significance of each basic atomic unit is given.

Tabulated data

Dependence of model term α on R_{nuc}

Table .2.: *Values of the dimensionless term α of the model potential in Eq. (2.36) for different internuclear distances R_{nuc} in a.u. Also given for the same R_{nuc} is the ionization potential $I_{H_2}(R_{nuc})$ of H_2 in Hartree. It is obtained using the H_2 ground-state potential-energy curve calculated by Wolniewicz [109]. Additionally, the ionization potential of a He atom [110] and the corresponding α value are provided in the limit $R_{nuc} \to 0$.*

R_{nuc}	$\alpha(R_{\text{nuc}})$	$I_{H_2}(R_{\text{nuc}})$
0	0.87910	0.903570
0.8	0.348416	0.715577
0.9	0.302668	0.693373
1.0	0.262548	0.672753
1.1	0.227258	0.653645
1.2	0.196111	0.635961
1.3	0.168525	0.619606
1.4	0.144021	0.604492
1.4487	0.133081	0.597555
1.5	0.122196	0.590531
1.6	0.102722	0.577647
1.7	0.0853182	0.565762
1.8	0.0697585	0.554815
1.9	0.055851	0.544745
2.0	0.0434376	0.535499
2.1	0.0323864	0.527029
2.2	0.0225906	0.519292
2.3	0.0139698	0.512251
2.4	0.00646727	0.505869
2.5	0.00012071	0.500115

Ionization and excitation for H_2^+

Table .3.: *Ionization and excitation cross sections for antiproton collisions with* H_2^+ *in* 10^{-16} cm^2 *which are shown in Figs. 6.1(a) and 6.1(b), respectively. The results are given for the mean value of the internuclear distance* $R_{nuc} = \langle R_{nuc} \rangle = 2.05$ *a.u. in accordance with the Frank-Condon approximation. The literature data for ionization were calculated by Sakimoto [73].*

E (keV)	σ_{ion}	$\sigma_{\mathrm{ion}}^{\mathrm{l}it}$	σ_{exc}
1	0.036		0.235
2	0.077	0.078	0.445
4	0.147		0.785
5	0.173		0.909
8	0.239		1.176
10	0.268	0.268	1.288
20	0.348	0.349	1.504
40	0.383		1.516
50	0.379	0.380	1.475
80	0.350		1.373
100	0.326	0.333	1.271
200	0.228	0.232	0.940
400	0.135		0.631
500	0.112	0.113	0.538
800	0.073		0.392
1000	0.060		0.392
2000	0.031		0.189
4000	0.016		0.102
8000	0.008		0.053

Ionization and excitation for H_2

Table .4.: *Ionization and excitation cross sections for antiproton collisions with H_2 in 10^{-16} cm^2 originating from the full two-electron description which are shown in Figs. 6.7(a) and 6.7(b), respectively. The results are orientation-averaged and given for the mean value of the internuclear distance $R_{nuc} = \langle R_{nuc} \rangle = 1.4478$ a.u. in accordance with the Frank-Condon approximation.*

E (keV)	σ_{ion}	σ_{exc}
1.11	0.570	0.236
1.56	0.686	0.270
2.21	0.822	0.309
3.13	0.974	0.356
4.42	1.136	0.420
6.25	1.297	0.493
8.84	1.447	0.587
12.5	1.573	0.695
17.7	1.668	0.818
25.0	1.729	0.947
35.4	1.749	1.031
50.0	1.730	1.113
70.7	1.659	1.120
100	1.531	1.089
141	1.358	1.031
200	1.154	0.905
283	0.946	0.750
400	0.753	0.613
566	0.578	0.501
800	0.442	0.408
1131	0.342	0.326
1600	0.264	0.253
2263	0.200	0.191
3200	0.152	0.141
4525	0.112	0.102
6400	0.086	0.073

Table .5.: *Comparison of cross sections for* $\bar{p}$ *+* H_2 *collisions for three orthogonal orientations using the Franck-Condon approximation* $\sigma(\Theta, \Phi) \equiv \sigma(\Theta, \Phi; \langle R_{nuc} \rangle)$ *and an integration over* R_{nuc} $\sigma_{int}(\Theta, \Phi) = \int |\chi_0|^2 \, \sigma(R_{nuc}, \Theta, \Phi) \, dR_{nuc}$ *in units of* 10^{-16} cm^2 *of the molecular axis and for four impact energies E = 6.25, 50, 400, and 3200 keV.*

E (keV)	6.25	50	400	3200
			Ionization	
			$(\Theta, \Phi) = (0, 0)$	
$\sigma_{int}(\Theta, \Phi)$	1.45267	1.76958	0.713342	0.145069
$\sigma(\Theta, \Phi; \langle R_{\mathrm{nuc}} \rangle)$	1.42826	1.75986	0.710460	0.143742
			$(\Theta, \Phi) = (\pi/2, 0)$	
$\sigma_{int}(\Theta, \Phi)$	1.45109	2.00764	0.795357	0.150944
$\sigma(\Theta, \Phi; \langle R_{\mathrm{nuc}} \rangle)$	1.42454	1.98850	0.792813	0.150305
			$(\Theta, \Phi) = (\pi/2, \pi/2)$	
$\sigma_{int}(\Theta, \Phi)$	1.06407	1.46735	0.700974	0.151599
$\sigma(\Theta, \Phi; \langle R_{\mathrm{nuc}} \rangle)$	1.06020	1.46324	0.692372	0.149430
			Excitation	
			$(\Theta, \Phi) = (0, 0)$	
$\sigma_{int}(\Theta, \Phi)$	0.498171	1.20222	0.662506	0.118055
$\sigma(\Theta, \Phi; \langle R_{\mathrm{nuc}} \rangle)$	0.486161	1.17206	0.653721	0.117381
			$(\Theta, \Phi) = (\pi/2, 0)$	
$\sigma_{int}(\Theta, \Phi)$	0.601189	1.33512	0.809984	0.177196
$\sigma(\Theta, \Phi; \langle R_{\mathrm{nuc}} \rangle)$	0.579524	1.29664	0.792430	0.174080
			$(\Theta, \Phi) = (\pi/2, \pi/2)$	
$\sigma_{int}(\Theta, \Phi)$	0.440488	0.858809	0.506685	0.108364
$\sigma(\Theta, \Phi; \langle R_{\mathrm{nuc}} \rangle)$	0.434856	0.851961	0.515543	0.107651

Stopping power for H, H_2, and He

Table .6.: *Stopping power S per atom for antiproton collisions with H, H_2, and He in 10^{-15} eV cm^2 / atom which are shown in Figs. 7.2, 7.3, and 7.4, respectively. The results for H_2 are given for the mean value of the internuclear distance $R_{nuc} = \langle R_{nuc} \rangle = 1.4487$ a.u.*

E (keV)	H	H_2	He
1	2.774	2.242	2.261
2	3.164	2.503	2.524
4	3.641	2.826	2.859
8	4.208	3.188	3.280
16	4.782	3.596	3.795
25	5.098	3.831	4.144
32	5.196	3.947	4.367
50	5.210	4.027	4.666
64	5.115	4.013	4.811
100	4.623	3.782	4.850
128	4.229	3.557	4.753
200	3.406	2.950	4.316
256	2.938	2.588	3.965
400	2.148	1.961	3.202
800	1.239	1.165	2.036
1600	0.681	0.656	1.189
3200	0.361	0.356	0.668
6400	0.187	0.187	0.358

Abbreviations

Abbreviation	Description
AD	Antiproton Decelerator
AI	Adiabatic Ionization
AO	Atomic Orbitals
ASACUSA	Atomic Spectroscopy And Collisions Using Slow Antiprotons
BGM	Basis-Generator Method
BO	Born-Oppenheimer
CC	Close-Coupling
CDW	Continuum Distorted Wave
CERN	Conseil Européen pour la Recherche Nucléaire European Organization for Nuclear Research
CGC	Clebsch Gordan Coefficients
CI	Configuraton-Interaction
CME	Coupling Matrix Elements
CPT	Charge conjugation, Parity change, Time reversal
COLTRIMS	Cold Target Recoil Ion Momentum Spectroscopy
CTMC	Classical Trajectory Monte-Carlo method
DCS	Differential Cross Section
DFT	Density-Functional Theory
DVR	Discrete-Variable Representation
DW	Distorted-Wave
ECTMC	Eikonal Classical Trajectory Monte Carlo
EE	Excitation Energies
END	Electron Nuclear Dynamics
FC	Franck-Condon
FIM	Forced-Impulse Method
IEM	Independent-Electron Model
IEV	Independent-EVent model
IMPACT_MONO	IMpact PArameter Calculation Tool for Molecular ONe electron Orbitals
IMPACT_MOT	IMpact PArameter Calculation Tool for Molecules with Two electrons
IMPACT_ONE	IMpact PArameter Calculation Tool for ONe Electron

Abbreviation	Description
IPM	Independent-Particle Model
LEAR	Low Energy Antiproton Ring
LHC	Large Hadron Collider
LTDCC	Lattice Time-Dependent Close-Coupling
LVB	Low-Velocity Bohr stopping model
MEAOCC	Many-Electron Atomic-Orbital Close-Coupling
MEHC	Many-Electron Hidden Crossing
MFIM	Multi-cut Forced Impulse Method
MO	Molecular Orbitals
NIST	National Institute of Standards and Technology
ODP	Optimized Dynamical Pseudostates
OEAOCC	One-Electron Atomic-Orbital Close-Coupling
QMTI	Quantum-Mechanical Time-Independent
$\bar{p}$	Antiproton
p	Proton
PSS	Perturbed-Stationary-State
SAE	Single-Active Electron
SCA	SemiClassical Approximation
SCTD	SemiClassical Time-Dependent
TCS	Total Cross Section
TDDFT	Time-Dependent Density Functional Theory
TDSE	Time-Dependent Schrödinger Equation
TM	(dipole) Transition Moments

Acknowledgments

First of all I am very grateful to PD Dr. Alejandro Saenz for proposing the interesting topic to me as well as for his supervision during my time as a PhD student in his group. At any time he found the right balance between freedom and guidance which led to pleasant but also productive working conditions. He was helping me a lot by trying to answer any kind of request in the most conclusive and intuitive way and was not even rejecting the simplest questions.

Also, I am very much obliged to the *Bundesminesterium für Bildung und Forschung* for the financial support facilitating this work as a part of the *FLAIR Horizon* project.

I would like to thank all members of the AMO group for the pleasant atmosphere and for all the discussions on physics as well as on many other topics which helped me to broaden my horizon. I am indebted to Manohar and Yulian for carefully proof-reading parts of my thesis.

Furthermore, I would like to acknowledge the open, friendly, and stimulating correspondences with the professors Tom Kirchner, Helge Knudsen, and Franz Kottmann including also intensive discussions on experimental and theoretical details and the exchange of unpublished data. I am also grateful to the kind and very helpful explanations given by the professors Evandro Lodi Rizzini, Hans Jürgen Lüdde, and Gregor Schiwietz.

I would like to thank my parents for their long-lasting support from the very first moment and for providing the conditions to evolve my personal beliefs and interests.

Finally, my love goes to my wife Inga and to my sons Clemens and Johann. I would like to express my deepest gratitude to my family for their unlimited support and love. They have been appreciative of my innermost desire to expand my understanding of the world surrounding us.

Bibliography

[1] A. Lühr and A. Saenz. Antiproton and proton collisions with the alkali-metal atoms Li, Na, and K. *Phys. Rev. A*, 77:052713, 2008.

[2] A. Lühr and A. Saenz. Antiproton collisions with molecular hydrogen. *Phys. Rev. A*, 78:032708, 2008.

[3] A. Lühr, Y. V. Vanne, and A. Saenz. Parameter-free one-center model potential for an effective one-electron description of molecular hydrogen. *Phys. Rev. A*, 78: 042510, 2008.

[4] A. Lühr, N. Fischer, and A. Saenz. Interaction of antiprotons with Rb atoms and a comparison of antiproton stopping powers of the atoms H, Li, Na, K, and Rb. *Hyperfine Interact.*, 194:51, 2009.

[5] A. Lühr and A. Saenz. Collisions of low-energy antiprotons with molecular hydrogen: ionization, excitation and stopping power. *Hyperfine Interact.*, 194:59, 2009.

[6] A. Lühr and A. Saenz. Stopping power of antiprotons in H, H_2, and He targets. *Phys. Rev. A*, 79:042901, 2009.

[7] A. Lühr and A. Saenz. Collisions of antiprotons with hydrogen molecular ions. *Phys. Rev. A*, 80:022705, 2009.

[8] A. Lühr and A. Saenz. Full two-electron calculations of antiproton collisions with molecular hydrogen. *Phys. Rev. A*, 81:010701(R), 2010.

[9] HIT (Heavy Ion Therapy). Heidelberger Ionenstrahl-Therapiezentrum. `http://www.klinikum.uni-heidelberg.de/Startseite-HIT.113005.0.html`, 2010.

[10] ASACUSA. Atomic Spectroscopy And Collisions Using Slow Antiprotons. `http://www.cern.ch/ASACUSA`, 2009.

[11] ATHENA. ApparaTus for High-precision Experiments on Neutral Antimatter. `http://athena.web.cern.ch/athena`, 2009.

[12] ALPHA. Antihydrogen Laser PHysics Apparatus. `http://alpha.web.cern.ch/alpha/`, 2009.

[13] ATRAP. Antimatter TRAP. `http://hussle.harvard.edu/~atrap/`, 2009.

[14] AEGIS. Antimatter Experiment: Gravity, Interferometry, Spectroscopy. `http://aegis.web.cern.ch/aegis/home.html`, 2009.

[15] G. Gabrielse, N. S. Bowden, P. Oxley, A. Speck, C. H. Storry, J. N. Tan, M. Wessels, D. Grzonka, W. Oelert, G. Schepers, T. Sefzick, J. Walz, H. Pittner, T. W. Hänsch, and E. A. Hessels. Background-free observation of cold antihydrogen with field-ionization analysis of its states. *Phys. Rev. Lett.*, 89:213401, 2002.

[16] M. Amoretti, C. Amsler, G. Bonomi, A. Bouchta, P. Bowe, C. Carraro, C. L. Cesar, M. Charlton, M. J. T. Collier, and M. Doser et al. Production and detection of cold antihydrogen atoms. *Nature*, 419:456, 2002.

[17] N. Kolachevsky, M. Fischer, S. G. Karshenboim, and T. W. Hänsch. High-precision optical measurement of the 2s hyperfine interval in atomic hydrogen. *Phys. Rev. Lett.*, 92:033003, 2004.

[18] T. W. Hänsch, J. Alnis, P. Fendel, M. Fischer, C. Gohle, M. Herrmann, R Holzwarth, N. Kolachevsky, Th. Udem, and M. Zimmermann. Precision spectroscopy of hydrogen and femtosecond laser frequency combs. *Phil. Trans. R. Soc. A*, 363:2155–2163, 2005.

[19] M. Hori, J. Eades, R. S. Hayano, T. Ishikawa, J. Sakaguchi, E. Widmann, H. Yamaguchi, H. A. Torii, B. Juhász, D. Horváth, and T. Yamazaki. Sub-ppm laser spectroscopy of antiprotonic helium and a CPT-violation limit on the antiprotonic charge and mass. *Phys. Rev. Lett.*, 87:093401, 2001.

[20] Toshimitsu Yamazaki, Norio Morita, Ryugo S. Hayano, Eberhard Widmann, and John Eades. Antiprotonic helium. *Phys. Rep.*, 366:183 – 329, 2002.

[21] Ryugo S. Hayano, Masaki Hori, Dezso Horvath, and Eberhard Widmann. Antiprotonic helium and CPT invariance. *Reports on Progress in Physics*, 70:1995–2065, 2007.

[22] G. Bonomi and AEGIS collaboration. Measuring the antihydrogen fall. *Hyperfine Interact.*, 193:297, 2009.

[23] H. Knudsen and J. F. Reading. Ionization of atoms by particle and antiparticle impact. *Phys. Rep.*, 212:107, 1992.

[24] FAIR. Facility for Antiproton and Ion Research. `http://www.gsi.de/fair/`, 2010.

[25] FLAIR. Facility for Low-energy Antiproton and Ion Research. `http://www.gsi.de/fair/experiments/flair/index_e.html`, 2010.

[26] SPARC. Stored Particle Atomic Research Collaboration. `http://www.gsi.de/fair/experiments/sparc/`, 2010.

[27] C. P. Welsch and J. Ulrich. FLAIR – a facility for low-energy antiproton and ion research. *Hyperfine Interact.*, 172:71, 2007.

[28] B. Zygelman, Alejandro Saenz, P. Froelich, S. Jonsell, and A. Dalgarno. Radiative association of atomic hydrogen with antihydrogen at subkelvin temperatures. *Phys. Rev. A*, 63:052722, 2001.

[29] Svante Jonsell, Alejandro Saenz, Piotr Froelich, Bernard Zygelman, and Alexander Dalgarno. Stability of hydrogen–antihydrogen mixtures at low energies. *Phys. Rev. A*, 64:052712, 2001.

[30] Svante Jonsell, Alejandro Saenz, Piotr Froelich, Bernard Zygelman, and Alexander Dalgarno. Hydrogen–antihydrogen scattering in the Born-Oppenheimer approximation. *J. Phys. B*, 37:1195, 2004.

[31] E. A. G. Armour, Y. Liu, and A. Vigier. Inclusion of the strong interaction in low-energy hydrogen–antihydrogen scattering using a complex potential. *J. Phys. B*, 38:L47–L54, 2005.

[32] V. Sharipov, L. Labzowsky, and G. Plunien. Potential energy curves for excited states of the hydrogen–antihydrogen system. *Phys. Rev. Lett.*, 97:103005, 2006.

[33] A. Yu. Voronin and P. Froelich. Resonant phenomena in antihydrogen-hydrogen scattering. *Phys. Rev. A*, 77:022505, 2008.

[34] L. H. Andersen, P. Hvelplund, H. Knudsen, S. P. Møller, J. O. P. Pedersen, S. Tang-Petersen, E. Uggerhøj, K. Elsener, and E. Morenzoni. Single ionization of helium by 40 - 3000 keV antiprotons. *Phys. Rev. A*, 41:6536–6539, 1990.

[35] P. Hvelplund, H. Knudsen, U. Mikkelsen, E. Morenzoni, S. P. Møller, E. Uggerhøj, and T. Worm. Ionization of helium and molecular hydrogen by slow antiprotons. *J. Phys. B*, 27:925–934, 1994.

[36] L. H. Andersen, P. Hvelplund, H. Knudsen, S. P. Møller, K. Elsener, K. G. Rensfelt, and E. Uggerhøj. Single and double ionization of helium by fast antiproton and proton impact. *Phys. Rev. Lett.*, 57:2147–2150, 1986.

[37] L. H. Andersen, P. Hvelplund, H. Knudsen, S. P. Møller, A. H. Sorensen, K. Elsener, K.-G. Rensfelt, and E. Uggerhoj. Multiple ionization of He, Ne, and Ar by fast protons and antiprotons. *Phys. Rev. A*, 36:3612–3629, 1987.

[38] L. H. Andersen, P. Hvelplund, H. Knudsen, S. P. Møller, J. O. P. Pedersen, S. Tang-Petersen, E. Uggerhøj, K. Elsener, and E. Morenzoni. Non-dissociative and dissociative ionisation of H_2 by 50-2000 keV antiprotons. *J. Phys. B*, 23:L395, 1990.

[39] H. Knudsen, U. Mikkelsen, K. Paludan, K. Kirsebom, S. P. Møller, E. Uggerhøj, J. Slevin, M. Charlton, and E. Morenzoni. Ionization of atomic hydrogen by 30–1000 kev antiprotons. *Phys. Rev. Lett.*, 74:4627–4630, 1995.

[40] J. C. Wells, D. R. Schultz, P. Gavras, and M. S. Pindzola. Numerical solution of the time-dependent Schrödinger equation for intermediate-energy collisions of antiprotons with hydrogen. *Phys. Rev. A*, 54:593, 1996.

[41] K. A. Hall, J. F. Reading, and A. L. Ford. Excitation and ionization of atomic hydrogen by antiprotons. *J. Phys. B*, 29:6123, 1996.

[42] A. Igarashi, S. Nakazaki, and A. Ohsaki. Ionization of atomic hydrogen by antiproton impact. *Phys. Rev. A*, 61:062712, 2000.

[43] Kazuhiro Sakimoto. A theoretical study of ionization processes in low-energy collisions between antiprotons and atomic hydrogen using discrete-variable-representation methods. *J. Phys. B*, 33:3149–3164, 2000.

[44] B. Pons. Monocentric close-coupling expansion to provide ejected electron distributions for ionization in atomic collisions. *Phys. Rev. Lett.*, 84:4569–4572, 2000.

[45] B. Pons. Ability of monocentric close-coupling expansions to describe ionization in atomic collisions. *Phys. Rev. A*, 63:012704, 2000.

[46] Xiao-Min Tong, Tsutomu Watanabe, Daiji Kato, and Shunsuke Ohtani. Ionization of atomic hydrogen by antiproton impact: A direct solution of the time-dependent Schrödinger equation. *Phys. Rev. A*, 64:022711, 2001.

[47] Nobuyuki Toshima. Two- and one-center close-coupling calculations for ionization of atomic hydrogen by antiproton impact. *Phys. Rev. A*, 64:024701, 2001. doi: 10.1103/PhysRevA.64.024701.

[48] J. Azuma, N. Toshima, K. Hino, and A. Igarashi. B-spline expansion of scattering equations for ionization of atomic hydrogen by antiproton impact. *Phys. Rev. A*, 64:062704, 2001.

[49] S. Sahoo, S. C. Mukherjee, and H. R. J. Walters. Ionization of atomic hydrogen and He^+ by slow antiprotons. *J. Phys. B*, 37:3227–3237, 2004.

[50] L. A. Wehrman, A. L. Ford and J. F. Reading. Double ionization of helium by slow antiprotons. *J. Phys. B*, 29:5831–5842, 1996.

[51] J. F. Reading, T. Bronk, A. L. Ford, L. A. Wehrman, and K. A. Hall. Multicut forced impulse method single-ionization cross sections for slow antiprotons on helium. *J. Phys. B*, 30:L189–L195, 1997.

[52] G. Bent, P. S. Krstić, and D. R. Schultz. The multielectron, hidden crossings method for inelastic processes in slow ion/atom–atom collisions. *J. Chem. Phys.*, 108:1459–1474, 1998.

[53] T. G. Lee, H. C. Tseng, and C. D. Lin. Evaluation of antiproton-impact ionization of He atoms below 40 kev. *Phys. Rev. A*, 61:062713, 2000.

[54] T. Kirchner, M. Horbatsch, E. Wagner, and H. J. Lüdde. Modelling of polarization and correlation effects in the ionization of helium by antiprotons. *J. Phys. B*, 35: 925–934, 2002.

[55] Xiao-Min Tong, Tsutomu Watanabe, Daiji Kato, and Shunsuke Ohtani. Single ionization of helium by antiprotons: A case study by self-interaction-free time-dependent density-functional theory. *Phys. Rev. A*, 66:032709, 2002.

[56] D. R. Schultz and P. S. Krstić. Ionization of helium by antiprotons: Fully correlated, four-dimensional lattice approach. *Phys. Rev. A*, 67:022712, 2003.

[57] M. Keim, A. Achenbach, H. J. Lüdde, and T. Kirchner. Microscopic response effects in collisions of antiprotons with helium atoms and lithium ions. *Phys. Rev. A*, 67:062711, 2003.

[58] A. Igarashi, S. Nakazaki, and A. Ohsaki. Ionization cross sections of helium and hydrogenic ions by antiproton impact. *Nucl. Instrum. Methods Phys. Res. B*, 214: 135–138, 2004.

[59] S. Sahoo, S.C. Mukherjee, and H.R.J. Walters. Single ionization of helium by antiproton impact. *Nucl. Instrum. Methods Phys. Res. B*, 233:318, 2005.

[60] C. Stary, H. J. Lüdde, and R. M. Dreizler. Optical potential description of collisions of p and $\bar{\mathrm{p}}$ with alkali atoms. *J. Phys. B*, 23:263–277, 1990.

[61] M. McCartney and D. S. F. Crothers. The single ionization of multielectron atoms using the continuum-distorted-wave eikonal-initial-state model. *J. Phys. B*, 26: 4561–4574, 1993.

[62] T. Kirchner, M. Horbatsch, and H. J. Lüdde. Time-dependent independent-particle model calculation of multiple capture and ionization processes in p-Ar, $\bar{\mathrm{p}}$-Ar, and He^2-Ar collisions. *Phys. Rev. A*, 66:052719, 2002.

[63] A. L. Ford and J. F. Reading. Improved forced impulse method calculations of single and double ionization of helium by collision with high-energy protons and antiprotons. *J. Phys. B*, 27:4215–4227, 1994.

[64] Hiroyuki A Torii, N Kuroda, M Shibata, H Imao, Y Nagata, D Barna, M Hori, Y Kanai, A Mohri, V L Varentsov, and Y Yamazaki. Atomic collision experiment using ultra-slow antiproton beams. *J. Phys. Conf. Ser.*, 80:012022, 2007.

[65] H. Knudsen. private communication, 2009.

[66] N. Kuroda, H. A. Torii, K. Yoshiki Franzen, Z. Wang, S. Yoneda, M. Inoue, M. Hori, B. Juhász, D. Horváth, H. Higaki, A. Mohri, J. Eades, K. Komaki, and Y. Yamazaki. Confinement of a large number of antiprotons and production of an ultraslow antiproton beam. *Phys. Rev. Lett.*, 94:023401, 2005.

[67] M. B. Shah and H. B. Gilbody. Ionisation of H_2 by fast protons and multiply charged ions of He, Li, C, N and O. *J. Phys. B*, 15:3441–3453, 1982.

[68] M. B. Shah, P. McCallion, and H. B. Gilbody. Electron capture and ionisation in collisions of slow H^+ and He^{2+} ions with helium. *J. Phys. B*, 22:3037–3045, 1989.

[69] M. E. Rudd, R. D. DuBois, L. H. Toburen, C. A. Ratcliffe, and T. V. Goffe. Cross sections for ionization of gases by 5-4000 keV protons and for electron capture by 5-150 keV protons. *Phys. Rev. A*, 28:3244–3257, 1983.

[70] M. E. Rudd, Y. K. Kim, D. H. Madison, and J. W. Gallagher. Electron production in proton collisions: total cross sections. *Rev. Mod. Phys.*, 57:965–994, 1985.

[71] D. Elizaga, L. F. Errea, J. D. Gorfinkiel, C. Illescas, L. Méndez, A. Macías, A. Riera, A. Rojas, O. J. Kroneisen, T. Kirchner, H. J. Lüdde, A. Henne, and R. M. Dreizler. Theoretical analysis of electron capture and electron loss in $Be^{4+} + H_2$ and $H^+ + H_2$ collisions. *J. Phys. B*, 32:857–875, 1999.

[72] A. M. Ermolaev. The ratio R_i for nondissociative ionization of molecular hydrogen by antiproton/proton impact. *Hyperfine Interact.*, 76:335, 1993.

[73] Kazuhiro Sakimoto. Ionization of hydrogen molecular ions by antiproton impacts. *Phys. Rev. A*, 71:062704, 2005.

[74] H. Bethe. Zur Theorie des Durchgangs schneller Korpuskularstrahlen durch Materie. *Ann. Phys.*, 5:325, 1930.

[75] L. H. Andersen, P. Hvelplund, H. Knudsen, S. P. Møller, J. O. P. Pedersen, E. Uggerhøj, K. Elsener, and E. Morenzoni. Measurements of the Z_1^3 contribution to the stopping power using MeV protons and antiprotons: the Barkas effect. *Phys. Rev. Lett.*, 62:1731, 1989.

[76] M. Agnello, G. Belli, G. Bendiscioli, A. Bertin, E. Botta, T. Bressani, M. Bruschi, M. P. Bussa, L. Busso, D. Calvo, B. Cereda, P. G. Cerello, C. Cicalò, M. Corradini, S. Costa, S. De Castro, A. Donzella, A. Feliciello, L. Ferrero, A. Filippi, V. Filippini, A. Fontana, D. Galli, R. Garfagnini, B. Giacobbe, P. Gianotti, and A. Grasso. Antiproton slowing down in H_2 and He and evidence of nuclear stopping power. *Phys. Rev. Lett.*, 74:371–374, 1995.

[77] E. Lodi Rizzini, A. Bianconi, M. P. Bussa, M. Corradini, A. Donzella, L. Venturelli, M. Bargiotti, A. Bertin, M. Bruschi, M. Capponi, S. De Castro, L. Fabbri, P. Faccioli, D. Galli, B. Giacobbe, U. Marconi, I. Massa, M. Piccinini, M. Poli, N. Semprini Cesari, R. Spighi, V. Vagnoni, S. Vecchi, M. Villa, A. Vitale, A. Zoccoli, and O. E. Gorchakov. Barkas effect for antiproton stopping in H_2. *Phys. Rev. Lett.*, 89:183201, 2002.

[78] E. Lodi Rizzini, A. Bianconi, M.P. Bussa, M. Corradini, A. Donzella, M. Leali, L. Venturelli, N. Zurlo, M. Bargiotti, A. Bertin, M. Bruschi, M. Capponi, S. De

Castro, R. Dona, L. Fabbri, P. Faccioli, B. Giacobbe, F. Grimaldi, I. Massa, M. Piccinini, N. Semprini Cesari, R. Spighi, S. Vecchi, M. Villa, A. Vitale, A. Zoccoli, O.E. Gorchakov, G.B. Pontecorvo, A.M. Rozhdestvensky, V.I. Tretyak, M. Poli, C. Guaraldo, C. Petrascu, F. Balestra, L. Busso, O.Y. Denisov, L. Ferrero, R. Garfagnini, A. Grasso, A. Maggiora, G. Piragino, F. Tosello, G. Zosi, G. Margagliotti, L. Santi, and S. Tessaro. Antiproton stopping power in He in the energy range 1-900 keV and the Barkas effect. *Phys. Lett. B*, 599:190, 2004.

[79] A. Adamo, M. Agnello, F. Balestra, G. Belli, G. Bendiscioli, A. Bertin, P. Boccaccio, G. C. Bonazzola, T. Bressani, M. Bruschi, M. P. Bussa, L. Busso, D. Calvo, M. Capponi, C. Cicalò, M. Corradini, S. Costa, I. D'Antone, S. De Castro, F. D'Isep, A. Donzella, I. V. Falomkin, L. Fava, A. Feliciello, L. Ferrero, V. Filippini, and D. Galli. Antiproton stopping power in hydrogen below 120 keV and the Barkas effect. *Phys. Rev. A*, 47:4517–4520, 1993.

[80] F. Kottmann. Formation and deexcitation of $(\mu\mathrm{He})^+$ and μp atoms. In V. P. Dzelepov, editor, *Proc. 2nd Int. Symp. on Muon and Pion Interactions with Matter*, page 268, Dubna, 1987. Joint Institute for Nuclear Research.

[81] P. Hauser, F. Kottmann, Ch. Lüchinger, and R. Schaeren. Slowing down of negative muons in gaseous H_2 and determination of the stopping power. In L. A. Schaller and C. Petitjean, editors, *Muonic atoms and molecules*, page 235, Basel, 1993. Birkhäuser.

[82] F. Kottmann. Experiments with low-energy μ^- in H_2 and He gases. In C. Rizzo and E. Zavattini, editors, *Proc. Int. School of Physics of Exotic Atoms*, page 297, Trieste, 1994. INFN.

[83] R. Schmidt, H. Daniel, F.J. Hartmann, P. Hauser, F. Kottmann, M. Mühlbauer, C. Petitjean, W. Schott, D. Taqqu, and P. Wojciechowski. Measurement of the Barkas effect in hydrogen. *Euro. Phys. J. D*, 3:119, 1998.

[84] G. Schiwietz, U. Wille, R. Díez Muiño, P. D. Fainstein, and P. L. Grande. Comprehensive analysis of the stopping power of antiprotons and negative muons in He and H_2 gas targets. *J. Phys. B*, 29:307–321, 1996.

[85] Remigio Cabrera-Trujillo, John R. Sabin, Yngve Öhrn, and Erik Deumens. Stopping of swift antiprotons by hydrogen atoms and the Barkas correction. *Phys. Rev. A*, 71:012901, 2005.

[86] Ernesto R. Custidiano and Mario M. Jakas. Classical-trajectory Monte Carlo calculations of the electronic stopping cross section for keV protons and antiprotons impinging on hydrogen atoms. *Phys. Rev. A*, 72:022708, 2005.

[87] James S. Cohen. Slowing down and capture of negative muons by hydrogen: Classical-trajectory Monte Carlo calculation. *Phys. Rev. A*, 27:167–179, 1983.

[88] J. Ullrich, editor. *Ten Years Of Cold Target Recoil Ion Momentum Spectroscopy and Reaction Microscopes.* Max-Planck-Institut für Kernphysik, Heidelberg, 2007.

[89] B. H. Bransden and C. J. Joachain. *Physics of atoms and molecules.* Prentice Hall, England, 2003.

[90] Mitio Inokuti. Inelastic collisions of fast charged particles with atoms and molecules—The Bethe theory revisited. *Rev. Mod. Phys.*, 43:297–347, 1971.

[91] M. Kimura and C. D. Lin. Unified treatment of slow atom-atom and ion-atom collisions. *Phys. Rev. A*, 31:590–592, 1985.

[92] Mineo Kimura and Neal F. Lane. The low-energy, heavy-particle collisions—a close-coupling treatment. *Adv. At., Mol., Opt. Phys.*, 26:79, 1989.

[93] J. S. Briggs, P. T. Greenland, and E. A. Solov'ev. The capture of slow antiprotons in noble gases. *J. Phys. B*, 32:197–212, 1999.

[94] B. H. Bransden and M. R. C. McDowell. *Charge Exchange and the Theory of Ion-Atom Collisions.* Clarendon, Oxford, 1992.

[95] R. McCarroll and A. Salin. Impact parameter treatment of atomic collisions. *J. Phys. B*, 1:163–171, 1968.

[96] Myroslav Zapukhlyak. *Einblicke in die atomare Vielteilchendynamik von Streuprozessen durch ab-initio-Rechnungen.* PhD thesis, Technische Universität Clausthal, Germany, 2008.

[97] T. N. Chang and X. Tang. Photoionization of two-electron atoms using a nonvariational configuration-interaction approach with discretized finite basis. *Phys. Rev. A*, 44:232–238, 1991.

[98] T. N. Chang. B-spline based configuration-interaction approach for photoionization of two-electron and divalent atoms. In T. N. Chang, editor, *Many-body Theory of Atomic Structure and Photoionization*, page 213. World Scientific, Singapore, 1993.

[99] Amalia Apalategui. *Procesos moltifotónicos y su control en* H_2^+ *y* H_2. PhD thesis, Universidad de Sevilla, Spain, 2001.

[100] A. Apalategui, A. Saenz, and P. Lambropoulos. Effect of vibration and internuclear axis orientation on multiphoton ionization of H_2^+. *J. Phys. B*, 33:2791, 2000.

[101] Amalia Apalategui and Alejandro Saenz. Multiphoton ionization of the hydrogen molecule H_2. *J. Phys. B*, 35:1909, 2002.

[102] T. N. Chang. He photoionization to the doubly excited $(2pnd)$ and $(sp, 2n^-)$ $^1p_0$ series. *Phys. Rev. A*, 47:3441–3443, 1993.

[103] T. N. Chang and X. Tang. Atomic-structure effects in multiphoton ionization of magnesium. *Phys. Rev. A*, 46:R2209, 1992.

[104] Amalia Apalategui, Alejandro Saenz, and Peter Lambropoulos. Ab initio investigation of the phase lag in coherent control of H_2. *Phys. Rev. Lett.*, 86:5454, 2001.

[105] Carl de Boor. *A Practical Guide to Splines.* Springer, New York, 1978.

[106] J Sapirstein and W R Johnson. The use of basis splines in theoretical atomic physics. *J. Phys. B*, 29:5213, 1996.

[107] A. Burgess. The determination of phases and amplitudes of wave functions. *Proc. Phys. Soc.*, 81:442–452, 1963.

[108] Y. V. Vanne and A. Saenz. Ionization of H_2 in intense ultrashort laser pulses: parallel versus perpendicular orientation. *J. Mod. Opt.*, 55:2665, 2008.

[109] L. Wolniewicz. Relativistic energies of the ground state of the hydrogen molecule. *J. Chem. Phys.*, 99:1851, 1993.

[110] NIST (National Institue of Standards and Technology). `http://physics.nist.gov/PhysRefData/ASD/index.html`, 2008.

[111] A. Saenz and P. Froelich. Effect of final-state interactions in allowed β decays. I. General formalism. *Phys. Rev. C*, 56:2132, 1997.

[112] A. Saenz and P. Froelich. Effect of final-state interactions in allowed β decays. II. Reliability of the β-decay spectrum for T_2. *Phys. Rev. C*, 56:2162, 1997.

[113] L F Errea, J D Gorfinkiel, A Macías, L Méndez, and A Riera. Implementation of the sudden approximation eikonal method in ion - diatom collisions. *J. Phys. B*, 30:3855–3872, 1997.

[114] G. Staszewska and L. Wolniewicz. Adiabatic energies of excited ${}^1\Sigma_u$ states of the hydrogen molecule. *J. Mol. Spectrosc.*, 212:208, 2002.

[115] L. Wolniewicz and G. Staszewska. Excited ${}^1\Pi_u$ states and the ${}^1\Pi_u^+ \rightarrow X\,{}^1\Sigma_g^+$ transition moments for the hydrogen molecule. *J. Mol. Spectrosc.*, 220:45, 2003.

[116] L. Wolniewicz and G. Staszewska. ${}^1\Sigma_u^+ \rightarrow X\,{}^1\Sigma_g^+$ transition moments for the hydrogen molecule. *J. Mol. Spectrosc.*, 217:181, 2003.

[117] Annie Spielfiedel. Ab initio calculation of electronic transition moments for singlet excited states of the H_2 molecule. *J. Mol. Spectrosc.*, 217:162, 2003.

[118] Ikhlas Drira. Ab initio calculation of the electronic transition moments for excited states of the H_2 molecule. *J. Mol. Spectrosc.*, 198:52, 1999.

[119] I. Sánchez and F. Martín. Representation of the electronic continuum of H_2 with B-spline basis. *J. Phys. B*, 30:679, 1997.

[120] L. C. Lee, R. W. Carlson, and D. L. Judge. The absorption cross sections of H_2 and D_2 from 180 to 780 Å. *J. Quant. Spectrosc. Radiat. Transfer*, 16:873, 1976.

[121] Y. M. Chung, E.-M. Lee, T. Masuoka, and James A. R. Samson. Dissociative photoionization of H_2 from 18 to 124 eV. *J. Chem. Phys.*, 99:885–889, 1993.

[122] C. J. Latimer, K. F. Dunn, F. P. O'Neill, M. A. MacDonald, and N. Kouchi. Photoionization of hydrogen and deuterium. *J. Chem. Phys.*, 102:722, 1995.

[123] Yulian V. Vanne and Alejandro Saenz. Ionization of molecular hydrogen and deuterium by frequency-doubled Ti:sapphire laser pulses. *Phys. Rev. A*, 80:053422, 2009.

[124] F. Martín. Ionization and dissociation using B splines: photoionization of the hydrogen molecule. *J. Phys. B*, 32:R197, 1999.

[125] M. Klapisch. A program for atomic wavefunction computations by the parametric potential method. *Comput. Phys. Commun.*, 2:239, 1971.

[126] S. Magnier, M. Aubert-Frécon, J. Hanssen, and C. Le Sech. Two-electron wavefunctions for the ground state of alkali negative ions. *J. Phys. B*, 32:5639, 1999.

[127] Nicolas Fischer. *Wechselwirkung zwischen langsamen Antiprotonen und Alkali Atomen.* Bachelor thesis, Humboldt-Universität Berlin, Germany, 2008.

[128] M. Abramowitz and I. A. Stegun. *Handbook of Mathematical Functions with Formulas, Graphs, and Mathematical Tables.* Dover Publications, Inc., New York, 1970.

[129] Tien Chi Chen. Evaluation techniques for quantum mechanical integrals involving orthogonal polynomials. *J. Math. Phys*, 12(6):1035–1038, 1971.

[130] K. Rykhlinskaya and S. Fritzsche. Generation of Clebsch-Gordan coefficients for the point and double groups. *Comp. Phys. Comm.*, 174:903, 2006.

[131] William H. Press, Saul A. Teukolsky, William T. Vetterling, and Brian P. Flannery. *Numerical Recipes in Fortran 77, Second Edition (Vol. 1 of Fortran Numerical Recipes).* Cambridge University Press, Cambridge, 1986.

[132] M. McGovern, D. Assafrão, J. R. Mohallem, Colm T. Whelan, and H. R. J. Walters. Differential and total cross sections for antiproton-impact ionization of atomic hydrogen and helium. *Phys. Rev. A*, 79:042707, 2009.

[133] I. Sánchez and F. Martín. The doubly-excited states of the H_2 molecule. *J. Chem. Phys.*, 106:7720, 1997.

[134] M. Zapukhlyak, T. Kirchner, A. Hasan, B. Tooke, and M. Schulz. Projectile angular-differential cross sections for transfer and transfer excitation in proton collisions with helium. *Phys. Rev. A*, 77:012720, 2008.

[135] A. Bertin, M. Bruschi, M. Capponi, I. D'Antone, S. De Castro, A. Ferretti, D. Galli, B. Giacobbe, U. Marconi, M. Piccinini, N. Semprini Cesari, R. Spighi, S. Vecchi, A. Vezzani, F. Vigotti, M. Villa, A. Vitale, A. Zoccoli, M. Corradini, A. Donzella, E. Lodi Rizzini, L. Venturelli, A. Zenoni, C. Cicalò, A. Masoni, G. Puddu, and S. Serci. Experimental antiproton nuclear stopping power in H_2 and D_2. *Phys. Rev. A*, 54:5441–5444, 1996.

[136] Manohar Awasthi, Yulian V. Vanne, Alejandro Saenz, Alberto Castro, and Piero Decleva. Single-active-electron approximation for describing molecules in ultrashort laser pulses and its application to molecular hydrogen. *Phys. Rev. A*, 77: 063403, 2008.

[137] H. J. Lüdde and R. M. Dreizler. Method for the calculation of global probabilities for many-electron systems. *J. Phys. B*, 16:3973–3981, 1983.

[138] Y. D. Wang, C. D. Lin, N. Toshima, and Z. Chen. Ionization and charge transfer in collisions of highly charged ions with helium at low velocity. *Phys. Rev. A*, 52: 2852–2858, 1995.

[139] V. Sidis. Vibronic phenomena in collisions of atomic and molecular-species. *Adv. At., Mol., Opt. Phys.*, 26:161–208, 1989.

[140] L. F. Errea, J. D. Gorfinkiel, A. Macías, L. Méndez, and A. Riera. Implementation of the sudden approximation eikonal method in ion - diatom collisions. *J. Phys. B*, 30:3855, 1997.

[141] M. B. Shah and H. B. Gilbody. Single and double ionisation of helium by H^+, He^{2+} and Li^{3+} ions. *J. Phys. B*, 18:899–913, 1985.

[142] Friedrich Aumayr and Hannspeter Winter. Total single-electron-capture cross sections for impact of H^+, ${H_2}^+$, He^+, and Ne^+ (2–20 keV) on Li. *Phys. Rev. A*, 31: 67–71, 1985.

[143] F. Aumayr, M. Fehringer and H. Winter. Inelastic H^+-Li(2s) collisions (2-20 keV). I. Experimental methods and Li(2p) excitation. *J. Phys. B*, 17:4185–4199, 1984.

[144] M. Zapukhlyak, T. Kirchner, H. J. Lüdde, S. Knoop, R. Morgenstern and R. Hoekstra. Inner- and outer-shell electron dynamics in proton collisions with sodium atoms. *J. Phys. B*, 38:2353–2369, 2005.

[145] F. Aumayr, G. Lakits and H. Winter. Charge transfer and target excitation in H^+-Na(3s) collisions (2-20 keV). *J. Phys. B*, 20:2025–2030, 1987.

[146] M. Gieler, P. Ziegelwanger, F. Aumayr, H. Winter and W. Fritsch. Experimental and theoretical investigation of electron capture and target excitation in (1-20 keV) H^+-K collisions. *J. Phys. B*, 24:647–655, 1991.

[147] J. Schweinzer, R. Brandenburg, I. Bray, R. Hoekstra, F. Aumayr, R. K. Janev and H. P. Winter. Database for inelastic collisions of lithium atoms with electrons, protons, and multiply charged ions. *Atomic Data and Nuclear Data Tables*, 72: 239–273, 1999.

[148] D. Wutte, R. K. Janev, F. Aumayr, M. Schneider, J. Schweinzer, J. J. Smith, and H. P. Winter. Cross sections for collision processes of Li atoms interacting with electrons, protons, multiply charged ions, and hydrogen molecules. *Atomic Data and Nuclear Data Tables*, 65:155, 1997.

[149] T. Tabata, R. Ito, N. Yohta, S. Toshizo, S. Masao and S. Toshio. Analytic cross sections for charge transfer of hydrogen atoms and ions colliding with metal vapors. *Nucl. Instrum. Methods Phys. Res. B*, 31:375–381, 1988.

[150] T. J. Morgan, R. E. Olson, A. S. Schlachter, and J. W. Gallagher. Charge transfer of hydrogen ions and atoms in metal vapors. *J. Phys. Chem. Ref. Data*, 14:971, 1985.

[151] R. Brandenburg, J. Schweinzer, F. Aumayr and H. P. Winter. Li (2p←2s) excitation by impact of slow ions. *J. Phys. B*, 31:2585–2599, 1998.

[152] L. Nagy and S. Fritzsche. Inner-shell excitation of lithium by fast charged projectiles. *J. Phys. B*, 33:L495–L503, 2000.

[153] R. Shingal and B. H. Bransden. Charge transfer, target excitation and ionisation in H^++Na(3s) collisions. *J. Phys. B*, 20:4815–4825, 1987.

[154] Ashok Jain and Thomas G. Winter. Electron transfer, target excitation, and ionization in H^+ + Na(3s) and H^+ + Na(3p) collisions in the coupled-Sturmian-pseudostate approach. *Phys. Rev. A*, 51:2963–2973, 1995.

[155] R. Shingal, B. H. Bransden, A. M. Ermolaev, D. R. Flower, C. W. Newby and C.J. Noble. Charge transfer in H^+-Na^0 collisions: atomic orbital calculations. *J. Phys. B*, 19:309–320, 1986.

[156] Wolfgang Fritsch. Atomic-basis study of electron transfer in H^+ + Na and H^+ + K collisions. *Phys. Rev. A*, 30:1135–1138, 1984.

[157] H. Knudsen. private communication, 2008.

[158] James S Cohen. Capture of negative exotic particles by atoms, ions and molecules. *Rep. Prog. Phys.*, 67:1769–1819, 2004.

[159] S. Sahoo, R. Das, N. C. Sil, S. C. Mukherjee, and K. Roy. Ionization of multielectron atoms using Slater-type wave functions. *Phys. Rev. A*, 62:022716, 2000.

[160] H. Knudsen, H.-P.E. Kristiansen, H.D. Thomsen, U.I. Uggerhøj, T. Ichioka, S.P. Møller, N. Kuroda, Y. Nagata, H.A. Torii, H. Imao, Y. Yamazaki, M. Charlton, C.A. Hunniford, R.W. McCullough, H.H. Andersen, and K. Tökési. Ionization of helium and argon by very slow antiproton impact. *Phys. Rev. Lett.*, 101:043201, 2008.

[161] T. Bronk, J. F. Reading, and A. L. Ford. Intermediate-state dynamic correlation in the ionization of helium. *J. Phys. B*, 31:2477–2488, 1998.

[162] M. Foster, J. Colgan, and M. S. Pindzola. Fully correlated electronic dynamics for antiproton impact ionization of helium. *Phys. Rev. Lett.*, 100:033201, 2008.

[163] E. Lindroth, J. F. Reading, M. Idrees, and A. L. Ford. Dynamic correlation effects in K-shell hole production by fast protons. *J. Phys. B*, 26:4585–4598, 1993.

[164] Xiaoxu Guan and Klaus Bartschat. Complete breakup of the helium atom by proton and antiproton impact. *Phys. Rev. Lett.*, 103:213201, 2009.

[165] Nils Henkel, Matthias Keim, Hans Jürgen Lüdde, and Tom Kirchner. Density-functional-theory investigation of antiproton-helium collisions. *Phys. Rev. A*, 80: 032704, 2009.

[166] D. R. Hartree. *The Calculation of Atomic Structures.* Wiley, New York, 1957. section 2.5.

[167] W. Kolos and L. Wolniewicz. Accurate computation of vibronic energies and of some expectation values for H_2, D_2, and T_2. *J. Chem. Phys.*, 41:3674–3678, 1964.

[168] Isao Shimamura. Moleculelike metastable states of antiprotonic and mesic helium. *Phys. Rev. A*, 46:3776–3788, 1992.

[169] M. W. Gealy, G. W. Kerby, Y.-Y. Hsu, and M. E. Rudd. Energy and angular distributions of electrons from ion impact on atomic and molecular hydrogen. I. 20–114 keV H^++H_2. *Phys. Rev. A*, 51:2247–2255, 1995.

[170] R. Shingal and C. D. Lin. Orientation-dependent atomic model for electron transfer in ion-molecule collisions: Applications to H^++H_2 and He^{2+}+H_2. *Phys. Rev. A*, 40:1302–1309, 1989.

[171] R. K. Janev, E. A. Solov'ev, and D. Jakimovski. The mechanism of double ionization of helium by slow antiprotons. *J. Phys. B*, 28:L615–L620, 1995.

[172] I. Ben-Itzhak, Vidhya Krishnamurthi, K. D. Carnes, H. Aliabadi, H. Knudsen, U. Mikkelsen, and B. D. Esry. Ionization and excitation of hydrogen molecules by fast proton impact. *J. Phys. B*, 29:L21–L28, 1996.

[173] I. Ben-Itzhak, E. Wells, D. Studanski, Vidhya Krishnamurthi, K. D. Carnes, and H. Knudsen. Double and single ionization of hydrogen molecules by fast-proton impact. *J. Phys. B*, 34:1143–1161, 2001.

[174] Kazuhiro Sakimoto. Protonium formation in collinear collisions between antiprotons and hydrogen molecular ions: Quantum-classical hybrid method versus adiabatic approximation. *Phys. Rev. A*, 69:042710, 2004.

[175] Jorge Fernandez and Fernando Martín. Electron and ion angular distributions in resonant dissociative photoionization of H_2 and D_2 using linearly polarized light. *New J. Phys.*, 11:043020, 2009.

[176] H. Bethe. Bremsformel für Elektronen relativistischer Geschwindigkeit. *Z. Phys.*, 76:293, 1932.

[177] Walter H. Barkas, John N. Dyer, and Harry H. Heckman. Resolution of the Σ^--mass anomaly. *Phys. Rev. Lett.*, 11:26–28, 1963.

[178] Jens Lindhard. The Barkas effect — or Z_1^3, Z_1^4-corrections to stopping of swift charged particles. *Nucl. Instrum. Methods*, 132:1, 1976.

[179] S. P. Møller, A. Csete, T. Ichioka, H. Knudsen, U. I. Uggerhøj, and H. H. Andersen. Antiproton stopping at low energies: Confirmation of velocity-proportional stopping power. *Phys. Rev. Lett.*, 88:193201, 2002.

[180] A. Bianconi, M. Corradini, A. Cristiano, M. Leali, E. Lodi Rizzini, L. Venturelli, N. Zurlo, and R. Donà. Experimental evidence of antiproton reflection by a solid surface. *Phys. Rev. A*, 78:022506, 2008.

[181] E. Lodi Rizzini. private communication, 2008.

[182] H. H. Andersen and J. F. Ziegler. *Hydrogen Stopping Powers and Ranges in All Elements.* Pergamon, New York, 1977.

[183] G. Schiwietz, P. L. Grande, C. Auth, H. Winter, and A. Salin. Angular dependence of energy loss in proton-helium collisions. *Phys. Rev. Lett.*, 72:2159, 1994.

[184] Pablo D. Fainstein, Victor H. Ponce, and Roberto D. Rivarola. Z_P^3 effects in the ionization of helium by ion impact. *Phys. Rev. A*, 36:3639–3641, 1987.

[185] M. M. Basko. On the low-velocity limit of the Bohr stopping formula. *Euro. Phys. J. D*, 32:9, 2005.

[186] P. L. Grande and G. Schiwietz. Coupled-channel calculations of the electronic energy loss. *Nucl. Instrum. Methods Phys. Res. B*, 132:264, 1997.

[187] Yulian V. Vanne and Alejandro Saenz. Numerical treatment of diatomic two-electron molecules using a B-spline based CI method. *J. Phys. B*, 37:4101, 2004.

[188] Richard F. Wallis, Robert Herman, and Harold Willis Milnes. Energy levels of an electron in the field of a finite dipole. *J. Mol. Spectrosc.*, 4:51, 1960.

[189] P. Decleva, A. Lisini, and M. Venuti. Multichannel continuum states by a least-squares approach in a spline basis: application to He and H^- photoionization. *J. Phys. B*, 27:4867, 1994.

[190] P. Lambropoulos, P. Maragakis, and Jian Zhang. Two-electron atoms in strong fields. *Phys. Rep.*, 305:203, 1998.

[191] John B. Delos. Theory of electronic transitions in slow atomic collisions. *Rev. Mod. Phys.*, 53:287–357, 1981.

[192] H. S. W. Massey and R. A. Smith. The passage of positive ions through gases. *Proc. R. Soc. London, Ser. A*, 142:142–172, 1933.

[193] B. Zygelman. Non-Abelian geometric phase and long-range atomic forces. *Phys. Rev. Lett.*, 64:256–259, 1990.

[194] B. Zygelman, D. L. Cooper, M. J. Ford, A. Dalgarno, J. Gerratt, and M. Raimondi. Charge transfer of N^{4+} with atomic hydrogen. *Phys. Rev. A*, 46:3846–3854, 1992.

[195] O. J. Kroneisen, H. J. Lüdde, T. Kirchner, and R. M. Dreizler. The basis generator method: optimized dynamical representation of the solution of time-dependent quantum problems. *J. Phys. A*, 32:2141–2156, 1999.

[196] Hans Jürgen Lüdde, Tobias Spranger, Marko Horbatsch, and Tom Kirchner. Non-perturbative, quantum-mechanical approach to ion collisions from molecular targets. *Phys. Rev. A*, 80:060702, 2009.

List of Figures

List of Tables

Selbständigkeitserklärung

Ich erkläre, dass ich die vorliegende Arbeit selbständig und nur unter Verwendung der angegebenen Literatur und Hilfsmittel angefertigt habe.

Berlin, den 04.01.2010 Armin Lühr